UNIVERSIDAD CARLOS III DE MADRID

Escuela Politécnica Superior - Leganés

DEPARTAMENTO DE TEORÍA DE LA SEÑAL Y COMUNICACIONES

DOCTORAL THESIS

IMPROVING THE CAPABILITIES FROM THE ANTENNA POINT OF VIEW AT THZ AND SUB-THZ FREQUENCIES

AUTHOR

Javier Montero de Paz

ADVISOR

Daniel Segovia Vargas

Tesis Doctoral: IMPROVING THE CAPABILITIES FROM THE ANTENNA POINT OF VIEW AT THZ AND SUB-THZ FREQUENCIES

Autor: Javier Montero de Paz

Director: Dr. Daniel Segovia Vargas

El tribunal nombrado para juzgar la tesis doctoral arriba citada, compuesto por los doctores

Presidente: Dr. Jordi Romeu Robert

Vocal: Dr. Yi Huang

Secretario: Dr. Luis Emilio García Castillo

acuerda otorgarle la calificación de

Leganés, a 23 de Julio de 2014

A mis amigos,
A mi familia,
A Marun, Edu y Julia

Por mucho que vuelvo
No encuentro mis recuerdos.
Los busco, los sueño;
Lo propio ya es ajeno.
Cayeron los bordes
Y el vaso ya está lleno.
Y ahora sólo intento vaciar
Sólo necesito despegar.
Fue tan largo el duelo que al final
Casi lo confundo con mi hogar.

Vetusta Morla - Cuarteles de Invierno

CONTENTS

AGRADECIMIENTOS / ACKNOWLEDGEMENTS

En este apartado me gustaría mencionar a todas aquellas personas que deberían ir junto a mí en la portada como autores pero que, por falta de espacio, no es posible incluir. Sin su ayuda, consejos o ánimos, nada de lo que aquí se publica podría haberse llevado a cabo. Por todo ello, infinitas gracias de corazón a todos vosotros.

Muchísimas gracias a Dani, mi director de tesis, por haberme dado la oportunidad de trabajar con un grupo humano tan excepcional. Muchas gracias por confiar en mí desde el primer momento y por proporcionarme todos los medios a tu alcance para conseguir escribir una tesis.

Gracias de corazón a Quique, mi director "no oficial", porque si no hubiese sido capaz de acabar la tesis sin la ayuda que me has dado yo sería una "mierda" como doctorando. Gracias por todos los consejos, por mantenerme siempre activo y por enseñarme a "meter la pierna larga y tal."

Muchas gracias al resto de miembros del GREMA, Álex, Sergio, Marta y Fran y muy especialmente a Luise, gracias al cual he podido disfrutar de una beca FPU estos últimos años.

Y ya que estamos con los agradecimientos dentro del grupo, no podría olvidarme de todos mis compañeros con los que he compartido tan buenos momentos en nuestra fortaleza particular, el 4.2E01.

Gracias a Óscar, Belén, Álex y Mario por los buenos momentos compartidos.

Gracias a Javi Herráiz por ser un profesional como la copa de un pino. Ojalá puedas crecer dentro del grupo y poner un poco de orden por aquí.

Gracias a Rubén, porque la universidad, y el departamento en concreto, no sabe lo que hace dejando que se vaya alguien tan excepcional como tú.

Gracias a Nacho por todas las conversaciones a primera hora de la mañana con un café en la mano y por todas las anécdotas. Todo grupo debería tener a alguien como Nacho.

Gracias a Adri por ser un tío "sensacional". Porque su llegada al laboratorio supuso un golpe de aire fresco y porque con su energía es capaz de mover montañas.

Gracias a Fercho, el gatuno para nosotros, porque no he conocido a un tío tan "positivo" en mi vida. Gracias por tener siempre una sonrisa y ver la vida desde el lado bueno.

Y por supuesto infinitas gracias a mis Awololooooo. Esos días sufriendo en la bici por el norte nos unieron de una manera muy especial y estoy orgulloso de poder decir que tengo unos amigos como vosotros. Aunque no seáis conscientes, no sabéis todo lo que me habéis ayudado.

Gracias a Iván, o Sr. Fernández, según corresponda. Por ser un tío que sabe de todo y que es capaz de resolver cualquier problema. Siempre que tengo cualquier duda, eres mi primera opción. Me alegré mucho cuando no te fuiste a Alemania.

Gracias a Edu, por ser una de las personas con el corazón más grande y, de largo, la persona más inteligente que conozco. Me hace muy feliz ver que poco a poco vas reconduciendo tu vida. Y muchas gracias por tus consejos cuando más los necesitaba.

Y gracias a Doñoro, mi compañero de fatigas, por todas esas sesiones de spinning, por esos partidos de baloncesto, y por esas comidas en la

universidad. Ojalá no tengas que irte tan lejos a trabajar, pero vayas donde vayas estoy convencido de que te irá genial, porque te lo mereces.

Como muy bien me dijo Edu una vez, "... espero que encontremos algo que nos haga felices y podamos dedicarnos tranquilamente a pedalear y a tomar cubatas todos juntos..."

Gracias a mis compañeros de sufrimiento en las clases de spinning de Nacor. Paco, Jose Ignacio, Gregor, Ara, Juanma, y tantos otros... Lo que no nos mata nos hace más fuertes! Y gracias muy especiales a Nacor, porque sus clases han supuesto una descarga de adrenalina y, algún día, la única motivación para venir a trabajar.

Muchas gracias al Grupo de Optoelectrónica y Tecnología Laser de la UC3M. En especial al grupo del Dr. Pablo Acedo junto con la Dra. Cristina de Dios y el Dr. Ángel Rubén Criado. Disfruté mucho en los trabajos que compartimos y en algún que otro viaje que coincidimos.

Asimismo muchísimas gracias al Dr. Guillermo Carpintero y a Álvaro Jiménez. Al primero por darme la oportunidad de colaborar en iPHOS y ayudarme a conseguir publicar parte del trabajo de esta tesis. Al segundo por los buenos ratos en el laboratorio.

Thank you so much to all the people from Darmstadt, specially to Ahmed, Sihab, Ion, Christian, Margarita, Matthias, Daniel, Jaqueline, ...

Thank you to Prof. Hans Hartnagel for supervising my stage at TU Darmstadt in the summer of 2011.

Special thanks to Dr. Oleg Cojocari, for reviewing this thesis and for letting me work with him and his team on ACST GmbH.

And of course, thank you so much to Daniel Schönherr. You made me feel as if I were home while I was in Darmstadt. And you helped me so much with the work I did there. I was so lucky to have met you.

I also want to thank Prof. Antti Räisänen and Prof. Zbynek Raida for reviewing this Ph.D. dissertation. All their very constructive comments have helped to improve the quality of this work.

Thank you to all the people from Erlangen University, specially to Prof. Gottfried Döhler, Dr. Sascha Preu and Dr. Stefan Malzer for their help with the LAE devices.

Muchas gracias al Dr. Iván Cámara Mayorga por su ayuda en la fabricación y medidas del prototipo a 1 THz de la antena "meander".

Thank you very much to the people of Rutherford Appleton Laboratory in the UK, specially to Prof. Peter Huggard and Dr. Jamie Crooks for their work on the CMOS detectors.

También me gustaría agradecer a mis compañeros de la carrera por todos esos años que compartimos y porque después de aquello sigamos siendo amigos.

Gracias a Juan y Ester por ser como sois. Aunque ahora nos veamos menos yo os sigo queriendo igual.

Y por supuesto gracias a Guille. Es una pena que una persona tan válida y con tantas inquietudes como tú se tenga que ir fuera de España a ganarse la vida. Gracias por todas esas conversaciones, por ayudarme siempre que lo he necesitado y por todos tus consejos. Estoy convencido de que vayas donde vayas te irá bien y solo espero poder seguir viéndote de vez en cuando y seguir compartiendo momentos tan grandes como los que hemos pasado.

Un millón de gracias a Cris por iluminar con tu sonrisa días oscuros. Has sido de lo mejor que me ha pasado este último año.

Como no podía ser de otra manera, infinitas gracias a todos los Plavi.

Gracias a Jaime y a Mario por tantos años jugando juntos y compartiendo batallitas.

Gracias a Rober, porque ha nacido una rivalidad en el pádel que espero que dure mucho. ¡Y por tener una casa que es un talismán en los grandes momentos!

Gracias a Diego, porque aunque estés lejos se te sigue queriendo igual y se te echa de menos.

Gracias a Dieguito por todas tus historias semanales que nos arrancan una sonrisa y por estar siempre ahí.

Gracias a Ruper, por enseñarme que lo importante de la vida son las pequeñas cosas. Me alegro mucho de que la vida te vaya tan bien.

Y por supuesto, gracias a Marco. Nunca seré consciente ni de una milésima parte de lo que tengo con tu amistad. Gracias por estar conmigo 27 años que ojalá sean más. Gracias por tener un corazón como el que tienes. Porque es genial tener a alguien con el que no necesites hablar para quedar. Porque me encantan nuestras rutinas.

Muchísimas gracias a toda la familia de Ángela. Gracias en especial a Elo, Ricardo, Miguel, la abuela Elo, Vicky, Miguel, Ana y Mois. Gracias por tratarme como me habéis tratado todos estos años, por hacerme sentir parte de vuestra familia y cuidarme tanto. Siento que no nos hayamos visto mucho este tiempo, pero que sepáis que os he echado de menos.

Y gracias en especial a Ángela. Porque las cosas nunca salen como uno tiene pensado, pero me hace muy feliz saber que lo que tuvimos fue tan fuerte que después de todo podemos seguir mirándonos a los ojos y sonreír. No sería lo que soy si no fuera por ti.

También muchísimas gracias a toda mi familia.

Gracias a Ricardo, Almudena, Richi y Miguel, porque dicen que la infancia es la época más feliz de la vida y siempre que recuerdo la mía estáis todos vosotros.

Gracias a la abuela Gabi, por todos los desayunos y comidas que siempre preparaste para mí y por ser todo un ejemplo a seguir con tus 92 años.

Gracias a la familia de Paz, porque aunque las enfermedades no nos están tratando muy bien últimamente, nuestras reuniones familiares son la envidia de todo el mundo. Gracias al abuelo Pepe, Mariví, Ángel, Paco, Vivi, Arancha, Yerai, Angelines, Jose Luis, Nacho, Rober, Julio y Ethan.

Gracias a María y a Javi, por ser la mejor pareja que conozco. Estoy convencido de que esta nueva etapa que empezáis va a ser la mejor de vuestra vida.

Y finalmente, gracias a Julia, Edu y Marun.

A ti Julia por ser la única persona que entiende como pienso. Por disfrutar de la vida de la manera que lo haces. Porque te afectan más los problemas ajenos que los propios. Y por ser tan especial para mí como eres.

A ti Edu por haber tenido una confianza ciega en mí. Por apoyarme siempre en todos los pasos que he dado. Por tener siempre buena cara y una paciencia infinita. Por esa sonrisa permanente en tu cara.

Y a ti Marun, porque no conozco a nadie que se preocupe más por los demás que tú. Gracias por ser como eres y por todo el tiempo que dedicas a los demás. Porque ya es hora de que alguien te lo agradezca. GRACIAS.

A todos vosotros, sé que no soy muy expresivo y que no lo digo muchas veces, pero sois o habéis sido importantísimos en mi vida y este trabajo me gustaría compartirlo con todos vosotros. Gracias de corazón.

Javi

RESUMEN

El objetivo de la presente tesis es mejorar las prestaciones de subsistemas (emisores y detectores) y sistemas (sistema de enfoque) en el rango de Terahercios (THz) y sub-THz desde el punto de vista de antena. En esta tesis, se ha demostrado que actuando únicamente sobre la antena se pueden obtener dispositivos con un mejor rendimiento (potencia emitida incrementada en emisores y responsividad mejorada en detectores).

La presente tesis se ha centrado en el análisis y diseño de antenas planas, y para ello se ha estudiado su comportamiento a frecuencias de THz y sub-THz. Obteniendo los diagramas de radiación de antenas planas sobre sustrato semi-infinito se ha observado una anomalía en el diagrama de radiación que no tiene significado físico, pero que aparece en todas las publicaciones que tratan este tema. El origen de esta anomalía se explica en el presente trabajo. Asimismo se ha diseñado un programa capaz de obtener de una manera rápida y precisa el diagrama de radiación de antenas planas que tienen como substrato una lente dieléctrica hiperhemiesférica.

Con respecto a sub-sistemas de THz y sub-THz se ha diseñado un emisor para generar señales de onda continua basado en "photomixers" a 1.05 THz de tal manera que la potencia transferida de éste a la antena sea maximizada. La mayor aportación es que se ha simplificado el diseño del mismo de tal manera que no hacen falta elementos externos (filtros,

etc.). Este emisor está previsto que sirva como oscilador local para un receptor heterodino en aplicaciones de radioastronomía. Con respecto a emisores de THz también se ha obtenido un circuito equivalente para obtener el diagrama de radiación basado en dipolos Hertzianos de los conocidos como "Large Area Emitters", que son dispositivos basados también en "photomixers" pero que no necesitan ningún tipo de antena para radiar potencia de THz.

Otras contribuciones importantes en esta tesis han sido el diseño de un receptor completo Quasi-Óptico basado en diodo Schottky trabajando en la banda E (60 GHz - 90 GHz) donde se ha maximizado la potencia entregada al diodo desde la antena. Este receptor está pensado para formar parte de un sistema de comunicaciones inalámbrico de muy alta velocidad. Dentro del apartado de receptores se ha diseñado también un receptor basado en Transistores de Efecto de Campo (FETs) y tecnología CMOS trabajando a 300 GHz.

Finalmente, se ha actuado sobre un sistema completo de enfoque para un radar a 300 GHz para aplicaciones de seguridad. La mayor contribución en este aspecto es que el sistema de enfoque, basado en dos espejos elípticos y uno plano, se ha diseñado de tal manera que el haz es capaz de escanear en un amplio rango sin apenas distorsión. Para ello se ha forzado que la distancia de escaneo se encuentre siempre en el foco del espejo de salida.

ABSTRACT

The main objective of this Ph.D. dissertation is to improve the capabilities of devices (emitters and detectors) and wireless systems (focusing system) at Terahertz (THz) and sub-THz frequencies from the antenna point of view. It has been proved that only acting over the antenna side, devices with better capabilities can be obtained (increased emitted power in emitters and improved responsivity in detectors).

This thesis is focused on the analysis and design of planar antennas, so their behaviour at THz and sub-THz frequencies has been studied. While obtaining the radiation pattern of planar antennas lying on semi-infinite substrate, an anomaly which appears in the radiation pattern has been observed. This anomaly does not have a physical meaning but appears in all the published papers. The origin of such anomaly is explained in this thesis. In addition, a program capable to obtain in an accurate way the radiation pattern of planar antennas lying on dielectric hyperhemispherical lenses has been designed.

Regarding THz and sub-THz sub-systems a continuous-wave photomixer based power emitter working at 1.05 THz has been designed in such a way that maximum power is transferred from the active device to the antenna. The main contribution is that the design has been simplified in such a way that no external elements (filters, etc.) are needed. This emitter is intended to be the local oscillator of a heterodyne detector for radioastronomy applications. In addition, an equivalent circuit

based on Hertzian dipoles to obtain the radiation pattern of the so-called "Large Area Emitters" has been derived. Such devices are photomixer based emitters with the main characteristic of not needing an antenna to emit terahertz power.

Other important contributions to this Ph.D. dissertation are the complete design of Quasi-Optical Schottky Barrier Diode receiver working within the E-Band (60 GHz - 90 GHz) where the power transferred from the antenna to the diode is maximized. This receiver will be part of a complete very high speed wireless communications system. Also in the detectors section, a CMOS Field Effect Transistor based receiver working at 300 GHz has been designed.

Finally, a work over a focusing system for a 300 GHz radar for security purposes has been done. The main contribution regarding this aspect is that the focusing system, based on two elliptical mirror and a plane one, has been designed in such a way that the beam is capable to scan over a very large area without distortion. To do so it has been imposed that the target distance is always placed at the focus of the output mirror.

LIST OF TERMS

AC	Alternating Current
AE	Antenna Emitter
AIA	Active Integrated Antenna
ALMA	Atacama Large Millimetre Array
ASE	Amplified Spontaneous Emission
BER	Bit Error Rate
BPM	Beam Propagation Method
BWO	Backward Wave Oscillator
CMOS	Complementary Metal Oxide Semiconductor
CPS	Coplanar Stripline
CPW	Coplanar Waveguide
CW	Continuous-Wave
DC	Direct Current
DCN	Deuterium Cyanide
DFTS	Dispersive Fourier-Transform Spectroscopy
DSB	Dual Side Band

DSB-SC	Double Side-Band Suppressed-Carrier
EDFA	Erbium Doped Fibre Amplifier
F/B	Front-to-back
FBW	Fractional Bandwidth
FEL	Free Electron Laser
FET	Field Effect Transistor
FIR	Far-Infrared
FIRST	Far Infrared Sub-millimetre Telescope
FNBW	First Null Beamwidth
GCPW	Grounded Coplanar Waveguide
GOTL	Optoelectronic and Laser Technology Group
GREMA	Radiofrequency, Electromagnetism, Microwaves and Antennas Group
GTD	General Theory of Diffraction
GUI	Graphical User Interface
HCN	Hydrogen Cyanide
HEB	Hot Electron Bolometer
HEMT	High Electron Mobility Transistor
HIFI	Heterodyne Instrument for the Far-Infrared
HPBW	Half Power Beamwidth
HR-Si	High Resistive Silicon
HS-PD	High Speed Photo Diode
IF	Intermediate Frequency
IMPATT	Impact Ionization Avalanche Transit-Time
iPHOS	Integrated Photonic Transceivers At Sub-Terahertz Wave Range for Ultra-Wideband Wireless Communications
IR	Infrared
IRAS	Infrared Astronomical Satellite
KAO	Kuiper Airbone Observatory
L-He	Liquid Helium
LAE	Large Area Emitter

LAQD	Large Area Quasi-Dipole
LNA	Low Noise Amplifier
LO	Local Oscillator
LT-GaAs	Low-Temperature grown GaAs
LTCC	Low-Temperature Co-firing Ceramic
MIM	Metal-Insulator-Metal
MMIC	Monolithic Microwave Integrated Circuits
MoM	Method-of-Moments
MOSFET	Metal Oxide Semiconductor Field Effect Transistor
MTP	Minimum Transmission Point
MZM	Mach-Zehnder Modulator
N-MOSFET	N channel MOSFET
NEP	Noise Equivalent Power
NRZ-OOK	Non-Return-to-Zero On-Off-Keying
OBPF	Optical Band-Pass Filter
OCS	Carbonyl Sulfide
PCB	Printed Circuit Board
PD	Photodiode
PO	Physical Optics
POW	Passive Optical Waveguide
QCL	Quantum Cascade Laser
QO	Quasi-Optical
RF	Radiofrequency
RMS	Root Mean Square
RoF	Radio-over-Fibre
RPM	Revolutions Per Minute
RTD	Resonant Tunnelling Diode
SBD	Schottky Barrier Diode
SEM	Scanning Electron Microscope
SIS	Superconductor-Insulator-Superconductor
SLL	Side Lobe Level

SMA	SubMiniature version A
SMF	Single Mode Fibre
SNR	Signal to Noise Ratio
SOFIA	Stratospheric Observatory for Infrared Astronomy
SP	Stationary Phase
SWR	Standing Wave Ratio
TDS	Time Domain Spectroscopy
TE	Transversal Electric
THz	Terahertz
TM	Transversal Magnetic
TRL	Thru-Reflect-Line
TUD	Technical University of Darmstadt
TUNNETT	Tunnel Injection Transit-Time
UC3M	Carlos III Univeristy in Madrid
UTC	Uni-Travelling-Carrier

PREFACE

Terahertz (THz) and sub-THz waves are finding a lot of applications in the last years and the Radiofrequency, Electromagnetism, Microwaves and Antennas Group (GREMA) of the Carlos III University in Madrid (UC3M) is involved in different research projects regarding these THz waves.

- "New Electronic and Optical Techniques for the development of Imaging Arrays (Cameras) in Millimetre Waves and Terahertz (THz)," Ministerio de Ciencia e Innovacion.
- "Integrated Photonic Transceivers At Sub-Terahertz Wave Range for Ultra-Wideband Wireless Communications (iPHOS)," European Commission, 7th Frame Program.
- "Terahertz Technology for Electromagnetic Sensing Applications-TERASENSE," Ministerio de Ciencia e Innovacion.
- "Development of an Integrated high Data Rate THz Wireless Communication system," Ministerio de Ciencia e Innovacion.

The first project is focused on the design of electronic and optical devices to develop imaging arrays at THz frequencies. The second one is an European project involving different European research groups to develop integrated photonic transceivers for ultra-wideband wireless communications at sub-terahertz frequencies. The last one is a Spanish project involving different Spanish research groups whose last aim is to design THz devices and to study THz waves to manufacture THz sensing systems.

Thanks to the participation on these projects the group has obtained interesting results and the first Ph.D. dissertation was recently presented:

- B. Andrés-García, "Enhancing the Radiated Power in the Terahertz Band," Ph.D. dissertation, Carlos III University, March, 2014.

In that thesis the developed work was focused on obtaining innovative techniques to enhance the radiated power at THz frequencies.

It is also important to mention the work developed by the Optoelectronic and Laser Technology Group (GOTL) of the UC3M working in close collaboration with GREMA during the last years. The following Ph.D. dissertation was also recently presented regarding photonic THz technology:

- Á. R. Criado Serrano, "New Photonic Architectures and Devices for Generation and Detection of Sub-THz and THz Waves," Ph.D. dissertation, Carlos III University, April, 2013.

The differences between the actual thesis in comparison with the previous ones is that its main objective is to improve the capabilities of devices and wireless systems at THz and sub-THz frequencies only acting over the antenna side. THz emitters and sub-THz detectors are improved by designing the antenna to enhance device capabilities. In addition, a full focusing system is designed with improved scanning capabilities.

After a brief introduction to THz waves and antennas in the first chapter of this thesis, the Chapter 2 is devoted to the radiation of planar antennas. Planar antennas are the most widely used kind of antennas nowadays because its easiness of manufacture and relatively low cost in comparison with other antenna topologies. New manufacture technologies such as Complementary Metal Oxide Semiconductor (CMOS), Low-Temperature Co-firing Ceramic (LTCC) or laser/mechanical drilling machines have contributed to the expansion of planar antennas. These antennas basically consist on a metal part which is printed over or inside a dielectric substrate. At lower frequencies, i.e. microwaves, the effect of such substrate is negligible because their thickness is not comparable with the working wavelength. But problems arise when we move to higher frequencies (millimetre or sub-millimetre band) because the effect of the substrate cannot be neglected any more. In order to analyse such effect, the radiation pattern of planar antennas on dielectric substrates at THz frequencies is analysed in the Chapter 2 of this Ph.D. dissertation. Different cases are studied: planar antennas lying on semi-infinite thickness substrate, planar antennas lying on finite thickness substrate and planar antennas lying in the middle of a finite thickness substrate. It will be shown that an anomaly appears at the critical angle when dealing with semi-infinite substrates and the reason of it will be explained. In addition, it will be noticed that radiation pattern is dramatically affected by the substrate and the use of dielectric lenses is highly recommended. Obtaining the radiation pattern of a planar antenna lying on a dielectric lens needs a very high number of computation resources and is time consuming. Also in this second chapter of the thesis a software to analyse such problems is developed. This chapter of the thesis has led to the publication of a JCR journal paper (first quartile) and a book chapter as well as a conference contribution.

In the third chapter of this Ph.D. dissertation Continuous-Wave (CW) THz emitters based on photomixers are presented and two are the main contributions to the state-of-the-art of such technology. The first one is an antenna design based on a meander dipole antenna which is designed in such a way that the THz power delivered from the photomixer to the antenna and then radiated is maximized. To do so, the antenna is forced to work out of its main resonance where it exhibits the optimal input impedance for the photomixer. This THz emitter is intended to be the local oscillator source of one of the heterodyne detectors in

the Stratospheric Observatory for Infrared Astronomy (SOFIA). The second contribution is to obtain a radiation equivalent circuit for the so-called Large Area Emitters (LAEs), which are an antenna free approach based on photomixers capable of, theoretically, provide high THz output power (only limited by the LAE area). Both works have been done in collaboration with the Max Planck Institute for Radioastronomy in Bonn, Germany (meander dipole antenna) and University of Erlangen-Nuremberg, Germany (LAEs). The main contributions related with the third chapter have been published or presented in 2 JCR journal papers (first quartile), 1 book chapter and 4 conferences.

The Chapter 4 is devoted to sub-THz detectors and the work developed consists on designing two direct detectors: a Quasi-Optical (QO) Schottky Barrier Diode (SBD) detector working within the E-Band (60 GHz - 90 GHz) and a plasma-wave Field Effect Transistor (FET) CMOS detector working at 300 GHz. A complete QO SBD receiver design and characterization is carried out in this chapter. The receiver is meant to take part of a very-high speed data wireless transmission system ($>$ 1 Gb/s) and is included in the iPHOS project previously presented. Regarding the FET direct detector, the very first steps for a 300 GHz receiver are presented. Its main application is an array for imaging applications (security). Both designs are formed from a planar antenna and a detector (either SBD or FET), with the possibility of including an optical device (lens). Their performance is improved by designing the antenna of each receiver in such a way that the total efficiency is maximized. The QO SBD detector work has been done in close collaboration with the Technical University of Darmstadt, Germany, where the author was on a three month stage in the summer of 2011, and ACST GmbH, also in Darmstadt. The work related with the CMOS FET detector has been carried out with the collaboration of Rutherford Appleton Laboratory in the UK. The main contributions related with the fourth chapter have been published or presented in 2 journal papers and 6 conferences.

In the fifth chapter a focusing system is designed for a 300 GHz radar for security purposes. While the previous chapters were focused on planar antennas, in this case a horn antenna and elliptical mirrors are used, thus leading to a more complex structure. On the other hand it can handle more power and provide better focusing capabilities. The main contribution of the chapter is to design the focusing system in such a

way that it can provide scanning capabilities but, at the same time, the beam is not distorted because it always works "in-focus". The focusing system consists of a horn antenna as feeding element, two elliptical mirrors and a plane one to provide beam-steering by rotation. Since the only mirror that is rotated to provide scanning capabilities is the plane one, the target distance is always at the output focus of the second elliptical mirror, so the beam is not distorted even for big displacements. In addition to the proposed system, the design methodology followed through the chapter is also relevant because it reduces computational time and effort, and obtained results are accurate enough. This work was included in the TERASENSE project presented before, and was the first attempt to design a focusing system for such project that always work in-focus. This chapter of the thesis has led to the publication of a journal paper and 2 conference contributions.

Finally, the main conclusions and future working lines are presented in the Chapter 6. The list of contributions resulting from the development of this thesis is shown in the *Publications* section at the end of this document.

CHAPTER 1

ANTENNAS IN THE THZ AND SUB-THZ REGIME

This chapter serves as a starting point of this Ph.D. dissertation where the reader can identify all the potentials this THz technology has. First, THz radiation is presented and some of the characteristics of THz waves are highlighted. In addition, a short historical background regarding THz waves research and its main achievements is included. Then, some of the most important applications of THz waves are commented.

Once the THz waves importance is highlighted, we will focus our attention to antennas, which is the main subject of the present Ph.D. dissertation. A short introduction to the antenna parameters is included in order to facilitate the understanding of some of the work that has been done. Finally, the main antenna topologies that are used in the THz regime are briefly explained. The design parameters of these antennas are commented and strengths and weaknesses of each type are highlighted.

The objective of this chapter is to introduce all the nomenclature and instruments that are used in this Ph.D. dissertation.

1.1 Introduction

Terahertz frequency band or electromagnetic signals at terahertz frequencies (0.3 THz - 3 THz) are receiving great attention in the electromagnetism community nowadays. THz frequency spectrum can be defined as the electromagnetic spectrum range with wavelengths between 1 mm and 100 µm (Figure 1.1). It is the frequency range in between the microwave band and the Infrared (IR) one, so the technologies of these two bands can be extrapolated to this frequency range as will be shown in Chapters 3 and 4. It is also called the sub-millimetre wavelength band.

At these frequencies, extremely short pulses can be generated, which are capable of obtaining high spatial resolutions, go across light opaque materials and visualize and identify microscopic structures by spectral analysis. Moreover, there exists a great interest in different applications of this technology such as defence and security, automobiles, biology and medicine [1].

In the next subsections the main characteristics of THz waves are briefly explained and main applications are highlighted. In addition, a historical background is included to mention the most important discoveries within this frequency range.

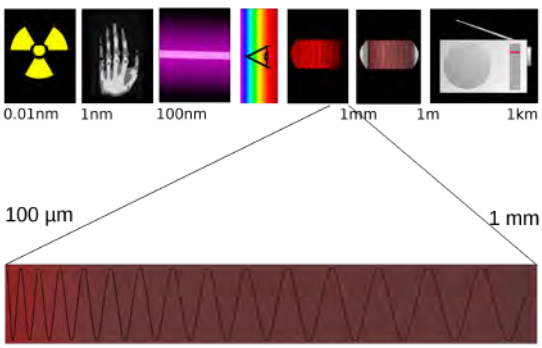

Figure 1.1: THz spectrum. Electromagnetic spectrum as a function of the wavelength with schematic of some applications.

1.1.1 THz Waves Characteristics

Frequently used units and their conversions at 1 THz are as follows:

- Frequency: $\nu = 1\,\mathrm{THz} = 1000\,\mathrm{GHz}$
- Angular frequency: $\omega = 2\pi\nu = 6.28\,\mathrm{THz}$
- Period: $\tau = 1/\nu = 1\,\mathrm{ps}$
- Wavelength: $\lambda = c/\nu = 0.3\,\mathrm{mm} = 300\,\mu\mathrm{m}$
- Wavenumber: $\bar{k} = k/2\pi = 1/\lambda = 33.3\,\mathrm{cm}^{-1}$
- Photon energy: $h\nu = \hbar\omega = 4.41\,\mathrm{meV}$
- Temperature: $T = h\nu/k_B = 48\,\mathrm{K}$

where c is the speed of light in vacuum, h is the Planck constant, and k_B is Boltzmann's constant.

The wave radiation at THz frequencies has the following characteristics [2]:

Penetration THz waves can go across common materials such as clothes and envelopes with a relatively low attenuation.

High Resolution Images THz wavelengths are small in comparison with microwave ones, so THz waves can be used to provide images with a sub-millimetre resolution.

Spectroscopy Most of the solid materials show characteristic spectral features in the 0.5 THz - 3 THz range. This allows that different chemical substances can be detected, even when they are sealed in a package or behind clothes.

Non-Ionizing THz radiation is non-ionizing and it can be used with very low power levels (µW) thanks to the availability of very high sensibility coherent detection schemes. This THz radiation characteristic makes it very suitable for medical and biological applications.

Intensity THz signals are much easier to focus and collimate than microwaves.

Despite all these really interesting characteristics of THz waves, there exist some drawbacks that have to be mentioned. For instance, atmospheric attenuation at these frequencies is really high and it is a critical point to develop sensors at THz frequencies in the Earth. In the Figure 1.2 the atmospheric attenuation as a function of frequency is depicted. It can be seen that there are certain frequencies within the THz range at which the attenuation is very high and should be avoided if the THz system is intended to be used in the Earth.

In addition, there exists the so-called "THz Gap" (which will be expanded in the Chapter 3). Although THz frequency band lies in the gap between microwave band and infrared band, the sources available in these two bands can not be used directly for THz range [4]. It is difficult to fabricate solid state sources in the THz range because the size becomes very small leading to very small power available. Also the efficiency of these sources drastically falls for higher THz range and the carrier transit time becomes very short compared to microwave frequency signals. On the other side, conventional laser sources are not available at THz band because suitable semiconductors are not available.

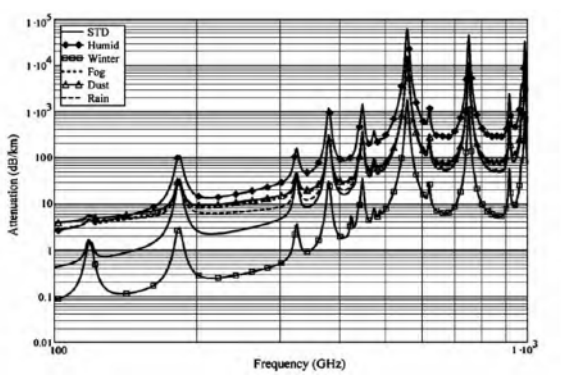

Figure 1.2: Atmospheric attenuation at pressures equivalent to sea level for 6 different conditions of humidity, temperature and atmospheric particles [3].

1.1.2 THz Historical Background

THz research started in the late 19th century and the beginning of the 20th. With no doubt, the main researcher on the topic during those years was German scientist Heinrich Rubens (1865 - 1922). Rubens' research concentrated on the extension of the IR spectral region to longer wavelengths into what soon became called the Far-Infrared (FIR). From 1892 to 1922, just 150 papers were published which included FIR research, and Rubens was author or co-author of more than 130 of them [5].

Figure 1.3: Heinrich Rubens.

During the early years of the 20th century, Hagen and Rubens showed that the reflectivity of metals depended on their electrical conductivity [6]. In 1910, R. W. Wood produced the first "blazed" diffraction grating, which allowed the concentration of the majority of light from a source into a single order and showed that gratings of this type could be used out to beyond 100 µm (3 THz) [7]. In 1911, Rubens and Baeyer showed that the mercury arc lamp (described in the Chapter 3 of the present work) in a quartz envelope was an excellent long-wavelength IR source [8]. Just before his death, Rubens was able to use all his spectroscopic skills to measure the absorption of water vapour out to 400 µm [9].

A year after H. Rubens' death, E. F. Nichols and J. D. Tear succeeded in joining the electric wave spectrum to the IR using a Hertzian oscillator for shorter wavelengths (220 µm) and a mercury arc source for longer ones (420 µm) [10]. In the 1930 - 1940 decade, several researches focus their attention on studying the absorption of gases in the 20 µm - 200 µm wavelength region [11–13] while during the World War II, perhaps, the most important improvement in the THz region was to extend the range of prism spectroscopy with new materials (up to 60 µm wavelength).

Figure 1.4: Ernest Fox Nichols.

After the war, one of the most significant advances was the introduction of the pneumatic detector ("Golay" [14]). Also in the 1940s, the first cooled bolometer was invented. This used the superconducting transition point of tantalum at 4.4 K, thus requiring the use of liquid helium [15]. In 1954, microwave spectroscopy was extended into the sub-mm region by Gordy's research group [16], thus providing a clear overlap with the longest wavelength IR spectroscopic systems. Walter Gordy was one of the most important researches in what he described as the "gap in the electromagnetic spectrum".

In 1959 the first convenient-to-use cooled device, the carbon bolometer, was invented [17] and the same year saw the first photoconductive detector to reach wavelengths longer than 100 µm [18]. Although no fundamental electronic source was produced for frequencies above 300 GHz in the 1950s, the first Backward Wave Oscillator (BWO) was designed [19]. Extension to higher frequencies followed in the 1960s and BWO are now available to above 1 THz, with a tuning range of 10 % of the centre frequency.

Figure 1.5: Marcel J.E. Golay.

Figure 1.6: Walter Gordy.

The 1960 decade was a very prolific time for sub-mm wave research. The main feature of this period is that it produced much of the instrumentation that is widely used today. Pyroelectric detectors date from this era as well as other detectors such as the n-InSb electron bolometer [20], the Ge bolometer [21], and a tunable FIR detector [22]. Another important step not only in the THz research but in the microwave was the invention of the so-called "honey-

comb" diode chip design for Schottky diode mixers by D. T. Young and J. C. Irvin [23]. But with no doubt, the major discovery at the start of this decade was the laser. The first THz laser, the water vapour laser, was invented in 1964 [24]. This decade was also the birth of Dispersive Fourier-Transform Spectroscopy (DFTS), which has proved to be a powerful technique for studying the optical constants of solids, liquids, and gases in the IR and THz regions [25]. At the end of the decade the Time Domain Spectroscopy (TDS) was born [26].

The year 1970 saw the arrival of one of the most useful laser sources, the optically excited THz gas laser [27]. This laser can produce hundreds of CW and many thousands of pulsed wavelengths throughout the THz region. The 1970s were the pioneering years for astronomy at THz frequencies, mainly because of significant progress in receivers and because high altitude observatories became available. Most notably, the Kuiper Airbone Observatory (KAO) started its operation in 1974. Another Helium cooled detector that dates from this era, and was to become very important, particularly for THz heterodyne systems, is the Superconductor-Insulator-Superconductor (SIS) mixer [28].

Figure 1.7: Kuiper Airborne Observatory (KAO).

The improvements in THz technology over the previous thirty years had led to a widespread recognition of the usefulness of this spectral region in many disciplines. But it was realized that heterodyne systems were required for these and other applications to achieve the necessary resolving power. The 1980s saw the first IR/THz space-borne observatory. The Infrared Astronomical Satellite (IRAS), launched in 1983, was the first observatory to perform an all-sky survey at IR wavelengths, including two THz bands around 60 µm and 100 µm. This was the first of a very successful series of space-borne IR/THz observatories. A fundamental source covering the frequency range from 1 THz to above 4 THz, invented in Russia and Japan in this decade, was the p-type Ge laser [29,30]. Operating at or near liquid helium temperature, this laser is a useful tunable pulsed source that can also be operated in near CW mode. Just before the close of this decade the first results of a new detector that was to

become widely used as a THz mixer were published by G. N. Goltsman and co-workers: the Hot Electron Bolometer (HEB) [31].

Figure 1.8: Infrared Astronomical Satellite (IRAS).

In the 1990's, the development of the optical communications and the higher bandwidth photomixers (photodiodes) produce a huge development of the photonic techniques for sub-THz and THz generation and detection that will continue up to nowadays. Although the THz Quantum Cascade Laser (QCL) appeared in 2002, the birth of the QCL technology was in this decade [32]. In addition, the first THz TDS imaging experiment was carried out [33] and a photodiode with a new structure (Uni-Travelling-Carrier (UTC) Photodiode (PD)) was developed [34], demonstrating a bandwidth of 70 GHz. The UTC was the first of several PD structures for sub-THz operation and was always linked to the development of the photonic CW sub-THz generation techniques.

1.1.3 THz Applications

THz and sub-THz detectors are finding a lot of applications nowadays, well together with an emitter on a THz/sub-THz system, well isolated to capture THz/sub-THz radiation from bodies all around the universe. Such applications range from THz/sub-THz communications, to material identification, cancer detection, imaging,...

Radioastronomy

THz waves play an important role in astrophysics due to the fact that THz radiation contains about half of the luminosity of the universe and 98% of all the photons emitted since the Big Bang. This importance is reflected in the number of missions that both European and American space agencies have launched in the last years regarding these THz/sub-THz waves. Herschel Space Observatory (formerly called Far

(a) **(b)** **(c)**

Figure 1.9: Some of the missions/projects currently undergoing related with astronomy and THz/sub-THz detection. (a) Herschel telescope, (b) Planck telescope and (c) ALMA observatory.

Infrared Sub-millimetre Telescope (FIRST)) is the only space observatory to cover a spectral range from the far infrared to sub-millimetre [35]. It has the largest single mirror ever built for a space telescope (3.5 metres in diameter) and will collect long-wavelength radiation from some of the coldest and most distant objects in the Universe. In addition, Planck was launched at the same time as Herschel telescope (February 2009) and is helping to provide answers to some of the most important questions in modern science: how did the Universe begin, how did it evolve to the state we observe today, and how will it continue to evolve in the future. Planck's objective is to analyse, with the highest accuracy ever achieved, the remnants of the radiation that filled the Universe immediately after the Big Bang - this we observe today as the Cosmic Microwave Background [36]. Back to the Earth, the biggest project regarding millimetre and sub-millimetre waves detection is the Atacama Large Millimetre Array (ALMA) [37]. ALMA will be the world's most powerful telescope for studying the Universe at sub-millimetre and millimetre wavelengths, on the boundary between infrared light and the longer radio waves.

An example of this kind of application is the THz emitter designed in the Chapter 3 of the present work.

Security

THz technology can be used in different security areas [38]. It can be used to detect and identify hidden explosives materials in an automated fashion without operator interpretation. Also, it can be used for screening people to detect metallic and non-metallic objects through clothing and other materials. This screening system would replace the current X-Ray systems which are available at airports or high-security areas [3]. In addition, they can investigate the contents of envelopes and paper packages without opening them. Finally, they can be used to detect of noxious or dangerous gases such as Hydrogen cyanide and Ammonia.

THz has major advantages over other technologies; it is sensitive to the presence of explosives, which is a major improvement over the standard "metal-only" detectors currently deployed. Unlike X-Rays, THz does not use ionizing radiation and is safe. The ability to use software to automatically recognize THz fingerprints also eliminates the need for operator interpretation of complex images as well as the significant privacy concerns that have plagued both millimetre wave and X-Ray technologies.

An example of this kind of application is the 300 GHz focusing system designed in the Chapter 5 of the present work.

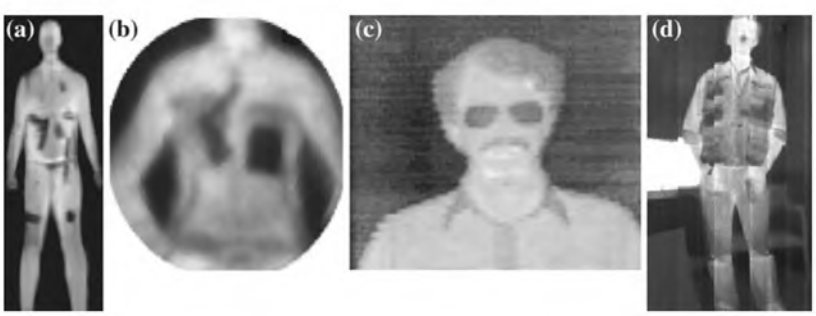

Figure 1.10: Passive indoor imaging at (a) 94 GHz [39], (b) 350 GHz [40], (c) 600 GHz (wearing glasses) [41] and (d) broadband (0.2 THz - 1 THz) [42]. The increase in the visibility of clothing is apparent when moving from the lower to the higher frequencies, by the change in contrast of shirt collars and seams (white is "hot") [38].

Medical Imaging

THz technology allows high-resolution subsurface imaging of tissue. It combines macroscopic and microscopic imaging that potentially allows the precise margin delineation of cancer tissue. Due in part to its ability to recognize spectral fingerprints, it provides good contrast between different types of soft tissue, and is a sensitive means of detecting the degree of water content as well as other cancer markers [43–45].

In addition, it can detect caries at an early stage in the enamel layers of human teeth and monitor early erosion of enamel (Figure 1.11b).

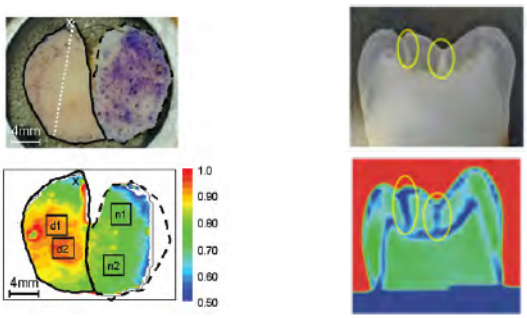

(a) (b)

Figure 1.11: Visible and THz images. (a) Basal cell carcinoma *ex vivo*, the most common form of skin cancer. The diseased tissue, on the left of the visible image, is marked by a solid boundary, the normal tissue on the right by a dashed boundary [46]. (b) Human tooth caries [47].

Non-destructive Testing

Regarding the art world, THz waves can be used to identify materials, authorship or degradation of artworks. For centuries, artists have applied paint to canvas, parchment, pottery and buildings producing many delicate and valuable works of art. Degradation caused by chemical reaction, sunlight, environment and other factors is a continuing process that conservators wish to slow down, stop or even reverse [47].

Key to the conservation process is understanding the chemical and physical structure of the work of art, how much deterioration has already

(a) **(b)** **(c)**

Figure 1.12: Composition of "Sacrifice to Vesta" at different transparency levels of visible and THz images. (a) Image in the visible, (b) 50 % visible, 50 % THz image and (c) 100 % THz image [48].

taken place and what were the causes. With this knowledge, the process of repair, restoration and care can start.

Using non-destructive THz waves techniques that can image the sub-surface structure of materials such as heritage plastics, film negatives and paint layers on canvas, walls or pottery can be used. Each layer of paint can be identified and thicknesses measured down to the base material; whether that is canvas or ceramic. De-lamination of the layers and causes such as "lead fatty acid inclusions" can be identified non-destructively. De-lamination from the base materials will also be detected and other sub-surface details such as an earlier painting or sketch may also be found [47].

In other areas of conservation, documents or manuscripts can be damaged simply by handling or opening the document. Because THz rays can penetrate through materials it is possible to image text on delicate manuscripts without removing the document cover. Regarding this text identification, THz waves have been used to identify the authorship of a Goya's painting ("Sacrifice to Vesta", Figure 1.12). A feature with a strong resemblance with one of Goya's known signatures is seen in the THz images that cannot be detected otherwise [48].

Communications

In the last years, the demand for higher data rates and bandwidth in wireless communications systems has dramatically increased. To achieve data rates of 10 Gbit/s - 20 Gbit/s, carrier frequencies in the millimetre or sub-millimetre wavelengths are needed [49]. Although THz communications are very attractive from the speed and capabilities point of view, the high atmospheric attenuation at these frequencies as well as the low power of the available THz sources makes THz wireless communication a very difficult task to be accomplished [50]. On the other hand, there are several bands in the millimetre-wave regime which can be used for high-data rate wireless communications [51].

An example of this kind of application is the E-Band Quasi-Optical Schottky Barrier Detector designed in the Chapter 4 of the present work.

1.2 Antennas in the THz and Sub-THz Regime

After a brief introduction on THz waves, explaining their most important characteristics and some of their applications, this section is devoted to antennas, which are the most important point in this PhD dissertation. First, the main parameters of antennas are explained and then the most widely used antenna topologies at these frequencies are introduced.

1.2.1 Fundamental Parameters of Antennas

In this section, the main parameters of antennas are briefly reviewed. These parameters are explained on a simplified way, but there exists a huge amount of books where the reader can go into further detail of any of them [52–57].

Radiation Pattern

A radiation pattern is a representation of the radiated field by an antenna as a function of the different directions of the space at a fixed distance. Normally spherical coordinates (r, θ, ϕ) are used and the representation is referred to the electric field. As the electric field is a vector magnitude, two orthogonal components at each point of the constant radius sphere defined by the spherical coordinates must be calculated (normally θ and ϕ). Field radiation pattern or power radiation pattern have the same information since power density is proportional to the square of the electric field module, and when they are represented in dB they are equal.

It is common to represent the radiation pattern in a 3-dimensional plot but also in a 2-dimensional one showing different cuts of the radiation pattern. In linearly polarized antennas (see polarization in the next section) E-Plane and H-Plane can be defined. E-Plane is the plane containing the direction of propagation and the E-field, while H-Plane is the plane containing the direction of propagation and the H-field. Both planes are perpendicular and its intersection represents a line which defines the direction of propagation.

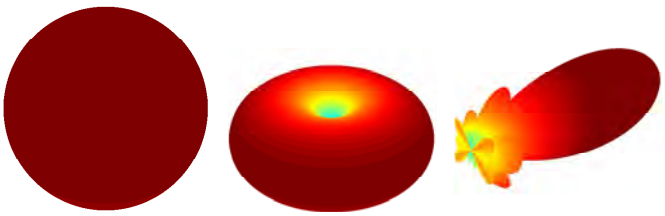

(a) **(b)** **(c)**

Figure 1.13: 3D radiation patterns. (a) Isotropic, (b) Omnidirectional and (c) Directive.

Depending on the shape of the radiation pattern three types of radiation patterns can be identified: isotropic (Figure 1.13a), omnidirectional (Figure 1.13b) and directive (Figure 1.13c).

Bi-dimensional cuts of the radiation pattern can be represented either in Polar or Cartesian coordinates. An example of both of them can be seen on Figures 1.14a and 1.14b. In the first case, the radius represents the intensity of the radiated electric field or the power density, while the angle represents the space direction. In the second case, the angle is represented in the abscissa axis while electric field or power density is represented in the ordinate axis. Field or power density can be represented on an absolute or on a relative way (normalized to the maximum), with natural or dB scales.

From a radiation pattern representation, several parameters can be extracted. The direction of the space where the radiation is maximum it is called the **main lobe** while the **secondary lobe** is the lobe with more amplitude among the rest of the lobes.

3 dB Beamwidth ($\Delta\theta_{3dB}$) or Half Power Beamwidth (HPBW) is the angular distance in the directions where the density power radiation pattern is equal to half the maximum.

Beamwidth Between Zeros ($\Delta\theta_c$) or First Null Beamwidth (FNBW) is the angular distance in the directions where main lobe has a minimum.

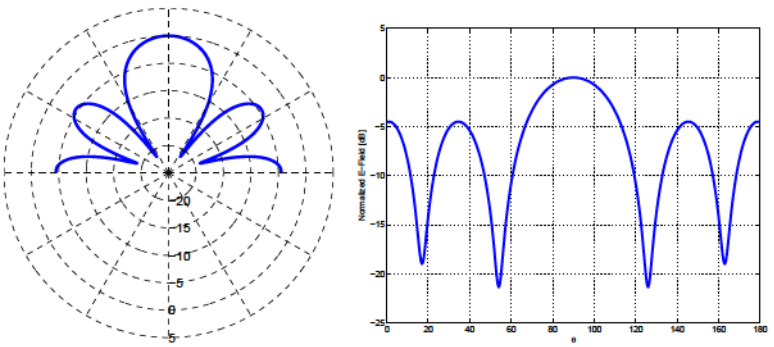

(a) (b)

Figure 1.14: Radiation pattern. (a) Polar and (b) Cartesian representation.

Side Lobe Level (SLL) is the relation between the value of the radiation pattern in the direction of maximum radiation and the value of the radiation pattern in the direction of the secondary lobe. It is normally expressed in dB.

Front-to-back (F/B) Radiation is the relation between the value of the radiation pattern in the direction of maximum radiation and the value of the radiation pattern in the opposite direction.

Directivity

Directivity of an antenna is defined as the relationship between power density radiated in a direction at a fixed distance and the power density that would be radiated at that distance by an isotropic antenna that radiates the same power as the antenna:

$$D(\theta, \phi) = \frac{S(\theta, \phi)}{P_r / (4\pi r^2)} \tag{1.1}$$

where $S(\theta, \phi)$ is power density, and P_r is radiated power.

If no angular distribution is specified, it is understood that the directivity refers to the maximum radiation direction:

$$D = \frac{S_{max}}{P_r / (4\pi r^2)} \tag{1.2}$$

The directivity can be obtained from the expression:

$$D = \frac{4\pi}{\iint_{4\pi} t(\theta, \phi)\, \mathrm{d}\Omega} \tag{1.3}$$

where

$$t(\theta, \phi) = \frac{S(\theta, \phi)}{S_{max}} \tag{1.4}$$

is the normalized radiation pattern.

In directive antennas, a good approximation to calculate the directivity is:

$$D = \frac{4\pi}{\Delta\theta_1 \cdot \Delta\theta_2} \tag{1.5}$$

where $\Delta\theta_1$ and $\Delta\theta_2$ are the HPBW in the two main planes of the radiation pattern.

Once the maximum directivity D and the normalized radiation pattern $t(\theta, \phi)$ are known, then it is easy to obtain the directivity at any direction:

$$D(\theta, \phi) = D \cdot t(\theta, \phi) \tag{1.6}$$

Gain

The gain (G) is directly related with directivity. Its definition is the same as the directivity one, but instead of comparing with the radiated power, the actual delivered power is used. Then, it is possible to take into account the losses of the antenna. The directivity and the gain are related by radiation efficiency (ϵ_{rad}):

$$G(\theta,\phi) = \frac{P(\theta,\phi)}{P_{delivered}/(4\pi r^2)} = \frac{P_r}{P_{delivered}} \cdot \frac{P(\theta,\phi)}{P_r/(4\pi r^2)}$$

$$= \epsilon_{rad} \cdot D(\theta,\phi) \tag{1.7}$$

Radiation Efficiency

The existence of losses in the antenna makes that not all the power delivered from the transmitter to the antenna is radiated to the free space. How much power is radiated to the free-space is defined by the radiation efficiency (ϵ_{rad}) which is defined between 0 (no power is radiated to the free-space) and 1 (all power delivered to the antenna is radiated to the free-space).

Effective Aperture Area and Aperture Efficiency

The effective aperture or effective area (A_{eff}) is defined as the relation between the power that the antenna delivers to its load (in a matched case, suppose antenna working in reception) and the power density of the incident wave. It is related to the directivity with the following formula:

$$\frac{A_{eff}}{D} = \frac{\lambda^2}{4\pi} \tag{1.8}$$

Effective aperture cannot be higher than the physical dimension of the antenna, so an aperture efficiency ($\epsilon_{aperture}$) that relates the effective area (A_{eff}) and the physical area (A_{phy}) of the antenna can be defined:

$$\epsilon_{aperture} = \frac{A_{eff}}{A_{phy}} \tag{1.9}$$

Phase Pattern and Phase Centre

Under some circumstances it is desirable to plot not the amplitude of the electric field (as in the radiation pattern) but the phase of the electric field. Such representation is called the phase pattern.

When observing an antenna at a great distance, its radiation can be seen as coming from a single point. In other words, its wave front is spherical. This point, centre of curvature of the surfaces with constant phase, it is called the phase centre of the antenna.

Polarization

Polarization represents the field vector orientation in a fixed point as a function of time. It can be identified by the geometric figure described, as time goes, by the end of the electric field vector in a fixed point of the space in the perpendicular plane to the propagation direction. Three figures can be generated: an ellipse (which is the most generic one), a segment (linear polarization) and a circumference (circular polarization).

The direction of rotation of the electric field, either in circularly polarized waves or elliptically ones, it is called right-hand polarization if it is clockwise and left-hand if it is counterclockwise.

Axial ratio of an elliptically polarized wave is defined as the ratio between the major and minor axis of the ellipse. It takes values between 1 and infinity. For a circularly polarized wave the axial ratio is 1.

Input Impedance

The input impedance of an antenna is the relation between the voltage and the current at the input of the antenna. It is normally a complex number that depends on the frequency:

$$Z_{in}(\omega) = R(\omega) + \jmath X(\omega) \tag{1.10}$$

If $X(\omega) = 0$ at some specific frequency, it is said that the antenna is resonant at that frequency. Knowing the input impedance of an antenna is a key factor because normally the antenna is connected to a transmission line or to an active device (transistor, diode, ...). If a mismatch occurs between the antenna and the device, then not all the power transmitted through the device will be delivered to the antenna (transmitter) or not all the power received by the antenna will be delivered to the device (receiver).

Radiation Resistance

When delivering power to an antenna, a part of it is radiated through the free-space. This quantity can be defined by a radiation resistance R_r which is defined as the resistance value that will dissipate the same power than the one radiated by the antenna:

$$P_r = I^2 \cdot R_r \tag{1.11}$$

Not all the power delivered to an antenna is radiated through the free-space. Associated to this, the losses resistance R_Ω can be defined. This resistance refers to the losses that appear in the antenna and is defined as the resistance value that will dissipate the same power as the one not radiated by the antenna.

$$P_{delivered} = P_r + P_{losses} = I^2 \cdot R_r + I^2 \cdot R_\Omega \tag{1.12}$$

This is related to the radiation efficiency (ϵ_{rad}) defined previously:

$$\epsilon_{rad} = \frac{P_r}{P_{delivered}} = \frac{P_r}{P_r + P_{losses}} = \frac{R_r}{R_r + R_\Omega} \tag{1.13}$$

Bandwidth

It represents the frequency margin where one particular property is satisfied. For the antenna case, two different kinds of parameters can be considered: impedance parameters or radiation parameters. Then the antenna bandwidth would be defined as the frequency margin where the impedance or the reflection coefficient is kept under some value and the shape radiation pattern is kept constant. It can be represented as the absolute value ($f_{max} - f_{min}$) or relative value (Fractional Bandwidth (FBW)):

$$FBW = \frac{f_{max} - f_{min}}{f_0} \tag{1.14}$$

For broadband antennas, it is common to represent the bandwidth in the form:

$$BW = \frac{f_{max}}{f_{min}} : 1 \tag{1.15}$$

The criteria used to determine the bandwidth of an antenna are related to the radiation pattern (directivity, polarization purity, beamwidth, SLL) or to the impedance (input impedance, reflection coefficient or Standing Wave Ratio (SWR)).

1.2.2 THz/sub-THz Antenna Topologies

In this section, the most common antenna topologies used in the THz gap are presented. Resonant antennas such as dipoles or slot antennas, as well as spirals, log-spirals, log-periodic and bow-ties are also presented and explained as self-complementary antennas. Finally horn antennas are included as the most typical non-planar antennas used in the THz/sub-THz regime.

Resonant + RF choke

Regarding resonant antennas working in the THz band, the most widely used are dipoles or topologies related with them. Either detectors or emitters devices possess a capacitive part at its input impedance that have a strong influence at higher frequencies. Traditionally, this capacitive part is compensated by including a Radiofrequency (RF) choke (normally a low pass filter) [58]. In Figure 1.15 an example of a dipole antenna with a RF choke is plotted. In this case the RF choke is a stepped impedance low pass filter.

Once this capacitive part is compensated, then an antenna with the same real part as the device is desired to maximize the power delivered to/from the antenna. Depending on the device, one topology or another will be more suitable. For instance, photomixers [59] possess a very high input impedance, so an antenna with a very high input impedance will be the best option. On the other hand, devices such as Schottky diodes or FET have a lower real part of the input impedance, so different antennas may be used. In [60] a detailed numerical study on some of these resonant antennas at THz frequencies is presented.

Dipole Antennas

Dipole antennas are one of the most simple antennas. They consist of two conducting arms that are fed in the middle of it. Depending on the shape of these two arms different topologies can be identified.

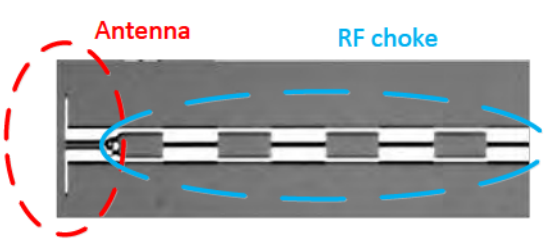

Figure 1.15: SEM picture of a dipole antenna with a stepped impedance low pass filter acting as RF choke.

$\lambda/2$ and λ Dipoles A schematic of a single dipole can be seen on the Figure 1.16a. Depending on the total length of the it (L_D), two kind of dipoles can be identified: $\lambda/2$ and λ dipoles. The main difference between them is the input impedance they can provide. $\lambda/2$ dipoles have a minimum of voltage and a maximum of current at the feeding point (red line), thus a minimum in the input impedance is obtained. This can be modified by changing the gap and the width of the dipole, but for a silicon substrate typically around $50\,\Omega$ is obtained at its resonance. On the other hand, λ dipoles have a maximum of voltage and a minimum of current at the feeding point (red line), thus a maximum in the input impedance is obtained. This can be modified by changing the gap and the width of the dipole, but for a silicon substrate typically around $250\,\Omega$ is obtained at its resonance. A typical $\lambda/2$ dipole antenna operating at 1 THz and laying over silicon substrate ($\epsilon_r = 11.7$) has $L_d \approx 45\,\mu m$ and $w_d \approx 3\,\mu m$ dimensions while a typical λ dipole antenna would have $L_d \approx 90\,\mu m$ and $w_d \approx 3\,\mu m$ dimensions.

Dual-Dipoles Dual antenna elements have several advantages over single antenna element designs. These include more symmetric beam patterns, leading to higher Gaussian beam efficiency and higher radiating resistance [61]. An schematic of a dual-dipole can be seen on the Figure 1.16b. The feeding point (red line) is placed in the middle of the antenna and two symmetric arms formed the dipole antenna configuration. Similar input impedance as a λ dipole is achieved with this configuration, but the radiation pattern is improved. A typical dual-dipole antenna over silicon substrate ($\epsilon_r = 11.7$) working at 1 THz has $A \approx 70\,\mu m$, $B \approx 50\,\mu m$, $C \approx 3\,\mu m$, $D \approx 1\,\mu m$, and $E \approx 5\,\mu m$. This topology has been widely used in the THz and sub-THz resonant systems designs [58, 62].

Meander Dipoles Meander dipole antenna is similar to a dipole where its radiating part is bent to a meander shape in order to reduce the antenna size [63]. A schematic of it with its main design parameters can be seen on the Figure 1.16c. Traditionally, this antenna is used to reduce the antenna size (antenna miniaturization) and in systems that need a very high value of the input impedance, since this antenna provides higher values of input impedance at its resonance than λ dipoles or dual-dipoles [63]. With this antenna topology, input impedances larger than $1000\,\Omega$ can be achieved. This antenna is also very suitable for biasing the active device (photomixer, diode, ...) placed in the middle of it. This

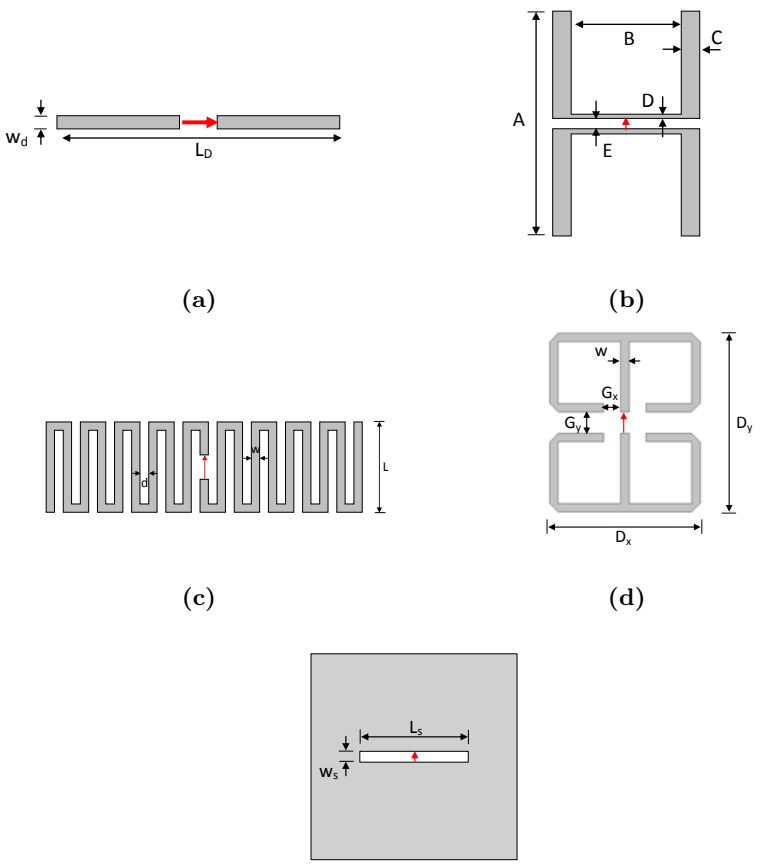

Figure 1.16: Schematic of resonant antennas used in the THz/sub-THz regime. (a) Single dipole,(b) Dual dipole, (c) Meander dipole, (d) Full-wavelength four-leaf-clover dipole and (e) Slot antenna

is due to the fact that almost no current is excited at higher frequencies in the borders of the arms, so biasing circuitry does not affect the high frequency behaviour of the antenna. On the other hand, lower values of radiation efficiency are achieved when comparing with conventional dipoles or dual-dipoles. A typical meander dipole antenna over silicon substrate ($\epsilon_r = 11.7$) working at 1 THz has $L \approx 45\,\mu m$, $w \approx 3\,\mu m$ and $d \approx 3\,\mu m$ dimensions.

Full-Wavelength Four-Leaf-Clover This antenna was proposed in [64] and a schematic of it can be seen on the Figure 1.16d with its design parameters. This antenna provides similar input impedance as the meander dipole (more than 1 kΩ) but with the advantage of being a dual antenna, thus improving the radiation pattern. A typical full-wavelength four-leaf-clover antenna over silicon substrate ($\epsilon_r = 11.7$) working at 1 THz has $D_x = D_y \approx 37\,\mu m$, $G_x = G_y \approx 2\,\mu m$, and $w \approx 3\,\mu m$.

Slot Antennas

Slot antennas are complementary to dipole antennas. While dipoles have an electric moment, the slot has a magnetic one (Babinet's principle [52]). According to it, a single slot antenna (Figure 1.16e) has a maximum on the input impedance at $L_s = \lambda/2$. All the dipoles mentioned above can be also manufactured in a slot topology but having half the length of them. Similar behaviour regarding the input impedance is expected. A typical single slot antenna operating at 1 THz and laying over silicon substrate ($\epsilon_r = 11.7$) has $L_s \approx 45\,\mu m$ and $w_s \approx 3\,\mu m$ dimensions.

Self-Complementary Antennas

Self complementary antennas are antennas where the metallic and non-metallic areas have the same shape and can be superimposed on each other by rotation. An antenna with a self-complementary structure has a constant input impedance, independently of the source frequency and shape of the structure. These are broadband antennas that can achieve a bandwidth of more than one octave [65].

According to [65], input impedance of self-complementary antennas are equal to:

$$Z_{in} = \frac{Z_0}{2} \tag{1.16}$$

where Z_0 is the intrinsic impedance of the medium. In the case of free-space, $Z_0 = \eta = 120\pi$. It can be seen that this impedance is always real and constant with frequency.

Self-complementary antennas are very attractive because they have excellent wideband radiation characteristics and because predicting resonant behaviour of a source is extremely difficult at high-frequency regions. So the use of antennas with a frequency independent response allows tests to be conducted over a wide spectral range with a single device. In applications such as spectroscopy, self-complementary antennas are the main option due to its broadband nature.

Among the available self-complementary topologies [65], three of them are the most widely used: log-spiral, log-periodic and bow-tie antennas. In the following sections each of them are briefly explained. In [66] a detailed numerical study on these three antennas at THz frequencies is presented.

Log-Spiral Antennas

The log-spiral antennas are self-complementary antennas when designed with specific parameters such as the proper arm length and width. The most important characteristic of these antennas is the constant input impedance (theoretical) not depending on frequency [65], when both the width of the arms and spacing between them are equal. Nevertheless, as self-complementary antennas, they are supposed to be infinite but due to practical reasons always are truncated, so the input impedance could not be constant over an infinite bandwidth, both in the high and the low band. The truncation has effects on the low frequency limit, where the size of the element is comparable to the wavelength and the energy spreads throughout all the structure; at high frequencies, the limitation is due to the source feed itself because of the roll-off and also to the truncation of the spiral on the inner side to place the feed.

The log-spiral design parameters are:

$$r_1 = ke^{a\phi}, r_2 = ke^{a(\phi-\delta)} \tag{1.17}$$

where r_1 and r_2 represent the inner and external radius of the spiral, respectively. The angle δ determines the arm width, and a and k are constants which control the growth rate of the spiral and the size of the terminal region respectively. In the Figure 1.17a a schematic of it is depicted. Its lower frequency is determined approximately by D_{out} while its higher frequency is determined by the gap in the middle of it.

Log-spiral antennas provide a relatively constant input impedance and circular polarization. Its radiation efficiency is high and they provide an almost constant radiation pattern.

Log-Periodic Antennas

The log-periodic antenna has a log-periodic circular-toothed structure with tooth and bow angles of $\alpha = \beta = 45°$ (for the self-complementary case). The ratio of the successive teeth (R_{n+1}/R_n) is 0.5 while the size ratio of the tooth and anti-tooth (r_n/R_n) is equal to $\sqrt{0.5}$. In the Figure 1.17b a schematic of it is depicted. Its lower frequency is determined approximately by D_{out} while its higher frequency is determined by the gap in the middle of it.

Log-periodic antennas possess a non-constant impedance and its polarization is not constant with frequency. In addition, its radiation efficiency decreases with frequency. On the other hand they have a good radiation pattern and can achieve a high directivity over a wide bandwidth. This topology is one of the most used at THz frequencies.

Bow-Tie Antennas

The bow-tie antenna has the shape depicted in the Figure 1.17c. It is similar to a dipole where its arms are wider at their extremes. A self-complementary bow-tie has an angle $\alpha = 90°$.

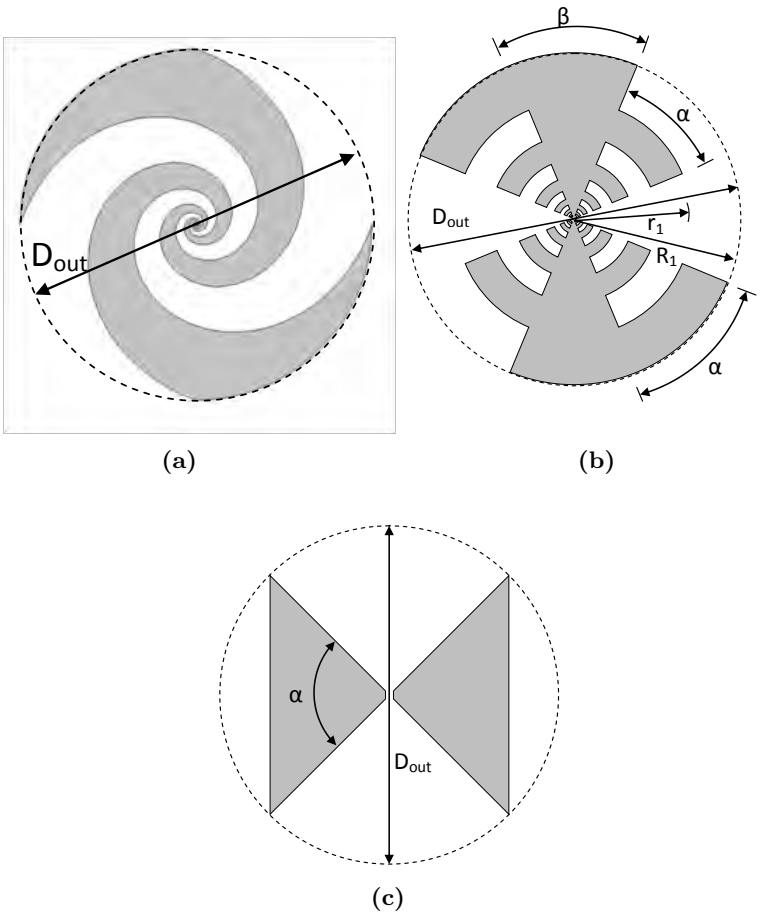

Figure 1.17: Schematic of self-complementary antennas used in the THz/sub-THz regime. (a) Log-spiral,(b) Log-periodic and (c) Bow-tie.

This self-complementary topology provides the most constant input impedance of the three analysed cases but, on the other hand, its radiation pattern gets worse with frequency.

Horn Antennas

A horn antenna is an antenna that consists on a waveguide where the section is gradually increased until an open extreme which behaves as an aperture. Two of the most common horn antennas can be seen on Figure 1.18 (pyramidal and conical horn antennas). These antennas are explained in more detail in the Chapter 5 of the present work, but its main characteristics are that they have a relative high gain, they are broadband (limited by the feeding waveguide), they can handle high power and they provide a very good Gaussian beam [52–57]. They are very common in waveguide based systems at frequencies lower than 1 THz.

(a) **(b)**

Figure 1.18: Horn antennas. (a) Pyramidal and (b) Conical.

1.3 References

[1] P. H. Siegel, "Terahertz Technology," *IEEE Transactions on Microwave Theory and Techniques*, vol. 50, no. 3, pp. 910–928, 2002.

[2] D. Woolard, E. Brown, M. Pepper, and M. Kemp, "Terahertz Frequency Sensing and Imaging: A Time of Reckoning Future Applications?" *Proceedings of the IEEE*, vol. 93, no. 10, pp. 1722–1743, Oct 2005.

[3] R. Appleby and H. Wallace, "Standoff Detection of Weapons and Contraband in the 100 GHz to 1 THz Region," *IEEE Transactions on Antennas and Propagation*, vol. 55, no. 11, pp. 2944–2956, Nov 2007.

[4] A. G. Davies, E. H. Linfield, and M. B. Johnston, "The Development of Terahertz Sources and their Applications," *Physics in Medicine and Biology*, vol. 47, no. 21, p. 3679, 2002.

[5] E. Bründermann, H.-W. Hübers, and M. Kimmitt, "Introduction," in *Terahertz Techniques*, ser. Springer Series in Optical Sciences. Springer Berlin Heidelberg, 2012, vol. 151, pp. 1–22.

[6] E. Hagen and H. Rubens, "XVI. On Some Relations Between the Optical and the Electrical Qualities of Metals," *Philosophical Magazine Series 6*, vol. 7, no. 38, pp. 157–179, 1904.

[7] R. W. Wood, "The Echelette Grating for the Infrared," *Philosophical Magazine*, vol. 20, pp. 770–778, 1910.

[8] H. Rubens and R. Wood, "XXVII. Focal Isolation of Long Heat-Waves," *Philosophical Magazine Series 6*, vol. 21, no. 122, pp. 249–261, 1911.

[9] H. Rubens, *Gittermessungen im Langwelligen Spektrum*, 1921.

[10] E. F. Nichols and J. D. Tear, "Joining the Infra-red and Electric Wave Spectra," *Proceedings of the National Academy of Sciences*, vol. 9, no. 6, pp. 211–214, 1923.

[11] C. H. Cartwright, "Black Bodies in the Extreme Infra-Red," *Phys. Rev.*, vol. 35, pp. 415–420, Feb 1930.

[12] H. M. Randall and J. Strong, "A Self Recording Spectrometer," *Review of Scientific Instruments*, vol. 2, no. 10, pp. 585–599, Oct 1931.

[13] J. Strong and S. C. Woo, "Far Infrared Spectra of Gases," *Phys. Rev.*, vol. 42, pp. 267–278, Oct 1932.

[14] M. J. E. Golay, "A Pneumatic InfraRed Detector," *Review of Scientific Instruments*, vol. 18, no. 5, pp. 357–362, 1947.

[15] D. H. Andrews, W. F. Brucksch, W. T. Ziegler, and E. R. Blanchard, "Attenuated Superconductors I. For Measuring InfraRed Radiation," *Review of Scientific Instruments*, vol. 13, no. 7, pp. 281–292, 1942.

[16] C. A. Burrus and W. Gordy, "Submillimeter Wave Spectroscopy," *Phys. Rev.*, vol. 93, pp. 897–898, Feb 1954.

[17] W. S. Boyle and J. K. F. Rodgers, "Performance Characteristics of a New Low-Temperature Bolometer," *J. Opt. Soc. Am.*, vol. 49, no. 1, pp. 66–69, Jan 1959.

[18] S. J. Fray and J. F. C. Oliver, "Photoconductive Detector of Radiation of Wavelength Greater than 50 μm," *Journal of Scientific Instruments*, vol. 36, no. 4, p. 195, 1959.

[19] R. Kompfner and N. T. Williams, "Backward-Wave Tubes," *Proceedings of the IRE*, vol. 41, no. 11, pp. 1602–1611, Nov 1953.

[20] E. Putley, "Impurity Photoconductivity in n-Type InSb," *Journal of Physics and Chemistry of Solids*, vol. 22, pp. 241 – 247, 1961.

[21] F. J. Low, "Low-Temperature Germanium Bolometer," *J. Opt. Soc. Am.*, vol. 51, no. 11, pp. 1300–1304, Nov 1961.

[22] M. Brown and M. Kimmitt, "Far-Infrared Resonant Photoconductivity in Indium Antimonide," *Infrared Physics*, vol. 5, no. 2, pp. 93 – 97, 1965.

[23] D. Young and J. Irvin, "Millimeter Fequency Conversion Using Au-n-type GaAs Schottky Barrier Epitaxial Diodes with a Novel Contacting Technique," *Proceedings of the IEEE*, vol. 53, no. 12, pp. 2130–2131, Dec 1965.

[24] A. Crocker, H. A. Gebbie, M. F. Kimmitt, and L. E. S. Mathias, "Stimulated Emission in the Far-Infrared," *Nature*, vol. 201, p. 250, 1964.

[25] J. E. Chamberlain, J. E. Gibbs, and H. A.Gebbie, "Refractometry in the Far-Infrared using a Two-Beam Interferometer," *Nature*, vol. 198, pp. 874–875, June 1963.

[26] A. Nicolson, "Broad-Band Microwave Transmission Characteristics from a Single Measurement of the Transient Response," *IEEE Transactions on Instrumentation and Measurement*, vol. 17, no. 4, pp. 395–402, Dec 1968.

[27] T. Chang and T. Bridges, "Laser Action at 452, 496, and 541 μm in Optically Pumped CH_3F," *Optics Communications*, vol. 1, no. 9, pp. 423 – 426, 1970.

[28] P. L. Richards, T. M. Shen, R. E. Harris, and F. L. Lloyd, "Quasiparticle Heterodyne Mixing in SIS Tunnel Junctions," *Applied Physics Letters*, vol. 34, no. 5, pp. 345–347, 1979.

[29] S. Komiyama, "Far-Infrared Emission from Population-Inverted Hot-Carrier System in p-Ge," *Phys. Rev. Lett.*, vol. 48, pp. 271–274, Jan 1982.

[30] A. Andronov, I. Zverev, V. Kozlov, Y. N. Nozdrin, S. Pavlov, and V. Shastin, "Stimulated Emission in the Long-Wavelength IR Region from Hot Holes in Ge in Crossed Electric and Magnetic Fields," *JETP. Lett*, vol. 40, pp. 804–806, 1984.

[31] E. M. Gershenson, M. E. Gershenson, G. N. Goltsman, A. D. Semenov, and A. V. Sergeev, "On the Limiting Characteristics of High-Speed Superconducting Bolometers," *Sov.Phys. J.of Tech. Phys.*, vol. 34, pp. 195–201, 1989.

[32] J. Faist, F. Capasso, D. Sivco, C. Sirtori, A. Hutchinson, and A. Cho, "Quantum Cascade Laser," *Science*, vol. 264, no. 5158, pp. 553–556, 1994.

[33] B. B. Hu and M. C. Nuss, "Imaging with Terahertz Waves," *Opt. Lett.*, vol. 20, no. 16, pp. 1716–1718, Aug 1995.

[34] Y. Muramoto, K. Kato, M. Mitsuhara, O. Nakajima, Y. Matsuoka, N. Shimizu, and T. Ishibashi, "High-Output-Voltage, High Speed, High Efficiency Uni-Travelling-Carrier Waveguide Photodiode," *Electronics Letters*, vol. 34, pp. 122–123, January 1998.

[35] ESA Science and Technology. (2014, April) Herschel. [Online]. Available: http://sci.esa.int/herschel/

[36] ——. (2014, April) Planck. [Online]. Available: http://sci.esa.int/planck/

[37] Atacama Large Millimeter/submillimeter Array. (2014, April) ALMA. [Online]. Available: http://www.almaobservatory.org/

[38] A. Luukanen, R. Appleby, M. Kemp, and N. Salmon, "Millimeter-Wave and Terahertz Imaging in Security Applications," in *Terahertz Spectroscopy and Imaging*, ser. Springer Series in Optical Sciences, K.-E. Peiponen, A. Zeitler, and M. Kuwata-Gonokami, Eds. Springer Berlin Heidelberg, 2013, vol. 171, pp. 491–520.

[39] C. A. Martin, J. A. Lovberg, W. H. Dean, and E. Ibrahim, "High-Resolution Passive Millimeter-Wave Security Screening Using Few Amplifiers," *Proc. SPIE*, vol. 6548, pp. 654 806–10, 2007.

[40] T. May, G. Zieger, S. Anders, V. Zakosarenko, H.-G. Meyer, M. Schubert, M. Starkloff, M. Rößler, G. Thorwirth, and U. Krause, "Safe VISITOR: Visible, Infrared, and Terahertz Object Recognition for Security Screening Application," *Proc. SPIE*, vol. 7309, pp. 73 090E–8, 2009.

[41] D. T. Petkie, C. Casto, F. C. D. Lucia, S. R. Murrill, B. Redman, R. L. Espinola, C. C. Franck, E. L. Jacobs, S. T. Griffin, C. E. Halford, J. Reynolds, S. O'Brien, and D. Tofsted, "Active and Passive Imaging in the THz Spectral Region: Phenomenology, Dynamic Range, Modes, and Illumination," *J. Opt. Soc. Am. B*, vol. 25, no. 9, pp. 1523–1531, Sep 2008.

[42] A. Luukanen, L. Grönberg, T. Haarnoja, P. Helistö, K. Kataja, M. Leivo, A. Rautiainen, J. Penttilä, J. E. Bjarnason, C. R. Dietlein, M. D. Ramirez, and E. N. Grossman, "Passive THz Imaging System for Stand-off Identification of Concealed Objects: Results from a Turn-Key 16 Pixel Imager," *Proc. SPIE*, vol. 6948, pp. 69 480O–9, 2008.

[43] J.-H. Son, *Terahertz Biomedical Science and Technology.* CRC Press, 2014.

[44] G.-S. Park, Y. H. Kim, H. Han, J. K. Han, J. Ahn, J.-H. Son, W.-Y. Park, and Y. U. Jeong, *Convergence of Terahertz Sciences in Biomedical Systems.* Springer, 2012.

[45] X. Yin, W.-H. N. Brian, and D. Abbott, *Terahertz Imaging for Biomedical Applications.* Springer, 2012.

[46] R. M. Woodward, V. P. Wallace, R. J. Pye, B. E. Cole, D. D. Arnone, E. H. Linfield, and M. Pepper, "Terahertz Pulse Imaging of ex vivo Basal Cell Carcinoma," *J Investig Dermatol*, vol. 120, no. 1, pp. 72–78, 2003.

[47] Teraview. (2014, June) Terahertz Waves Applications. [Online]. Available: http://www.teraview.com/applications/index.html

[48] C. Seco-Martorell, V. López-Domínguez, G. Arauz-Garofalo, A. Redo-Sanchez, J. Palacios, and J. Tejada, "Goya's Artwork Imaging with Terahertz Waves," *Opt. Express*, vol. 21, no. 15, pp. 17 800–17 805, Jul 2013.

[49] D. Saeedkia, "Terahertz Wireless Communications," in *Handbook of terahertz technology for imaging, sensing and communications.* Elsevier, 2013, pp. 156–216.

[50] H.-J. Song and T. Nagatsuma, "Present and Future of Terahertz Communications," *IEEE Transactions on Terahertz Science and Technology*, vol. 1, no. 1, pp. 256–263, Sept 2011.

[51] Z. Pi and F. Khan, "An Introduction to Millimeter-Wave Mobile Broadband Systems," *IEEE Communications Magazine*, vol. 49, no. 6, pp. 101–107, June 2011.

[52] C. A. Balanis, *Antenna Theory: Analysis and Design.* John Wiley & Sons, 2012.

[53] W. L. Stutzman and G. A. Thiele, *Antenna Theory and Design.* John Wiley & Sons, 2012.

[54] R. E. Collin, *Antennas and Radiowave Propagation.* McGraw-Hill New York, 1985.

[55] J. D. Kraus, *Antennas*. McGraw-Hill Education, 1988.

[56] A. A. Oliner, D. R. Jackson, and J. Volakis, *Antenna Engineering Handbook*. McGraw Hill, 2007.

[57] R. C. Johnson and H. Jasik, *Antenna Engineering Handbook*. New York, McGraw-Hill Book Company, 1984.

[58] S. M. Duffy, S. Verghese, A. McIntosh, A. Jackson, A. Gossard, and S. Matsuura, "Accurate Modeling of Dual Dipole and Slot Elements used with Photomixers for Coherent Terahertz Output Power," *IEEE Transactions on Microwave Theory and Techniques*, vol. 49, no. 6, pp. 1032–1038, 2001.

[59] S. Preu, G. Döhler, S. Malzer, L. Wang, and A. Gossard, "Tunable, Continuous-Wave Terahertz Photomixer Sources and Applications," *Journal of Applied Physics*, vol. 109, p. 061301, 2011.

[60] T. K. Nguyen and I. Park, "Resonant Antennas on Semi-Infinite and Lens Substrates at Terahertz Frequency," in *Convergence of Terahertz Sciences in Biomedical Systems*. Springer, 2012, pp. 181–193.

[61] D. F. Filipovic, W. Y. Ali-Ahmad, and G. M. Rebeiz, "Millimeter-Wave Double-Dipole Antennas for High-Gain Integrated Reflector Illumination," *IEEE Transactions on Microwave Theory and Techniques*, vol. 40, no. 5, pp. 962–967, May 1992.

[62] D. F. Filipovic, S. S. Gearhart, and G. M. Rebeiz, "Double-Slot Antennas on Extended Hemispherical and Elliptical Silicon Dielectric Lenses," *IEEE Transactions on Microwave Theory and Techniques*, vol. 41, no. 10, pp. 1738–1749, 1993.

[63] T. Endo, Y. Sunahara, S. Satoh, and T. Katagi, "Resonant Frequency and Radiation Efficiency of Meander Line Antennas," *Electronics and Communications in Japan (Part II: Electronics)*, vol. 83, no. 1, pp. 52–58, 2000.

[64] I. Woo, T. K. Nguyen, H. Han, H. Lim, and I. Park, "Four-Leaf-Clover-Shaped Antenna for a THz Photomixer," *Optics Express*, vol. 18, no. 18, pp. 18 532–18 542, August 2010.

[65] Y. Mushiake, "Self-Complementary Antennas," *IEEE Antennas and Propagation Magazine*, vol. 34, no. 6, pp. 23–29, December 1992.

[66] T. K. Nguyen, T. A. Ho, H. Han, and I. Park, "Numerical Study of Self-Complementary Antenna Characteristics on Substrate Lenses at Terahertz Frequency," *Journal of Infrared, Millimeter, and Terahertz Waves*, vol. 33, no. 11, pp. 1123–1137, 2012.

CHAPTER 2

PLANAR ANTENNAS LYING ON DIELECTRIC SLABS

In this chapter, the radiation pattern of antennas lying on dielectric slabs is analysed. First of all, an introduction explaining how the substrate affects the radiation pattern at THz and sub-THz frequencies and the importance of correctly analysing it is presented. Then, a Method-of-Moments (MoM) based software to analyse antennas lying on both semi-infinite and multilayered substrates has been developed and radiation patterns are analysed. Once radiation patterns are presented, the two main contributions of this chapter are discussed. The first one consists of explaining the anomalies that appear in the radiation pattern of both vertical and horizontal dipoles when laying on the interface between vacuum and a semi-infinite substrate. The other main contribution consists of designing a software capable of analysing radiation patterns of any antenna having an extended hemispherical dielectric lens as substrate.

The developed tools for obtaining the radiation pattern of antennas both over multilayered substrate or dielectric lens will be used in Chapters 3 and 4 in order to calculate the radiation pattern of the so called LAEs and the radiation pattern of the developed detectors (Schottky and Metal Oxide Semiconductor Field Effect Transistor (MOSFET)).

2.1 Introduction

The analysis of antennas embedded or just laying on the interface of two electrically different media has been compiled from a broad spectrum of researches [1–7]. The interest of these kinds of antennas and topologies has been increased in the last years due to, for example, the potential new devices for THz generation based on the use of the substrate semiconductor properties avoiding the use of antennas. The equivalent electromagnetic model of these new devices called LAEs is no more complex than an array of Hertzian dipoles laying on the interface of the semiconductor and air [8]. The lattice and geometry of this array will be parametrized as a function of the excitation of the device and the physical geometry of the semiconductor device. Knowledge on the radiation pattern of such arrays is required by the scientific community.

Antennas lying over a dielectric medium have some special features that distinguish them from antennas in free-space. In free-space, the power radiated from a planar antenna divides equally above and below the plane by symmetry, while an antenna on a dielectric mainly radiates into the dielectric. This results both from the way in which elementary sources radiate and from the way in which waves propagate along metals at a dielectric interface [2]. This can be explained by the impedance of both media. Let us assume that a dipole is placed on the interface between air and a dielectric. If the dipole is used as a receiving antenna, it measures the electric field parallel to it which is the field transmitted through the interface. In the transmission-line model of wave propagation [9], a wave from a high impedance material (air) is incident on a low-impedance material (dielectric). The transmitted electric field is small, so the dipole response is small. The effect is the same as looking at the voltage across a coaxial cable terminated with a low resistance. When the wave is incident from the dielectric side, the transmitted electric field is large and the dipole response is large, since the material has a lower impedance than the air. The analogous situation in coaxial cable is the voltage seen at a high-impedance load. The result is that the response is larger when the wave is incident from the dielectric. By reciprocity, the power transmitted from the dipole is larger in the dielectric [2]. Because any antenna can be seen as a collection of elementary Hertzian dipoles, it can be said that an antenna would ordinarily radiate more strongly into the dielectric [2]. Another factor that favours

the radiation into the dielectric is the way in which the waves propagate along metals at a dielectric interface. The waves tend to propagate at a velocity that is intermediate between the velocity of waves in the air and the velocity of waves in the dielectric [3,10]. Usually, the wave propagates with a velocity close to that characteristic of a material with a dielectric constant equal to the mean of the two dielectric constant. The effect is that the wave is slow as far as the air is concerned, and mainly evanescent waves are excited. On the other hand, for the dielectric the wave is fast, and the radiation is strong there. The effect is that of a leaky-wave antenna, with radiation primarily in the dielectric [2]. So it seems clear that the energy should be focused in from the dielectric side.

Another issue that has to be taken into account is the thickness of the substrates at THz and sub-THz frequencies which is in the order of some wavelengths. Under these conditions, the substrate is very thick and its effect has to be taken into account. From the ray point of view (Figure 2.1), the rays incident with an angle larger than the critical angle are completely reflected and trapped as surface waves [2]. This surface wave power will be discussed in Section 2.3.2 and is a key issue since it can dominate the radiated power. These surface waves can be controlled by the inclusion of a lens on the back side of the substrate with the same dielectric constant. This eliminates the problem, because, as shown in Figure 2.2, the rays now impinge nearly normal to the surface and do not suffer total internal reflection. The substrate lens takes ad-

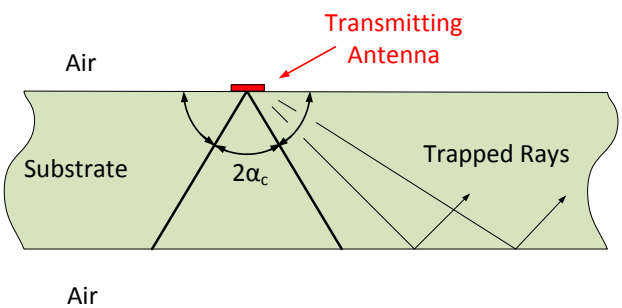

Figure 2.1: Transmitting antenna on a dielectric substrate showing the rays trapped as surface waves. The critical angle is represented as α_c.

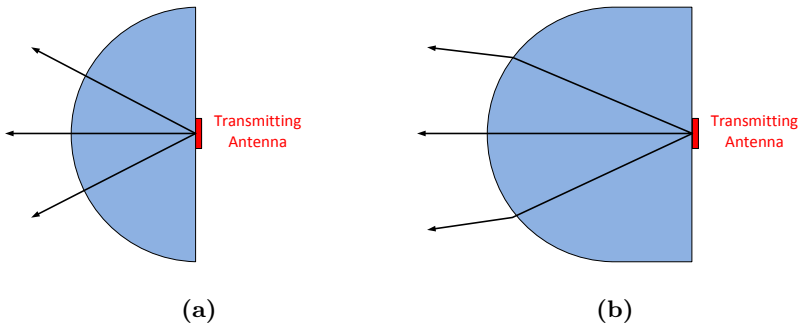

Figure 2.2: Substrate lenses. (a) Hemisphere and (b) Extended hemisphere.

vantage of the sensitivity of an antenna to radiation from the substrate side and eliminates the surface waves. In addition, directivity is improved. The disadvantages of the substrate lens are those of any system using refractive optics: absorption and reflection losses [2]. Among the available dielectric lenses, two are particularly attractive because they are aplanatic, adding no spherical aberration or coma [11]. These are the hemispherical lens (Figure 2.2a) and the extended hemispherical lens (Figure 2.2b). Analysis of the latter one is carried out in the Section 2.5.

2.2 Radiation Pattern of a Dipole over a Semi-Infinite Substrate

In some cases, a good approximation to obtain radiation pattern of antennas laying over a dielectric at THz frequencies is to consider the thickness of such substrate infinite. At THz frequencies, available substrates have a thickness of several λ (typical 350 µm thickness Silicon wafers correspond to $\sim 4\lambda$ at 1 THz) and available commercial full-wave electromagnetic simulators would need a lot of computational time and resources to solve the problem because the size of it, in terms of λ, is very high. For all the above, it seems reasonable to consider such thickness as infinite. In some applications, such as hyperhemispherical dielectric lenses design (Section 2.5) this radiation pattern over semi-infinite substrate is needed. In this section, the radiation pattern of the most elementary antenna, Hertzian dipole, over semi-infinite substrate is calculated. To do so, analytical expressions have been derived as well an in-house developed MoM based software [12] and results of both of them are compared. Regarding available commercial electromagnetic softwares, only those based on MoM correctly calculate radiation pattern of antennas over semi-infinite substrate (e.g. FEKO [13]), while others such as CST [14] fail or at least there is an open discussion on the topic of how to correctly calculate it [15].

Analytical expressions for the radiation pattern of an electric dipole located in a dielectric medium 1 at distance z_0 from the interface to a different dielectric medium 2 have been derived, based on Lukosz's work [4–6]. The radiation patterns of dipoles located on the interface ($z_0 = 0$) and oriented perpendicular and parallel to it, are particularly examined. The results are similar to the ones presented in [1–6] and the rigorous mathematical methodology theory can be followed in [4–6]. Both media 1 and 2 are assumed to be isotropic, homogeneous, and non-absorbing dielectrics with refractive indices n_1 and n_2, respectively. Summarizing the methodology presented in [4–6], first, the unperturbed dipole field is represented as a superposition of s- and p-polarized plane and evanescent waves. When these waves are incident on a plane $z =$ constant they are called Transversal Electric (TE) waves or s-polarized waves since the electric field is perpendicular to the plane of incidence. A Transversal Magnetic (TM) wave or p-polarized wave is defined when the magnetic

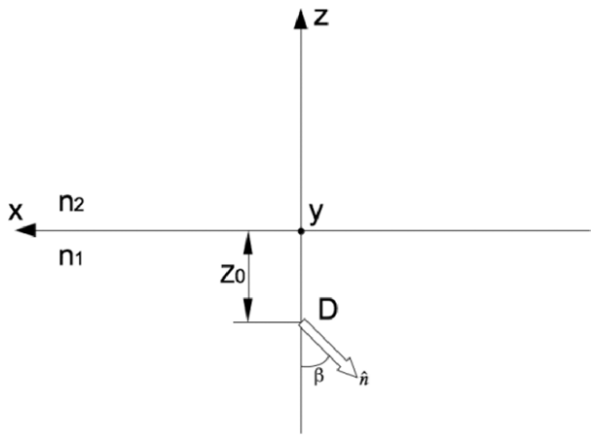

Figure 2.3: D dipole located in medium 1 at distance z_0 from the interface to medium 2. The unit vector $\hat{n}$ in direction of the dipole moment lies in the x-z plane.

field is perpendicular to the plane of incidence. This representation is rigorously valid both in the dipole's far field and near field. Then, the reflection and refraction of each of these plane and evanescent waves incident onto the interface are considered separately. In Figure 2.3 an schematic of the problem is depicted.

In the following subsections horizontal dipole and vertical dipole are treated separately.

2.2.1 Vertical Dipole

In Figure 2.4 the radiation pattern of a vertical dipole lying on the interface between two semi-infinite media is depicted. In-house MoM based software with the exact Green's function has been used as the electromagnetic simulator [12]. Upper medium is vacuum while lower medium is GaAs ($\epsilon_r = 12.9$). It can be seen how the radiation pattern does not depend on the angular coordinate ϕ (the same as a vertical dipole on an unbounded medium) and a maximum in the radiation pattern appears at the critical angle ($\alpha_c = \arcsin(1/12.9) = 16.16^\circ \rightarrow \theta = 180^\circ - \alpha_c = 163.84^\circ$). These results are completely similar to those presented in the literature [1–6].

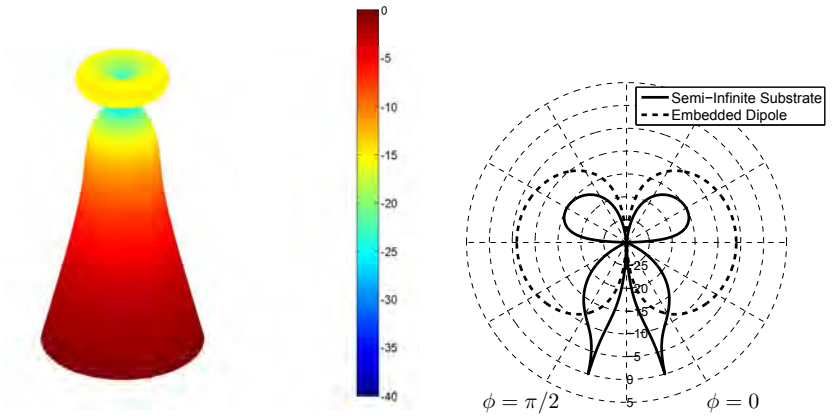

(a) **(b)**

Figure 2.4: Radiation pattern of a dipole laying in the interface between two media $n_1 = \sqrt{12.9}$ (GaAs), $n_2 = 1$, with $\beta = 0^\circ$. (a) 3D plot and (b) Polar plot comparing with embedded dipole ($n_1 = n_2 = \sqrt{12.9}$).

In Figures 2.5-2.6 the angular distribution of the emitted power of a vertical electric dipole normalized to the unbounded medium ($n_1 = n_2 = 1$) case is depicted. The radiation patterns only depend on the distance z_0 and on the refractive index n_1 and n_2. Maximum of the radiation pattern occurs at the critical angle ($\alpha_c = \arcsin(n_2/n_1)$) where the radiation pattern has an uncertainty and it remains at the same angular point never mind the distance z_0.

The power radiated in a direction beyond the critical angle, α_c, of the medium exponentially decreases with the dipole's distance z_0 from the interface. Here $\Delta z(\alpha_2)$ is the penetration depth of that evanescent wave in the dipole field whose refraction at the interface rises the transmitted plane wave with angle of refraction α_2. For distances $z_0 \gg \Delta z(\alpha_2)$ the evanescent wave does not reach the interface, and no transmitted light appears in medium 2 at $\alpha_2 > \alpha_c$.

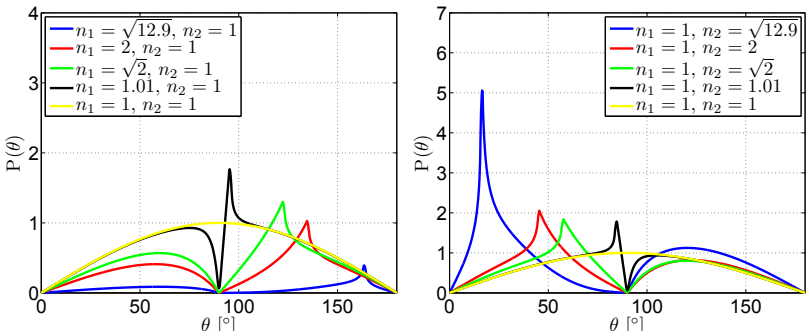

Figure 2.5: Angular distribution $P(\theta)$ of emitted power normalized to $n_1 = 1$ and $n_2 = 1$ case vs angle θ for vertical electric dipoles located on the interface ($z_0 = 0$). (a) $n_2 = 1$ and $n_1 = \sqrt{12.9}$ (blue line), $n_1 = 2$ (red line), $n_1 = \sqrt{2}$ (green line) and $n_1 = 1.01$ (black line). (b) $n_1 = 1$ and $n_2 = \sqrt{12.9}$ (blue line), $n_2 = 2$ (red line), $n_2 = \sqrt{2}$ (green line) and $n_2 = 1.01$ (black line). Yellow curve gives $P_\infty(\theta)$ for dipoles in an unbounded medium 1 ($n_1 = n_2 = 1$).

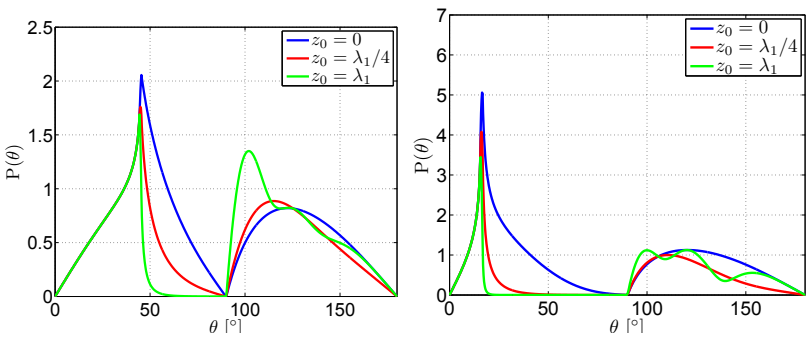

Figure 2.6: Angular distribution $P(\theta)$ of emitted power normalized to $n_1 = 1$ and $n_2 = 1$ case vs angle θ for vertical electric dipoles located at different distances z_0. (a) $n_2 = \sqrt{2}$ and $n_1 = 1$. $z_0 = 0$ (blue line), $z_0 = \lambda_1/4$ (red line) and $z_0 = \lambda_1$ (green line). (b) $n_2 = \sqrt{12.9}$ and $n_1 = 1$. $z_0 = 0$ (blue line), $z_0 = \lambda_1/4$ (red line) and $z_0 = \lambda_1$ (green line).

2.2.2 Horizontal Dipole

In this section the case for the radiation pattern of a horizontal dipole ($\beta = 90°$) laying on the interface of two media (Figure 2.7) is analysed. In-house MoM based software with the exact Green's function has been used as the electromagnetic simulator [12]. These results are completely similar to those presented in the literature [1–6]. In Figures 2.8-2.11 the angular distribution of the emitted power of a horizontal electric dipole normalized to the unbounded medium ($n_1 = n_2 = 1$) case is depicted. The radiation patterns only depend on the distance z_0 and refractive index n_1 and n_2. Maximum of the radiation pattern occurs at the critical angle ($\alpha_c = \arcsin(n_2/n_1)$) for the H-Plane and a null appears at the same angle in the E-Plane, where the radiation pattern has an uncertainty and it remains at the same angular point never mind the distance z_0.

The power radiated in a direction beyond the critical angle, α_c, of the medium exponentially decreases with the dipole's distance z_0 from the interface. Here $\Delta z(\alpha_2)$ is the penetration depth of that evanescent

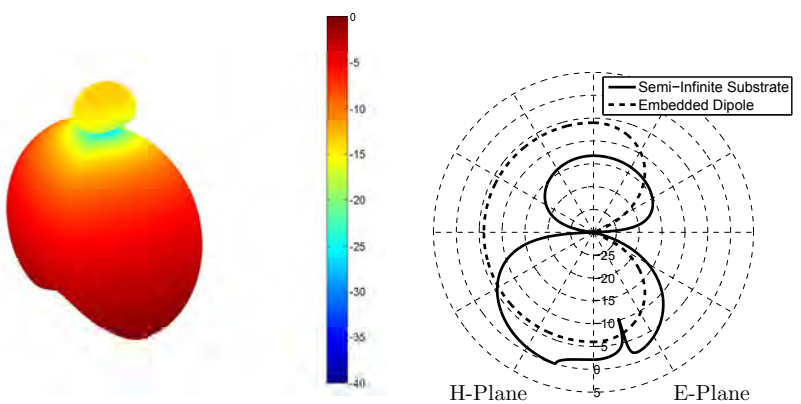

(a) **(b)**

Figure 2.7: Radiation pattern of a horizontal dipole laying in the interface between two media $n_1 = \sqrt{12.9}$ (GaAs), $n_2 = 1$, with $\beta = 90°$. (a) 3D plot and (b) Polar plot comparing with embedded dipole ($n_1 = n_2 = \sqrt{12.9}$).

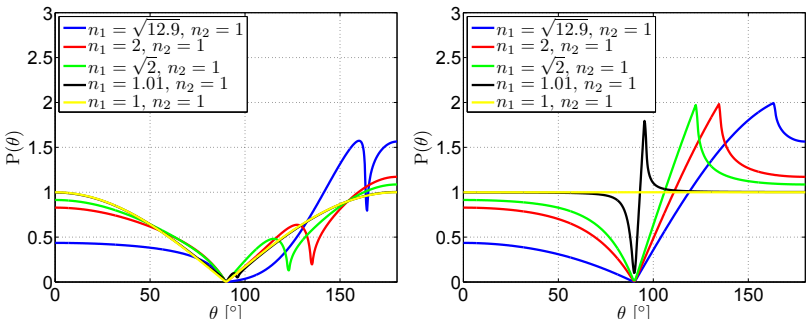

Figure 2.8: Angular distribution $P(\theta)$ of emitted power normalized to $n_1 = 1$ and $n_2 = 1$ case vs angle θ for vertical electric dipoles located on the interface ($z_0 = 0$). $n_2 = 1$ and $n_1 = \sqrt{12.9}$ (blue line), $n_1 = 2$ (red line), $n_1 = \sqrt{2}$ (green line) and $n_1 = 1.01$ (black line). Yellow curve gives $P_\infty(\theta)$ for dipoles in an unbounded medium 1 ($n_1 = n_2 = 1$). (a) E-Plane and (b) H-Plane.

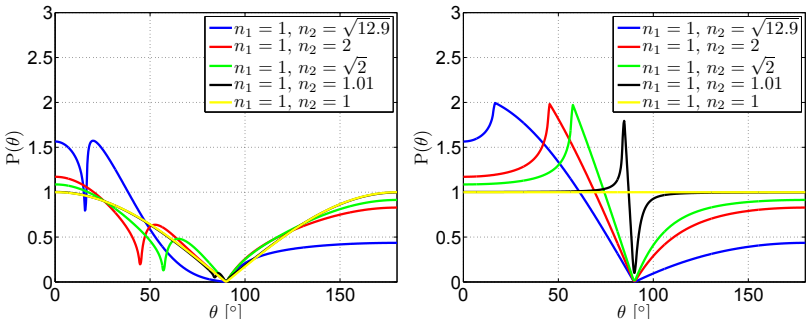

Figure 2.9: Angular distribution $P(\theta)$ of emitted power normalized to $n_1 = 1$ and $n_2 = 1$ case vs angle θ for horizontal electric dipoles located on the interface ($z_0 = 0$). $n_1 = 1$ and $n_2 = \sqrt{12.9}$ (blue line), $n_2 = 2$ (red line), $n_2 = \sqrt{2}$ (green line) and $n_2 = 1.01$ (black line). Yellow curve gives $P_\infty(\theta)$ for dipoles in an unbounded medium 1 ($n_1 = n_2 = 1$). (a) E-Plane and (b) H-Plane.

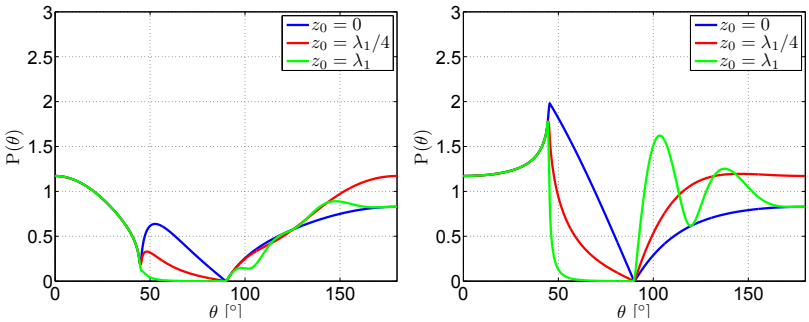

Figure 2.10: Angular distribution $P(\theta)$ of emitted power normalized to $n_1 = 1$ and $n_2 = 1$ case vs angle θ for horizontal electric dipoles located at different distances. z_0. $n_2 = \sqrt{2}$ and $n_1 = 1$. $z_0 = 0$ (blue line), $z_0 = \lambda_1/4$ (red line) and $z_0 = \lambda_1$ (green line). (a) E-Plane and (b) H-Plane.

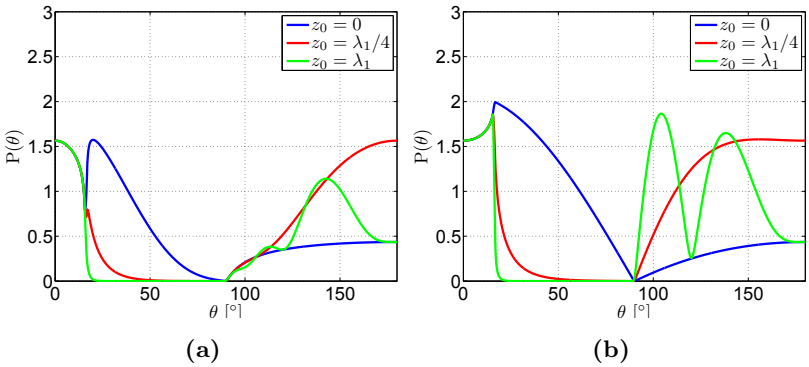

Figure 2.11: Angular distribution $P(\theta)$ of emitted power normalized to $n_1 = 1$ and $n_2 = 1$ case vs angle θ for horizontal electric dipoles located at different distances. $n_2 = \sqrt{12.9}$ and $n_1 = 1$. $z_0 = 0$ (blue line), $z_0 = \lambda_1/4$ (red line) and $z_0 = \lambda_1$ (green line). (a) E-Plane and (b) H-Plane.

wave in the dipole field whose refraction at the interface gives rise to the transmitted plane wave with angle of refraction α_2. For distances $z_0 \gg \Delta z\,(\alpha_2)$ the evanescent wave does not reach the interface, and no transmitted light appears in medium 2 at $\alpha_2 > \alpha_c$.

2.3 Radiation Pattern of a Dipole in a Multilayered Media

In this section, the radiation pattern of a Hertzian dipole (both vertical and horizontal) when lying above or inside a multilayered media is described. While in previous section the substrate lying beneath the antenna has been considered to have semi-infinite thickness, this case is not real and is useful only under certain circumstances. It will be shown that this finite thickness substrate changes the radiation pattern of antennas placed above or inside the substrate.

First of all, the case of both horizontal and vertical Hertzian dipoles when placed over a common 350 µm GaAs wafer is analysed for different frequencies and compared with radiation patterns obtained in the previous section. Then, the Hertzian dipole is placed inside the GaAs wafer and radiation pattern as well as radiated power is calculated. It will be shown that when a dipole is placed in between a dielectric, a Fabry-Perot behaviour appears and part of the power is kept through the dielectric and it is not radiated to the air. This case is very useful for the electromagnetic equivalent radiated power circuit for vertical LAEs that is obtained in Section 3.3.

2.3.1 Hertzian Dipole over Finite Thickness Substrate

A 350 µm GaAs ($n = \sqrt{12.9}$) substrate and a Hertzian dipole laying over it is considered in this section. For $z > 350\,\mu m$ and $z < 0$ air ($\epsilon_r = 1$) is set as background material while for $0 < z < 350\,\mu m$ GaAs is considered. In the following two subsections a Hertzian dipole placed along the z-direction (vertical dipole) and along the x-direction (horizontal dipole), both lying on $z = 350\,\mu m$, is analysed.

Vertical Dipole

In Figure 2.12 the radiation patterns for a vertical Hertzian dipole lying over a 350 µm GaAs substrate is depicted and compared to the semi-infinite case from Section 2.2.1. It can be seen that, while in the semi-infinite case radiation pattern does not depend on the frequency, in this finite case frequency plays an important role. Although physical dimensions of the GaAs wafer are the same, in terms of the wavelength it changes with frequency, so an effect on the radiation pattern is expected. Maximum at the critical angle does not exist any more and it is translated to angles close to $\theta = 90°$ (interface between air and GaAs). So it seems that considering the substrate thickness as infinite is not a good option in most of the cases, no matter how large the substrate is. In Section 2.5 it will be shown that considering substrate thickness as infinite is a good approximation for calculating radiation patterns of antennas with a hyperhemispherical lens as substrate.

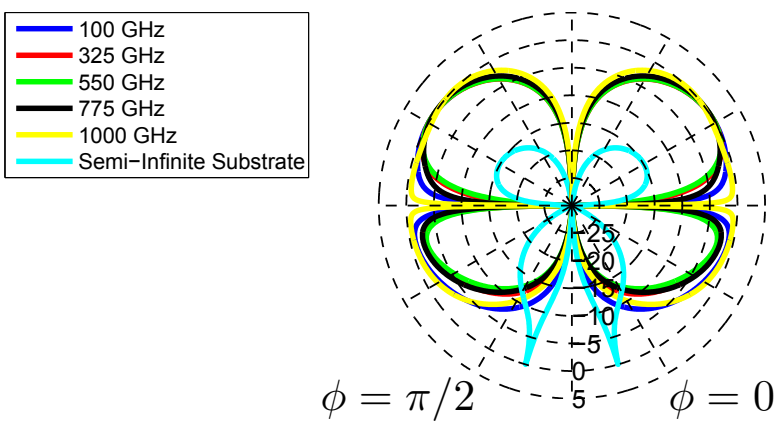

Figure 2.12: Radiation patterns of a vertical Hertzian dipole lying over a 350 µm GaAs substrate for different frequencies and for semi-infinite GaAs case.

Horizontal Dipole

In Figure 2.13 the radiation patterns for an horizontal (x-direction, $\phi = 0°$) Hertzian dipole lying over a 350 µm GaAs substrate is depicted

and compared to the semi-infinite case from Section 2.2.2. It can be seen that, while in the semi-infinite case the radiation pattern does not depend on the frequency, in this finite case frequency plays an important role. Although the physical dimensions of the GaAs wafer are the same, in terms of the wavelength it changes with frequency, so an effect on the radiation pattern is expected. Neither maximum nor null at the critical angle exist and the maximum is translated to angles close to $\theta = 90^\circ$ (interface between air and GaAs). So it seems that considering the substrate thickness as infinite is not a good option in most of the cases, no matter how large the substrate is. In Section 2.5 it will be shown that considering substrate thickness as infinite is a good approximation for calculating radiation patterns of antennas with a hyperhemispherical lens as substrate.

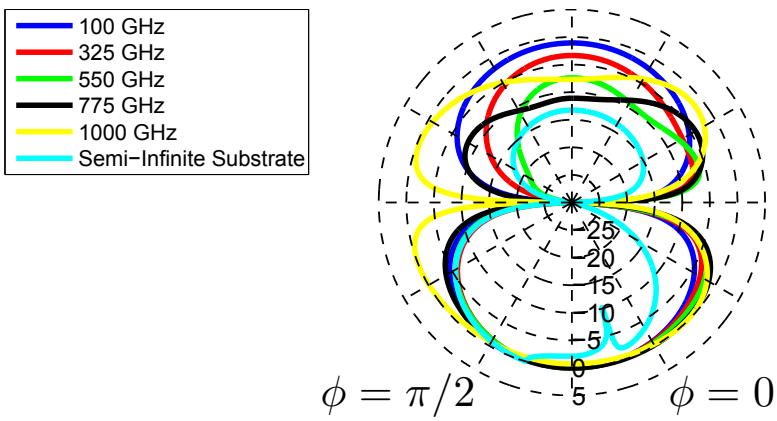

Figure 2.13: Radiation patterns of a horizontal Hertzian dipole lying over a 350 µm GaAs substrate for different frequencies and for semi-infinite GaAs case.

2.3.2 Hertzian Dipole inside Finite Thickness Substrate

Recently, with the improvements in the CMOS manufacture process (an example of it is shown in the Section 4.3 of the present work), antennas integrated with other circuits are receiving great attention at THz and sub-THz frequencies [16]. In such technology, antennas are included between different dielectric media so it is a key point to correctly calculate the radiation pattern of them. Another important application

where antennas are placed inside finite thickness substrate are LAEs. This antenna free scheme is explained in detail in Section 3.3 where an electromagnetic radiation pattern equivalent circuit is obtained by discretizing the continuous currents into an array of Hertzian dipoles. As an example of the effect that a dielectric with finite thickness has on the radiation pattern, both vertical and horizontal Hertzian dipoles are analysed.

Vertical Dipole

In this section the vertical dipole case is analysed. A Hertzian dipole oriented across the z-direction is placed in the middle of a 350 µm thickness GaAs wafer and results are depicted in Figure 2.14a. It can be seen that a perfectly symmetric radiation pattern is obtained in both $\phi = 0^\circ$ and $\phi = 90^\circ$ planes with a small variation due to frequency. When the dipole is displaced inside the GaAs wafer up to 25 µm away from the top of the wafer the radiation pattern displayed in Figure 2.14b is obtained. In that case the radiation pattern is not symmetric any more and depending on the frequency more power is radiated through $z > 0$ or $z < 0$.

Horizontal Dipole

In this section the horizontal dipole case is analysed. A Hertzian dipole oriented across the x-direction is placed in the middle of a 350 µm thickness GaAs wafer and results are depicted in Figure 2.15a. It can be seen that a perfectly symmetric radiation pattern is obtained in both E-Plane ($\phi = 0^\circ$) and H-Plane ($\phi = 90^\circ$) with a small variation due to frequency, making wider one plane or the other. When the dipole is shifted inside the GaAs wafer up to 25 µm away from the top of the wafer the radiation pattern displayed in Figure 2.15b is obtained. In that case the radiation pattern is not symmetric any more and depending on the frequency more power is radiated through $z > 0$ or $z < 0$.

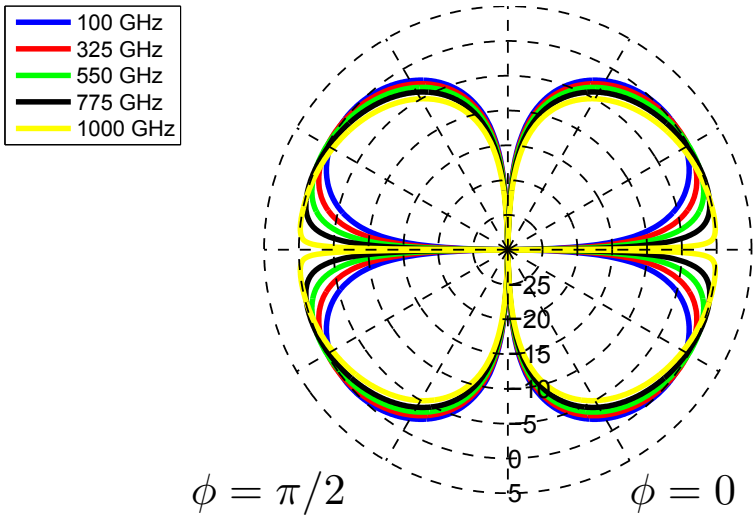

(a)

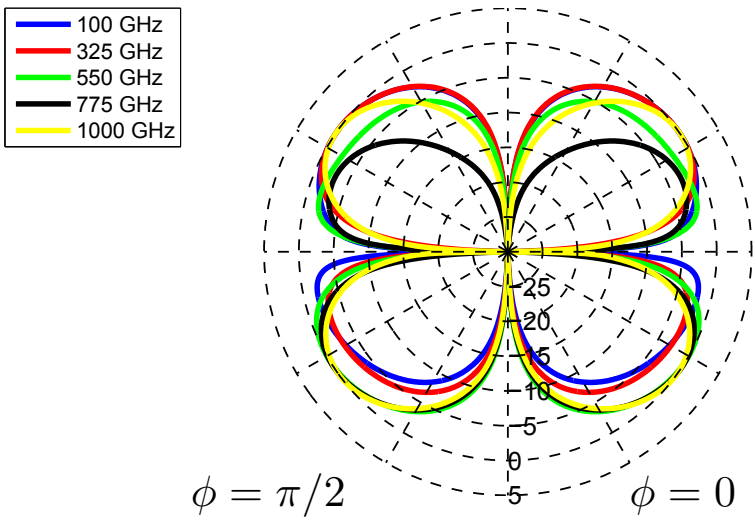

(b)

Figure 2.14: Radiation patterns of a vertical Hertzian dipole inside a 350 µm GaAs substrate for different frequencies. (a) Dipole in the middle of the wafer and (b) Dipole at 25 µm from the upper part of the wafer.

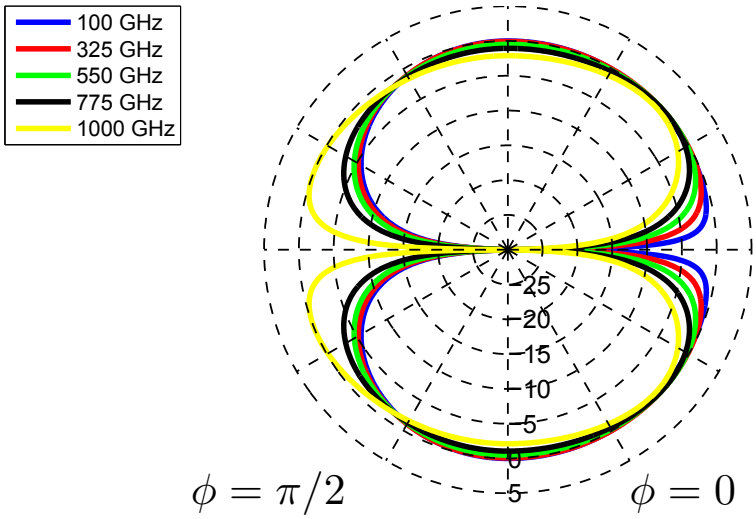

(a)

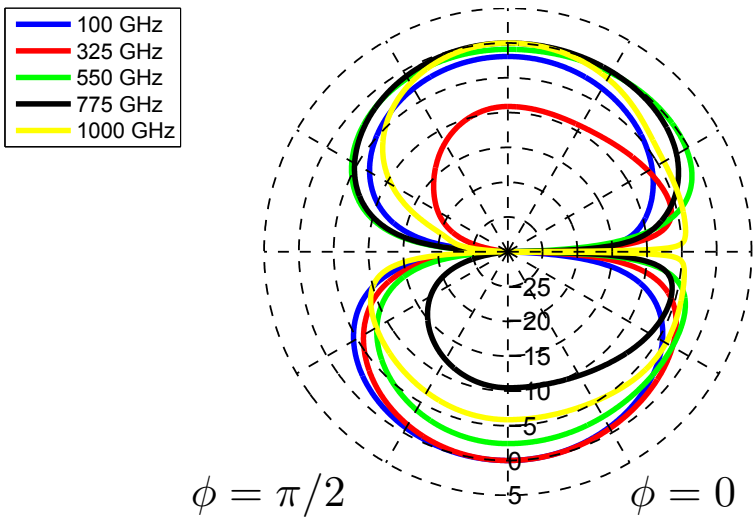

(b)

Figure 2.15: Radiation patterns of a horizontal Hertzian dipole inside a 350 µm GaAs substrate for different frequencies. (a) Dipole in the middle of the wafer and (b) Dipole at 25 µm from the upper part of the wafer.

Another key issue is to calculate the amount of power that is radiated outside the wafer and how much power is retained inside it thus reducing the radiation efficiency. In Figure 2.16a radiated power normalized to the embedded dipole in GaAs case is depicted over frequency. It can be seen that the radiated power of the horizontal dipole is much higher than for the vertical dipole (in the plot the radiated power for the vertical dipole is multiplied by a factor of 20 to have a friendlier picture). This is due to the fact that vertical position of the dipole makes it easier to excite a guided dielectric mode, thus reducing the radiated amount of power. In addition, there are certain frequencies at which the radiated power is much higher than others. Here is where the Fabry-Perot behaviour can be appreciated. Those radiated power peaks are separated 240 GHz approximately ($\lambda \approx 350\,\mu m$ when considering GaAs) and alternate maxima with minima every 120 GHz approximately ($\lambda/2 \approx 175\,\mu m$ when considering GaAs). The obtained results are exactly the same as the ones predicted by Brueck on his paper related to the radiation pattern of dipoles embedded in a dielectric slab [7].

The radiation patterns of both horizontal and vertical Hertzian dipoles when placed in the middle of a 350 µm GaAs wafer are depicted in Figures 2.16b−2.16e at 4 different frequencies. The figures 2.16b and 2.16d represent the radiation pattern at 486 GHz and 605 GHz for the horizontal and vertical dipoles respectively. These frequencies correspond to two of the peaks in the radiated power of the figure 2.16a. In the figures 2.16c and 2.16e the radiation pattern normalized to previous ones at 600 GHz and 470 GHz for the horizontal and vertical dipole are depicted. These frequencies correspond to two of the minima in the radiated power of Figure 2.16a. It can be seen how the radiation pattern significantly change from a maximum to a minimum in the radiated power due to the fact that less power is radiated and more power remains inside the wafer.

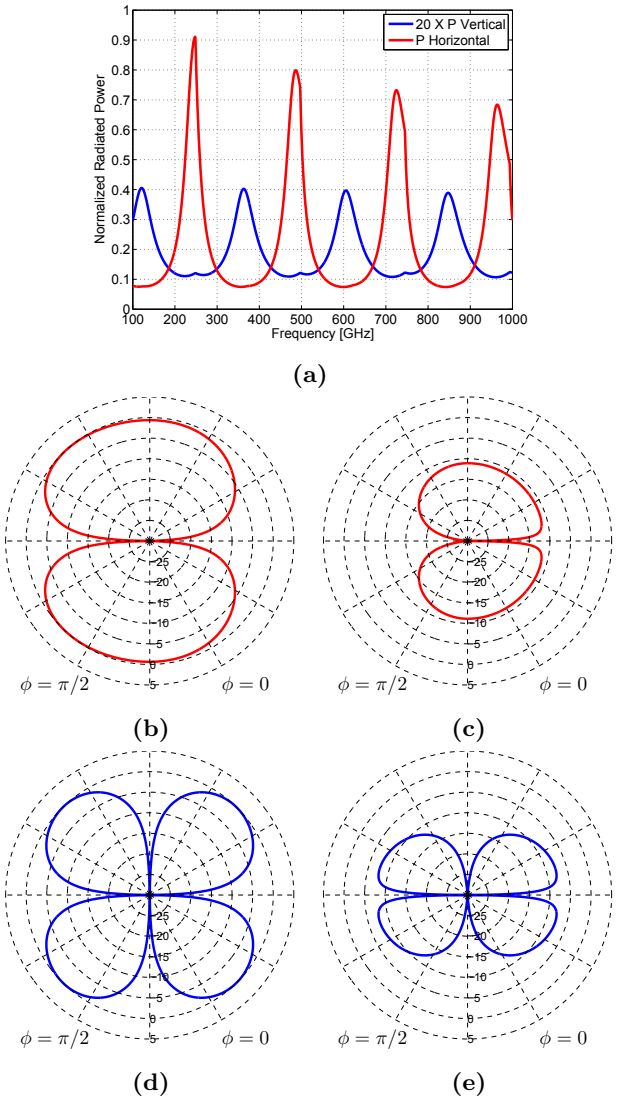

Figure 2.16: Fabry-Perot behaviour on the radiation pattern. (a) Normalized radiated power to the embedded dipole case ($\epsilon_r = 12.9$) for an horizontal (red line) and vertical (blue line) Hertzian dipoles lying in the middle of a 350 µm GaAs wafer as a function of frequency. (b) Horizontal dipole at 486 GHz and (c) 600 GHz normalized to the 486 GHz case. (d) Vertical dipole at 605 GHz and (c) 470 GHz normalized to the 605 GHz case.

2.4 Anomalies in the Radiation Pattern

Several approaches have been done for solving the problem of calculating the emitted power and the radiation pattern of dipoles and slots laying on the interface between two media as mentioned in the above sections [1–6]. However, in spite of that all of them present pretty similar results based on the use of MoM [1] or by using rigorous mathematical methodology theory [4–6], there exists a problem in the radiation pattern. The radiation pattern from a dipole laying on the interface of two media presents some potential singularities that are discussed in this section and, up to the author knowledge, there is no explanation in the literature for them.

If one tries to give an explanation to the radiation patterns shown before (Sections 2.2.1 and 2.2.2), it is possible to extract some interesting conclusions. As it is well explained by Pozar, Brewitt-Taylor and Rutledge in their excellent papers [1–3], for the dipole, the H-plane pattern in the dielectric has a maximum at the critical angle $\theta_c = \pi - \sin^{-1}(1/\sqrt{\epsilon_r})$ whereas the E-plane pattern has a minimum there. Both patterns have a null at the interface except the H-plane pattern for $\epsilon_r = \epsilon_{r1}/\epsilon_{r2} = 1.0$, as discussed by Rutledge et al. [2]. A maximum and/or minimum at the critical angle does not occur for slot antennas because the conducting plane effectively isolates the two media, as it is well explained by Pozar [1].

However, it is interesting to have a look at the maximum of the radiation patterns. If we take again the results from Sections 2.2.1 and 2.2.2, we can plot the two cases, vertical and horizontal dipoles, on the interface between two media with relative refractive index $n = n_1/n_2 = \sqrt{12.9}$ and air in rectangular coordinates (Figure 2.17).

If we apply a well-known theorem from Signal Theory (Bernstein's theorem) with direct application to Antenna Theory (as it is well explained in the book [17]), it can be found that if F_1 is an upper limit of the radiation function $F(\tau)$, being $\tau = \sin(\theta)$, and D the dimension of the aperture, and supposing that the radiation pattern $F(\tau)$ possesses a bounded spectrum $(-\nu_0, +\nu_0)$, it follows from Bernstein's theorem that the relative slope of the pattern is limited by the spatial frequency bandwidth of the antenna:

$$\frac{1}{F_1}\frac{dF}{d\tau} \leq 2\pi\nu_0 = \pi\frac{D}{\lambda} \tag{2.1}$$

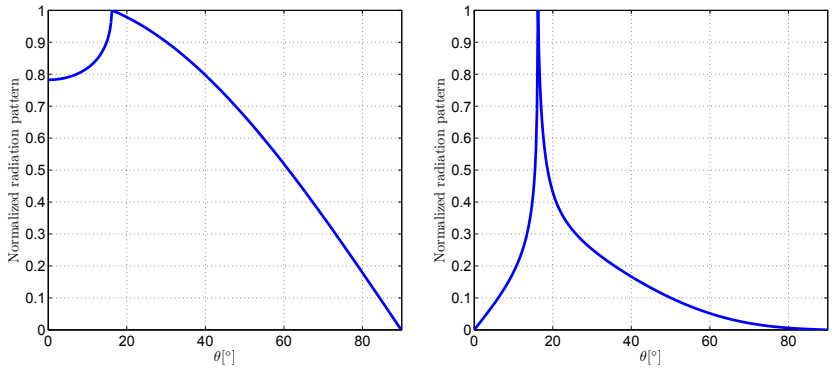

(a) **(b)**

Figure 2.17: Radiation pattern of a dipole at the interface. Relative refractive index $n = \sqrt{12.9}$. (a) Horizontal dipole H-plane, (b) Vertical dipole E-plane

The slope limitation plays an important role, such as with the angular sensitivity of tracking antennas. This is also the case with radar antennas where it is desired that the gain falls rapidly to zero below the horizon to avoid ground clutter. More generally, Bernstein's theorem implies a limit to all derivatives of bounded signals with bounded spectra:

$$\frac{1}{F_1} F^{(n)}(\tau) \leq (2\pi\nu_0)^n \tag{2.2}$$

So, it is possible to deduce a relationship between the dimension D of the aperture and the HPBW of the main lobe of the radiation pattern. This, easily manipulated, implies the Rayleigh limit for the accuracy resolution in far field.

Calculating the derivative of the radiation pattern of a dipole (horizontal and vertical) lying above a semi-infinite medium from Figure 2.17 results the Figure 2.18. In any event, the result of Bernstein's theorem says that the first derivative is bounded, which could be right for our pattern of interest since this pattern has a slope discontinuity, but the slopes are finite. But then the second derivative of the pattern vs. angle will be infinite at the point of the slope discontinuity, and so Bernstein's theorem will not be satisfied. So if these results apply to any size antenna, the patterns we are looking at seem to violate this theorem.

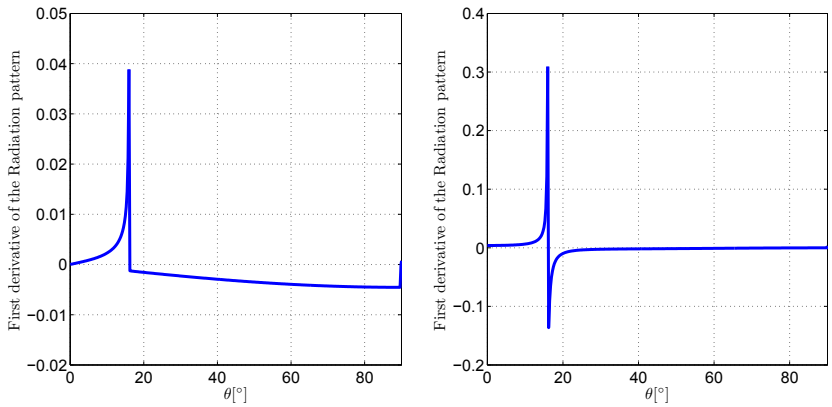

(a) **(b)**

Figure 2.18: First derivative from the radiation pattern of a dipole at the interface. Relative refractive index $n = \sqrt{12.9}$. (a) Horizontal dipole H-plane and (b) Vertical dipole E-plane.

An alternative argument is that the far-field cannot have a slope discontinuity because the field must satisfy Maxwell's equations (in the far-field), and taking the curl of an E-field with a slope discontinuity will produce a step function in **H**, and doing a curl on **H** to find **E** would lead to a delta function, etc. - which is clearly incorrect.

This discontinuity in the H-plane pattern occurs because the Stationary Phase (SP) approximation (which has been used to derive the far-field expressions in most of the references) breaks down at the critical angle. The SP method, in simple form, has an integrand of the form $F(x)e^{-jkf(x)}dx$ where $F(x)$ is assumed to have a well-behaved phase near the stationary point. Examination of the integrand for the half-space problem, however, shows that $F(x)$ goes from real to complex at the critical angle, thus violating this assumption, and producing the non-physical change in slope. The problem apparently is with the application of the stationary phase method.

This anomaly in the radiation pattern studied in this section is also presented in many other antenna structures, as can be read in [18]. So, care in the application of the SP method should be taken into account.

2.5 Dielectric Lenses as Substrate for Antennas

A way of designing millimetre and sub-millimetre hyper-hemispherical dielectric lens antennas is presented in this section. This approach consists of obtaining the radiated fields of a planar antenna via a full-wave electromagnetic simulator (CST [14], FEKO [13], etc.) or in-house software (as the one used in previous sections) and using them as inputs to a ray tracing and Physical Optics (PO) technique. This approximation reduces the overall computing time and resources, as well as makes it possible to design a wide variety of different lens antennas. Across the section, the obtained results are compared with those previously reported by different authors in order to validate the program.

2.5.1 Hyper-Hemispherical Dielectric Lenses

Dielectric lenses have been one of the most used elements in the millimetre and the sub-millimetre frequency range as substrate for planar antennas. With such substrate, radiation pattern of planar antennas is improved since the directivity is increased as well as gaussicity, while back radiation is reduced [2, 19]. As mentioned before, at these frequencies, available substrates are too thick in terms of the wavelength. This results on an increase of the losses due to the fact that unwanted modes are generated inside the substrate [20] as it has been showed in the above sections. Using a dielectric lens as substrate, these modes are not generated because of the lens geometry.

Ideal shape of a dielectric lens is the ellipsoidal one [21,22]. However, it is very difficult to manufacture, so using it is not practical. An elliptical lens can be approximated by an extended hemispherical one [19] (Figure 2.19) or a hyper-hemispherical one (basically a truncated sphere), which are much easier to fabricate. These two characteristics make them the most used kind of lenses. Both extended hemispherical and hyper-hemispherical lenses behave in a similar manner and the methodology explained here is valid for both kind of lenses.

In order to design this kind of lenses, the computational strength of current full-wave electromagnetic simulators (CST [14], HFSS [23], FEKO [13], ...) is combined with ray tracing techniques and conventional

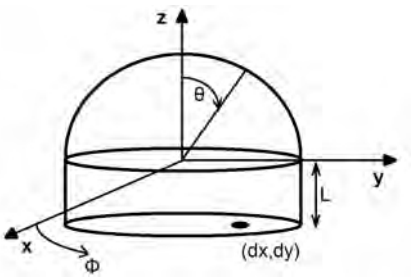

Figure 2.19: Extended hemispherical dielectric lens geometry.

PO. The problem of designing planar antennas with dielectric lenses is that dimensions of dielectric lenses are in the order of several wavelengths ($7\lambda \sim 15\lambda$), while typically planar antennas are smaller than λ. For that reason, simulating the whole structure (planar antenna + dielectric lens) will take a lot of time and, in some cases, the amount of computational resources needed will exceed the available ones.

2.5.2 Lens Design

A planar antenna placed over a high permittivity substrate radiates most of the power into it (as has been showed in Section 2.2), so an unidirectional radiation pattern is obtained [19]. An extended hemispherical geometry is used for the dielectric lens since it can approximate the elliptical lens behaviour and it is easier to manufacture. Such geometry can be seen on Figure 2.19.

The dielectric lens consists of a hemisphere with radius R and a cylindrical block with length L. Planar antenna is placed on the bottom of the lens with a displacement dx, dy from the axis origin.

The dielectric extended hemispherical lenses satisfy sine condition, which guarantees circular coma absence, and they do not have circular aberrations. This implies that if an optical system is designed in such a way that all rays are focused to a point, an extended hemispherical lens can be included in the system and the rays will be focused to the same point [19].

With this lens, the directivity of the planar antenna is increased and the radiation pattern fits well to a Gaussian beam system. The most influential parameter on the system directivity is the length of the cylindrical block (L) as will be shown in the next subsection. This is due to the fact that the antenna must be placed at the focus of the lens, but in this case the lens is hemispherical so a cylindrical block must be included to place the antenna in the focus of the equivalent elliptical lens.

2.5.3 Methodology Description

The methodology followed for the design of planar antennas over dielectric extended hemispherical lens can be divided in two parts. The first one consists of designing the planar antenna on a commercial full-wave electromagnetic simulator (CST [14], FEKO [13], ...) or in-house software (as the one used in the previous sections). To do so, the antenna is placed over a semi-infinite dielectric substrate with the same permittivity of the lens. With this simulation, the radiated fields are obtained as a function of spherical coordinates θ and ϕ.

Once the radiated fields are obtained, a ray tracing technique is carried out from a point (antenna position) with the same direction as the propagation one. The lens geometry can be divided into four parts (Figure 2.20, [24]). The first one (Figure 2.20a) is limited by the total reflection angle. In this region both transmitted and reflected waves appear and it is the main part contributing to the radiation pattern of the lens. In the developed software, this region is the only one considered to obtain the radiation pattern. The second region (Figure 2.20b) is the one between the critical angle and the end of the hemisphere. Here no transmitted waves appear since the incident angle is higher than the critical one and all the incident waves are reflected. Evanescent waves appear outside the lens that do not contribute to the radiated field. The third region (Figure 2.20c) is limited by the end of the hemisphere and the critical angle in the slab. In this region, the incident angle is higher than the critical angle, so only reflected waves appear. Even lower evanescent waves appear outside the lens when comparing with the second region because directive antennas are used. The contribution to the far field calculation can be neglected. Finally, the fourth region (Figure 2.20d)

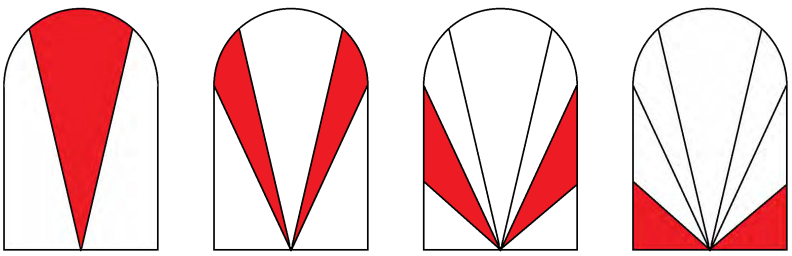

Figure 2.20: Regions into which the extended hemispherical lens can be divided. (a) Spherical region where transmitted and reflected rays appear, (b) Spherical region where total reflection occurs, (c) Planar region where total reflection occurs and (d) Planar region where transmitted and reflected rays appear.

is limited by the critical angle in the slab and the end of it (both transmitted and reflected waves). In this part, the lowest radiation intensity of the antenna is obtained and the contribution to the far field can also be neglected. Reflected rays among the different regions can be reflected again and impinge on the lens-air interface, thus contributing to the generated final field, but its contribution will be of low significance [25].

After that, PO is applied to generate the currents in the surface of the first region of the lens (Figure 2.20a). Finally, the radiation pattern generated by those currents is obtained. Steps to do this second part are the following.

The first one is to decompose electric and magnetic field in TE and TM components in the lens-air interface using the formulas of the reflection and transmission coefficients when a wave impinges on a dielectric with permittivity ϵ_r [26]:

$$\Gamma_{TE} = \frac{\sqrt{\epsilon_r}\cos\theta_i - \sqrt{1-\epsilon_r \sin^2\theta_i}}{\sqrt{\epsilon_r}\cos\theta_i + \sqrt{1-\epsilon_r \sin^2\theta_i}} \tag{2.3}$$

$$\tau_{TE} = 1 + \Gamma_{TE} \tag{2.4}$$

$$\Gamma_{TM} = \frac{\sqrt{\epsilon_r}\cos\theta_i\sqrt{1-\epsilon_r\sin^2\theta_i} - \cos\theta_i}{\sqrt{\epsilon_r}\cos\theta_i\sqrt{1-\epsilon_r\sin^2\theta_i} + \cos\theta_i} \tag{2.5}$$

$$\tau_{TM} = (1+\Gamma_{TM})\,\frac{\cos\theta_i}{\sqrt{1-\epsilon_r\sin^2\theta_i}} \tag{2.6}$$

where ϵ_r is the dielectric constant of the lens material, θ_i is the incidence angle with respect to the normal lens surface, and Γ and τ are TE and TM reflection and transmission coefficients.

Once the electric and magnetic fields have been defined (primary fields), the electric ($\mathbf{J_s}$) and magnetic ($\mathbf{M_s}$) current densities are obtained outside the lens surface [26]:

$$\mathbf{J_s} = \hat{\mathbf{n}} \times \mathbf{H} \tag{2.7}$$

$$\mathbf{M_s} = -\hat{\mathbf{n}} \times \mathbf{E} \tag{2.8}$$

where $\hat{\mathbf{n}}$ is the normalized normal vector to the interface.

From this magnetic and electric density currents, θ and ϕ components of the electric field in far-field are calculated [26]:

$$E_\theta \cong -\frac{\jmath k e^{-\jmath kr}}{4\pi r}\left(L_\phi + \mu N_\theta\right) \tag{2.9}$$

$$E_\phi \cong +\frac{\jmath k e^{-\jmath kr}}{4\pi r}\left(L_\theta + \mu N_\phi\right)... \tag{2.10}$$

where $\mathbf{N}$ and $\mathbf{L}$ are the radiation vectors defined by [26]:

$$\mathbf{N} = \iint_{s'} \mathbf{J_s} e^{\jmath kr'\cos\psi} ds' \tag{2.11}$$

$$\mathbf{L} = \iint_{s'} \mathbf{M_s} e^{jkr' \cos\psi} ds' \tag{2.12}$$

where s' is the external surface of the lens, r' is the distance from the origin to where the equivalent magnetic and electric density currents are calculated, r is the distance from the origin to the observation point and ψ is the angle between r and r'.

2.5.4 Results

For the lens design program development, MATLAB has been used as programming tool and a simple Graphical User Interface (GUI) has been designed (Figure 2.21). Input parameters to such GUI are lens dimensions, working frequency, lens permittivity, antenna position and data file with simulated radiated primary fields. 3D and 2D radiation patterns are obtained, as well as beamwidth and directivity.

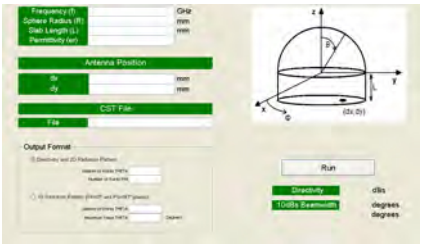

Figure 2.21: GUI of the developed program.

In order to check the correct operation of the program several simulations have been carried out and results are compared with different published papers.

The first one is a log-spiral planar antenna working at 600 GHz. An antenna with the same dimensions as the one in [27] was designed in CST Microwave Studio [14] over semi-infinite silicon substrate. The obtained radiated fields were used as input parameter to the developed program and a silicon ($\epsilon_r = 11.7$) extended hemispherical lens with dimensions $R = 6.35\,\text{mm}$ and $L = 2.4\,\text{mm}$ was designed. Figure 2.22 shows the obtained results. A 10 dB beamwidth of 2.22° and a directivity of 35.85 dB were obtained, which are identical results to the ones obtained in [27].

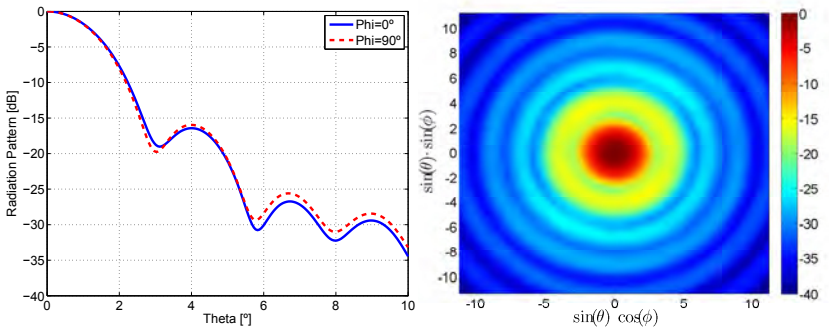

(a) **(b)**

Figure 2.22: 600 GHz log-spiral antenna with silicon extended hemispherical lens. (a) Radiation pattern at $\phi = 0$ and $\phi = 90^{\circ}$ and (b) Radiation pattern as a function of θ angle.

A second demonstration of the operation of the program was carried out by comparing results obtained in [19]. In this case, a double-slot antenna working at 246 GHz is used as feeding element. A silicon (ϵ_r = 11.7) extended hemispherical lens with a radius of 6.85 mm was used. Directivity variation as a function of the length of the cylindrical block (L) is plotted in Figure 2.23.

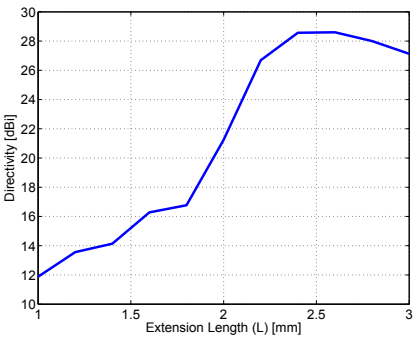

Figure 2.23: 246 GHz double-slot antenna. Directivity as a function of the slab length (L).

Obtained results are pretty similar to the ones presented in [19], and it can be noticed how the slab length (L) affects dramatically the overall system directivity.

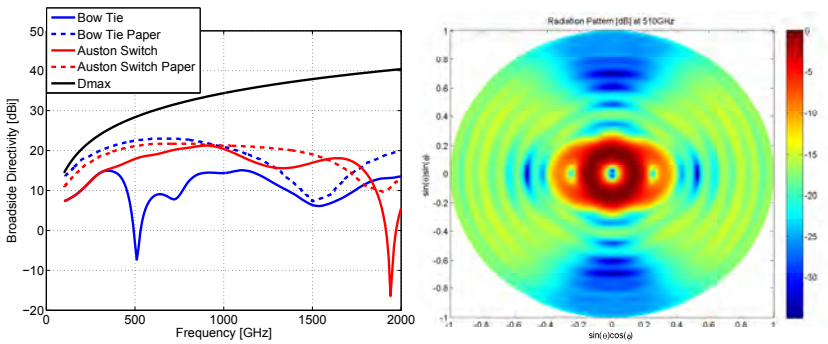

(a) **(b)**

Figure 2.24: (a) Comparison with [28]. Directivity vs. frequency. Continuous line represents the simulated results while dashed line represents the results obtained by authors in [28]. Blue lines are the bow-tie case, red lines are Auston switch case and black line is the maximum achievable directivity. (b) Simulated radiation pattern obtained for the Bow Tie at 510 GHz.

In both examples showed above, CST Microwave Studio [14] was used to obtain the primary fields and obtained results fit pretty well with the predicted ones. However, it has been observed that sometimes the obtained results are not the expected ones with this software. While trying to validate the results obtained in [28] some uncertainties arise. In that paper, authors simulate two well-known antennas (bow-tie and Auston switch) with CST Microwave Studio over semi-infinite silicon substrate in the frequency range 100 GHz - 2000 GHz. With the obtained primary fields, then the radiation pattern when using a silicon lens with 5 mm radius and 1.55 mm slab length (L) is obtained. In the Figure 2.24a, with dashed lines, the directivity of the same bow-tie and Austin switch obtained via CST [14] + developed software are depicted. Results are mainly the same as the ones presented by authors [28]. On the other hand, when the exact Green's function of a semi-infinite substrate is used (FEKO [13] instead of CST [14]), continuous lines in Figure 2.24a are obtained. It can be seen that a null in broadside direction is obtained at 510 GHz (Figure 2.24b) that is not contemplated when using CST [14] as the electromagnetic software to obtain the primary fields. These results were reported in [15] and a discussion on the topic is now open. It seems that CST [14] makes a good approximation on obtaining the far-field

when an antenna is placed over a semi-infinite medium, but not enough accurate in some cases. FEKO [13] (Green's function and MoM) obtains the exact radiation pattern of an antenna placed over a semi-infinite medium, so it seems to be a more suitable option when dealing with these topologies.

2.6 Conclusions

In this chapter, the radiation pattern of planar antennas at THz and sub-THz frequencies has been analysed. At THz/sub-THz frequencies, available substrates are very thick in terms of the wavelength, which dramatically affects the radiation pattern of planar antennas. To analyse such radiation patterns, both analytical and MoM based solutions have been derived for the most elementary antenna, the Hertzian dipole.

First, an approximation that consists of considering that the substrate has semi-infinite thickness has been done. Radiation pattern results of both vertical and horizontal Hertzian dipoles lying on the interface between two semi-infinite media have been obtained. It has been shown that most of the power is radiated through the substrate and a maximum appears, in both cases, at the critical angle. This maximum depends only on the relationship between the refraction index of both media considered (normally vacuum and another substrate) and if the dipole is moved away from the interface this maximum does not change.

Secondly, finite thickness substrate is considered and results were compared with the semi-infinite case. As an example, typical 350 µm GaAs wafer has been considered. The radiation pattern of both vertical and horizontal Hertzian dipoles lying on the top of the wafer have been obtained and the results are different than the ones obtained with semi-infinite substrate. The first difference is that now results depend on frequency. That is clear since in terms of the wavelength the substrate has different thickness. The second difference is that the maximum that appears in the semi-infinite case does not appear any more. And the third main difference is that, at least for the vertical dipole case, now most of the power is not radiated through the substrate. So considering semi-infinite substrate approximation is a good option in some cases (dielectric lens) but is not accurate and practical in most of them.

The next step was to include the dipole inside the wafer and analyse its radiation pattern. This case is suitable for CMOS integrated chips or LAEs (Section 3.3). The same GaAs 350 µm wafer was considered and both vertical and horizontal Hertzian dipoles were analysed. It has been shown that the radiation pattern is completely different as the ones obtained previously and depending on the position where the dipole is placed inside the wafer more power is radiated to the bottom side or to the top one. Also, the amount of power that is effectively radiated outside of the wafer is obtained. When placing a dipole inside a dielectric medium, substrate modes can be excited and most of the power can be kept inside the dielectric. A dipole lying in the middle of a 350 µm GaAs wafer has been simulated and the radiated power outside the wafer has been obtained. It is shown that a Fabry-Perot behaviour appears, with maxima in the radiated power at certain frequencies and minima at others ($\lambda/4$ separation between maximum and minimum). Much more power is radiated when an horizontal dipole is considered compared to the vertical one. This is due to the fact that vertical dipole excites substrate modes more easily because of its vertical electric field. So, when dealing with antennas placed inside a dielectric medium, not only the radiation pattern must be correctly obtained but also the amount of power that is effectively radiated has to be taken into account.

One of the main contributions of this chapter was to analyse what happens in the radiation patterns of dipoles lying over a semi-infinite substrate. As it is shown in Section 2.2, a sharp peak appears in the maximum of the radiation pattern. It has been showed in Section 2.4 why this sharp peak is physically meaningless applying the Bernstein's theorem. The origin of these anomalies in the radiation patterns is due to the SP approximation (which has been used to derive the far-field expressions in most of the references) that breaks down at the critical angle.

Finally, the other main contribution of this chapter was to develop a program which is capable of obtaining the radiation pattern of a planar antenna placed over a dielectric extended hemispherical lens. The program makes use of the potential of commercially available full-wave electromagnetic softwares and PO/ray-tracing techniques. First, radiation pattern of a planar antenna lying over semi-infinite substrate was obtained via CST, FEKO, ..., and then, the lens is divided into four

regions and currents generated in the lens surface are obtained. Finally, the radiation pattern generated by those currents is calculated. With this method, the radiation pattern of a planar antenna placed over a dielectric extended hemispherical lens can be easily obtained and the amount of computational resources, as well as computational time, are drastically reduced. The obtained results were compared with some results available in the literature and which electromagnetic software is better to be used as the one to obtain the primary fields is discussed. It was shown that CST makes a good approximation and is valid in most of the cases, but FEKO solves the problem with the exact solution since it makes use of the Green's function of a semi-infinite medium.

Both MoM based and dielectric lens developed softwares are the key tools to analyse radiation patterns in Chapters 3 and 4 of this Ph.D. dissertation.

This chapter of the thesis has led to the publication of a JCR journal paper (first quartile) and a book chapter as well as a conference contribution (see Publications section at the end of this document).

2.7 References

[1] M. Kominami, D. Pozar, and D. Schaubert, "Dipole and Slot Elements and Arrays on Semi-Infinite Substrates," *IEEE Transactions on Antennas and Propagation*, vol. 33, no. 6, pp. 600–607, 1985.

[2] D. B. Rutledge, D. P. Neikirk, and D. P. Kasilingam, "Integrated Circuit Antennas," *Infrared and millimeter waves*, vol. 10, no. part 2, pp. 1–90, 1983.

[3] C. Brewitt-Taylor, D. Gunton, and H. Rees, "Planar Antennas on a Dielectric Surface," *Electronics Letters*, vol. 17, no. 20, pp. 729–731, 1981.

[4] W. Lukosz and R. Kunz, "Light Emission by Magnetic and Electric Dipoles Close to a Plane Interface. I. Total Radiated Power," *JOSA*, vol. 67, no. 12, pp. 1607–1615, 1977.

[5] ——, "Light Emission by Magnetic and Electric Dipoles Close to a Plane Dielectric Interface. II. Radiation Patterns of Perpendicular Oriented Dipoles," *JOSA*, vol. 67, no. 12, pp. 1615–1619, 1977.

[6] W. Lukosz, "Light Emission by Magnetic and Electric Dipoles Close to a Plane Dielectric Interface. III. Radiation Patterns of Dipoles with Arbitrary Orientation," *JOSA*, vol. 69, no. 11, pp. 1495–1503, 1979.

[7] S. Brueck, "Radiation from a Dipole Embedded in a Dielectric Slab," *IEEE Journal of Selected Topics in Quantum Electronics*, vol. 6, no. 6, pp. 899–910, 2000.

[8] S. Preu, G. Döhler, S. Malzer, L. Wang, and A. Gossard, "Tunable, Continuous-Wave Terahertz Photomixer Sources and Applications," *Journal of Applied Physics*, vol. 109, p. 061301, 2011.

[9] S. Ramo, J. R. Whinnery, and T. Van Duzer, *Fields and Waves in Communication Electronics*. John Wiley & Sons, 2007.

[10] D. B. Rutledge, *Submillimeter Integrated Circuit Antennas and Detectors*. Ph. D. Thesis, University of California, Berkeley, California, 1980.

[11] M. Born and E. Wolf, *Principles of Optics*. Pergamon Oxford Ed., 1980.

[12] K. Michalski and J. Mosig, "Multilayered Media Green's functions in Integral Equation Formulations," *IEEE Transactions on Antennas and Propagation*, vol. 45, no. 3, pp. 508–519, Mar 1997.

[13] EM Simulation Software. (2014, May) FEKO. [Online]. Available: http://www.feko.info/

[14] Computer Simulation Technology. (2014, April) CST. [Online]. Available: https://www.cst.com/

[15] L. García-Muñoz, "Comments on "THz Time-Domain Sensing: The Antenna Dispersion Problem and a Possible Solution."," *IEEE Transactions on Terahertz Science and Technology*, vol. 4, no. 1, pp. 125–126, Jan 2014.

[16] K. Sengupta and A. Hajimiri, "A 0.28 THz Power-Generation and Beam-Steering Array in CMOS Based on Distributed Active Radiators," *IEEE Journal of Solid-State Circuits*, vol. 47, no. 12, pp. 3013–3031, Dec 2012.

[17] S. Drabowitch, A. Papiernik, H. Griffiths, J. Encinas, and B. L. Smith, *Modern Antennas*. Springer, 1998.

[18] D. R. Jackson, P. Burghignoli, G. Lovat, F. Capolino, J. Chen, D. R. Wilton, and A. A. Oliner, "The Fundamental Physics of Directive Beaming at Microwave and Optical Frequencies and The Role of Leaky Waves," *Proceedings of the IEEE*, vol. 99, no. 10, pp. 1780–1805, 2011.

[19] D. F. Filipovic, S. S. Gearhart, and G. M. Rebeiz, "Double-Slot Antennas on Extended Hemispherical and Elliptical Silicon Dielectric Lenses," *IEEE Transactions on Microwave Theory and Techniques*, vol. 41, no. 10, pp. 1738–1749, 1993.

[20] G. M. Rebeiz, "Millimeter-Wave and Terahertz Integrated Circuit Antennas," *Proceedings of the IEEE*, vol. 80, no. 11, pp. 1748–1770, 1992.

[21] A. Oliner, D. Jackson, and J. Volakis, *Antenna Engineering Handbook*. McGraw Hill, 2007.

[22] R. E. Collin, *Antennas and Radiowave Propagation.* McGraw-Hill New York, 1985.

[23] ANSYS Simulation Driven Product Development. (2014, May) HFSS. [Online]. Available: http://www.ansys.com/

[24] S.-Y. Chen and P. Hsu, "A Simplified Method to Calculate Far-Field Patterns of Extended Hemispherical Dielectric Lens," in *Microwave Conference, 2007. APMC 2007. Asia-Pacific.* IEEE, 2007, pp. 1–4.

[25] A. Neto, S. Maci, and P. De Maagt, "Reflections Inside an Elliptical Dielectric Lens Antenna," *IEE Proceedings-Microwaves, Antennas and Propagation*, vol. 145, no. 3, pp. 243–247, 1998.

[26] C. A. Balanis, *Antenna Theory: Analysis and Design.* John Wiley & Sons, 2012.

[27] W. Miao, Y. Delorme, F. Dauplay, G. Beaudin, Q. Yao, and S. Shi, "Simulation of an Integrated Log-Spiral Antenna at Terahertz," in *8th International Symposium on Antennas, Propagation and EM Theory, 2008. ISAPE 2008.* IEEE, 2008, pp. 58–61.

[28] N. Llombart and A. Neto, "THz Time-Domain Sensing: The Antenna Dispersion Problem and a Possible Solution," *IEEE Transactions on Terahertz Science and Technology*, vol. 2, no. 4, pp. 416–423, July 2012.

CHAPTER 3

THZ EMITTERS. PHOTOMIXERS AND LARGE AREA EMITTERS

This chapter is devoted to THz emitters and two approaches to increase the THz emitted power are presented. The first one is a CW THz Antenna Emitter (AE) photomixing scheme, where an antenna is designed in such a way that the emitted power is maximized and the overall emitter is simplified because the typical RF choke is eliminated. The second approach is an antenna-free scheme of photomixing where the THz radiation is directly originated from the acceleration of photo-induced charge carriers generated within a large semiconductor area. This is called LAE and the work developed here consists of designing an electromagnetic equivalent circuit based on infinitesimal dipoles to estimate its the radiation pattern.

The chapter is organized in three sections. In the first one, a brief introduction on THz/sub-THz emitters is done. The main parameters of such emitters are introduced and a classification of them is presented. The second section is devoted to CW THz photomixing AE while in the third section the LAE concept is discussed and a Hertzian dipoles based equivalent circuit is presented.

3.1 Introduction to THz Emitters

Maximizing THz emitted power is one of the hot topics in the electronic and photonic communities nowadays [1]. THz waves have been presented as one of the most promising research lines due to its unique capabilities. Extremely short pulses can be generated, which are capable of obtaining high spatial resolutions, going across light opaque materials and visualizing and identifying microscopic structures by spectral analysis. As mentioned in Chapter 1, THz waves can find a lot of applications that range from radioastronomy to imaging, security, biomedical, industrial, etc [1]. However, the low amount of power that current devices can generate at these frequencies is the main drawback that these applications find to be developed, so increasing this power is a key issue [2].

Two main approaches are being followed nowadays to generate THz waves at room temperature [1]. The first one is a purely electronic approach based on up-conversion [3] while the second one consists on electro-optical down-conversion ("photomixing") [4]. In addition, direct quantum mechanical frequency generation (QCLs [5]) is a well established THz source. Unfortunately, nowadays it cannot work at room temperature. Another interesting approach to generate THz CW power is the LAE concept [6]. This is an antenna-free new scheme of photomixing where the THz radiation is directly originated from the acceleration of photo-induced charge carriers generated within a large semiconductor area. This concept will be expanded on Section 3.3. In the Figure 3.1 the so-called "THz Gap" is depicted. It can be seen how as we move from microwave frequencies to THz frequencies the emitted power of available THz sources decreases. The same happens when the approach is made from optical frequencies down to THz frequencies. This lack of available THz sources with enough power is, perhaps, the main drawback of THz waves.

In this chapter introduction, main parameters of THz emitters are presented and briefly described, and then a classification of THz emitters is included.

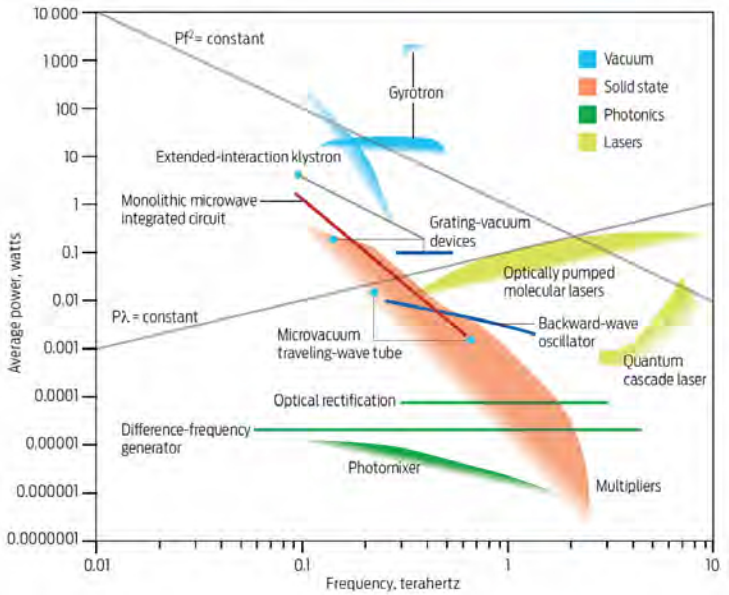

Figure 3.1: The "THz Gap". Main THz sources and its output power [7].

3.1.1 Emitter Parameters

Among the different parameters that can be defined for an emitter performance, the most important ones are the following:

Pulsed/CW operation A power generator can emit either pulsed or CW radiation (or both). In this work we will focus on CW operation, but there exists a lot of devices and applications where pulsed radiation is important (THz TDS [8], THz Imaging for security [9] and biomedical applications [10], etc.).

Maximum Power This parameter represents the maximum output power demonstrated for a given technology. It is strongly related to the working frequency and, when mentioning the maximum output power of an emitter, it is important to highlight at which frequency this value is measured. In the Figure 3.1 the output power of most of the available THz sources is depicted.

Frequency Range Frequency range in which it is possible to generate signals within a minimum performance. Depending on the technology used devices will work better at frequencies closer to optical ones or closer to microwave ones.

Tunability This parameter represents if the working frequency can be easily changed or if the emitter works at a fixed frequency.

Phase Noise Phase Noise is the frequency domain representation of rapid, short-term, random fluctuations in the phase of a waveform, caused by time domain instabilities. The lower this value is, the better performance the device has.

Size This is a very important parameter since a lot of THz emitters occupy a large space and need of external devices such as coolers to work properly. If a compact emitter is needed, size must be a key parameter.

Coherent/Incoherent Coherent sources are defined as those having a significant degree of both temporal and spatial coherence in the generated signals.

Cooling Some THz emitters need to be cooled in order to work properly. Room temperature operation is defined for those systems where no cooling is needed.

3.1.2 Classification of THz Emitters

In this section a classification of CW THz/sub-THz sources is included [11–13]. THz/sub-THz emitters are divided into three categories. First one includes the direct emitters or oscillators; second one includes the generation of THz/sub-THz signals by downconversion from optical ones; and third category includes the devices capable of generate THz/sub-THz signals by upconversion of electronic signals.

Direct/Oscillators

Among the available direct THz generators or THz oscillators it must be differentiated between thermal sources, gas lasers, bulk semiconductor lasers, QCLs, electron beam sources, electronic diode oscillators and plasmonic FET. All of them are explained within this subsection.

Thermal Sources

Thermal THz sources include the globar and the plasma sources.

Globar A Globar, or glowing bar, is a silicon carbide rod heated to about 1500 K by passing an electric current through it [11]. This rod is typically 20 mm - 60 mm long and 5 mm in diameter, capped with metallic electrodes contained in water-cooled housing with a slit to allow light out with the angular spread required for spectroscopy [13]. Its relatively uniform output is advantageous for spectroscopy, but its lower working frequency is 3 THz.

Plasma Sources Two different devices can be included in this plasma sources group: mercury arc lamps and metal halide lamps. They are incoherent sources that have an emission spectrum similar to that of the Blackbody. A mercury arc lamp is a broadband THz light source that emits a continuous THz spectrum from 300 GHz to 30 THz. The lamp consumes 125 W and requires water-cooling. Its output is a combination of the emission of the arc itself, which is at 5000 K, and the quartz envelope that reaches 1000 K. Metal halide lamp has an approximately spherical diameter of 3 mm and consumes only 21 W and a surface temperature of nearly 1400 K. It is more suitable where a small source size is required [13].

(a) **(b)** **(c)**

Figure 3.2: (a) Globar, (b) Mercury Arc Lamp and (c) Metal Halide Lamp.

Gas Lasers

The gas lasers emitting at THz frequencies can be divided into two groups: Electrically excited and Optically excited gas lasers.

Electrically Excited Gas Lasers The THz emission in electrically excited gas lasers is due to the population inversion between rotational levels of vibrational states of the gas compounds, achieved by the electric excitation of the gas tubes. H_2O, D_2O, NH_3, Carbonyl Sulfide (OCS), H_2S, SO_2, Deuterium Cyanide (DCN) and Hydrogen Cyanide (HCN) are the typical gases employed, but among them, only DCN and HCN are useful sources (1 THz - 1.5 THz, $\sim$ 600 mW for a 6.5 m long laser [14]). A schematic of it can be seen on the Figure 3.3. H_2O gas lasers have a huge emission range from 1 THz - 40 THz, but their very limited power makes them impractical sources [13].

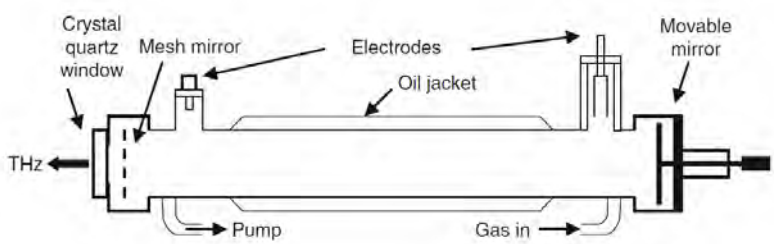

Figure 3.3: Design of a HCN or DCN laser [13].

Optically Excited Gas Lasers In an optically excited gas laser, the vibrational states of the molecules are achieved by optical pump, usually a CO_2 laser. The gas lasers pumped by a CO_2 laser have been the main CW sources above 0.3 THz for many years. They need stabilization of both power and frequency. Today, they are still used, especially in radioastronomy and fusion plasma diagnostics applications, and they cover the frequency range from 0.15 THz to 8 THz with an output power ranging from several µW up to several 100 mW [13, 15].

Bulk Semiconductor Lasers

This type of lasers is widely used in the visible region (data storage in CD and DVD players, telecommunications, etc.). They consist of a p-doped/n-doped junction and use direct band gap transitions in GaAs, InGaAs, etc. Due to electron-hole recombination, photons are emitted. The problem arise when working at THz frequencies, because this mechanism cannot be used due to the smallest direct band gaps in semiconductor materials are found to be at higher frequencies than 18 THz. However, with special mechanisms in bulk semiconductors laser action can be supported [13]. There exist two main types of bulk semiconductor lasers: Germanium lasers and Donors in doped Silicon.

Germanium Lasers By applying crossed magnetic and electric fields in p-doped Germanium, a population inversion is created between heavy and light holes and amplification and laser action occurs over a wide frequency range. Ge lasers have a broadband multi-mode emission, which is tunable in the range from 1 THz to beyond 4 THz by the applied fields. The linewidth is less than 1 MHz [13, 16].

Optically Excited Donors in Doped Silicon Population inversion and laser emission is obtained by doping Silicon with group V impurities. This population inversion can be achieved either by optical excitation with radiation from a CO_2 laser or by resonant optical excitation with radiation from a Free Electron Laser (FEL). Typically, these lasers are small square-shaped crystals with a length of a few millimetres, which need to be cooled to below 30 K. Laser transitions occur from 2.5 THz to 7 THz, with additional ones in the 1 THz to 2 THz range [13, 17].

Quantum Cascade Lasers

In a QCL, an electron is injected into the laser structure and cascades down a potential staircase, which is created by a series of quantum wells exposed to an electric field. At each step, a photon is emitted. QCLs are unipolar devices, only electrons take part in the laser process. In addition, the whole laser process occurs between conduction band states and a cascading scheme is employed where one electron can generate many photons [13, 18]. The lowest working frequencies of these devices

is 0.8 THz while the highest one is around 5 THz. They are very narrow-band devices ($\sim$ 10 GHz) and need to be cooled (maximum temperature $\sim$ 130 K). The output power that can be reached goes up to 140 mW [13].

Electron Beam Sources

Backward Wave Oscillator BWO working principle is similar to the "travelling wave amplifier" mechanism. The BWO is formed by a very sophisticated high vacuum diode whose cathode, which is warmed by a low voltage heater, emits electrons that are accelerated by a high voltage field and travel towards the anode. The electrons are collimated by a very uniform magnetic field and pass over a comb-like slow-wave structure to produce the required bunching for the transfer of the kinetic energy of the electrons to an electromagnetic wave. The working frequency of the BWOs is $\sim$ 150 GHz to $\sim$ 1.4 THz, with an output power ranging from 100 mW to 1 mW in that frequency range. The major advantage of BWOs is their tunability because the output frequency is approximately proportional to the square root of the voltage across the tube [13, 19].

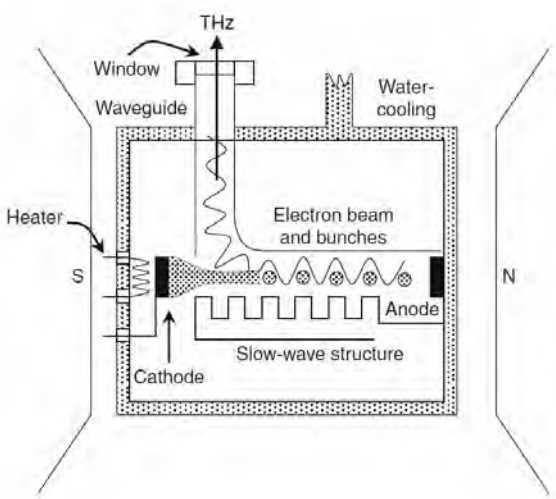

Figure 3.4: Design of a high frequency BWO [13].

Electronic Diode Oscillators

These sources are based on microwave frequency diode oscillators that are designed and implemented for higher frequency operation. Between the variety of topologies based on diodes that have been reported, it can be mentioned: Gunn diodes [20], Impact Ionization Avalanche Transit-Time (IMPATT) diodes [21], Tunnel Injection Transit-Time (TUNNETT) diodes [22] or Resonant Tunnelling Diodes (RTDs) [23, 24], being RTDs the most promising technology nowadays for the direct generation of THz signals below 1 THz - 2 THz. Gunn and IMPATT diodes can work up to 140 GHz (480 GHz using harmonics [21]) and provide around 30 mW at 100 GHz. TUNNETT diodes has been proven to work up to 706 GHz with very low output power (0.1 nW) [22]. RTD diodes can provide around 10 µW at 1 THz [23, 24].

Plasmonic Field-Effect Transistors

Although the electron decay time of FETs has been traditionally the limit factor of the maximum frequency of these devices, in the last years the identification of operation well above the theoretical bandwidth has produced a significant research effort in the use of FETs for both generation and detection of THz waves. In order to achieve 1 THz and above operation, plasmonic operation has to be produced in the device, thus requiring extremely short gate dimensions or cryogenic cooling. Nevertheless, detection has a much better performance (even better than widely used solutions) and offers a much higher potential than generation (see Section 4.1.2). The High Electron Mobility Transistors (HEMTs) are one of the FETs with more potential. They include a heterojunction of two materials with different bandgap and are mainly based on GaAs, InGaAs and InP materials. The main application field of HEMTs is as amplifiers in Monolithic Microwave Integrated Circuitss (MMICs), where they have shown gain capabilities from microwave region up to 480 GHz, with some predictions of operation above 1 THz. However, they have been already used for THz generation [25] and detection [26]. They show broadband emission over several hundreds of GHz, up to 6.5 THz. In this broadband emission, there are some resonances due to plasma wave excitations. In summary, their performance seems to be more adequate for amplification (HEMTs) and detection rather than for generation purposes.

Optical Downconversion

Photomixing

Photomixing is nowadays one of the most commonly used system to generate CW THz signals due to its broadband nature and its reasonable output power. It consists of two lasers working at two different frequencies ω_1 and ω_2 which are spatially overlapped to generate a terahertz beat-note. These lasers are then used to illuminate an ultra-fast semi-conductor material (III-V family): Low-Temperature grown GaAs (LT-GaAs), Schottky diode, Metal-Insulator-Metal (MIM) diode or photodiodes. An applied electric field allows the conductivity variation to be converted into a current which is radiated by a pair of antenna. The frequency of this current is the difference between both laser frequencies ($\omega_{THz} = \omega_1 - \omega_2$) [4, 13]. The main characteristics of CW photomixing are its broadband nature (0.1 THz - 5 THz), high tunability by changing the frequency of one of the lasers (modifying either its current or its temperature) and low conversion efficiency from the light into the THz frequency range. This CW photomixing is explained in more detail on Section 3.2.1.

Electronic Harmonic Generation

Generation based on electronic upconversion is carried out by using Schottky multipliers. This is one of the most extended technologies for sub-THz and THz generation, mainly due to the high performance they can provide.

Schottky Multipliers

The harmonic generation of THz waves from a microwave source reference is typically accomplished by SBD as they are currently the best electronic multipliers at high frequencies. A chain of SBDs, used as frequency doublers or triplers is used to multiply a reference signal that is provided by microwave sources such as BWO, IMPATT or Gunn diodes.

They can be divided into two groups: varactors and varistors, the latter ones provides higher frequency operation. The CW THz sources based in SBDs are commercially available from a few years to now, being the most widely used in several applications in the THz range. Their main limitations are the low output power and its tunability range. The latter is limited and determined by the bandwidth of the waveguides employed. To overcome this and cover wide frequency ranges, several multiplier chains covering different frequency ranges can be used. In [27], authors obtained a 2.48 THz - 2.75 THz CW signal with more than 1 µW output power based on a multiplication chain and Schottky diodes.

3.2 Meander Dipole Antenna to Increase CW THz Photomixing Emitted Power

A typical CW THz photomixing emitter consists on a semiconductor device (photomixer), a planar antenna (broadband or resonant depending on the application) and a silicon hyper-hemispherical lens (Section 2.5) to increase directivity and avoid substrate waves [28]. Traditionally, photomixing is used in broadband applications such as spectrometry because of its high frequency tunability, so broadband antennas are preferred. However, it is also utilized as signal generator for Local Oscillator (LO) on receivers [29]. In that case, a resonant antenna would be more suitable.

In [30], the authors proposed a methodology to design resonant antennas to increase output power. Photomixers have a relatively high capacitive susceptance that is compensated with a RF choke. In addition, they exhibit a very low conductance value (typically lower than $(10\,\mathrm{k}\Omega)^{-1}$), so a resonant antenna with a very high input impedance at its resonance would be desirable. With this approach, at least two components must be designed separately and then be joined together: the RF choke and the antenna. Several attempts have been followed to design antennas with a very high value of its input impedance at its resonance [30, 31] to be included in CW THz photomixing devices. But all of them include the RF choke to compensate the capacitive susceptance, so the design of the overall structure is somehow complicated.

In this section we propose for the first time the meander dipole antenna [32] as a solution to compensate both the capacitive susceptance and the conductance of the photomixer in a single element. The antenna design approach is based on the Active Integrated Antenna (AIA) concept [33, 34], in order to improve both matching and radiation efficiencies. The novelty of this work is that we forced the meander dipole antenna to work out of its main resonance, at lower frequencies, where it exhibits a clearly inductive behaviour. The proposed antenna design can be followed independently of the photomixer used and it consists on trying to maximize the radiated power obtained from it.

This section is organized as follows. After a brief introduction, the CW THz emitter structure is presented. The photomixer with its equivalent circuit and its main parameters are shown. The following section is devoted to meander dipole antenna and its behaviour. Matching, radiation and total efficiencies are calculated and a final design working at 1.05 THz is presented and compared with a similar log-periodic based CW THz AE. Finally, both meander dipole and log-periodic are manufactured and performance of both of them is compared.

3.2.1 Introduction to CW THz Generation by Photomixing

As outlined in the chapter introduction, in the traditional approach for CW THz generation by photomixing a THz current is generated in a semiconductor device using two heterodyned laser beams of photon energies $h\,(\nu_0 \pm \nu_{THz}/2)$ (with the same power, $P_L/2$, and polarization), differing in photon frequency by the THz frequency ν_{THz} (being h the Planck constant and ν_0 the central frequency). As a first step, the heterodyned laser signal is absorbed on typical length scales shorter than 1 µm, i.e. much shorter than the THz wavelength. In the second step the resulting photo-current is fed into an antenna, which then emits THz radiation [4]. A typical schematic of the CW THz generation by photomixing AE device can be seen on Figure 3.5.

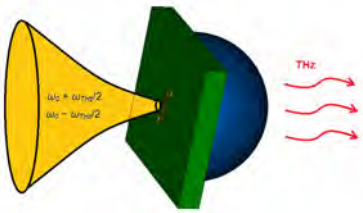

Figure 3.5: Schematic of the CW THz photomixing AE. Two optical lasers impinge on the photomixer device which is integrated with an antenna over GaAs substrate (green part). A silicon lens (blue part) is included to avoid substrate reflections and increase directivity.

Photomixer Based Emitters State-of-the-Art

Four different CW THz photomixing schemes are the most used ones. They are differentiated by the photomixer they used. The first one uses a photoconductive material (typically LT-GaAs) as the non-linear element to obtain the THz signal. The second one uses a Schottky diode as the non-linear element while the third one uses a MIM diode. The last one uses a photodiode as the non-linear element. They are described in this section and state-of-the-art results are presented.

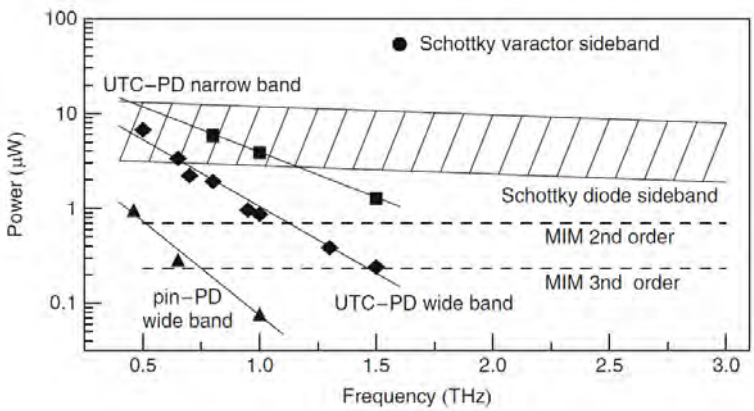

Figure 3.6: Output power of different photomixers [13].

Low-Temperature-Grown Gallium Arsenide

This material provides a very short recombination time ($\sim 0.2\,\mathrm{ps}$), which is very suitable for a fast response of the emitter material in the THz regime. The material can therefore follow THz frequencies, which allows the fabrication of THz detectors, mixers, and even THz emitters. LT-GaAs photomixers work at wavelengths around 800 nm. At telecommunication wavelengths of 1550 nm GaAs becomes transparent, so other materials such InP are needed [13].

Schottky Diodes

Schottky diodes can be used to generate THz signal by sideband generation. When a Schottky diode is illuminated with radiation from two sources, sidebands are generated. One source is a THz gas laser operating at ν_{THz} and emitting more than 10 mW of power. The other is a microwave source operating at ν_{MW}. Schottky diode generates the sideband frequencies $\nu_{SB} = \nu_{THz} \pm m\nu_{MW}$ with $m = 1, 2, 3, \ldots$. One problem is that laser radiation is emitted as well as reflected from the Schottky diode, and most of the power in the emitted beam is at the fundamental laser frequency. Almost the entire frequency range from 0.5 THz to 3 THz is accessible by sideband generation [13].

10.5 µW have been obtained at 1.6 THz [35] and 55 µW at 1.6 THz with a varactor Schottky diode [36].

Metal-Insulator-Metal Diodes

The mechanism of obtaining THz radiation is similar to the photomixing concept over photoconductors and photodiodes. Radiation of two lasers operating in the IR or visible spectral region are mixed in a nonlinear element: a MIM diode in this case. Although the nonlinearity of the I-V curve of a MIM diode is much smaller than that of a Schottky diode, it is a more efficient mixer at 10 µm wavelength.

This configuration has proven operation up to 9.1 THz with an output power in the order of 1 µW [37].

Photodiodes

Two different kinds of photodiodes can be used as THz signal generation: pin-PD and UTC-PD. Both of them are illuminated by two signals from lasers working in the telecommunication wavelengths (1550 nm) and frequency difference is the THz signal. While pin-PDs are capable to provide several µW in the sub-THz band, UTC-PDs increase both the operation frequency and the output power reaching 10 µW at 1 THz [38].

3.2.2 Photomixer

In this section, the photomixer included in the designed AE is presented. In our particular design, an interdigitated LT-GaAs based photomixer is used as the non-linear device to generate the THz signal. It consists of eight interdigitated fingers, with a finger gap = 1 μm, and finger width = 200 nm. A Scanning Electron Microscope (SEM) photograph of it can be seen on the Figure 3.7a. Following [30], the small-signal equivalent circuit of the Figure 3.7b is obtained, with $C = 2$ fF being the parasitic capacitance from the fringing fields between the 200 nm wide fingers and $G = (10\,\mathrm{k\Omega})^{-1}$ the conductance given by I_{DC}/V_{DC}. Also the antenna admittance ($Y_a(\omega)$) is included in the equivalent circuit of Figure 3.7b.

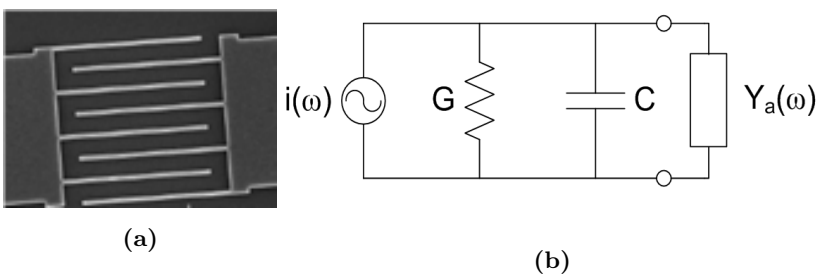

Figure 3.7: (a) SEM photograph of the interdigitated LT-GaAs photomixer and (b) its equivalent circuit.

3.2.3 Meander Dipole Antenna Design

From the antenna point of view only two parameters can be optimized in order to maximize the THz emitted power: the radiation efficiency (ϵ_{rad}) and the matching efficiency (M). Matching efficiency is defined with the M-factor given by [39]:

$$M = \frac{4R_a R_p}{(R_a + R_p)^2 + (X_a + X_p)^2} \tag{3.1}$$

where $Z_a = R_a + \jmath X_a$ is the input impedance of the antenna and $Z_p = R_p + \jmath X_p$ is the input impedance of the photomixer.

The antenna efficiency can then be defined as the product of these two efficiencies and the polarization efficiency (ϵ_{pol}) [40]:

$$\epsilon_{ant} = \epsilon_{rad} \cdot M \cdot \epsilon_{pol} \tag{3.2}$$

This efficiency expresses how far the system from the ideal behaviour of the emitter is. Maximizing this efficiency will enhance the performance of the emitter and it is the key factor that we have used to optimize the design of the antenna. This design is based on the AIA concept ([33, 34]) and tries to maximize the antenna efficiency as defined in Equation 3.2. In its design, both the matching and the radiation efficiency must be considered. With the photomixer parameters mentioned before, the input impedance ($Z_p(\omega) = 1/Y_p(\omega) = 1/(G + \jmath\omega C)$) is found to be $0.57 - \jmath 75.8$ at 1.05 THz, so an antenna with an input impedance of $0.57 + \jmath 75.8$ at that frequency will maximize the Equation 3.1. This low value of the real part and the relative high value of the imaginary part are very difficult to be simultaneously obtained with a simple resonant antenna.

Meander dipole antenna is similar to a dipole where its radiating part is bent to a meander shape in order to reduce the antenna size [32]. An schematic of it with its main design parameters can be seen on Figure 3.8a. Traditionally, this antenna is used to reduce the antenna size

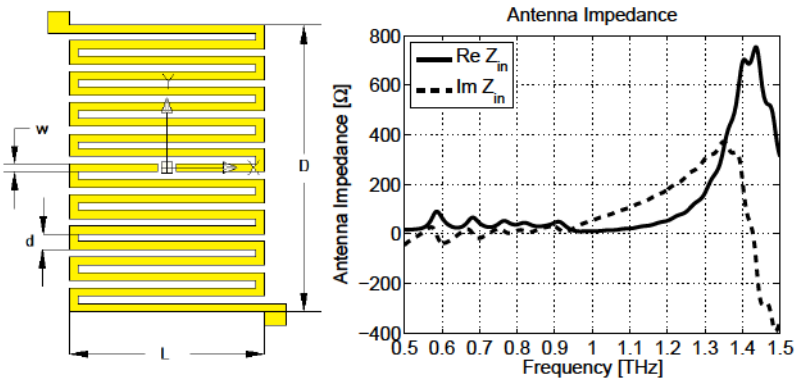

Figure 3.8: Meander dipole antenna: (a) Schematic and main design parameters. (b) Simulated input impedance of a meandered dipole antenna over semi-infinite silicon substrate with parameters: $L = 37\,\mu m$, $w = 3.5\,\mu m$, $d = 2\,\mu m$, $D = 105.5\,\mu m$ and 9 bends per arm.

(antenna miniaturization) and in systems that need a very high value of the input impedance, since this antenna provides higher values of input impedance at its resonance (Figure 3.8a) than λ-dipoles or dual-dipoles [32]. In the THz region, this antenna has been used under the name of "folded dipole" to obtain a very high input impedance [41–44]. The novelty that we have pursued in the present work with the meander dipole antenna rises from using it out of its main resonance region [34], as at lower frequencies than its resonance it exhibits a low real part and an inductive behaviour (shown in Figure 3.8b, frequency range from 0.9 THz to 1.3 THz) suitable for matching it with the photomixer capacitive behaviour. With such design, we expect to achieve a conjugate matching between the antenna and the photomixer without any additional element, increasing the matching efficiency. The antenna will show the optimal input impedance to the photomixer, so an AIA is obtained [33]. According to [33,34], this design philosophy will improve the system parameters and the figure of merit of the overall transmitter. This same approach has been also followed in [45] with the design of a millimetre-wave QO SBD receiver (Section 4.2 of this work). Unfortunately, the mismatch obtained with a broadband antenna in that case was not that huge, so little improvement was achieved.

Parametric Study

In order to analyse the effect of each parameter on the antenna efficiency, several simulations have been done and the results can be seen on the Figure 3.9 and the Figure 3.10. To carry out simulations, full-wave electromagnetic simulator CST Microwave Studio was used. Silicon semi-infinite substrate was set as background material in order to reduce computational time [31]. Both the matching and the radiation efficiency are shown, as well as the antenna efficiency (Equation 3.2, assuming ϵ_{pol} = 1).

Some conclusions can be extracted from these simulations. L parameter changes the resonant frequency of the meander antenna: the higher the value of L is the lower the resonant frequency is (larger size of the antenna). In addition, the closer the lines of the meander dipole antenna are (lower value of d), the lower the radiation efficiency is. This is due to the fact that currents have opposite directions so they cancel each other [32]. It is important to keep enough space between lines in order to have a relatively high value of the radiation efficiency. Regarding the number of bends, it has been noticed that for a number of bends higher than 3 (total length of the dipole $> 2\lambda$), neither the input impedance nor the radiation efficiency change significantly. Finally, w does not have an important role in both efficiencies and can be kept constant on optimization.

It is important to highlight that radiation efficiency keeps a relatively high value up to frequencies lower than 2/3 of its main resonance frequency. In all the above simulations, main resonance is located somewhere close to 1.5 THz (see Figure 3.8b) and our design frequency is 1.05 THz.

1.05 THz Prototype Design and Characterization

Finally, a prototype working at 1.05 THz as a LO for a radioastronomy heterodyne detector [29] was designed and manufactured. The main parameters were $L = 37\,\mu m$, $w = 3.5\,\mu m$, $d = 2\,\mu m$, $D = 105.5\,\mu m$ and 9 bends per arm (Figure 3.11a). Separation between the middle arm and the following next (up or down) were fixed to 3.5 µm to keep enough

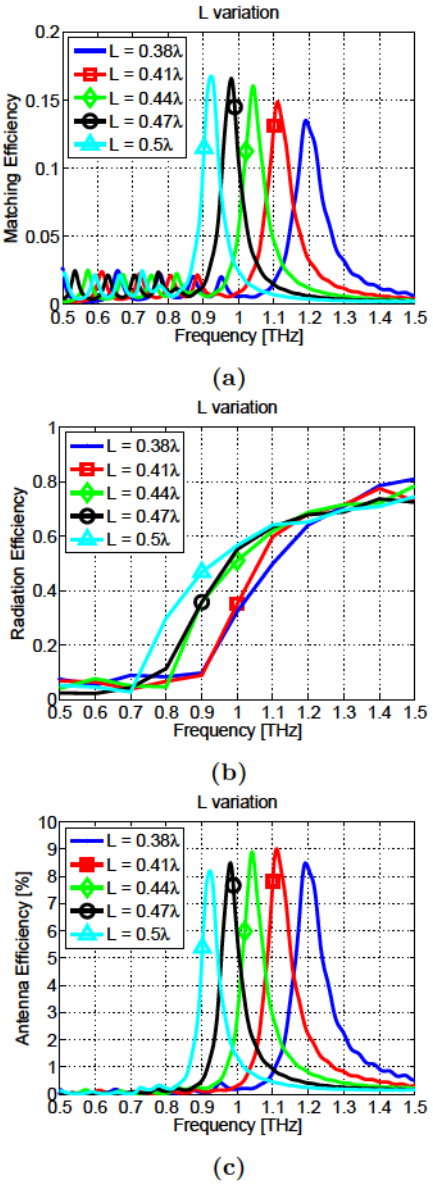

Figure 3.9: L variation. (a) Matching efficiency, (b) radiation efficiency and (c) antenna efficiency. $w = 0.044\lambda$, $d = 0.08\lambda$.

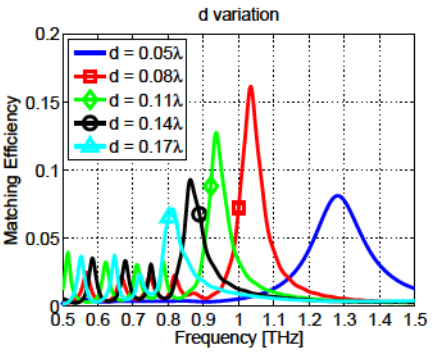

(a)

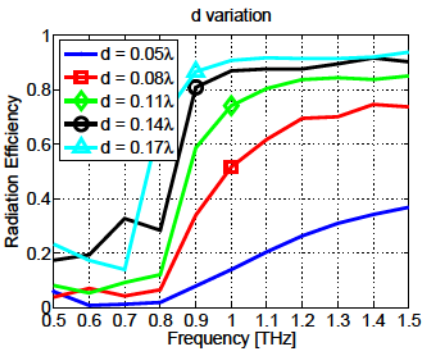

(b)

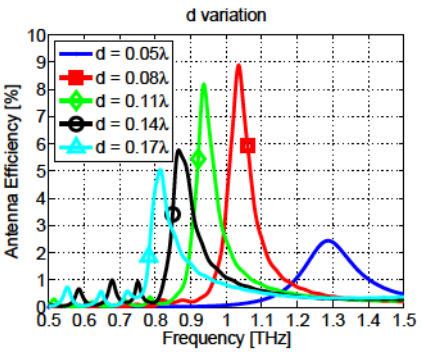

(c)

Figure 3.10: d variation. (a) Matching efficiency, (b) radiation efficiency and (c) antenna efficiency. $w = 0.044\lambda$, $L = 0.44\lambda$.

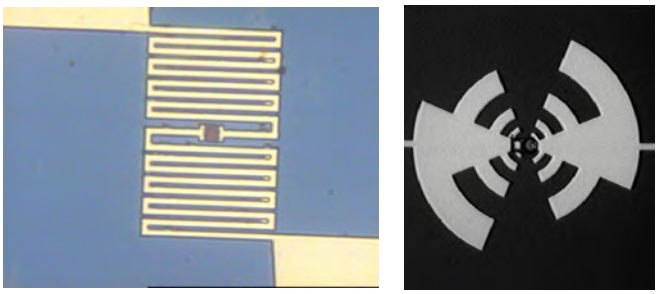

(a) **(b)**

Figure 3.11: Photograph of the manufactured (a) meander dipole and (b) log-periodic antenna integrated with the LT-GaAs photomixer device.

space for the photomixer device. Simulated input impedance can be seen on Figure 3.8b. With such antenna an antenna efficiency of 7.05 % at 1.05 THz is estimated, with matching and radiation efficiencies equal to 14.73 % and 47.83 % respectively. For the sake of comparison, a self-complementary log-periodic antenna [40] was designed and its antenna efficiency calculated. Its maximum and minimum dimensions are 200 µm and 10 µm respectively (Figure 3.11b). In contrast to the meander dipole design, broadband antennas exhibit an almost constant impedance with frequency (self-complementary antennas: $60\pi/\sqrt{\epsilon_r}$ for the real part and 0 for the imaginary part [40]), so the improvement that can be achieved in the matching efficiency is not significant. In this second AE, an antenna efficiency of 1.73 % is estimated with matching efficiency equal to 2.01 % and radiation efficiency equal to 86.03 %. Figure 3.12 shows the simulated power improvement obtained with the meander dipole AE given by $\epsilon_{ant}^{meander}/\epsilon_{ant}^{log-per}$. A 6 dB improvement at 1.05 THz is expected with the meander dipole antenna.

Two AE, one with the meander dipole antenna and the other with the log-periodic antenna were manufactured (Figure 3.11). In both of them, the same photomixer structure (Section 3.2.1) and lens (10 mm diameter hyperhemispherical high resistivity silicon lens) were used. It is worth highlighting that the main challenge with the meander dipole antenna is that it is a highly resonant antenna, so a small variation in the manufacturing process or in the permittivity of the material would change its performance.

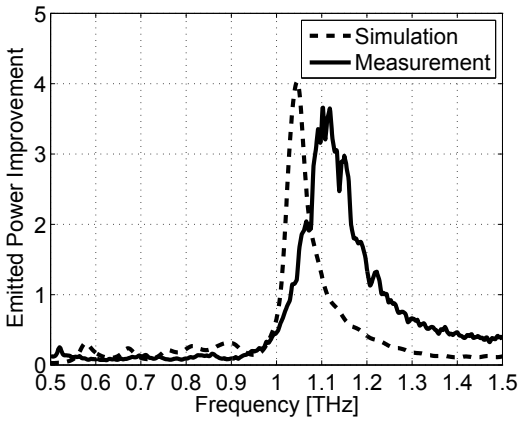

Figure 3.12: Emitted power improvement when comparing meander dipole antenna with log-periodic antenna ($\epsilon_{ant}^{meander}/\epsilon_{ant}^{log-per}$).

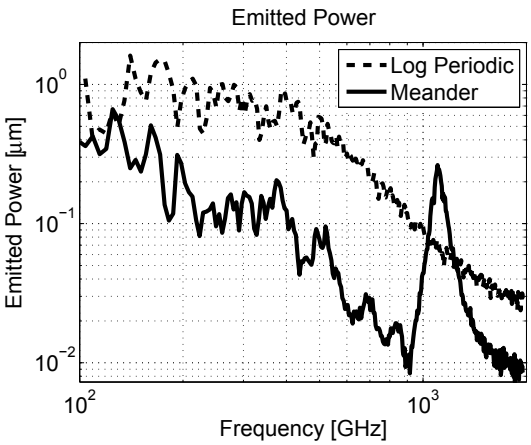

Figure 3.13: Measured THz emitted power of both AEs: meander dipole antenna and log-periodic antenna.

A typical CW THz photomixing measurements setup was utilized to characterize the emitted power. It consists of two 850 nm lasers that illuminate the photomixer device. THz frequency is tuned and THz emitted power is measured from 80 GHz up to 2 THz. The photomixer output THz frequency depends on the frequency of the two lasers impinging over it. In the measurements shown in the Figure 3.13, the frequency of one of the lasers remains constant while the other is changed to obtain the desired output THz frequency. This frequency change can be done either by modifying the current or the temperature of the laser. The THz radiation emitted by the antenna with the lens is, first, chopped with an optical chopper and then beam focused with two parabolic mirrors. The THz signal impinges a diamond window Golay cell connected to a lock-in amplifier which uses as the reference signal the chopper one. The measured output power with both the meander and the log-periodic AEs are shown in Figure 3.13.

It can be observed that at 1.1 THz a maximum in the emitted power with the meander AE is obtained (0.26 µW). If we compare both power measurements (meander and log-per AE) the plot in Figure 3.12 is obtained. A small shift from 1.05 THz to 1.1 THz can be appreciated but the power improvement is approximately the same (6 dB). In addition, the simulated quality factor (Q-factor) is 18.33, while the measured one is 10.11. This Q-factor decrease is due to the fact that additional losses not contemplated in the simulations such as losses in the silicon dielectric are occurring.

3.3 Large Area Emitters

This section is devoted to photomixing in LAEs. This antenna-free approach is motivated by the attempt to overcome the power limitations imposed on the conventional AEs [4,46] like the one presented in Section 3.2 and AE-arrays. In the LAE, the source of the THz radiation is the acceleration of the photogenerated carriers in a permanent electric field, induced in the semiconductor [4,47]. This acceleration process typically takes place on a ps or sub-ps time scale and results in a THz wave emitted by each photogenerated carrier [4,47]. The coherent superposition of all the THz waves originating from the THz periodic carrier generation induced by the two beating laser beams, yields a macroscopic THz field emitted by LAE. Along this chapter, it is shown in detail that the THz emission by each accelerated individual photo carrier can be interpreted as the emission of a corresponding transient Hertzian dipole with a single elementary charge. In order to establish the relation to planar antenna arrays, the quasi-continuum of such coherent elementary Hertzian dipoles is discretized into a (sufficiently dense) array of Hertzian dipoles with correspondingly larger dipole charge. Simple estimates [4] show that the length of these Hertzian dipoles is much shorter than half a wavelength, which turns them into quite inefficient radiating structures. This drawback, however, is over-compensated by a strongly increased dipole charge, resulting from the fact that much higher laser power can be applied to LAEs. Heating by the absorbed laser power and by photocurrent represents the limiting factor for both AEs and LAEs, particularly at the focal point, since the generated heat is highest there. An increase of the illumination spot size by a factor 10 to 33, e.g., increases the maximum tolerable laser power and, hence, the induced dipole charge, by a factor of $10^2 = 100$ to $33^2 \approx 1000$. This corresponds to an increase of the device size from $8\,\mu m \times 8\,\mu m$ (the dimensions of a typical antenna-coupled device), to $80\,\mu m \times 80\,\mu m$, or $250\,\mu m \times 250\,\mu m$.

Interestingly, the short dipole length implies even an advantage at higher frequencies compared to AEs. For the latter, the THz power is strongly limited by the RC-roll-off. The radiation resistance of a Hertzian dipole scales with the square of its length and becomes so small, that the RC roll-off frequency shifts to frequencies well beyond the THz range, and is not a limiting factor for the LAEs any more. Apart from the THz power issues, LAEs are very appealing regarding fabrication

and operation. LAEs require only very simple processing steps for the fabrication. For the illumination, an expanded large laser spot can be used, whereas AE-arrays require a sophisticated set-up for the coherent illumination of the individual AEs and, possibly, another demanding mounting process shaping the THz beam by lenses.

In this section, the attention is focused on the aspects related to the emission of the radiation, rather than on details of carrier generation and transport. LAEs are broadband THz emitters, and because of this very wide Fourier spectrum of frequencies, and hence wavelengths, a quantitative analysis of these results is complicated. It is shown below that this results in a wide range of radiation patterns for the different Fourier components. For a laser pulse with a given Gaussian laser spot size of (sufficiently large) width ρ_0, e.g., the high-frequency (short-wavelength) components may turn out quite strongly collimated, whereas the low-frequency (long-wavelength) components may exhibit much wider lobes. The study carried out on in this work is restricted to LAEs based on CW photomixing and it will be shown that it represents a very promising approach for THz emitters with high power and excellent beam profile.

This section is organized in the following way. First, a short introduction on CW THz photomixing with LAEs is included. Main characteristics, working principle and state-of-the-art results are presented. In the next subsection, an equivalent electromagnetic circuit based on Hertzian dipoles to generate the radiation pattern of vertical LAEs is obtained. Finally, three different LAEs are simulated and results are commented.

3.3.1 Introduction of CW Photomixing with LAEs

AEs can be very efficient THz emitters, provided the incoming optical power P_L is efficiently transformed into a THz Alternating Current (AC) I_{THz}. In p-i-n photomixers, a responsivity close to the ideal value $R^{id} = I_{THz}/P_L = e/h\nu_0$ (assuming that each incoming photon of energy $h\nu_0$ contributes one elementary charge e to the photocurrent I_{THz}) can be achieved, at sufficiently low THz frequencies (up to about 100 GHz). Due to the antenna resistance, of the order of $R_a = 70\,\Omega$ [4, 46], one can approach an ideal conversion efficiency of ($\eta^{id}_{conv} = P^{id}_{THz}/P_L =$

$1/2R_a \left(e/h\nu_0\right)^2 P_L$ ($\approx 27.3\%$ at $P_L = 5\,\mathrm{mW}$, for telecommunication laser wavelength of, e.g., 1550 nm). In practice, however, much lower THz power is obtained because of the RC roll-off and the transport roll-off, which strongly reduces the THz current fed into the antenna at higher frequencies. In photoconductive photomixers as the one used in Section 3.2, the responsivity is far below the ideal value, because of the low photoconductive gain, resulting in strongly reduced currents, even at low frequencies. Unfortunately, the small active area of the AE, required to minimize the RC roll-off, imposes strict limits to the maximum tolerable laser power. Focusing the laser beam onto a very small area, results in a strong heating [4]. Apart from that, the increased laser power yields to high photo-carrier densities, which are screening the applied Direct Current (DC) electric fields [4] required for their transport.

Much higher total laser power can be applied without the risk of thermal failure and without causing screening if an alternative THz emitter concept is found allowing the laser power to be spread over a large area comparable with the size of a typical antenna, or even larger. Such a LAE concept [Figure 3.14(a) and (b)] can be implemented by taking advantage of the fact that the charge carriers generated in the semiconductor become elementary Hertzian dipole sources of THz radiation, if subjected to an accelerating DC electric field $\mathbf{E_{DC}}$. The THz fields of the dipoles interfere constructively and the radiated power increases quadratically with the laser power. This dependence is identical to the case of antenna emitters as long as the illuminated area is small compared with the THz wavelength [4]. In this case, the angular distribution of the THz power will be the same as that for an elementary dipole [Large Area Quasi-Dipole (LAQD)]. If, however, the size of the illuminated area becomes comparable with the THz wavelength or even larger, interference effects become essential (in the far field) and the radiation pattern become narrower like in an array of THz antennas. It is found that the maximum radiation intensity still increases quadratically with laser power for the direction of coherent superposition. The total THz power, however, increases only linearly with the laser power as the beam width decreases in the limit of a very large area or array ($\rho_0 \gg \lambda_{THz}$). This can be seen better in the Figure 3.15. Optical power can be increased up to a point where the device would break because of heating. Up to this point the relation between generated THz power and optical impinging power is quadratic. Beyond this point, the optical intensity can not be

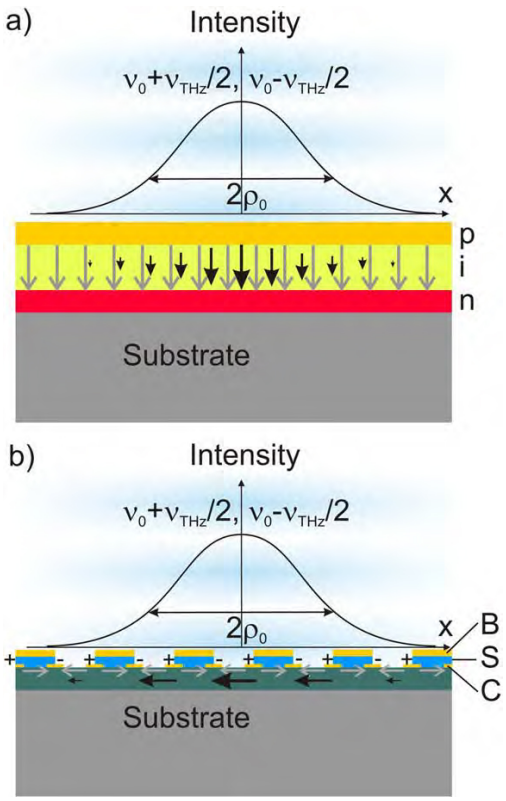

Figure 3.14: Schematic diagram illustrating the principle of photomixing in LAEs. The orientation of the constant electric field (indicated by faint arrows), can be (a) vertical or (b) horizontal. The dipole density is indicated by the black arrows and it is proportional to the intensity distribution in the laser beam. To avoid destructive interference between carriers accelerated in opposite directions every other stripe between the contacts has to be blocked (B) for charge carrier generation by an opaque mask. The dipole length is determined by the short lifetime of the material and of the order of tens of nm [6].

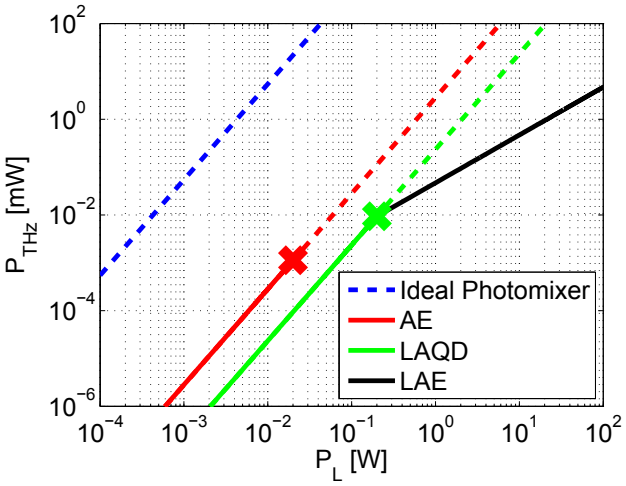

Figure 3.15: Comparison between expected THz power generated by an ideal photomixer (blue), AE (red) and LAE (green) as a function of the optical power. Crosses represent the point where it is expected the device to break because of thermal failure.

incremented any more. What it is proposed with the LAE concept is spread that optical power over a bigger area without increasing the intensity. Theoretically, now it is possible to increase up to infinity the optical power thus the generated THz power.

LAE's State-of-the-Art

Recently, LAEs based on excitation with fs-laser pulses have been successfully demonstrated and very-broad-band high-power THz radiation with spectra ranging from 100 GHz up to several THz has been observed [48–51]. Also, the emission of narrowband pulsed THz radiation from large-area structure was reported by Krause et al. [52]. This represents an interesting approach, which is suitable for combining the increased conversion efficiency of pulsed excitation with the advantages of (nearly) uniform radiation pattern for single frequency generation.

Regarding CW photomixing with LAEs, its working principle has been demonstrated for the first time in [53] and beam-scanning capabilities have been shown [53]. Also, its performance as detector is discussed

in [54]. Authors obtained 2 µW at 1.2 THz, with an optical power impinging the LAE of 900 mW. This signal comes from two femtosecond-lasers working at 800 nm in CW mode. A horizontal LAE (Figure 3.14b) is used with a total area equal to 7 mm × 7 mm. Also, it was demonstrated that by changing the size of the optical spot and, in consequence, the illuminated area of the LAE, the output beam becomes narrower so the output THz power is increased. In Figure 3.16 the results obtained in [53] are depicted. Beam-steering capabilities are also demonstrated by physical rotating one of the optical lasers. It is shown that a very small rotation in one of the optical lasers yields to a ± 45° THz beam displacement (Figure 3.17).

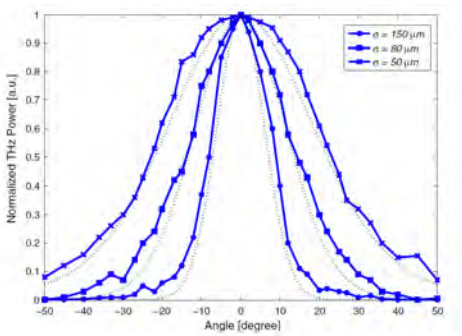

Figure 3.16: Normalized angular distribution of the radiated THz beam mapped out for three different spot sizes. Dotted curves show the analytically calculated beam pattern of the same LAE for comparison [53].

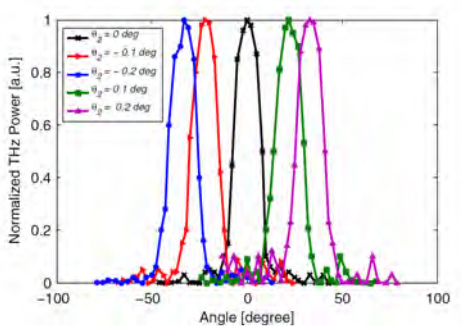

Figure 3.17: Normalized angular distribution of the radiated THz beam for different incident angles of one of the lasers' beam [53].

3.3.2 Radiation Equivalent Circuit of LAEs

In this section a radiation equivalent circuit of LAEs based on Hertzian dipoles is derived. This is carried out by discretizing the generated photocurrents into an array of Hertzian dipoles.

Radiation from LAEs

A single electron in a semiconductor of dielectric constant ϵ_{sc}, characterized by an effective mass m_c (typically $m_c \approx (0.04, \ldots, 0.07)\, m_0$, where $m_0 = 9.1 \times 10^{-31}$ kg is the mass of a free electron), emits a THz pulse if accelerated by an electric field $\mathbf{E_{DC}}$. The total THz power $P^e_{THz}(t)$ is given by [4, 46, 47]:

$$P^e_{THz}(t) = \left(\frac{Z_0}{6\pi}\right) \frac{e^2 \left[a(t)\right]^2 n_{sc}}{c^2} \tag{3.3}$$

Here, $e = 1.602 \times 10^{-19}$ C is the elementary charge, $c = 3 \times 10^{10}$ cm/s the vacuum velocity of light, $Z_0 = (\epsilon_0 c)^{-1} = 377\,\Omega$ the impedance of free space and $n_{sc} = (\epsilon_{sc})^{1/2}$ the refractive index of the semiconductor. In typical III-V semiconductors and at sufficiently high electric fields ($>$ kV/cm) the time dependent acceleration $a(t)$ can be approximated by an initial "ballistic" acceleration $\mathbf{a_1} = e\mathbf{E_{DC}}/m_c$ up to a maximum ballistic velocity of about $v^{max}_{bal} \approx 10^8$ cm/s (in GaAs) and 2×10^8 cm/s (in InGaAs, e.g.), followed by a deceleration due to scattering, which can be approximated by $\mathbf{a_2} = -\mathbf{a_1}$ [4,55]. The superposition of the transient THz fields of the carriers generated by the modulated laser power $P_L(t)$ yields in the LAQD-limit (remember, a semiconductor area equivalent to a $\lambda/2$ dipole):

$$P^{LAQD}_{THz} = \frac{1}{2} R_{LAQD} \left| I_{THz}\left(\omega_{THz}\right)\right|^2 \tag{3.4}$$

with

$$R_{LAQD} = \left(\frac{2Z_0 n_{sc}}{3\pi}\right)\left(\frac{v_{bal}}{c}\right)^2 = (3.2 \ldots 12.8) \cdot 10^{-3}\Omega$$
$$\text{for } v_{bal} = (1 \ldots 2) \cdot 10^8 \text{cm/s} \tag{3.5}$$

$$I_{THz}\left(\omega_{THz}\right) = I_{0,pin} \cdot f\left(\omega_{THz}\right) \tag{3.6}$$

The frequency dependent factor:

$$f\left(\omega_{THz}\right) = \frac{\left(1 - \cos\left(\omega_{THz}\tau_{bal}\right)\right)}{\omega_{THz}\tau_{bal}} \tag{3.7}$$

increases linearly with $\omega_{THz}\tau_{bal}$ at low frequencies, reaches the maxima at about $\omega_{THz}\tau_{bal} \approx (3/4)\,\pi$ and $(2n+1)\,\pi$ and the minima at $\omega_{THz}\tau_{bal} \approx 2n\pi\,(n = 1, 2, 3, \ldots)$. In other words, at low frequencies $\left(\omega_{THz} \ll \tau_{bal}^{-1}\right)$, the THz field contribution of accelerated carriers are strongly reduced due to destructive interference with the opposite field contribution of decelerated, previously generated, carriers as the acceleration and deceleration times, $\tau_{bal} \approx v_{bal}/a_1 = v_{bal}m_c/\left(eE_{DC}\right)$, are short compared to the THz period, $T_{THz} = 1/\nu_{THz}$. The main maximum of $f\left(\omega_{THz} = 3\pi/\left(4\tau_{bal}\right)\right) \approx 0.72$ occurs close to the frequency v_{bal} at which the acceleration and deceleration times closely correspond to half a THz period T_{THz}. The ballistic acceleration time $\tau_{bal} = v_{bal}/a = v_{bal}m_c/\left(eE_{DC}\right)$ can be adapted to fulfil the condition for maximum THz power, $\tau_{bal} = (3/8)\,T_{THz} = 3/\left(8\nu_{THz}\right)$. This condition yields $6\,\mathrm{kV\,cm^{-1}} < E_{DC} < 60\,\mathrm{kV\,cm^{-1}}$ for 0.5 THz $< \nu_{THz} <$ 5 THz for InGaAs, e. g.. For the optimum adapted fields, the THz power becomes:

$$\begin{aligned} P_{THz}^{LAQD} &= \frac{1}{2} \cdot (1.76 \ldots 6.7) \cdot 10^{-3}\Omega \cdot I_{pin}^2 \\ &\text{for } v_{bal} = (1 \ldots 2) \cdot 10^8\,\mathrm{cm\,s^{-1}} \end{aligned} \tag{3.8}$$

The angular dependence of the radiation intensity, i.e., the power emitted per solid angle $d\Omega = \sin\theta d\theta d\phi$, is the same for a LAQD as for a Hertzian dipole in the far-field. It increases quadratically with the sine of the angle between the accelerating DC-field $\mathbf{E_{DC}}$ and the vector $\mathbf{r}$ from the centre of the LAE device to the observation point. For a field in z-direction, $\mathbf{E_{DC}} = E_{DC}\,(0, 0, 1)$, this angle is identical with the polar angle θ and one obtains from Equation 3.4 for the radiation intensity:

$$U_v^{LAQD}\left(\theta\right) = \left(\frac{3}{8\pi}\right) \cdot P_{THz}^{LAQD} \cdot \sin^2\left(\theta\right) \tag{3.9}$$

which is very similar to the radiation intensity of a Hertzian dipole placed in the z-direction. For an electric field in the x-direction, $\mathbf{E_{DC}} = E_{DC}(1,0,0)$, the radiation intensity depends on both the polar angle θ and the azimuth angle ϕ:

$$U_h^{LAQD}(\theta,\phi) = \left(\frac{3}{8\pi}\right) \cdot P_{THz}^{LAQD} \cdot \left(1 - \sin^2(\theta) \cdot \cos^2(\phi)\right) \tag{3.10}$$

which is similar to the radiation intensity of an Hertzian dipole placed in the x-direction.

The previous considerations apply to a (hypothetical) LAQD embedded into an infinite bulk semiconductor. However, the absorption of the laser radiation will take place in the semiconductor close to its interface to air at $z = 0$. The radiation pattern of Hertzian dipoles placed in a semiconductor close to the surface (distance $z_0 \ll \lambda$)) is very different to the one embedded within the infinite bulk (as shown in Chapter 2). So this radiation pattern has to be taken into account when calculating radiation intensities of both LAQDs and LAEs.

In the next section, the actual "continuous array" of elementary dipoles (LAE) is subdivided into a discrete, but sufficiently dense, array of Hertzian dipoles of correspondingly enhanced dipole charge. With such discretization, radiation pattern and intensity of LAEs can be easily estimated. This work is only devoted to vertical LAEs since, although horizontal LAEs are very attractive from the theoretical point of view, practically it turns out to be difficult to fabricate efficient LAEs for CW operation with horizontal DC-field, allowing for ballistic transport without suffering from field screening due to saturation effects. The saturation problems can be overcome if a semiconductor with short recombination lifetimes is used. This, however, results in non-ballistic transport and strongly reduced values for the radiation resistance in Equation 3.5. The maximum ballistic electron velocity, v_{bal}, has to be replaced by the saturation velocity, v_s, which is by a factor $\sim 3 - 10$ times smaller. As the THz power quadratically scales with radiation resistance, this implies a reduction by a factor of $\sim 9 - 100$ compared with the ideal value of P_{THz}^{LAQD} in Equation 3.4.

Description of Vertical LAE Equivalent Circuit

The main parameter which defines the behaviour of the array of Herztian dipoles and that has to be carefully chosen is the distance between them, a. Two considerations have to be taken into account when discretizing continuous currents of the LAE:

- The "weight factors", that is the amplitude of the feed of each element of the array, of neighbouring elements should only differ in small amounts. That is similar to say that elements must be very close in order to correctly emulate the behaviour of continuous currents. An appropriate value of it is $a \ll \rho_0$, being ρ_0^2 the variance of the optical Gaussian beam impinging in the LAE (Figure 3.14) [6].
- The phase delays between neighbouring elements should be small in order to avoid non-desired side lobes ($a < \lambda_0 / (4 \cdot n_{sc})$).

If both of them are fulfilled, then the radiation behaviour of the discretized array of Hertzian dipoles laying close to the interface air-semiconductor is expected to be equivalent of the LAE's radiation behaviour.

A schematic of a vertical LAE can be seen on Figure 3.18 and the Hertzian dipoles equivalent circuit is introduced in Figure 3.19. Three period n-i-pn-i-p structure is considered so 3 vertical dipoles in the z-direction are included. In addition, the mesas' width is 165 µm, so taking into account that ($a < \lambda_0 / (4 \cdot n_{sc})$), at 1 THz the maximum distance between dipoles must be 21 µm over InP ($n_{sc} = 3.6$), so 10 dipoles or more ($m = 10$) must be considered on each mesa (x-direction). The same distance between dipoles in the y-direction is considered.

3.3.3 Simulations of Vertical LAE Equivalent Circuit

Three LAE structures are considered in this section:

- LAE 1: 1786 µm × 1800 µm. 10 mesas in the x-direction.
- LAE 2: 4580 µm × 4242.5 µm. 25 mesas in the x-direction.
- LAE 3: 5028 µm × 2283 µm. 28 mesas in the x-direction.

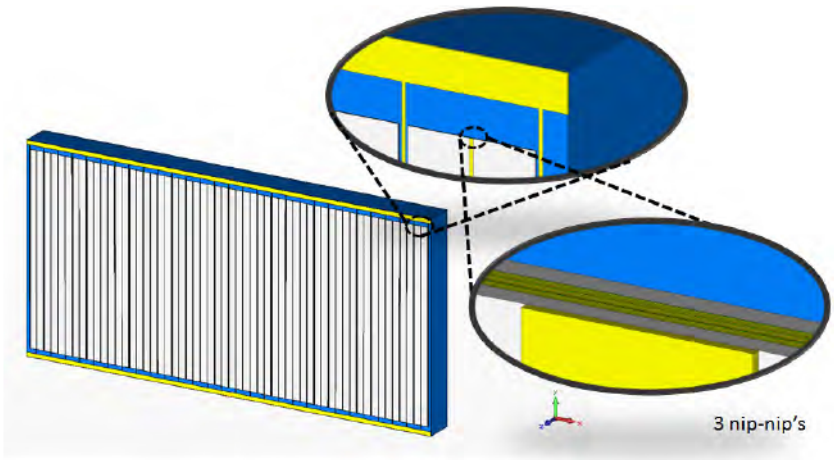

Figure 3.18: Schematic of a vertical LAE. Three nip periods are included. Blue is InP, yellow represents gold, green are the n- and p-doped substrates and white is InGaAs.

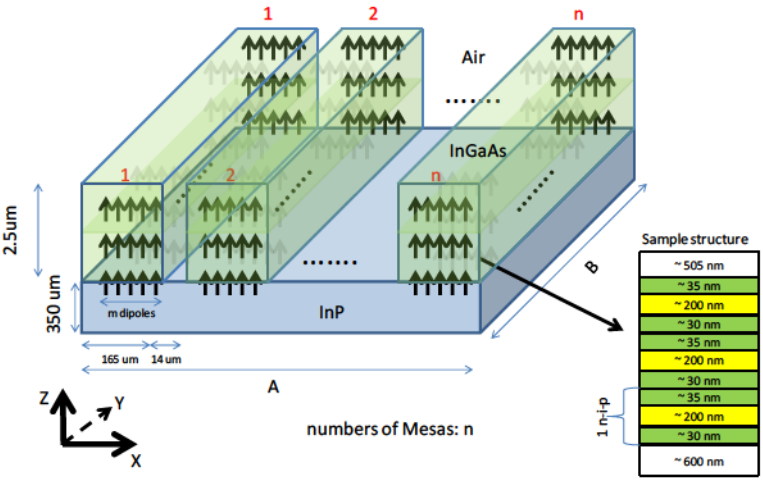

Figure 3.19: Equivalent discretized circuit of the vertical LAE. Blue is InP, yellow represents gold, green are the n- and p-doped substrates and white is InGaAs. Three nip periods are included.

Optimum Illumination Angle

First of all, it is critical to check what is the optimal illumination angle of the fibre optic with respect to the LAE. In the Figure 3.20, a simplified illumination scheme is plotted, where the illumination angle α is shown. For all the simulations carried out in this work, only illumination across the x-direction is considered. Regarding the "optical point-of-view", optimal illumination angle would be the Brewster angle. If a polarized optical signal impinges the LAE (or any dielectric) under this angle, no reflection appears and all the signal is transmitted through the dielectric. For our particular case, Brewster's angle is $\alpha = 74.48°$ (InP).

Regarding the "electromagnetic point-of view", the optimal angle would be the one that provides a higher value of the radiation intensity at its maximum. To check which angle is the optimal one, a parametric analysis is carried out changing the α angle over the LAE 1 at 1 THz. Results are plotted in the Figure 3.21. It can be seen that the highest radiation intensity is obtained when illuminating tangentially to the surface of the LAE ($\alpha = 90°$), which is not possible. Moreover, differences with respect to Brewster's angle illumination are not significant and SLLs are higher when $\alpha = 90°$.

So taking into account both optical and electromagnetic optimal angles, it is chosen the Brewster angle (74.48°) as the optimal one.

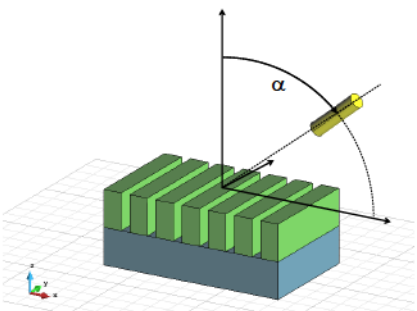

Figure 3.20: Schematic of a vertical LAE and its fibre optic illumination (yellow block).

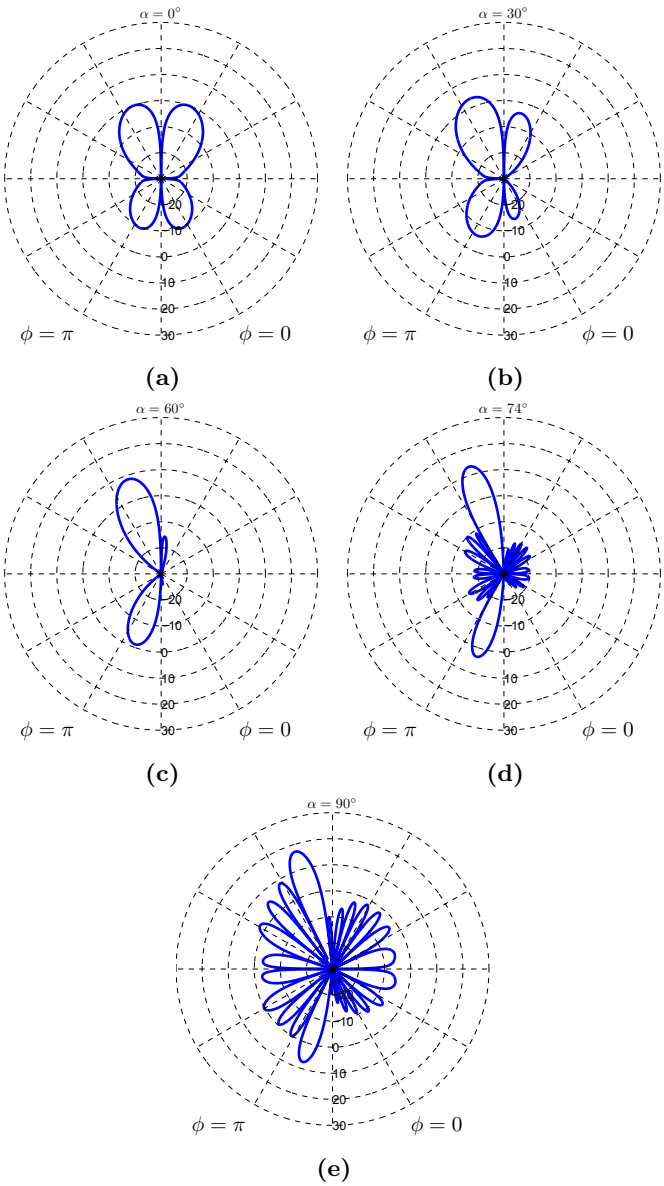

Figure 3.21: Radiation intensity of LAE 1 at 1 THz when $\rho_0 = 130\,\mu m$ normalized to the $\alpha = 0^\circ$ case: (a) $\alpha = 0^\circ$, (b) $\alpha = 30^\circ$, (c) $\alpha = 60^\circ$, (d) $\alpha = 74.48^\circ$ and (e) $\alpha = 90^\circ$.

For illuminating the LAE, a Gaussian beam has been considered as the output optical signal coming out of the optic fibre:

$$I_0 = \exp\left\{\frac{-(x-x_0)^2}{2\rho_0^2} + \frac{-(y-y_0)^2}{2\rho_0^2}\right\} \tag{3.11}$$

being ρ_0 the standard deviation of the distribution, and x_0 and y_0 the centre of the LAE. In Figure 3.22 the normalized amplitude of the optical Gaussian beam over the LAE 1 when illuminating with the Brewster angle is plotted for two different standard deviation of the amplitude (ρ_0 = 150 µm and ρ_0 = 460 µm). It can be seen that there is not a circular spot any more but an elliptical one due to this angle and that the higher ρ_0, the more similar to an uniform illumination.

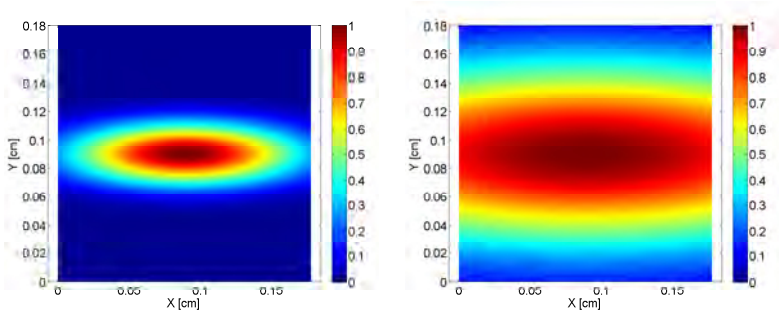

(a) **(b)**

Figure 3.22: Normalized amplitude of the optical signal impinging the LAE 1 under Brewster's angle illumination when (a) ρ_0 = 150 µm and (b) ρ_0 = 460 µm.

Spot Size (ρ_0) Variation

In this section, the size of the of the optical spot (ρ_0) is changed in order to check the radiation performance of each LAE. The wider the spot, the higher the power of the optical signal and it is expected the higher the THz generated signal.

LAE 1 The directivity and the SLL for the LAE 1 at 1 THz when changing the spot size (ρ_0) is depicted in the Figure 3.23a and the Figure 3.23b respectively. It can be seen that the larger the spot size the higher the directivity up to a saturation point because of the size of the LAE. In addition, the SLL increases as ρ_0 increases. This is due to the fact that when making the spot larger, the illumination of the LAE becomes more similar to a uniform one, thus leading to higher side lobes.

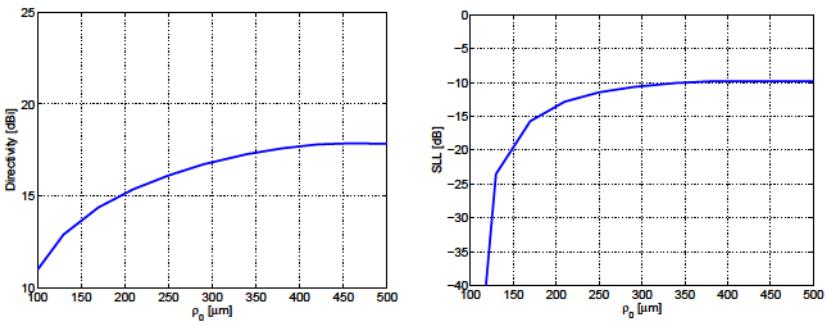

(a) (b)

Figure 3.23: Spot size variation at 1 THz over LAE 1: (a) Directivity and (b) SLL.

In the following Figure 3.24, radiation intensities for different ρ_0 values are depicted, normalized to the $\rho_0 = 90\,\mu m$ case. It can be seen how, as the illumination is more uniform, side lobes are greater. Two main lobes appear at $\theta = -15.52°$ and $\theta = -164.48°$ and the radiation intensity increases quadratically with the spot size ρ_0. In order to check how both $\theta = -15.52°$ and $\theta = -164.48°$ beams get narrower we have to look at the plane where these beams are. These two planes are shown in the Figure 3.25, where the radiation pattern of LAE 1 at 1 THz when $\rho_0 = 240\,\mu m$ is plotted. In the Figure 3.26 the radiation intensity of LAE 1 is plotted when illuminating with the Brewster angle for different spot sizes. Figure 3.26a shows the main beam at the plane where it is contained and Figure 3.26b shows the secondary beam at the plane where it is contained. It can be seen how, as the spot size increases, both beams get narrower (same behaviour as the one shown in the literature for the horizontal LAE, Section 3.3.1).

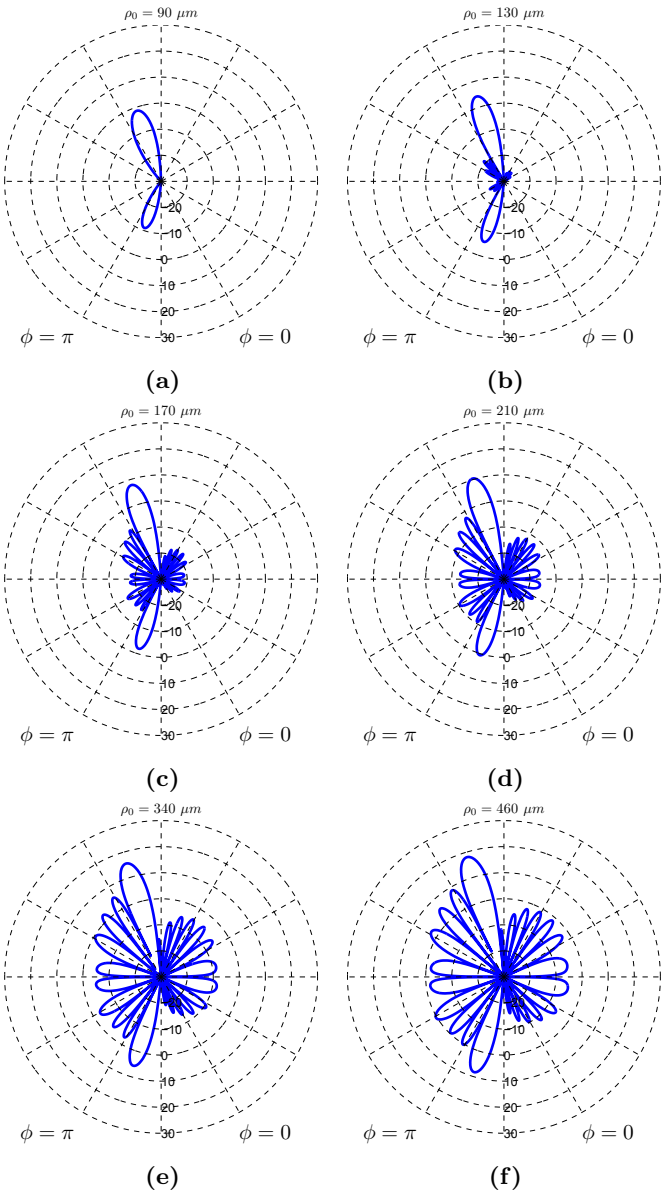

Figure 3.24: Radiation intensities normalized to $\rho_0 = 90\,\mu m$ for different spot sizes in the LAE 1 at 1 THz. (a) $\rho_0 = 90\,\mu m$, (b) $\rho_0 = 130\,\mu m$, (c) $\rho_0 = 170\,\mu m$, (d) $\rho_0 = 210\,\mu m$, (e) $\rho_0 = 340\,\mu m$ and (f) $\rho_0 = 460\,\mu m$.

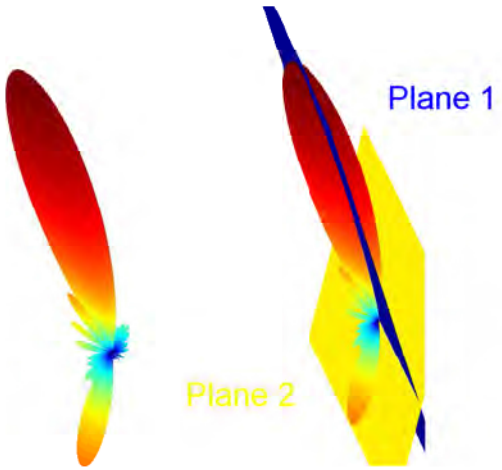

(a) (b)

Figure 3.25: Radiation pattern of LAE 1 at 1 THz when $\rho_0 = 250\,\mu m$. (a) Radiation pattern and (b) Radiation pattern and main lobe and secondary lobe planes.

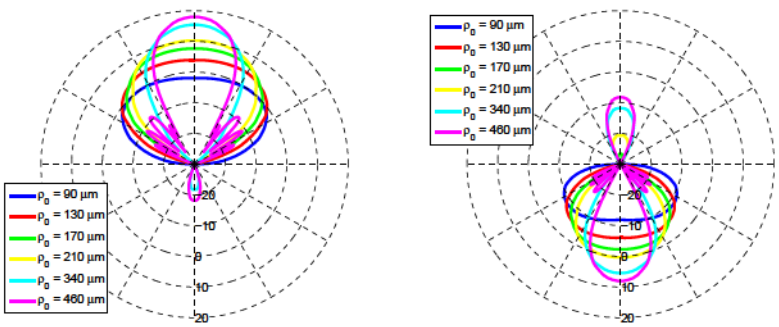

(a) (b)

Figure 3.26: Radiation intensities normalized to $\rho_0 = 90\,\mu m$ for different spot sizes in the LAE 1 at 1 THz. (a) Plane of the main lobe and (b) Plane of the secondary lobe.

LAE 2 The directivity and the SLL for the LAE 2 at 1 THz when changing the spot size (ρ_0) is depicted in the Figure 3.27a and the Figure 3.27b respectively. It can be seen that the larger the spot size the higher the directivity up to a saturation point because of the size of the LAE. In addition, SLL increases as ρ_0 increases. This is due to the fact that when making the spot larger, the illumination of the LAE becomes more similar to a uniform one, thus leading to higher side lobes.

In the following Figure 3.28, the radiation intensities at 1 THz for different ρ_0 values are depicted, normalized to the $\rho_0 = 90\,\mu m$ case. It can be seen how, as the illumination is more uniform, side lobes are greater. Two main lobes appear at $\theta = -15.52°$ and $\theta = -164.48°$ and radiation intensity increases quadratically with the spot size ρ_0. In order to check how both $\theta = -15.52°$ and $\theta = -164.48°$ beams get narrower we have to look at the plane where these beams are. These two planes are shown in the Figure 3.25. In the Figure 3.29 the radiation intensity of LAE 2 at 1 THz is plotted when illuminating with the Brewster angle for different spot sizes. The Figure 3.29a shows the main beam at the plane where it is contained and the Figure 3.29b shows the secondary beam at the plane where it is contained. It can be seen how, as the spot size increases, both beams get narrower (same behaviour as the one shown in the literature for the horizontal LAE, Section 3.3.1).

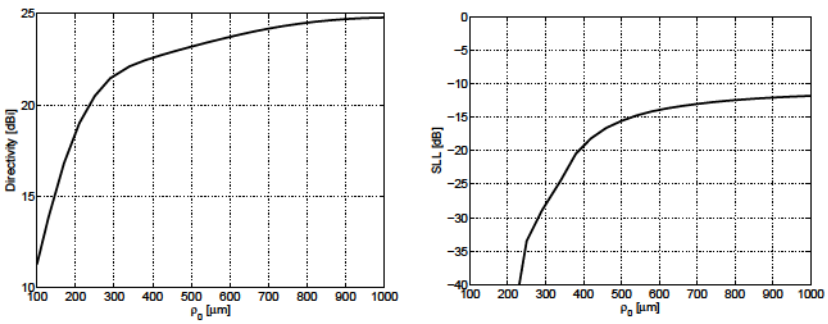

(a) (b)

Figure 3.27: Spot size variation at 1 THz over LAE 2: (a) Directivity and (b) SLL.

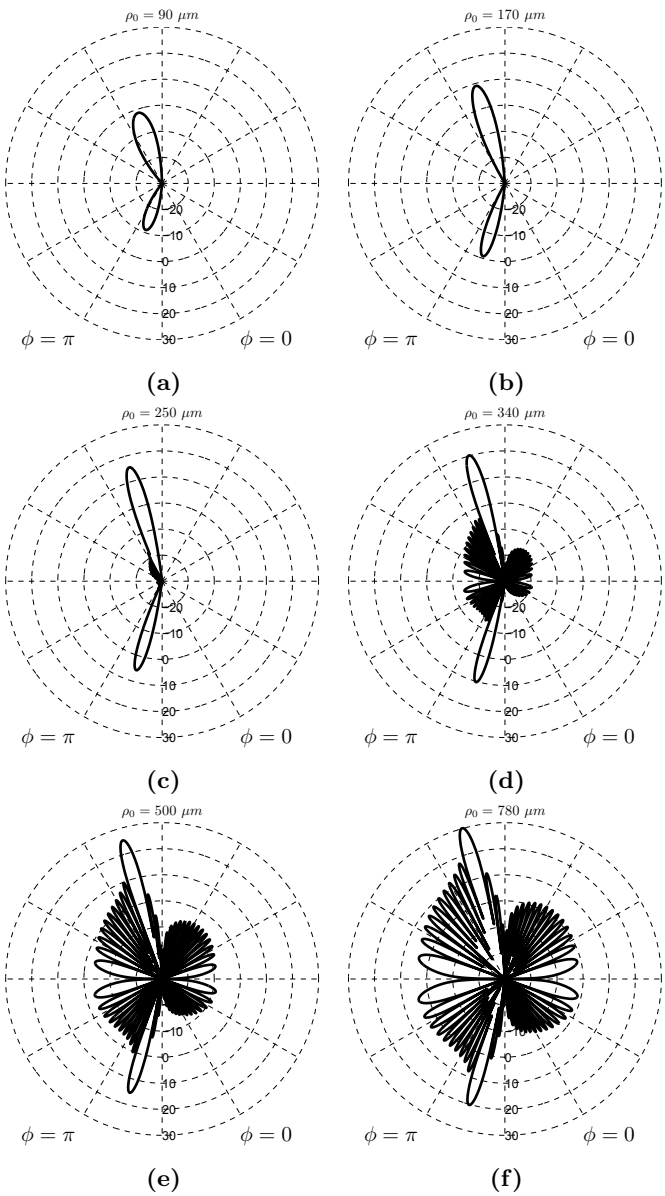

Figure 3.28: Radiation intensities at 1 THz normalized to $\rho_0 = 90\,\mu m$ for different spot sizes in the LAE 2. (a) $\rho_0 = 90\,\mu m$, (b) $\rho_0 = 170\,\mu m$, (c) $\rho_0 = 250\,\mu m$, (d) $\rho_0 = 340\,\mu m$, (e) $\rho_0 = 500\,\mu m$ and (f) $\rho_0 = 780\,\mu m$.

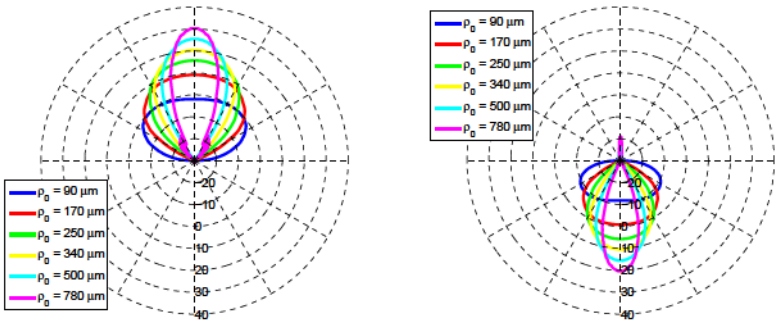

(a) (b)

Figure 3.29: Radiation intensities normalized to $\rho_0 = 90\,\mu m$ for different spot sizes in the LAE 2 at 1 THz. (a) Plane of the main lobe and (b) Plane of the secondary lobe.

LAE 3 The directivity and the SLL for the LAE 3 at 1 THz when changing the spot size (ρ_0) is depicted in the Figure 3.30a and the Figure 3.30b respectively. It can be seen that the larger the spot size the higher the directivity up to a saturation point because of the size of the LAE. In addition, SLL increases as ρ_0 increases. This is due to the fact that when making the spot larger, the illumination of the LAE becomes more similar to a uniform one, thus leading to higher side lobes.

In the following Figure 3.32, the radiation intensities for different ρ_0 values are depicted, normalized to the $\rho_0 = 90\,\mu m$ case. It can be seen how, as the illumination is more uniform, side lobes are greater. Two main lobes appear at $\theta = -15.52°$ and $\theta = -164.48°$ and the radiation intensity increases quadratically with the spot size ρ_0. In order to check how both $\theta = -15.52°$ and $\theta = -164.48°$ beams get narrower we have to look at the plane where these beams are. These two planes are shown in the Figure 3.25. In the Figure 3.31 the radiation intensity of LAE 3 at 1 THz is plotted when illuminating with the Brewster angle for different spot sizes. The Figure 3.31a shows the main beam at the plane where it is contained and the Figure 3.31b shows the secondary beam at the plane where it is contained. It can be seen how, as the spot size increases, both beams get narrower (same behaviour as the one shown in the literature for the horizontal LAE, Section 3.3.1).

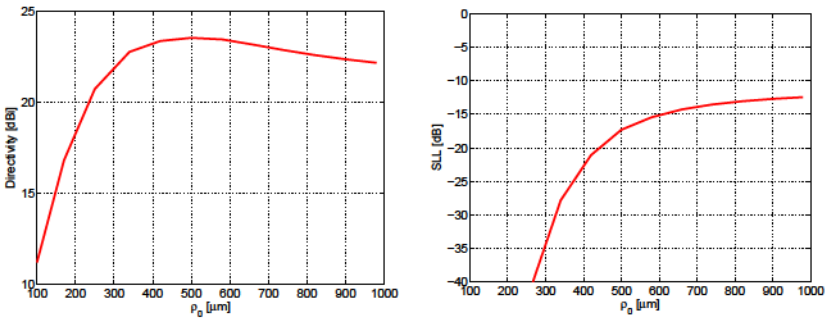

(a) (b)

Figure 3.30: Spot size variation at 1 THz over LAE 3: (a) Directivity and (b) SLL.

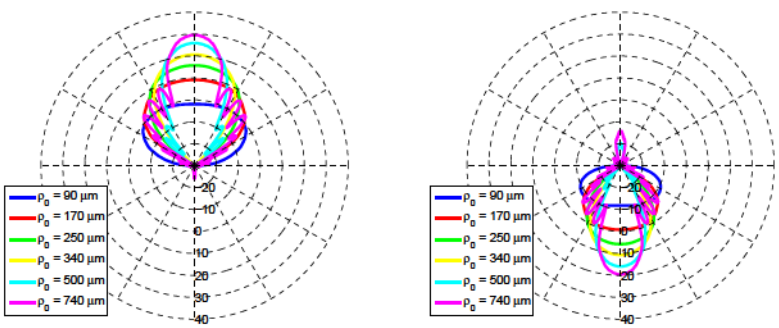

(a) (b)

Figure 3.31: Radiation intensities normalized to $\rho_0 = 90\,\mu\text{m}$ for different spot sizes in the LAE 3 at 1 THz. (a) Plane of the main lobe and (b) Plane of the secondary lobe.

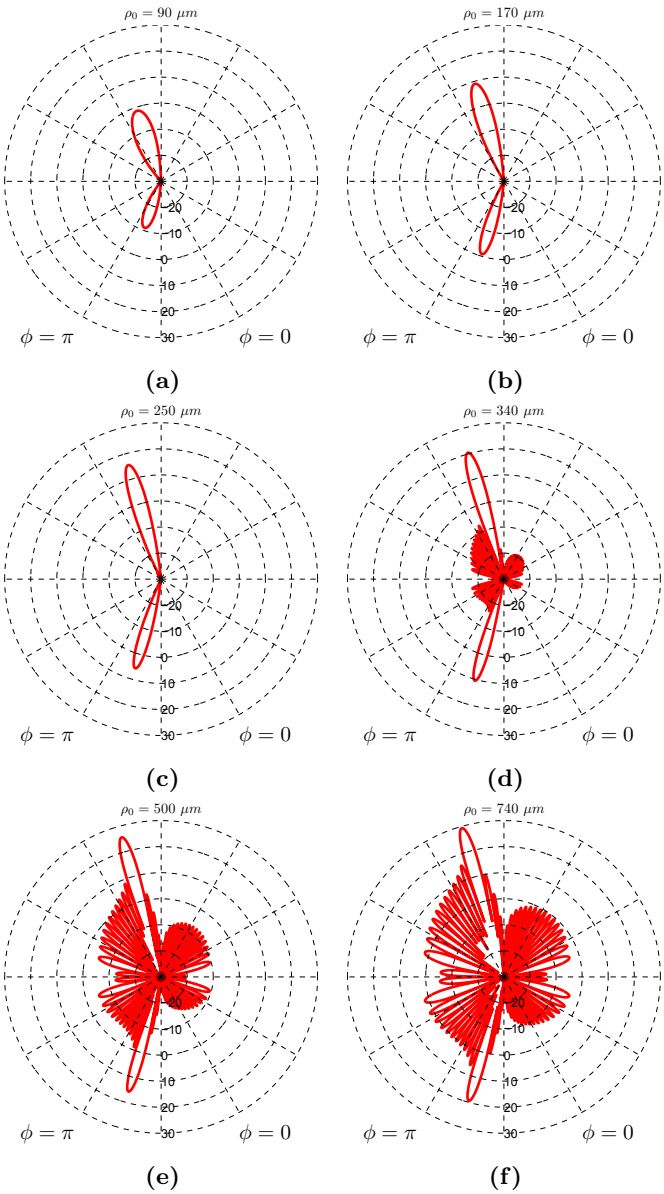

Figure 3.32: Radiation intensities normalized to $\rho_0 = 90\,\mu m$ for different spot sizes in the LAE 3 at 1 THz. (a) $\rho_0 = 90\,\mu m$, (b) $\rho_0 = 170\,\mu m$, (c) $\rho_0 = 250\,\mu m$, (d) $\rho_0 = 340\,\mu m$, (e) $\rho_0 = 500\,\mu m$ and (f) $\rho_0 = 740\,\mu m$.

3.4 Conclusions

In this chapter, two main approaches for CW THz generation by photomixing had been analysed: one based on AEs and the other based on LAEs. Contributions from the antenna point of view have been proposed in both cases.

The meander dipole antenna has been presented as a solution to match both capacitive susceptance and conductance of photomixers while maintaining a relatively high value of radiation efficiency. To achieve such a goal, the antenna has been forced to work out of its main resonance, at lower frequencies, where it exhibits an inductive behaviour. With this approach, there is no need to include a RF choke, so the design of an antenna for CW THz based on photomixing is simplified to just the design of the meander dipole antenna. A joint design process of the antenna is proposed where both matching and radiation efficiencies (AIA concept) are taken into account. The proposed antenna design can be followed independently of the photomixer used and it consists on trying to maximize the radiated power obtained from it. A prototype working at 1.05 THz was designed, manufactured and measured, and the obtained results show a 6 dB improvement in THz output power when compared with the log-periodic prototype. This result is comparable with previously reported ones [30] at 1 THz but with the novelty of not using the RF choke.

Regarding LAEs, a radiation equivalent circuit based on Hertzian dipoles has been proposed. The LAEs are very promising devices because, theoretically, there is no upper limit in the amount of THz power they can generate. With this equivalent circuit model it has been shown that the main lobe direction in the vertical LAEs is not perpendicular to the LAE surface, but it depends on the angle of illumination with the fibre optic. It has been determined that the optimal illumination angle is the Brewster angle and it produces a maxima in the radiation pattern at 1 THz in $\theta = -15.52^\circ$ and $\theta = -164.48^\circ$ respectively.

It has been shown that the higher the illumination optical spot, the higher the radiation intensity at THz frequencies. But if the spot is too big, then side lobes appear and the radiation pattern is deteriorated. Three different vertical LAEs with different sizes had been simulated and

their radiation intensities, as well as the directivity and the SLL have been calculated. It has been shown that, regarding radiation pattern, the optimal spot size (ρ_0) is approximately 7.5 % the length of the LAE in the illumination direction. With such spot size, the SLL is lower than -25 dB and directivity reaches a reasonable level.

The main contributions related with the third chapter have been published or presented in 2 JCR journal papers (first quartile), 1 book chapter and 4 conferences (see Publications section at the end of this document).

3.5 References

[1] P. Siegel, "Terahertz Technology," *IEEE Transactions on Microwave Theory and Techniques*, vol. 50, no. 3, pp. 910–928, 2002.

[2] A. Rivera-Lavado, L. E. García-Muñoz, G. Döhler, S. Malzer, S. Preu, S. Bauerschmidt, J. Montero-de Paz, E. Ugarte-Muñoz, B. Andrés-García, V. Izquierdo-Bermúdez *et al.*, "Arrays and New Antenna Topologies for Increasing THz Power Generation Using Photomixers," *Journal of Infrared, Millimeter, and Terahertz Waves*, vol. 34, no. 2, pp. 97–108, 2013.

[3] J. C. Pearson, B. J. Drouin, A. Maestrini, I. Mehdi, J. Ward, R. H. Lin, S. Yu, J. J. Gill, B. Thomas, C. Lee *et al.*, "Demonstration of a Room Temperature 2.48–2.75 THz Coherent Spectroscopy Source," *Review of Scientific Instruments*, vol. 82, no. 9, p. 093105, 2011.

[4] S. Preu, G. Döhler, S. Malzer, L. Wang, and A. Gossard, "Tunable, Continuous-Wave Terahertz Photomixer Sources and Applications," *Journal of Applied Physics*, vol. 109, p. 061301, 2011.

[5] H.-W. Hübers, S. Pavlov, A. Semenov, R. Köhler, L. Mahler, A. Tredicucci, H. Beere, D. Ritchie, and E. Linfield, "Terahertz Quantum Cascade Laser as Local Oscillator in a Heterodyne Receiver," *Opt. Express*, vol. 13, no. 15, pp. 5890–5896, 2005.

[6] G. Dohler, L. García-Muñoz, S. Preu, S. Malzer, S. Bauerschmidt, J. Montero-de Paz, E. Ugarte-Muñoz, A. Rivera-Lavado, V. Gonzalez-Posadas, and D. Segovia-Vargas, "From Arrays of THz

Antennas to Large-Area Emitters," *IEEE Transactions on Terahertz Science and Technology*, vol. 3, no. 5, pp. 532–544, 2013.

[7] C. Armstrong, "The Truth about Terahertz," *IEEE Spectrum*, vol. 49, no. 9, pp. 36–41, September 2012.

[8] M. Nuss and J. Orenstein, "Terahertz Time-Domain Spectroscopy," in *Millimeter and Submillimeter Wave Spectroscopy of Solids*, ser. Topics in Applied Physics, G. Grüner, Ed. Springer Berlin Heidelberg, 1998, vol. 74, pp. 7–50.

[9] M. C. Kemp, P. F. Taday, B. E. Cole, J. A. Cluff, A. J. Fitzgerald, and W. R. Tribe, "Security Applications of Terahertz Technology," *Proc. SPIE*, vol. 5070, pp. 44–52, 2003.

[10] E. Pickwell and V. P. Wallace, "Biomedical Applications of Terahertz Technology," *Journal of Physics D: Applied Physics*, vol. 39, no. 17, p. R301, 2006.

[11] R. A. Lewis, *Terahertz Physics*. Cambridge University Press, 2013.

[12] Y.-S. Lee, "Continuous-Wave Terahertz Sources and Detectors," in *Principles of Terahertz Science and Technology*. Springer US, 2009, pp. 1–41.

[13] E. Bründermann, H.-W. Hübers, and M. Kimmitt, "Sources," in *Terahertz Techniques*, ser. Springer Series in Optical Sciences. Springer Berlin Heidelberg, 2012, vol. 151, pp. 103–168.

[14] J. P. Kotthaus, "High Power Output from a Submillimeter CW Gas Laser," *Appl. Opt.*, vol. 7, no. 12, pp. 2422–2423, Dec 1968.

[15] G. Dodel, "On the History of Far-Infrared (FIR) Gas Lasers: Thirty-Five Years of Research and Application," *Infrared Physics & Technology*, vol. 40, no. 3, pp. 127 – 139, 1999.

[16] E. Bründermann, *Widely Tunable Far-Infrared Hot-Hole Semiconductor Lasers*. John Wiley & Sons, Inc., 2005, pp. 279–350.

[17] H.-W. Hübers, S. G. Pavlov, and V. N. Shastin, "Terahertz Lasers based on Germanium and Silicon," *Semiconductor Science and Technology*, vol. 20, no. 7, p. S211, 2005.

[18] B. S. Williams, "Terahertz Quantum-Cascade Lasers," *Nature Photonics*, vol. 1, no. 9, pp. 517–525, 2007.

[19] M. Philipp, U. Graf, A. Wagner-Gentner, D. Rabanus, and F. Lewen, "Compact 1.9 THz BWO Local-Oscillator for the GREAT Heterodyne Receiver," *Infrared Physics & Technology*, vol. 51, no. 1, pp. 54 – 59, 2007.

[20] H. Eisele, "480 GHz Oscillator with an InP Gunn Device," *Electronics Letters*, vol. 46, pp. 422–423, March 2010.

[21] A. Íñiguez-de-la Torre, I. Íñiguez-de-la Torre, J. Mateos, T. González, P. Sangaré, M. Faucher, B. Grimbert, V. Brandli, G. Ducournau, and C. Gaquière, "Searching for THz Gunn Oscillations in GaN Planar Nanodiodes," *Journal of Applied Physics*, vol. 111, no. 11, 2012.

[22] J. Nishizawa, P. Plotka, T. Kurabayashi, and H. Makabe, "706 GHz GaAs CW Fundamental-Mode TUNNETT Diodes Fabricated with Molecular Layer Epitaxy," *physica status solidi (c)*, vol. 5, no. 9, pp. 2802–2804, 2008.

[23] S. Suzuki, M. Asada, A. Teranishi, H. Sugiyama, and H. Yokoyama, "Fundamental Oscillation of Resonant Tunneling Diodes above 1 THz at Room Temperature," *Applied Physics Letters*, vol. 97, no. 24, 2010.

[24] M. Feiginov, C. Sydlo, O. Cojocari, and P. Meissner, "Resonant-Tunnelling-Diode Oscillators Operating at Frequencies above 1.1 THz," *Applied Physics Letters*, vol. 99, no. 23, 2011.

[25] W. Knap, J. Lusakowski, T. Parenty, S. Bollaert, A. Cappy, V. V. Popov, and M. S. Shur, "Terahertz Emission by Plasma Waves in 60 nm Gate High Electron Mobility Transistors," *Applied Physics Letters*, vol. 84, no. 13, 2004.

[26] W. Knap, F. Teppe, Y. Meziani, N. Dyakonova, J. Lusakowski, F. Boeuf, T. Skotnicki, D. Maude, S. Rumyantsev, and M. Shur, "Plasma Wave Detection of Sub-Terahertz and Terahertz Radiation by Silicon Field-Effect Transistors," *Applied Physics Letters*, vol. 85, no. 4, pp. 675–677, 2004.

[27] A. Maestrini, I. Mehdi, J. Siles, J. Ward, R. Lin, B. Thomas, C. Lee, J. Gill, G. Chattopadhyay, E. Schlecht, J. Pearson, and P. Siegel, "Design and Characterization of a Room Temperature All-Solid-State Electronic Source Tunable From 2.48 to 2.75 THz," *IEEE Transactions on Terahertz Science and Technology*, vol. 2, no. 2, pp. 177–185, March 2012.

[28] D. B. Rutledge, D. P. Neikirk, and D. P. Kasilingam, "Integrated Circuit Antennas," *Infrared and millimeter waves*, vol. 10, no. part 2, pp. 1–90, 1983.

[29] I. C. Mayorga, A. Schmitz, T. Klein, C. Leinz, and R. Gusten, "First In-Field Application of a Full Photonic Local Oscillator to Terahertz Astronomy," *IEEE Transactions on Terahertz Science and Technology*, vol. 2, no. 4, pp. 393–399, 2012.

[30] S. M. Duffy, S. Verghese, A. McIntosh, A. Jackson, A. Gossard, and S. Matsuura, "Accurate Modeling of Dual Dipole and Slot Elements used with Photomixers for Coherent Terahertz Output Power," *IEEE Transactions on Microwave Theory and Techniques*, vol. 49, no. 6, pp. 1032–1038, 2001.

[31] T. K. Nguyen and I. Park, "Resonant Antennas on Semi-Infinite and Lens Substrates at Terahertz Frequency," in *Convergence of Terahertz Sciences in Biomedical Systems*. Springer, 2012, pp. 181–193.

[32] T. Endo, Y. Sunahara, S. Satoh, and T. Katagi, "Resonant Frequency and Radiation Efficiency of Meander Line Antennas," *Electronics and Communications in Japan (Part II: Electronics)*, vol. 83, no. 1, pp. 52–58, 2000.

[33] K. Chang, R. A. York, P. S. Hall, and T. Itoh, "Active Integrated Antennas," *IEEE Transactions on Microwave Theory and Techniques*, vol. 50, no. 3, pp. 937–944, 2002.

[34] D. Segovia-Vargas, D. Castro-Galan, L. E. García-Muñoz, and V. Gonzalez-Posadas, "Broadband Active Receiving Patch with Resistive Equalization," *IEEE Transactions on Microwave Theory and Techniques*, vol. 56, no. 1, pp. 56–64, 2008.

[35] E. Mueller and J. Waldman, "Power and Spatial Mode Measurements of Sideband Generated, Spatially Filtered, Submillimeter Radiation," *IEEE Transactions on Microwave Theory and Techniques*, vol. 42, no. 10, pp. 1891–1895, Oct 1994.

[36] D. Kurtz, J. Hesler, T. Crowe, and I. Weikle, R.M., "Submillimeter-Wave Sideband Generation Using Varactor Schottky Diodes," *IEEE Transactions on Microwave Theory and Techniques*, vol. 50, no. 11, pp. 2610–2617, Nov 2002.

[37] H. Odashima, L. R. Zink, and K. M. Evenson, "Tunable Far-Infrared Spectroscopy Extended to 9.1 THz," *Opt. Lett.*, vol. 24, no. 6, pp. 406–407, Mar 1999.

[38] B. Sartorius, M. Schlak, D. Stanze, H. Roehle, H. Künzel, D. Schmidt, H.-G. Bach, R. Kunkel, and M. Schell, "Continuous Wave Terahertz Systems Exploiting 1.5 μm Telecom Technologies," *Opt. Express*, vol. 17, no. 17, pp. 15 001–15 007, Aug 2009.

[39] R. E. Collin, *Foundations for Microwave Engineering*. Wiley. com, 2007.

[40] C. A. Balanis, *Antenna Theory: Analysis and Design*. John Wiley & Sons, 2012.

[41] K. Moon, H. Han, and I. Park, "Terahertz Folded Half-Wavelength Dipole Antenna for High Output Power," in *Microwave Photonics, 2005. MWP 2005. International Topical Meeting on*, Oct 2005, pp. 301–304.

[42] H. Ryu, S. Kim, M. Kwak, K. Kang, and S.-O. Park, "A Folded Dipole Antenna Having Extremely High Input Impedance for Continuous-Wave Terahertz Power Enhancement," in *33rd International Conference on Infrared, Millimeter and Terahertz Waves, 2008. IRMMW-THz 2008*, 2008, pp. 1–2.

[43] K. Baaske, K. Ezdi, C. Jordens, O. Peters, M. Mikulics, and M. Koch, "Folded Dipole Antenna for Increased CW THz Output Power," in *34th International Conference on Infrared, Millimeter, and Terahertz Waves, 2009. IRMMW-THz 2009*, Sept 2009, pp. 1–2.

[44] H. Tanoto, J. H. Teng, Q. Y. Wu, M. Sun, Z. N. Chen, S. A. Maier, B. Wang, C. C. Chum, G. Y. Si, A. J. Danner, and S. J. Chua, "Greatly Enhanced Continuous-Wave Terahertz Emission by Nano-Electrodes in a Photoconductive Photomixer," *Nature Photonics*, vol. 6, no. 2, pp. 121–126, 2012.

[45] J. Montero-de Paz, I. Oprea, V. Rymanov, S. Babiel, L. E. García-Muñoz, A. Lisauskas, M. Hoefle, Á. Jimenez, O. Cojocari, D. Segovia-Vargas *et al.*, "Compact Modules for Wireless Communication Systems in the E-Band (71–76 GHz)," *Journal of Infrared, Millimeter, and Terahertz Waves*, pp. 1–16, 2013.

[46] E. Brown, K. Intosh, K. Nichols, and C. Dennis, "Photomixing up to 3.8 THz in Low-Temperature-Grown GaAs," *Applied Physics Letters*, vol. 66, no. 3, pp. 285–287, 1995.

[47] X.-C. Zhang and D. Auston, "Optoelectronic Measurement of Semiconductor Surfaces and Interfaces with Femtosecond Optics," *Journal of applied physics*, vol. 71, no. 1, pp. 326–338, 1992.

[48] M. Beck, H. Schäfer, G. Klatt, J. Demsar, S. Winnerl, M. Helm, T. Dekorsy *et al.*, *Impulsive Terahertz Radiation with High Electric Fields from an Amplifier-Driven Large-Area Photoconductive Antenna*. Bibliothek der Universität Konstanz, 2010.

[49] A. Dreyhaupt, S. Winnerl, M. Helm, and T. Dekorsy, "Optimum Excitation Conditions for the Generation of High-Electric-Field Terahertz Radiation from an Oscillator-Driven Photoconductive Device," *Optics letters*, vol. 31, no. 10, pp. 1546–1548, 2006.

[50] M. Awad, M. Nagel, H. Kurz, J. Herfort, and K. Ploog, "Characterization of Low Temperature GaAs Antenna Array Terahertz Emitters," *Applied Physics Letters*, vol. 91, no. 18, pp. 181 124–181 124, 2007.

[51] S. Preu, M. Mittendorff, H. Lu, H. B. Weber, S. Winnerl, and A. Gossard, "1550 nm ErAs: In (Al) GaAs Large Area Photoconductive Emitters," *Applied Physics Letters*, vol. 101, no. 10, pp. 101 105–101 105, 2012.

[52] J. Krause, M. Wagner, S. Winnerl, M. Helm, and D. Stehr, "Tunable Narrowband THz Pulse Generation in Scalable Large Area

Photoconductive Antennas," *Optics Express*, vol. 19, no. 20, pp. 19 114–19 121, 2011.

[53] A. Eshaghi, M. Shahabadi, and L. Chrostowski, "Radiation Characteristics of Large-Area Photomixer Used for Generation of Continuous-Wave Terahertz Radiation," *Journal Optical Society of America B*, vol. 29, no. 4, pp. 813–817, 2012.

[54] A. Eshaghi, M. Shahabadi, L. Chrostowski, and S. Kamal, "Large-Area Microstructured Photomixer as Scannable Detector of Continuous-Wave Terahertz Radiation," *Journal Optical Society of America B*, vol. 29, no. 12, pp. 3254–3258, Dec 2012.

[55] A. Leitenstorfer, S. Hunsche, J. Shah, M. Nuss, and W. Knox, "Femtosecond High-Field Transport in Compound Semiconductors," *Physical Review B*, vol. 61, no. 24, p. 16642, 2000.

CHAPTER 4

SUB-TERAHERTZ RECTIFYING DETECTORS

Once THz emitters were discussed in the previous chapter, it is time to focus on the other key devices of a wireless system: the detectors. In this chapter two direct detectors technologies will be discussed: QO SBD detector and FET direct detector based on CMOS technology. We have focused on those two topologies since among all available THz/sub-THz detectors, they are the ones with best capabilities regarding compactness, room temperature operation and easy array integration. In addition, their performance can also be improved from the antenna point of view.

A complete QO SBD receiver design and characterization is carried out in this chapter. The receiver is designed to work within the E-Band (60 GHz - 90 GHz) and it is meant to take part of a very-high speed data wireless transmission system ($>$ 1 Gbit/s). Regarding the CMOS FET direct detector, the very first steps for a 300 GHz receiver are presented. Its main application is an array for imaging applications (security). Both designs are formed from a planar antenna and a detector (either SBD or FET), with the possibility of including an optical device (lens). Their performance is improved by designing the antenna of each receiver in such a way that the total efficiency is maximized.

The chapter is organized in three sections. In the first one, a brief introduction on THz/sub-THz detectors is done. The main parameters of such detectors are introduced and a classification of them is presented. The second section is devoted to QO SBD receiver. Finally, the third section discusses the CMOS FET direct detector.

4.1 Introduction to THz/sub-THz Detectors

THz/sub-THz detectors are devices that are capable to detect invisible THz/sub-THz radiation and convert it into something perceptible to human being [1]. They are transducers that convert an incoming signal (THz/sub-THz radiation) into some convenient form which can be observed, recorded and analysed. The signal, an electromagnetic wave, has an amplitude and a phase with an information that can be recovered [2]. As mentioned in the Chapter 1 of the present work, THz/sub-THz detectors are a key component of a lot of systems nowadays. They are finding a lot of applications in astronomy, security, wireless communications, etc. In this chapter we will focus on two of those applications: wireless communications and security. In order to make such systems cost-effective, it is desirable to use un-cooled detectors, as well as being compact, easy to manufacture and easy to integrate on array configuration [3, 4].

There are several parameters that describe the performance of a detector that will be summarised in the next subsection. In the following one, a classification of THz/sub-THz detectors is presented and the performance of each type is briefly described. In this chapter we will focus on CW THz/sub-THz detection since we are interesting on a single carrier frequency, but there also exists Pulsed THz/sub-THz detectors and more information of them can be found in [1, 2].

4.1.1 Detector Parameters

In this subsection, the main THz/sub-THz detector parameters are briefly summarised. These parameters describe the detector performance and are the key component to choose between different detectors depending on the application.

Responsivity This parameter describes the conversion efficiency of the detector. It is defined as the ratio of the output, an electrical signal (either voltage or current), to the input (THz/sub-THz radiation power). Depending on the output signal, the responsivity can be called voltage responsivity, expressed in volts per watt and defined as:

$$R_V \equiv \frac{dV}{dP} \tag{4.1}$$

or current responsivity:

$$R_I \equiv \frac{dI}{dP} \tag{4.2}$$

expressed in amps per watt. Generally speaking, high responsivity is desirable. This is an important characteristic, but perhaps not the most important, as the limit to what can be measured is expressed by the Noise Equivalent Power (NEP), not the responsivity [1, 2].

Linearity Linearity expresses the power range where the responsivity behaves in the same way. The extent to which the detector responsivity varies with the input power is termed the non-linearity. Ideally, we want a detector to have the same responsivity regardless of the size of the input signal. [1, 2].

Noise Equivalent Power This parameter expresses the amount of signal power needed to fall on the detector so that the signal at the detector output is exactly the same size as the signal produced by the background noise. Or what is the same, the amount of signal power required to yield a Signal to Noise Ratio (SNR) of unity at the output of the detector in a 1 Hz bandwidth. The lower NEP a detector has the more sensitive it is and lower signals can be detected [1, 2].

Range Range is related with power and specifies the maximum signal that the detector can bear before it can be damaged. Normally, detectors are devices highly sensitive and a very high amount of power would cause irreversible damage to it [1, 2].

Speed There are two parameters related with speed in detectors: response speed and time constant. In fact, both parameters are related and define the time that a detector needs to respond to a change in the input signal and register the new value of the THz/sub-THz field [1, 2].

Spectral Response It is the responsivity as a function of the frequency of the detector. Detectors can be either broadband or narrowband, depending on the application one detector would be more suitable than other [1, 2].

Polarisation Many sensor are sensitive to radiation of one polarization (linear, elliptical or circular) while other detectors are not. It is usually undesirable to have a detector whose polarisation response varies with frequency [1].

Environmental Factors Some detectors are placed under controlled conditions in a laboratory; others find themselves in more difficult environments such as on a satellite in earth orbit. In addition, some detectors need to be cooled while others can work at room temperature. The ideal is to have a compact, light, and robust sensor that operates at ambient temperature and pressure [1].

4.1.2 Classification of THz/sub-THz Detectors

There exists a huge variety of detectors working at these frequencies nowadays, and improvements and new topologies are made every year. Traditionally, detectors are divided in two main groups: coherent and incoherent detection systems (see Figure 4.1). Coherent detection systems allow detecting both the amplitude and the phase of the signal, while incoherent detection systems allow only amplitude signal detection. Traditionally, coherent detection systems use heterodyne circuit design, while incoherent detection systems use direct detection detectors [5, 6].

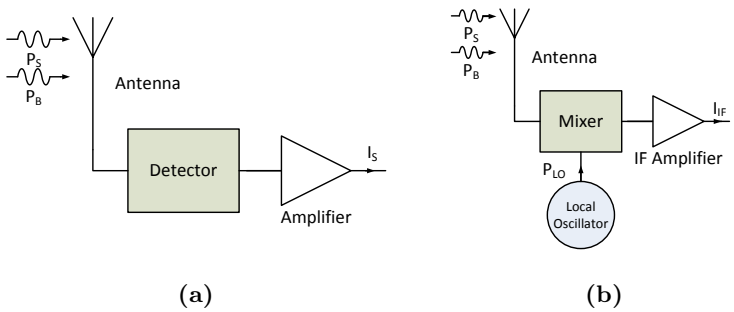

Figure 4.1: (a) Direct detection scheme. (b) Heterodyne detection scheme.

Direct Detection Detectors

The simplest direct detection schematic can be seen in Figure 4.1a. It consists on an antenna that collects both the signal (P_S) and the background (P_B) radiation (either thermal or transmitted power from an emitter) and transfer them to the detector device which rectifies them from RF (THz/sub-THz) to baseband. In most practical cases the baseband is defined by amplitude or frequency modulation of the incoming signal to reduce the effect of gain drifts and 1/f noise that occurs in the THz electronics. Then, an amplifier can be included to increase the received signal level. Finally, the generated signal (I_S) have to be processed. In the THz/sub-THz region, direct detectors typically are power to voltage or power to current converters. They transform an RF power signal into a baseband voltage or current one. The most important figure of merit of such detectors are both the responsivity and the NEP [5, 6].

Direct detection detectors can be classified in three different groups: Thermal detectors, Photoconductive detectors and Electronic rectifiers. Below, each type of detector is described and detectors belonging to each group are presented.

Thermal

Thermal direct detectors absorb THz/sub-THz radiation energy and convert it into heat. Then, a thermometer attached to a heat sink measures the temperature change induced by this heat. Each type of thermal detector is distinguished by the specific scheme it uses to measure the temperature difference between the absorber and the heat sink. The absorbed radiation energy is determined by calibrating the measurement output [1,2,7]. The most interesting property of thermal detectors is that they respond to radiation over a very broad spectral range, which can not be done with other types of detectors. On the other hand, thermal detectors are relatively slow because the radiation absorber must reach thermal equilibrium before a temperature measurement can take place. The time constant of a typical bolometer is $\sim 0.1\,\text{ms}$ at $4\,\text{K}$ temperature. Golay cells and pyroelectric detectors work at ambient temperature, but they are much slower than bolometers, with time constants on the order of $1\,\text{s}$. Because of the strong influence of ambient temperature, detection of desired THz radiation requires special care to compensate for environmental effects. A common, yet powerful, scheme to distinguish desired THz radiation from background signal is to modulate the intensity of the incident THz beam and measure the consequent changes in output signal [1, 2, 7].

The most important THz/sub-THz thermal detectors are bolometers, pyroelectric detectors, Golay cells, thermopile and power-meters. All of them are briefly explained below.

Bolometers A bolometer is a cryogenic detector which operates at or below Liquid Helium (L-He) ($4\,\text{K}$) temperature for high detection sensitivity. It is equipped with an electrical resistance thermometer to measure the temperature of the radiation absorber. They measure heat through a change in their electrical resistance. Usually, the thermometer is made of a heavily doped semiconductor such as Si or Ge, exploiting the fact that the resistance of such materials is susceptible to temperature. An schematic of a bolometer can be seen on Figure 4.2. Responsivity of a typical Si bolometer is $\sim 10^7\ \text{V/W}$ at L-He temperature ($4\,\text{K}$) and the typical NEP is $\sim 10^{-14}\ \text{W}/\sqrt{\text{Hz}}$ [1, 2, 7].

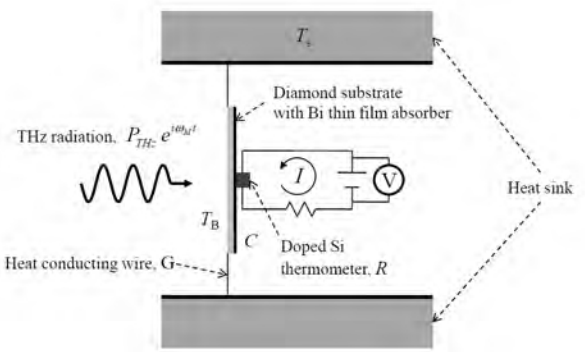

Figure 4.2: Schematic diagram of a typical composite bolometer [7].

Pyroelectric A pyroelectric detector is a detector formed by a pyroelectric material in which temperature changes force a change in the dielectric constant of the material. This is produced by spontaneous electric polarization changes due to temperature. A key component of this type of detector is a capacitor containing this pyroelectric material. A change in the detector temperature causes an electric charge to appear across the electrodes. The current flow neutralizing this bias is the measure used to determine the temperature variation [1, 2, 7]. An schematic of this kind of detector can be seen on Figure 4.3. Typical responsivity and NEP of a pyroelectric detector at a modulation frequency of ~ 10 Hz are ~ 1 kV/W and $\sim 10^{-9}$ W/$\sqrt{\text{Hz}}$, respectively.

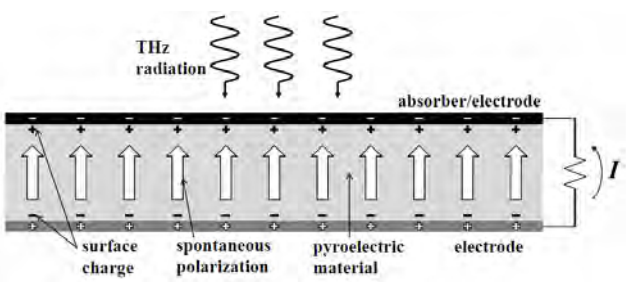

Figure 4.3: Schematic diagram of a typical pyroelectric detector [7].

Golay Cell A Golay cell is a thermal detector where the heat is transferred to a small volume of gas in a sealed chamber behind the absorber so that pressure increases in the chamber. A reflective and flexible membrane is attached to the back side of the chamber, and an optical reflectivity measurement detects the membrane deformation induced by the pressure increase [1,2,7]. An schematic of a Golay cell is shown in Figure 4.4. The Golay cell is the most sensitive detector among thermal radiation detectors which operates at room temperature. Responsivity of a Golay cell is in the range of kV/W when the modulation frequency is a few tens of hertz. Typically obtained NEP is $(0.1 - 1) \cdot 10^{-9}$ W/$\sqrt{\text{Hz}}$.

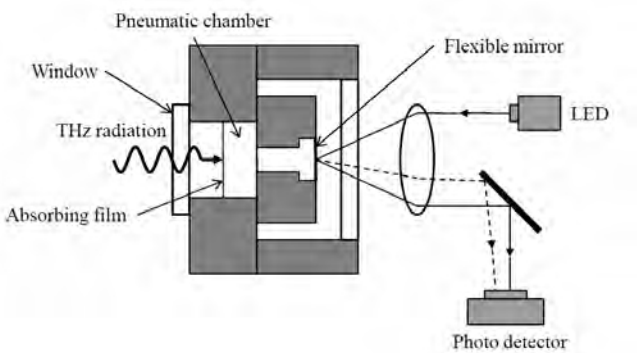

Figure 4.4: Schematic diagram of a Golay Cell [7].

Thermopile When two different metals are in contact, the mismatch of their Fermi levels results in an electromotive force across the contact. This is called the thermoelectric effect and the magnitude of this force depends on the temperature [2]. In order to use thermopiles for the detection of radiation, they have to be combined with an absorber. Ideally, it has complete absorption across the whole frequency band of interest. In addition, a reference temperature needs to be provided, which should be highly stable. Typical responsivity and NEP values of a thermopile detector are in the order of tens of V/W and 10^{-10} W/$\sqrt{\text{Hz}}$, respectively. In Figure 4.5 and schematic of a thermopile detector is shown.

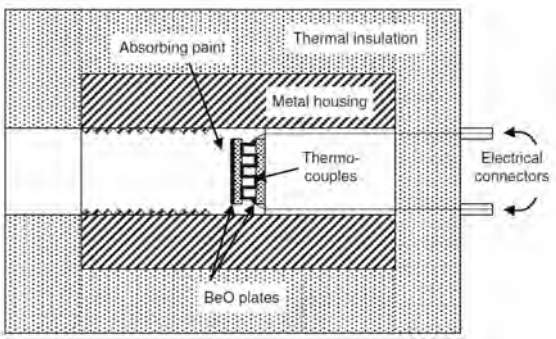

Figure 4.5: Cross section of a thermopile [2].

Power Meters Inside this group, calorimetric, photoacustic and photon drag effect detectors are included.

Calorimetric power meters are composed by two identical waveguides which are mounted in a chamber that is thermally well insulated. They are terminated with absorbers which can be electrically heated. For the measurement, the THz/sub-THz signal is coupled into one waveguide, while the absorber of the other is electrically heated until the temperature difference between the two loads vanishes. With some corrections, the electrically dissipated power is then equal to the THz/sub-THz power [2]. An schematic of it can be seen on Figure 4.6.

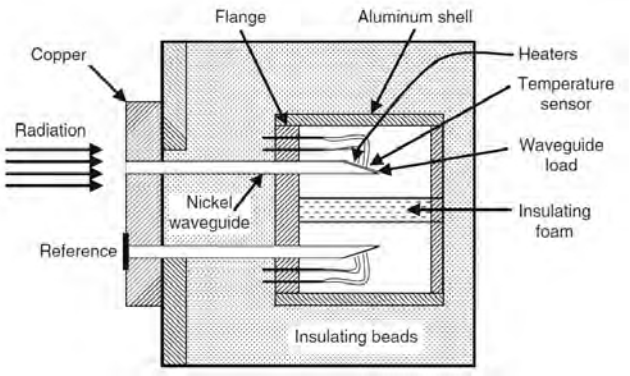

Figure 4.6: Diagram of the power detector head of a calorimetric power meter [2].

Another type of power meter is based on the photoacoustic effect. Two closely spaced parallel windows form a sealed gas cell. A thin metal film which absorbs a known fraction of the incident THz/sub-THz radiation is placed between them. Chopping the incident radiation leads to a modulation of the film's temperature, which in turn induces a modulation of the pressure in the cell. This modulation is detected by a pressure transducer (microphone) and measured with a lock-in amplifier. The modulated pressure change is closely related to the total absorbed power [2]. An schematic of it can be seen on Figure 4.7.

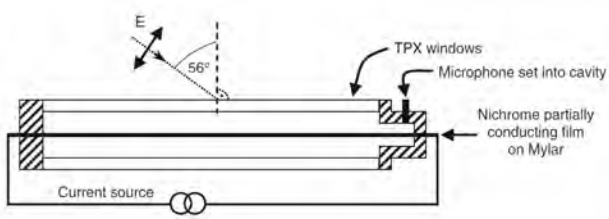

Figure 4.7: Thomas Keating Ltd. power meter. Accurate measurements require polarized radiation at the Brewster angle 55.5° [2].

Finally, a further method of measuring power in the THz region is to use detection based on the photon drag effect. Photon drag is a simple manifestation of photon pressure, because it generates an electric field in a semiconductor by transferring momentum from an incident light beam to charge carriers. The magnitude of the electron field is a linear function of the light intensity. A typical photon drag device consists of a cylindrical rod of semiconductor material, with sufficient doping to absorb radiation over the length of the rod at the wavelength of interest. When light is directed onto the end face of the rod, an electric field is induced, which can be observed as a voltage if electrodes are placed at either end of the device [2].

Photoconductive

Photoconductive detectors measure a resistance change produced by the interaction of photons with electrons within a material. If a current is passed through the detector element, this resistance can be measured so does the incoming energy which produced that change. The essential difference between thermal detectors and photodetectors is that in the former the incoming energy produces a measurable temperature change, while in the latter the energy of the photons interacts with electrons [2]. The conductivity of a piece of material, typically a semiconductor, is monitored. When THz/sub-THz radiation falls on the photoconductive material, the conductivity changes. The THz/sub-THz frequency photons are usually too low energy to create electron-hole pairs. Rather, they modulate the passage of a pre-existing current [1]. Several photoconductive detectors have been designed with different materials. Among them, the most used ones with best detection capabilities are the ones made of Germanium (Ge) and Gallium Arsenide (GaAs).

Extrinsic Germanium Detectors Ge:Ga has been the most widely studied and widely used THz photoconductive detector since its introduction in 1965. Single Ge:Ga detectors and detector arrays have been employed for THz astronomy since the 1980's. In its conventional form, it has good response from about 2.4 THz to 7 THz, but it was later realized that its ionization energy could be reduced by applying a compressive force, and in this mode the low-frequency limit is extended to close to 1.5 THz, but with lower response at high frequencies. The optimization of this type of detector is complex but a very remarkable performance has been achieved under low background conditions, with NEP values close to 10^{-17} W/$\sqrt{\text{Hz}}$. Commercial systems, typically used in higher background laboratories, reach values of $10^{-12} - 10^{-13}$W/$\sqrt{\text{Hz}}$. For optimum response above 6 THz, Be-doped Ge photoconductors have been developed. Under reduced backgrounds, NEPs are close to 10^{-16} W/$\sqrt{\text{Hz}}$, giving a significant advantage over Ge:Ga in the 6 THz–10 THz region [2].

Gallium Arsenide Detectors GaAs is a good candidate to be used as THz/sub-THz photoconductive detector since it has several absorption peaks in the frequency range between 0.7 THz and 2 THz. At the frequency of peak response, 1.06 THz, NEPs of 4×10^{-14} W/$\sqrt{\text{Hz}}$ have been obtained with n-GaAs with donor concentrations of 2×10^{14} cm^3

and low compensation by acceptors. Response times of 250 ns have been measured in detectors with low compensation and 25 ns in those with much higher acceptor concentration. In practice, it is difficult to achieve good responsivity and high speed simultaneously, due to the resistance of GaAs detectors, which is typically in the GΩ range [2].

Electronic Rectifiers

A rectifier is a device that is able to generate a DC current from an AC excitation. Due to a nonlinear relationship between the bias voltage and the generated current, the AC excitation is downconverted to DC due to selfmixing mechanisms. In this sense, a rectifier can also be used as mixer for downconversion to an Intermediate Frequency (IF) in a heterodyne system. Schottky diodes and FETs have been largely used as rectifiers in the microwave region during decades, and one of the approaches for THz detection is the extension of these devices to higher frequencies. They are replacing detection solutions based on thermal detection as they are able to provide similar NEP values (but not similar to superconducting bolometers), room-temperature operation and higher frequency bandwidth. However, their maximum operation frequency is at last term limited by parasitic effect and the difficult of manufacturing devices within the sub-µm range [2–4, 6].

Schottky Barrier Diodes SBD detectors have been long used since 1940s for microwave detection and mixing because of their high responsivity and ability to operate at ambient or cryogenic temperatures. Typical responsivity and NEP values for these devices for zero biasing are in the order of 1000 V/W and 5 pW/$\sqrt{\text{Hz}}$ at 100 GHz and 100 V/W with a NEP of 50 pW/$\sqrt{\text{Hz}}$ at 1 THz respectively [8]. They are explained in detail in Section 4.2.

Field Effect Transistors The study of FET as THz detectors was initiated by Dyakonov-Shur publication [9]. Typical responsivities are similar to the ones obtained with SBD and NEP values are around $100 - 200$ pW/$\sqrt{\text{Hz}}$ at 1 THz [8]. They are explained in detail in Section 4.3.

Heterodyne Detectors

Today, the heterodyne principle is the basis of nearly all radio and television receivers as well as wireless telecommunication. Heterodyne detection is based on frequency downconversion in a nonlinear device, accomplished by mixing RF signal with a reference radiation at a fixed frequency (Figure 4.1b). The front-end deals with the THz/sub-THz radiation and its major components are [5]:

- A LO that delivers the reference frequency to the mixer.
- A mixer onto which the signal radiation and the radiation from the LO impinge. The mixer delivers an output at the difference of the signal and the LO frequencies, the so-called IF.
- Optical elements that couple the signal radiation and the LO radiation onto the mixer.

We assume that the nonlinear device, the mixer, is characterised by a quadratic nonlinearity. For the signal and the reference radiation given as $E_S \cos(\omega_S t)$ and $E_{LO} \cos(\omega_{LO} t)$, the output signal contains the five frequency components:

$$\begin{aligned} V_O &= \chi \left[E_S \cos(\omega_S t) + E_{LO} \cos(\omega_{LO} t) \right]^2 \\ &= \frac{1}{2} \chi \left(E_S^2 + E_{LO}^2 \right) \\ &\quad + \frac{1}{2} \chi E_S^2 \cos(2\omega_S t) \\ &\quad + \frac{1}{2} \chi E_{LO}^2 \cos(2\omega_{LO} t) \\ &\quad + \frac{1}{2} \chi E_S E_{LO} \cos\left[(\omega_S + \omega_{LO}) t \right] \\ &\quad + \frac{1}{2} \chi E_S E_{LO} \cos\left[(\omega_S - \omega_{LO}) t \right] \end{aligned} \tag{4.3}$$

where χ is the quadratic nonlinear coefficient. The heterodyne detector filters out the first four components and measures the last term of the difference frequency (IF), $\omega_{IF} = |\omega_S - \omega_{LO}|$ [7].

The LO output power is a crucial factor in determining the detector performance, as V_O is proportional to E_{LO}. Solid-state emitters have been commonly used as LOs in the region of 0.11 THz–1 THz, and gas lasers above 1 THz. QCLs are a promising THz LO for future applications because of their compactness and high power. Another key component of heterodyne detection is a mixer with nonlinear characteristics. Schottky diodes are commonly used as mixers in the spectral range below 1 THz. Above 1 THz, the most sensitive mixers are cryogenic detectors such as hot-electron bolometers [2, 5–7].

Schottky Barrier Diodes This is the technology traditionally available for THz/sub-THz receivers together with a gas laser LO. The noise temperature of such receivers has essentially reached a limit of about $50h\nu/k_B$ in the frequency range below 3 THz, with h being the Planck constant, ν the frequency and k_B the Boltzmann constant. Above 3 THz, there occurs a steep increase, mainly due to the reduced performance of the diode itself (parasitic effects) and antenna performance [2].

Superconductor-Insulator-Superconductor The SIS mixer is a sandwich of two superconductors separated by a thin ($\sim$ 20Å) insulating layer. Nowadays, SIS mixers are used in virtually all astronomical heterodyne receivers operating below 1.3 THz. The conversion loss of a typical SIS-based heterodyne receiver is $\sim$ 13 dB. About 3 dB of the losses are in the optics and $\sim$ 3 dB are in the tuning circuit. The remaining $\sim$ 7 dB are due to the mixing process in the junction itself. The signal bandwidth of a SIS mixer is typically 10 %–30 % of its centre frequency, with the larger FBW at the low-frequency end [2]. The SIS mixers used in the Heterodyne Instrument for the Far-Infrared (HIFI) on ESA's Herschel Space Observatory are an example [10].

Hot Electron Bolometers Unlike SBD and SIS mixers, HEB mixer is a thermal detector. In principle, any type of bolometer can be used as a mixer. Dual Side Band (DSB) noise temperatures achieved with HEB mixers range from 400 K at 0.6 THz up to 3800 K at 5.2 THz. Up to 2.5 THz, the noise temperature closely follows the slope $10h\nu/k_B$, with somewhat worse values above 3 THz. This is caused by increasing the losses in the optical components and lower efficiency of the hybrid antenna. Non uniform distribution of the current in the bridge, due to the skin-effect, may also contribute, because it changes the IF matching. In comparison with SBD mixer, HEB requires three or four orders of magnitude less LO power [2].

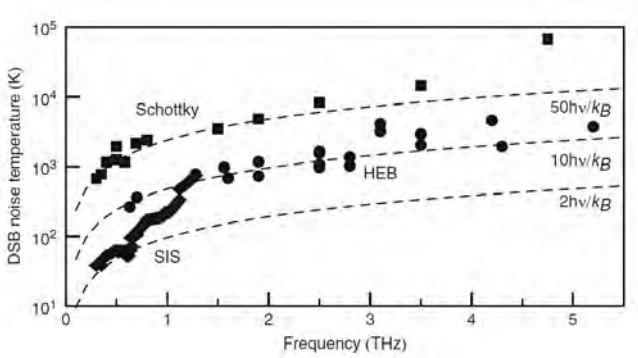

Figure 4.8: DSB noise temperatures achieved with Schottky diode mixers (squares), SIS mixers (diamonds), and HEB (circles) [2].

Comparison between Heterodyne and Direct Detection

An advantage of systems with direct detection is their relative simplicity and possibility to design large format arrays. Regarding heterodyne detectors, three characteristics of them make them more suitable for some applications. First, since the signal which carries the information is downconverted, low-frequency amplifiers can be employed. This allows the use of heterodyne receivers even at extremely high frequencies, where direct amplification is not possible due to the lack of high-speed amplifiers. The second advantage is its high-frequency selectivity. For telecommunication, this means that it is possible to make very efficient use of a given frequency band, i.e., many transmitting channels can be fitted into it. For spectroscopy applications, it means that high spectral resolution is possible. The third advantage is also based on the narrow bandwidth detection process. The noise can be reduced by choosing a detection bandwidth similar to the signal bandwidth and, because the signal is narrow band, the noise will be correspondingly low [2].

Heterodyne detection offers higher spectral resolution $\nu/\Delta\nu \sim 10^5 - 10^6$ because $\nu_{IF} \ll \nu$. But for heterodyne systems, especially for SBD in the THz region, a critical component is the LO source. At the same time, direct detectors, as a rule operating in wider spectral range, can provide sufficient resolution. They are preferable for moderate spectral resolution $\nu/\Delta\nu \sim 10^3 - 10^4$ or lower and they are also preferable for imaging. Direct detectors can be used in those applications where responsivity is more important than the spectral resolution [6].

4.2 Quasi-Optical Schottky Barrier Diode Detector

In this section, a QO SBD detector working within the E-Band (60 GHz - 90 GHz) is designed, manufactured and characterised. In addition, it is used as a receiver for a 1 Gbit/s wireless transmission system at 76 GHz. A QO SBD detector is basically a SBD detector with a planar antenna and a silicon lens to improve its directivity.

This section is organised as follows. First, an introduction to SBD direct detectors is carried out. The main design parameters, as well as the state-of-the art results are presented. Secondly, the zero bias SBD used as the detector in the receiver is presented and characterised. To do so, both DC and high frequency measurements of the SBD have been done and the equivalent circuit is obtained. Then, three planar antennas were designed, each of them providing different capabilities to the receiver and radiation improvement is analysed by the design of a hyper-hemispherical silicon lens. A low frequency 50 Ω Coplanar Stripline (CPS) to Coplanar Waveguide (CPW) transition is designed and the whole structure is manufactured and packaged. The receiver is fully characterised and an experiment is carried out. This consists of a 1 Gbit/s wireless data transmission where the designed QO SBD detector is used as the receiver. Finally some conclusions are included.

4.2.1 Introduction to Schottky Barrier Diode Rectifiers

The Schottky Barrier Diode

A SBD is one of the simplest semiconductor devices, whose model representation (current-voltage (I-V) and voltage-capacitance (V-C) characteristics and the equivalent circuit) describes with sufficient accuracy its actual behaviour for up to millimetre and lower sub-millimetre band [11].

The SBD is a two-terminal semiconductor device that utilizes the nonlinear properties of a metal-semiconductor contact. The rectifying properties arise from the presence of an electrostatic barrier between the metal (the anode) and the semiconductor (the cathode). The barrier is

created by the unequal work functions of the metal and semiconductor and conduction is controlled primarily by thermionic emission of majority carriers over the barrier. The Schottky diode is therefore a majority carrier device whose cut-off frequency is not limited by minority carrier effects.

The electrical properties of a Schottky diode are predominantly defined by the metal and semiconductor combination and the size an condition of the contacting surfaces. Operation at high frequencies requires low series resistance and low junction capacitance. This implies the use of a semiconductor with high carrier mobility and saturation velocity. Most Schottky diodes currently used are made on silicon (Si) or gallium arsenide (GaAs) semiconductor. Carrier mobility is greater for the n-type materials than for the p-type. Hence, the n-type semiconductors are used almost exclusively for Schottky diodes. Many metals can create a Schottky barrier on either Si or GaAs semiconductors; platinum, gold and aluminium are commonly used [12]. A schematic of a SBD can be seen on Figure 4.9.

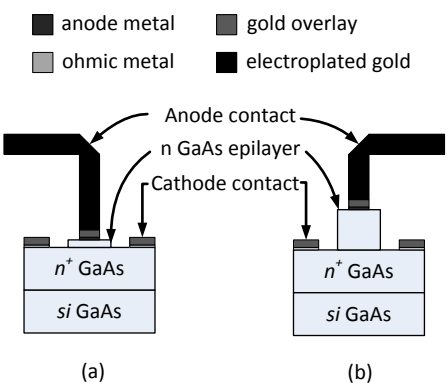

Figure 4.9: Cross-sectional view of planar Schottky barrier diodes intended for use as (a) Varistor and (b) Varactor (adapted from [12]).

The I-V characteristic of a SBD with a series resistance R_s and a parallel leakage resistance R_l is usually given by [13]:

$$I = I_s \left(e^{\frac{q}{\eta k T}(V - R_s I)} - 1 \right) + \frac{1}{R_l}(V - R_s I) \tag{4.4}$$

being k the Boltzmann constant ($1.38 \times 10^{-23}\,\mathrm{m^2 s^{-2} kg K^{-1}}$) and T the absolute temperature in Kelvin. The differential resistance (R_{diff}) or junction resistance (R_j) and the current responsivity (R_I) under square-law detection conditions are obtained from it [14]:

$$R_{diff} = R_j = \frac{1}{\frac{dI}{dV}} = \frac{dV}{dI} \tag{4.5}$$

$$R_I = \frac{\frac{d^2 I}{dV^2}}{2\left(\frac{dI}{dV}\right)} \tag{4.6}$$

The equivalent circuit model of Schottky diode is the following:

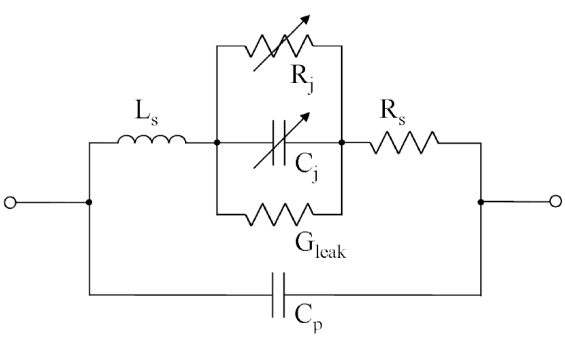

Figure 4.10: Equivalent circuit model of a Schottky diode.

Different parameters that appear in Equations 4.4 - 4.6 and in the equivalent circuit model are the following:

Differential Resistance (R_{diff}) or Junction Resistance (R_j) It is the relation between the applied voltage and the obtained current in the diode's junction.

Ideality Factor (η) Accounts for unavoidable imperfections in the junction and for other secondary phenomena that thermionic emission theory cannot predict [15]. $\eta = 1$ means pure thermionic emission, and its increase would be due to any deviation from this ideal model [12]. Typical values range from 1 to 2.

Series Resistance (R_S) Is a parasitic series resistance associated with the bulk semiconductor substrate and any contact resistance arising from soldered connections, whisker, etc. [14]. The lower this value is the better the SBD is because it means that diode has low losses. Typical R_S values in millimetre and sub-millimetre bands are $<10\,\Omega$.

Junction Capacitance (C_j) The capacitance of a Schottky barrier chip results from two sources mainly: the depletion layer under the metal-semiconductor contact and the capacitance of the oxide layer under the bonding pad [16]. This is a critical parameter for high frequency diode operation. The lower the capacitance is, the higher the working frequency is. Values lower than a few fF are needed for millimetre and sub-millimetre wave operation. When no bias is applied to the diode (Zero bias) then $C_j = C_{j0}$.

Saturation Current (I_S) This current depends on the junction area, and the metal and semiconductor used to form the junction [14].

Leakage Resistance (R_l) or Conductance (G_l) A diode ideally only has current when is forward biased but, in fact, it also has when it is reversely biased so that a small amount of current appears. This relation between the applied voltage and the reverse current is the leakage resistance ($R_l = 1/G_l$). Typical values of this resistance are in the order of kΩ - MΩ.

Knowing all this parameters is a critical point when designing a QO SBD detector, not only to know the maximum responsivity that can be achieved, but also because the input impedance of the diode is a key factor when designing the optimized antenna and the low frequency circuit attached to the diode. This diode characterization is done in Section 4.2.2.

SBD and QO SBD Detectors State-of-the-Art

Detectors based on SBD rectifiers are nowadays one of the most used detectors in the THz and sub-THz frequency band. This is due to the fact that they are able to operate cooled or un-cooled, they are easy to integrate with other devices, they can operate with no biasing (zero bias Schottky diodes) and their performance is similar to thermal detectors in terms of both responsivity and NEP. The problem of those devices comes from the presence of parasitic effects that limit their use in higher frequencies. The current cut-off frequency of SBD are in the order of tens of THz but this does not mean that they can be used up to these frequencies, mainly because the parasitic effects.

There exists commercially available waveguide SBD detectors. For instance, Virginia Diodes [8] provides SBD detectors in waveguide packaging with responsivity values of 2500 V/W and NEP of 2 pW/$\sqrt{\text{Hz}}$ at frequencies around 100 GHz respectively and a responsivity of 100 V/W and NEP of 40 pW/$\sqrt{\text{Hz}}$ at 1 THz. In [17] authors obtained a responsivity value of around 23000 V/W at 90 GHz with a NEP of 0.21 pW/$\sqrt{\text{Hz}}$.

Regarding QO SBD detector, responsivity values typically range from 300 to 1000 V/W over a frequency range from 150 GHz to 400 GHz [3]. Virginia Diodes [8] provides QO SBD detectors in the 100 GHz to 1 THz range with a typical responsivity of 500 V/W while ACST GmbH [18] provides responsivity values of around 800 V/W at 100 GHz and 3 V/W at 1 THz (not including the pre-amplifier), with typical NEP of 4 pW/$\sqrt{\text{Hz}}$ at 100 GHz and 100 pW/$\sqrt{\text{Hz}}$ at 1 THz. It has to be pointed out that QO SBD detectors have lower responsivities and higher NEP values than SBD detectors because not only the isolated diode affects the overall performance, but also the antenna, the lens and the low frequency circuit.

4.2.2 Zero Bias SBD Characterization

In this section, the zero bias SBD used in the development of the QO SBD power detector is presented. The Schottky diode is fully characterized by low frequency and high frequency measurements so that an equivalent circuit can be obtained. With such equivalent circuit, the optimal antenna can then be designed.

The zero-bias detector diodes are fabricated by the Film-Diode process recently developed by ACST GmbH [18], which aims at ultimate performance in millimetre and sub-millimetre wave devices. Diode fabrication implies two-side processing of the semiconductor wafer. Schottky contact is formed on the front side of the epilayer, whereas the ohmic-contact consists of two elements: one of them is around the Schottky contact on the top of the epilayers, whereas the second one is formed by the back side metallisation process directly under the Schottky contact. This approach reduces the series resistance of the diode and facilitates the uniform distribution of the current density across the whole anode area. This reduces the excess noise, which may be caused by local current overgrowing.

Two mesas are formed from the epilayer. The cathode mesa is formed directly under the Schottky contact. The anode mesa maintains structure planarity and does not affect the electrical performance of the diode. Both mesas are metallised from the back side with an Ohmic metallisation and also serve as contact pads for the discrete diode structure.

Mechanical robustness of the whole structure is provided by a few micrometer thin transferred membrane substrate. The membrane-substrate is optically transparent. This feature greatly facilitates accurate positioning of the diode structure for its mounting onto the antenna feed. A photograph of the Schottky diode across a 70 µm gap on CPW line on 50 µm quartz glass can be seen on Figure 4.11

The design and realization of the Schottky barrier diode receivers require the knowledge of a large number of diode parameters that define the diode's performance and which are essential for accurate non-linear simulations. Since standard direct C/V measurements fail for this diode

type, due to the low zero-bias junction capacitance in combination with the low differential resistance at 0 V, a detailed RF characterization is essential for a correct parameter extraction in order to achieve reliable simulation results for the receiver design. Therefore the Schottky diode is mounted on CPW test structures (Figure 4.11), and measurements are performed within the relevant RF frequency band.

The main parameters that need to be extracted from the measurements are the diode's saturation current I_s, the zero bias junction capacitance C_{j0}, the series resistance R_s, the ideality factor η and also the diode parasitic elements as the parallel capacitance C_p and junction leakage conductance G_{leak}. Traditionally, these parameters can be extracted by I/V measurements for low frequency characterization and a LRC-meter to obtain the capacitance. Unfortunately, because of the low value of the zero-bias junction capacitance C_{j0} and low differential resistance R_{diff} of the detector diode at 0 V it is not possible to measure it with a LCR-meter and precise S-parameter measurements must be undertaken to obtain C_{j0}. Both I/V and S-parameters measurements were carried out in the laboratories of the Technical University of Darmstadt (TUD).

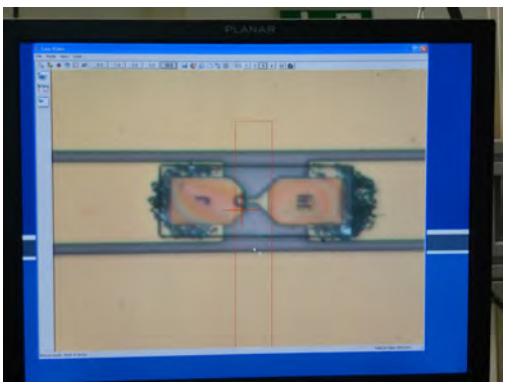

Figure 4.11: Photograph of the zero bias Schottky diode placed over a CPW line for characterization purposes with the vector network analyser.

I/V Measurements

The typical I/V curve of the diode is measured using first a picoamperimeter from Keithley (Figure 4.12a) and then a precision semiconductor parameter analyser from Hewlet Packard (Figure 4.12b). In both cases, the probe station showed in Figure 4.12c is used. The obtained results can be seen on Figure 4.13. In such plot not only the I/V curve of the Schottky diode is shown but also the differential resistance R_{diff} and the current responsivity as defined in Equations 4.5 and 4.6 respectively. An excellent current responsivity value of 14.5 A/W with a typical differential resistance of 273 Ω can be extracted (voltage responsivity of 14.5 A/W × 273 Ω = 3958 V/W).

Following the methodology presented in [19] which, in fact, follows the one presented in [13], series resistance R_s, ideality factor η, saturation current I_s and junction leakage conductance G_{leak} can be obtained [14].

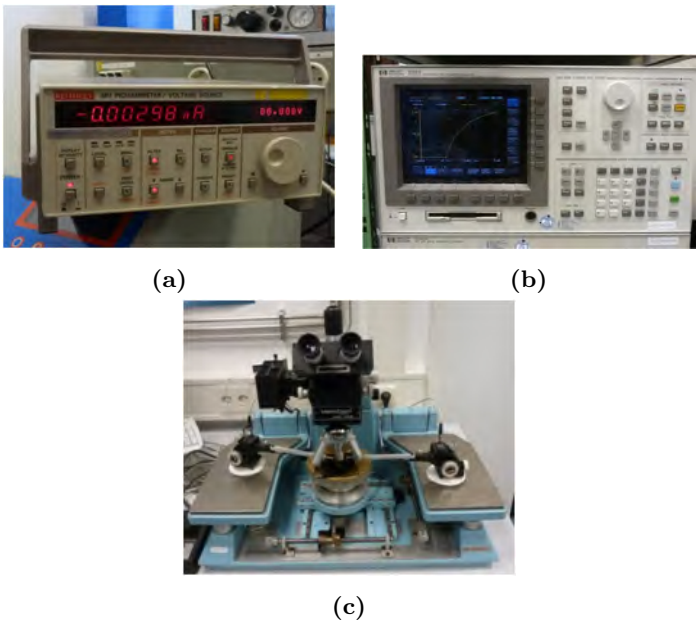

Figure 4.12: Devices used for obtaining Schottky diode I/V curve. (a) Keithley 487 Picoammeter, (b) Precision semiconductor parameter analyser Hewlet Packard 4156A and (c) Probe station.

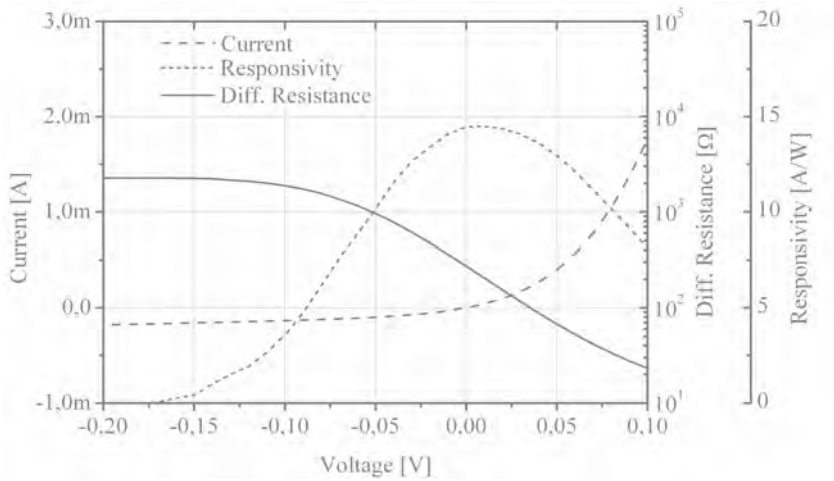

Figure 4.13: I/V measurement results for the applied diode type.

First and second derivatives of Equation 4.4, neglecting the second term due to the very high value of parallel leakage resistance, leads to:

$$\frac{dV}{dI} = \frac{\eta kT}{q}\frac{1}{I + I_s} + R_s \tag{4.7}$$

$$\frac{d^2V}{dI^2} = -\frac{\eta kT}{q}\frac{1}{(I + I_s)^2} \tag{4.8}$$

and equations 4.9 and 4.10 can be derived:

$$I = \sqrt{\frac{\eta kT}{q}}\sqrt{-\frac{d^2V}{dI^2}} + R_s \tag{4.9}$$

$$\frac{dV}{dI} = \sqrt{\frac{\eta kT}{q}}\sqrt{-\frac{d^2V}{dI^2}} + R_s \tag{4.10}$$

From Equations 4.9 and 4.10, R_s, η and I_s can be obtained. If we plot I from Equation 4.9 against $1/\sqrt{-d^2V/dI^2}$, η can be obtained from the slope of the plot and I_s from the intercept with $I = 0$. In addition, knowing the value of I_s, R_s can be obtained from the plot of Equation 4.7 against $1/(I + I_s)$ when $dV/dI = 0$ and η can be confirmed from the slope of the curve. An alternative method is to use the Equation 4.10. Again, the ideality factor η and series resistance R_s can be obtained from the slope and the interception with y-axis, respectively, of the plot of Equation 4.10 against $\sqrt{-d^2V/dI^2}$.

In the reverse bias region, the leakage current becomes more important [13] and then R_l can not be neglected in Equation 4.4. Following the same procedure as before but without neglecting leakage resistance the following expression is obtained [13]:

$$-\frac{d^2V}{dI^2}\Big/\left(\frac{dV}{dI}-R_s\right)^2=\frac{q}{\eta kT}\left[1-\frac{1}{R_l}\left(\frac{dV}{dI}-R_s\right)\right] \tag{4.11}$$

In usual circumstances, R_s is much smaller than dV/dI in most of the reverse bias region [13], so it can be neglected. Then, by plotting $\left(-d^2V/dI^2\right)/\left(dV/dI\right)^2$ against dV/dI, leakage resistance $R_l = 1/G_{leak}$ and ideality factor η can be estimated.

Following that procedure with our SBD and making use of additional curve fitting by comparing the Agilent ADS [20] DC diode model with the measured I/V curve, the values of table 4.1 from I/V measurements were obtained.

From I/V measurements						From S-Parameter measurements		
R_{diff} [Ω]	Resp.[A/W]	R_s [Ω]	I_s [μA]	η	G_{leak} [μS]	C_{j0} [fF]	C_p [fF]	L_s [pH]
273	14.5	3.0	105	1.20	460	33.1	2.9	33

Table 4.1: Extracted parameters of zero-bias Schottky diode

S-Parameters Measurements

In order to obtain the value of the junction capacitance C_{j0}, as well as the parasitic capacitances and inductances of the diode, S-parameters measurements in the W-Band (70 GHz - 110 GHz) were undertaken. To be able to extract the diode impedance, the effects of the CPW line where the diode is mounted (Figure 4.11) should be eliminated. To do so, a Thru-Reflect-Line (TRL) calibration [21] must be done. Following Agilent TRL calibration rules [21], 3 standards were designed as well as test structures in CPW with several gaps in order to measure transmission and reflection. These calibration standards are the so called Reflect standard, which is a CPW line ended in an open or short circuit, the Thru standard which is a CPW line with length equal to 2 times the Reflection standard length and the Line standard which is a CPW line with a length equal to the Thru standard plus $\lambda/4$ at calibration central frequency. Measurements were carried out with a vector network analyser from Anritsu with external headers to measure in the W-Band (Figure 4.14).

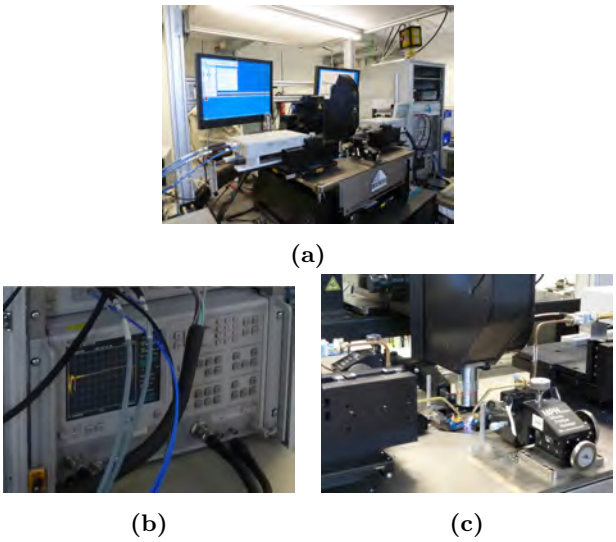

(a)

(b) **(c)**

Figure 4.14: Devices used for obtaining Schottky diode capacitances and inductances. (a) Whole set-up, (b) Anritsu Vector Network Analyser (c) Probe station.

Results are plotted in Figure 4.15 (S-Parameters) and in Figure 4.16 (input impedance). It can be noticed that the SBD has a clearly capacitive behaviour, with a relatively low value of the real part of the input impedance and a negative higher value of the imaginary part.

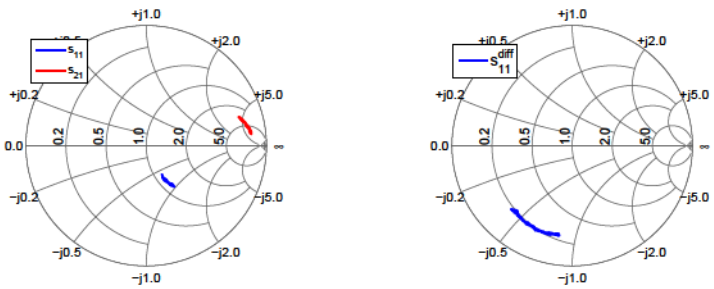

(a) (b)

Figure 4.15: Measured S-parameters of the SBD (80 GHz - 100 GHz). (a) s_{11} and s_{21}. (b) Differential s_{11} parameter.

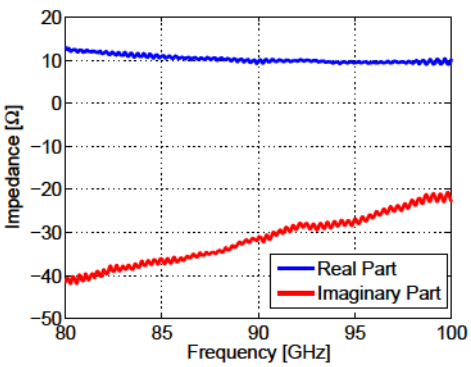

Figure 4.16: Measured input impedance of the SBD

Equivalent Circuit Model

Making use of both the low-frequency and high frequency measurements, with the diode parameters obtained from Section 4.2.2 and the other variables extracted by performing the curve fitting to the measured data, the equivalent circuit of Figure 4.10 is obtained, with the parameters shown on Table 4.1.

In order to validate the obtained equivalent circuit model, both measured and simulated data are plotted simultaneously. To carry on simulations, AWR Microwave Office [22] was used as circuit simulator. The results can be seen on Figures 4.17 and 4.18. It can be noted that the equivalent circuit model perfectly fits with the measured data.

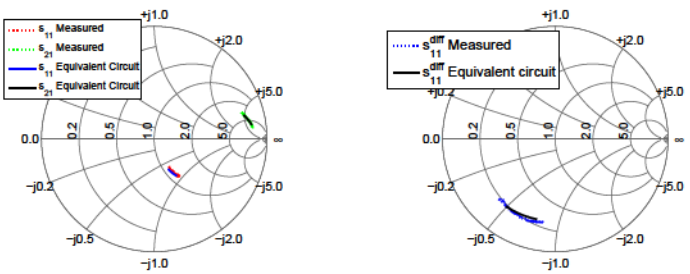

(a) (b)

Figure 4.17: Measured and simulated S-parameters of the SBD (80 GHz - 100 GHz). (a) s_{11} and s_{21}. (b) Differential s_{11} parameter.

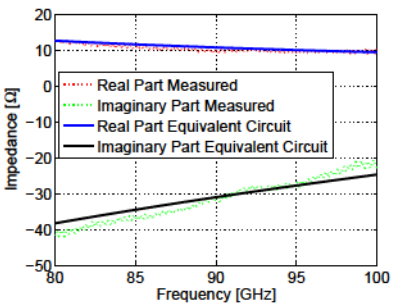

Figure 4.18: Measured and simulated input impedance of the SBD.

With the equivalent circuit model obtained in this section millimetre-wave circuits can be designed accurately. This equivalent circuit is a key step to develop the detector in the next section.

4.2.3 Receiver Design and Characterization

Once the SBD has been fully characterized, in this section it is integrated with other devices in order to obtain a compact receiver. The receiver is based on a SBD module, operating in the E-band (71 GHz - 76 GHz) and direct envelope detection is used, avoiding the need of a LO signal. The receiver module, shown in Figure 4.19, comprises a hyperhemispherical Si lens, a zero-bias SBD which is mounted on a planar antenna, and a 50 Ω low frequency impedance matching output transition. Since the output of the receiver is a 50 Ω CPW line, the inclusion of a video amplifier is possible. It can be either directly soldered to the line over FR-4 or connected by a SubMiniature version A (SMA) connector at the output of the SBD receiver.

Antenna Design

Three different antenna designs have been tested, analysing the receiver performance. Each one of them has been designed in order to maximize the power delivered from the antenna to the SBD at the millimetrewave carrier frequency range, matching the impedance of the antenna to the Schottky.

The receiver core is formed by the zero-bias Schottky diode presented in the previous section and the planar antenna. The interaction of the two elements at the carrier frequency (within the 71 GHz - 76 GHz frequency band) can be analysed with the high frequency band equivalent circuit presented in Figure 4.20.

In the design of the antenna, both gain (directivity × radiation efficiency) as well as the matching between antenna and active element (matching efficiency) need to be taken into account [23–28]. In the next paragraphs, we will discuss the impedance match at the carrier frequency through the optimization of the mismatching factor (M-factor), defined as the ratio between the power delivered to a load (P_L) and the maximum power available from a generator (P_{avs}) [29, 30]:

$$M = \frac{P_L}{P_{avs}} = \frac{4R_dR_a}{(R_a + R_d)^2 + (X_a + X_d)^2} \tag{4.12}$$

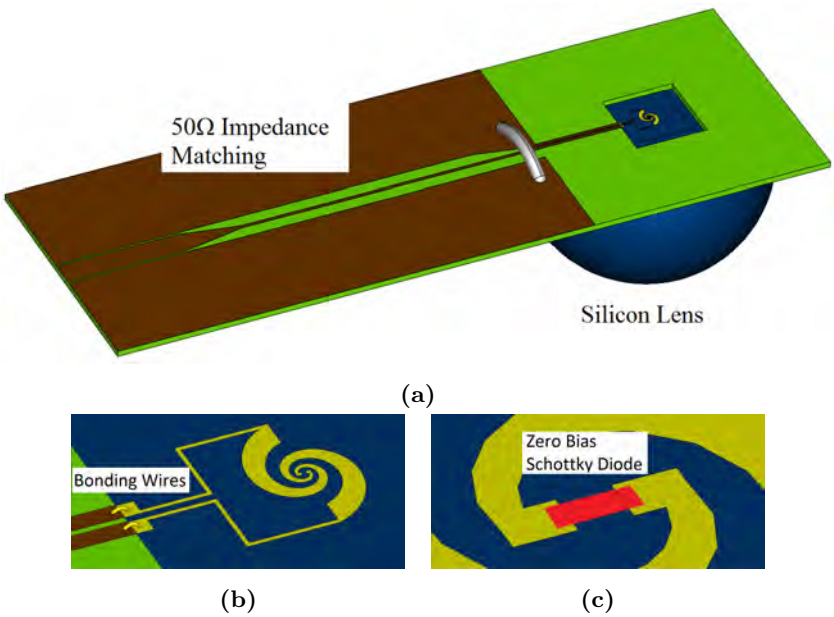

Figure 4.19: Schematic of the QO SBD Video Detector with log-spiral antenna. Materials: dark blue part is the silicon lens and silicon substrate where the gold (yellow part) planar antenna is grown, while the green part is FR-4 material and the brown part is copper. The bonding wires are included to connect gold lines over silicon to copper lines over FR-4 and a metallic wire is inserted to interconnect both ground planes of CPW line. The Zero Bias Schottky diode is epoxied in the middle of the antenna. (a) Complete QO SBD Video Detector 3D schematic. (b) Antenna zoom. (c) Schottky diode zoom.

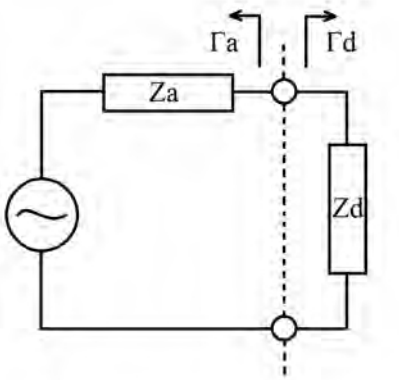

Figure 4.20: Higher band equivalent circuit of the SDB receiver

where $Z_d = R_d + \jmath X_d$ is the impedance of the diode (load) and $Z_a = R_a + \jmath X_a$ is the impedance of the antenna (generator) (see Figure 4.20). When M=1 all the available power from the source is delivered to the load and it can be obtained the well known conjugate matching condition which states that the maximum power transferred to the load is achieved when $Z_a = Z_d^*$ ($\Gamma_a = \Gamma_d^*$). Taking this into account, as well as the SBD impedance obtained in the previous section, an antenna with a $14.5 + \jmath 43.3\ \Omega$ input impedance at 76 GHz will be desirable (see Figure 4.21).

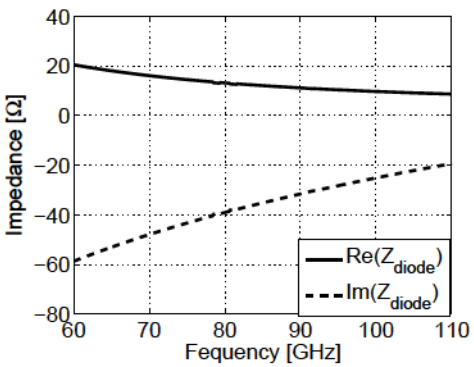

Figure 4.21: Input impedance of the SBD's equivalent circuit calculated in Section 4.2.2 in the E-Band (60 GHz - 90 GHz).

We have designed and fabricated three different planar antenna types: meander dipole [31], log-spiral and log periodic [32], to evaluate which one provides the best performance to the receiver module (see Section 1.2.2 for more information on these antennas). The three designs are depicted in Figure 4.22.

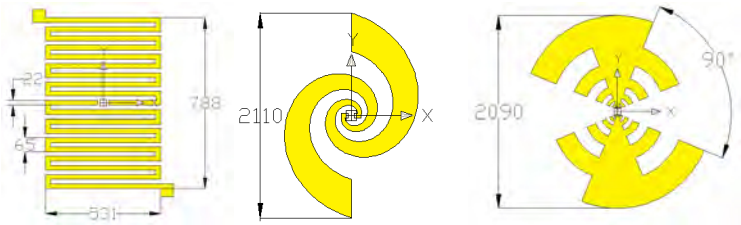

Figure 4.22: Antennas designed. (a) Meander Dipole, (b) Log-Spiral and (c) Log-Periodic. Units in µm.

The first one, shown on Figure 4.22a, is a meander dipole antenna which has been widely used in receiver designs due to its very high input impedance. This antenna has been demonstrated to be suitable for some devices such as photomixers [26, 27]. Since photomixers have an important capacitive part at its input impedance, which implies a loss of power because the M-factor decreases drastically, traditionally this capacitive part has been compensated including a RF filter with an inductive part [28] (see Section 3.2 for more information). However, this results in an increase on the complexity and dimensions of the receiver. The main idea with the meander dipole antenna design is to use it out of its main resonance [29], at lower frequencies, where it exhibits an inductive behaviour (very low real part and higher positive imaginary part of its input impedance). With such design, we expect to achieve direct conjugate matching between antenna and Schottky diode without additional elements. The dimensions of the antenna can be seen on Figure 4.22a, the input impedance in Figure 4.23 and the simulated mismatching factor is plotted in Figure 4.24. At 76 GHz the input impedance of the antenna placed over a semi-infinite silicon substrate is $9.3 + \jmath 42.8\ \Omega$ so an M-factor equal to 0.96 is expected. The main challenge with the meander dipole antenna is that it is a highly resonant antenna, so a small variation in the manufacture process would change its response. Moreover, we have designed the antenna to work out of its main resonance

so it is expected that the radiation efficiency would be lower. It has been observed that at main resonance the simulated radiation efficiency is closed to 70 %, while at 76 GHz it is 38 % (see Figure 4.25).

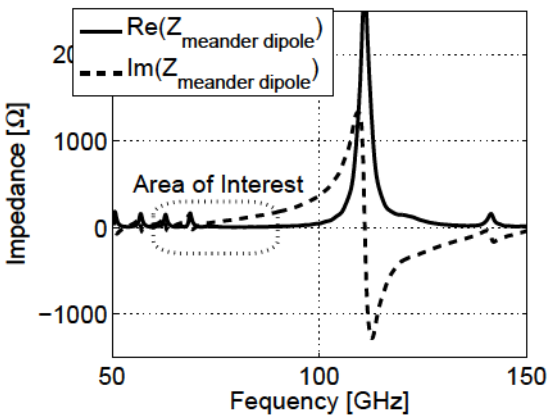

Figure 4.23: Input impedance of Meander Antenna.

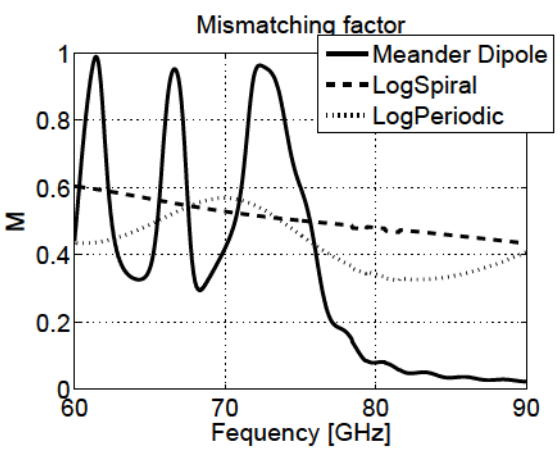

Figure 4.24: Simulated mismatching factor of the three planar antennas placed over semi-infinite silicon substrate.

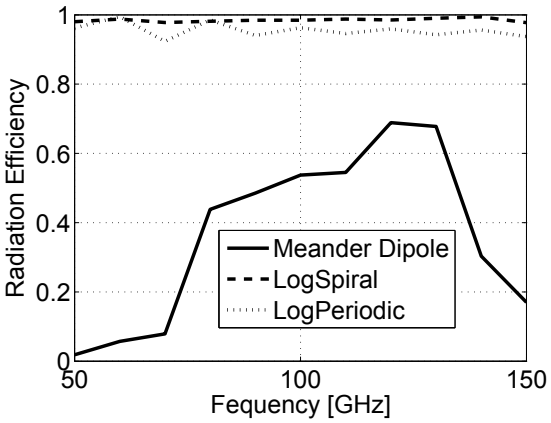

Figure 4.25: Simulated radiation efficiency of the three planar antennas placed over semi-infinite silicon substrate.

In order to compare the performance achieved by the meander dipole design, two broadband antennas were also proposed: a log spiral (Figure 4.22b) and a log periodic (Figure 4.22c). These are broadband antennas that will make full use of the broadband nature of the QO approach. The log-spiral design parameters are:

$$r_1 = ke^{\alpha\phi}, r_2 = ke^{\alpha(\phi-\delta)} \tag{4.13}$$

where r_1 and r_2 represent the inner and external radius of the spiral, respectively. In our particular design k =100 µm, $\alpha = 0.3$, $\phi = 5°$ and $\delta = 90°$. The log-periodic antenna was designed with $\tau = \sigma^2 = 0.5$, where τ is the ratio of the radial sizes of successive teeth, and σ is the size ratio of tooth and anti-tooth. For the sake of comparison, the designed mismatching factor within the E-Band for the three antenna designs are plotted together in Figure 4.24. As the M-factor for both broadband antennas is nearly constant around 0.5, a 3 dB improvement would be expected with the meander dipole antenna. But not only the mismatching factor is important. Also the radiation efficiency must be taken into account. In Figure 4.25 simulated radiation efficiency of the three antennas when placed over semi-infinite silicon substrate is depicted. It can be seen that while both broadband antennas have a radiation efficiency

close to 100 %, the meander dipole radiation efficiency is much lower. For the shake of comparison, the total efficiency is plotted in Figure 4.26. It can be seen that all the improvement made with the meander dipole in the mismatching factor is lost due to its low radiation efficiency value. In this particular case the obtained improvement is not as good as the one obtained in Section 3.2 of these Ph.D. dissertation. This is due to the fact that input impedance of the diode is closer to the input impedance of broadband antennas over silicon substrate in comparison with the photomixer case. So the improvement in the M-factor is not as big as the one obtained in the Section 3.2. Regarding the two broadband antennas, log-periodic have around 3 dB more total efficiency due to its lineal polarization.

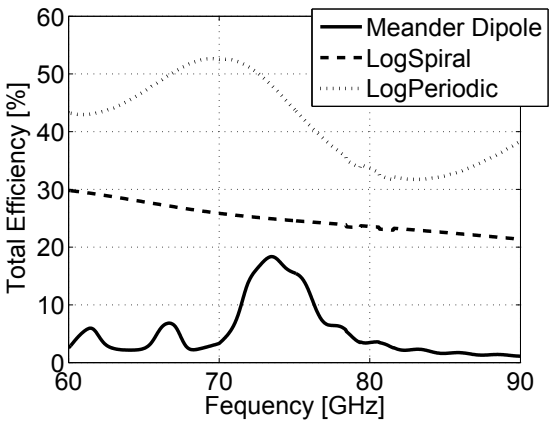

Figure 4.26: Simulated total efficiency of the three planar antennas placed over semi-infinite silicon substrate.

Hyperhemispherical Silicon Lens

Once the three planar antennas have been presented and designed, and the matching between the Schottky diode and the planar antennas has been studied, the next step is to maximize the directivity specifying a suitable dielectric lens in order to provide focusing capabilities and control surface waves [33]. This section discusses the design of the lens parameters to increase the receiver directivity.

Among the different types of dielectric lenses, we have selected a hyperhemispherical silicon one (Section 2.5) due to its good performance and its easiness of manufacture. Using an in-house program based on PO [34] (Section 2.5), we have analysed the silicon lens in order to obtain maximum directivity. The results are presented in Figure 4.27, where the simulated directivity obtained as a function of the lens diameter (D) and slab length (L) is plotted for the three antennas. For a lens diameter of 20 mm, a directivity of 19.7 dB is expected for the meander dipole while the broadband antennas are around 21.5 dB. In Figure 4.27b it can be seen how as we change the slab length, the directivity obtained changes as we move far away or closer to the lens focal point. For 20 mm diameter lens a slab length of 3.5 mm is observed to be the optimal one. A 20 mm diameter lens has been selected because it provides a high value of directivity while maintaining a reasonably low value of propagation losses. In addition, selecting a bigger lens results in an increase in the manufacturing complexity as well as in the overall receiver size.

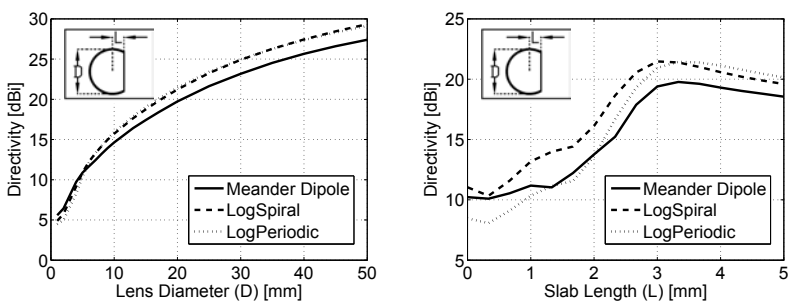

(a) **(b)**

Figure 4.27: (a) Simulated directivity as a function of the lens diameter (L=0.35*D/2), (b) Simulated directivity as a function of the slab length for a lens diameter of 20 mm.

CPS - CPW 50 Ω Transition

Once the optimized silicon lens dimensions and the three planar antenna designs have been specified, we now turn to the baseband frequency problem. Usually, designers are only concerned on the high frequency band that we have discussed previously, to maximize the power delivered from the antenna to the diode. However, it is also important to quantify the losses between the Schottky diode and the output in the overall receiver at the data frequency (which it is assumed to be around 1 GHz), especially in the case of a QO receiver module, in which no amplifiers can be located between the antenna and the SBD.

For this purpose, we required the measurement of the scattering parameters of the antenna on its location within the receiver module, which is the antenna grown over high resistive silicon, with an output CPS line, a bond wire to a CPS over FR-4, with the whole block mounted on the 20 mm diameter silicon lens. The schematic of the measurement set-up is provided for the Log-Spiral antenna in Figure 4.28, where it is indicated the used scattering parameter ports. The same set-ups were used in the case of the Meander Dipole and the Log-Periodic antennas. Detail of the manufactured antennas can be seen in the photographs of Figure 4.29.

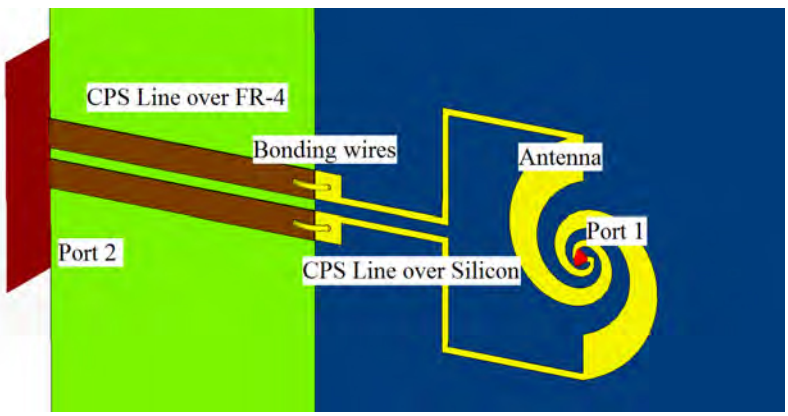

Figure 4.28: Schematic of s_{21} and s_{22} measurements. In the Port 1 the Schottky diode would be mounted. Antenna is made of gold and grown over high resistive silicon. Bonding wires are included to go from silicon substrate to FR-4 substrate.

(a) Meandered Dipole **(b)** Log-Spiral **(c)** Log-Periodic

Figure 4.29: Photograph of the manufactured antennas.

We have characterized the three receivers by measuring their s_{21} and s_{22} scattering parameters. While the s_{21} parameter allows us evaluate the losses along the antenna, the CPS line and the bonding wires, the s_{22} measurements quantify the mismatching between the CPS port (Port 2), and the Schottky diode. The most important results come from the s_{22} measurements with the Schottky diode mounted in Port 1, which indicate the need of a transition or impedance matching network between the antenna and the output leading to a video amplifier. Results can be seen on Figure 4.30a and 4.30b. In the three cases, a reflection coefficient of about 0.75 ($-2.5\,\mathrm{dB}$) is obtained at 1 GHz, so we are losing more than 3.5 dB due to mismatching between the port and the antenna + diode.

These data allowed us to design an optimal transition between the antenna CPS line to a CPW on FR4 Printed Circuit Board (PCB) in order to provide a $50\,\Omega$ output impedance to which a video amplifier can then be used, reducing the back reflections. The overall circuit consists on a CPS-CPW transition with a CPW stepped impedance matching network. It has been optimized with the full-wave electromagnetic simulator CST Microwave Studio [35]. An schematic of the designed transition can be seen on Figure 4.31. The simulated results after optimization can be seen on Figure 4.30c and 4.30d, where the best matching is achieved at 1 GHz ($s_{22} < -15\,\mathrm{dB}$).

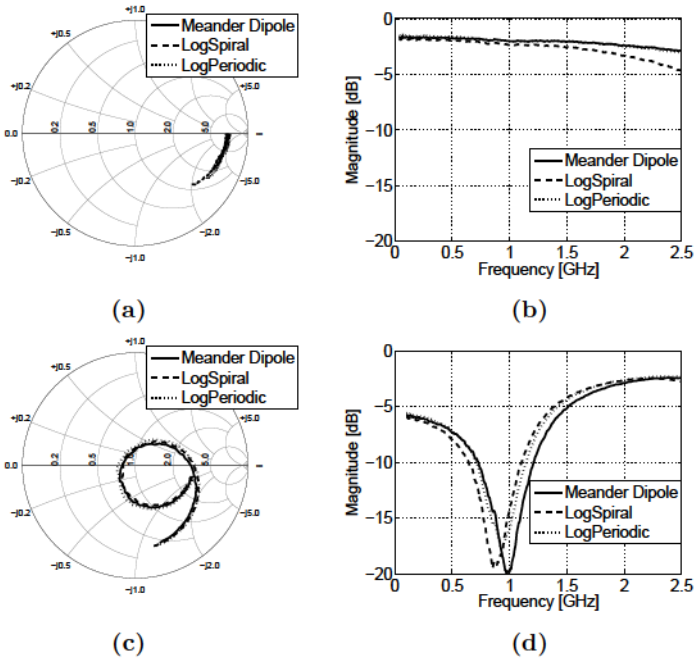

Figure 4.30: s_{22} measurements (100 MHz - 2 GHz). Before matching network: (a) Smith chart and (b) rectangular plot in dB. s_{22} simulations (100 MHz - 2 GHz). After matching network: (c) Smith chart and (d) rectangular plot in dB.

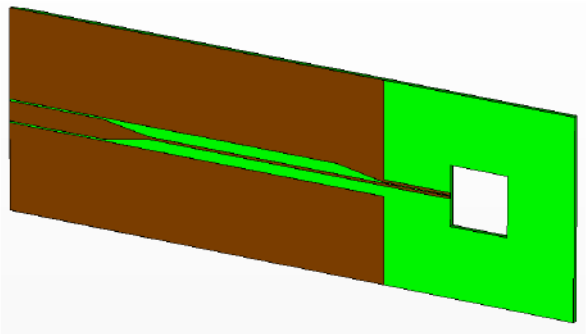

Figure 4.31: Designed CPS - CPW 50 Ω transition. Brown part corresponds to copper, green part to FR-4 substrate and the squared hole in the right is where the antenna with SBD and silicon lens are placed.

Receiver Assembly

The assembled QO SBD module is shown in Figure 4.32. The size of the uncased SBD module is approximately $20\times60\,\mathrm{mm}^2$, not including the SMA output connector and the lens (20 mm). The SBD chip was mounted on a high resistive silicon substrate, on which the antenna was fabricated. This substrate is then mounted on the hyper-hemispherical Si lens, in a face-up configuration so that the mm and sub-mm waves are introduced from the backside of the wafer in order to make the dielectric constant discontinuity between the planar antenna and the Si lens smaller and to make the electrical connection easier. The silicon lens (as mentioned before) was designed to have a point-focus for plane wave input signal, and it has no anti-reflection coating. The output is provided on an SMA connector.

(a)

(b)

Figure 4.32: Photograph of the receiver module: (a) Front view of the cased module showing the Si lens, and (b) Back view of uncased module, showing the Log-Spiral antenna on High Resistive Silicon (HR-Si) and the impedance matching transition to the SMA output connector.

Characterization of the Receiver Module

We have compared the performance of broadband versus resonant antennas comparing the responses of the Meander dipole, Log-Spiral and Log-Periodic receiver modules. They were measured over the entire E-band (60 - 90 GHz) using a frequency multiplier and frequency synthesizer (complete measurement set-up in Figure 4.33 and 4.34). A large aperture absolute power-energy meter from Thomas Keating Ltd. (Section 4.1.2) was used to estimate both total radiated power by placing it directly at the output of the E-band source as well as to estimate the power density in the detector plane (at 65 cm distance from the output horn).

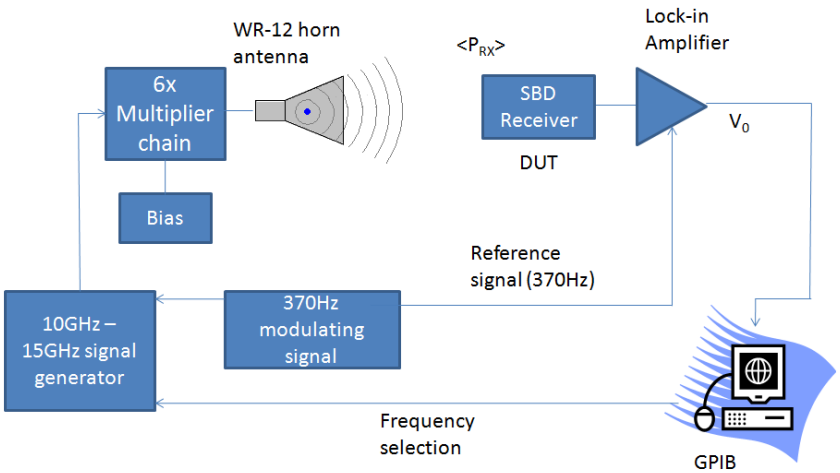

Figure 4.33: Responsivity measurement setup.

The responsivity ($\gamma_{V/W}$), as the signal produced by the power arriving to the SBD receiver, is shown on Figure 4.35. In order to estimate the responsivity of module, we used the simulated directivity of the three antennas. With this value we can now calculate the effective area of each of them:

$$\gamma_{V/W} = \frac{V_0}{P_{SBD}} = \frac{2\sqrt{2}V_0^{RMS}}{< P_{RX} > A_{eff}} \tag{4.14}$$

$$A_{eff} = \frac{\lambda_0^2}{4\pi} D \tag{4.15}$$

where V_0^{RMS} is the output Root Mean Square (RMS) voltage of the lock-in amplifier, P_{SBD} is the power arriving on the SBD receiver, $< P_{RX} >$ is the power density at the detector plane, A_{eff} is the effective area of the lens + antenna and D is the simulated directivity.

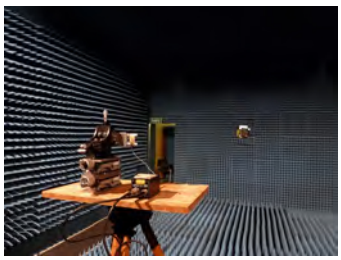

(a)

(b)

(c)

Figure 4.34: Devices used for responsivity and NEP receiver characterization. (a) Anechoic chamber, (b) Millimeter Wave Generator G4-143e (c) Pyramidal horn antenna.

The effective area normalized peak responsivity of the diode in the 71 GHz - 76 GHz band is found to be 814.4 V/W and 740.3 V/W for the meander dipole and the log spiral antenna respectively. The module with log-periodic antenna exhibits a responsivity value reaching 1278 V/W at 72 GHz, establishing this as the optimum frequency to operate a wireless link using this module. These values have to be compared with the highest achievable responsivity for these devices of 3958 V/W which can

be derived from low-frequency characterization (see Figure 4.13) under assumption that we have a perfect impedance match and there is no loss in parasitic series resistance. This difference from the highest achievable responsivity can be explained by the 3 dB losses due to mismatch between the log periodic antenna and the SBD (Figure 4.24) and 1.5 dB additional losses such as reflections in the silicon-air interface, misalignments in the measuring process, polarization, etc. On the other hand, the poorer behaviour of the meander dipole is attributed to a low radiation efficiency. As mentioned before, the meander dipole is working out of its main resonance, so a lower radiation efficiency is expected. Looking into the results and assuming that perfect matching is obtained at 74 GHz, 29 % (−5.37 dB) radiating efficiency is calculated, which is close to the 38 % simulated value obtained in the Section 4.2.3. This value is calculated by knowing that meander dipole is 814.4/3958 = 0.2058 (−6.87 dB) away from maximum responsivity value and estimating 1.5 dB additional losses such in the log-periodic and log-spiral cases. With such assumption −5.37 dB (−6.87 dB + 1.5 dB) radiation efficiency is calculated. With respect to the broadband antennas, we have used a log-periodic design on the wireless transmission experiment since we expect to have a response 3 dB above the log-spiral due to the circular polarization losses on the log-spiral receiver module.

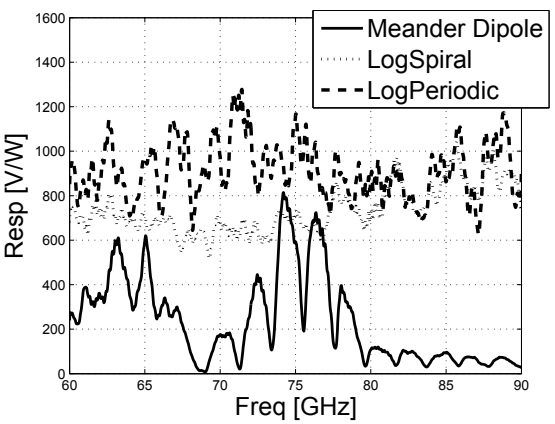

Figure 4.35: Responsivity spectra measured over the E-band for the Meander Dipole, Log-Spiral and Log-Periodic receiver modules.

To observe the broadband behaviour of both broadband designs (log-periodic and log-spiral receiver modules), measurements in the F-Band (90 GHz–140 GHz) were also carried out. Results of responsivity of both modules from 60 GHz to 140 GHz are plotted in Figure 4.36. Regarding the NEP, a value of 2.5 $pW/\sqrt{Hz}$ is estimated taking into account only the thermal noise [3].

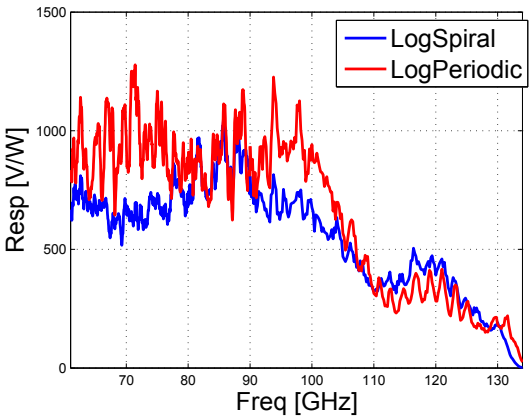

Figure 4.36: Responsivity spectra measured over the E-band and F-Band for the Log-Spiral and Log-Periodic receiver modules.

The observed results are in the order of previous reported quasi optical SBD receivers. In [8] a typical responsivity value of 500 V/W in the 100 GHz - 1 THz is presented, while in [36] a peak of 1000 V/W at 300 GHz is obtained. The main advantage in our designs is that they don't have any amplifier nor bias to the diode, so no external power is needed to make them work.

4.2.4 Wireless Link at 72 GHz

For realization of an ultra-wideband photonic E-band transmitter [37], [38], comprising a flat frequency response over the 71 GHz - 76 GHz frequency band, novel InGaAs(P)/InP-based 1.55 µm double mushroom-type waveguide High Speed Photo Diodes (HS-PDs) were developed and fabricated using conventional photolithography, selective wet-chemical as well as dry-chemical etching and metal evaporation.

In detail, the active HS-PD structure features a partially p-doped, partially non-intentionally doped InGaAs core layer. The active absorbing core is additionally wet-chemically under-etched, forming a mushroom shape structure, to overcome the trade-off between the junction capacitance and the series resistance [39]. For efficient fibre-chip coupling considering the coupling loss of $\sim 1.7\,\mathrm{dB}$ at the chip facet, a mushroom-type approach is applied for the InGaAsP/InP-based Passive Optical Waveguide (POW). This topology provides low-loss optical mode propagation up to the opto-electrical conversion within the active HS-PD section utilizing vertical mode coupling in the order of 90 %. Based on Beam Propagation Method (BPM) analyses, an absorption rate larger than 70 % within the $\sim 20\,\mu\mathrm{m}$ active photodiode length was achieved. The pioneer approach relating to the integration of a mushroom-type POW and further details were already reported in [40].

For characterization, a coplanar $50\,\Omega$ RF probe was used to measure the RF power levels generated by the HS-PD with a tapered Grounded Coplanar Waveguide (GCPW) circuitry connected to GCPW bond pads, which are matched to a $50\,\Omega$ output impedance. A microscope photograph of the fabricated HS-PD in-line with a tapered single-mode fibre for optical coupling and a coplanar RF probe for electrical coupling is presented in Figure 4.37.

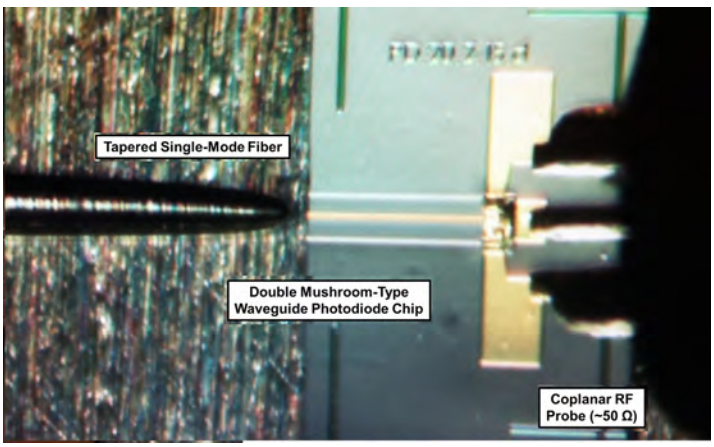

Figure 4.37: Top view of the fabricated 1.55 µm double-waveguide HS-PD in-line with a tapered single-mode fibre and a coplanar RF probe

Applying a driving voltage of -8 V to the uncooled operated HS-PD without an anti-reflection coated facet, an output RF power exceeding 0 dBm (1 mW) is achieved at a frequency of 72.8 GHz and a 16 mA photocurrent level. Additionally, high linearity of the HS-PD speaks in its favour since no saturation of the output power increasing quadratically with the photocurrent is identified up to the photocurrent of 16 mA. For safety reasons, the HS-PD was only tested up to 16 mA in order not to thermally destroy the HS-PD without additional cooling. Maximum photocurrent levels for safe and cooled operation are expected to exceed 16 mA. Besides the achieved power levels and the high-linearity behaviour, the HS-PDs also deliver an excellent frequency flatness of $< \pm 0.5$ dB and a return loss of >20 dB along the entire 70 GHz frequency band.

For validating the fabricated high-power HS-PD and the SBD module with the log-periodic antenna, a Radio-over-Fibre (RoF) system experiment has been set-up (Figure 4.38).

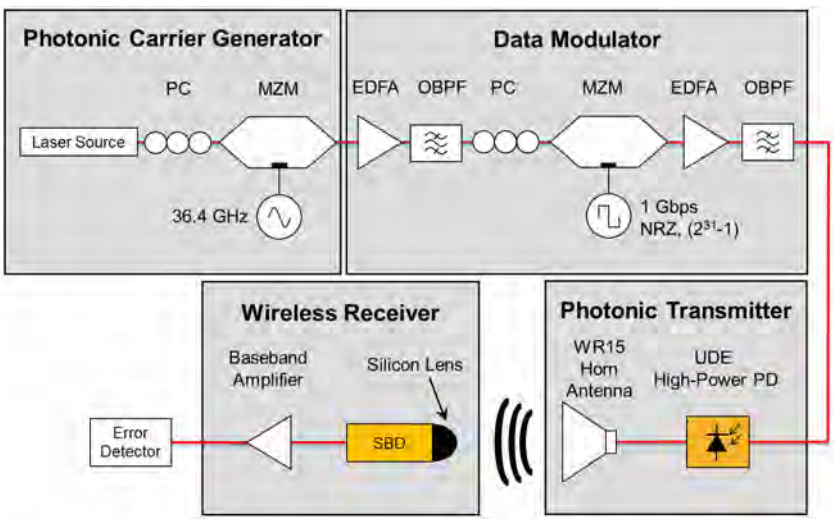

Figure 4.38: Schematic of the 71 - 76 GHz RoF set-up for validating the high-power HS-PD and SBD module.

In this wireless transmitter unit, the RF carrier in the frequency range of 71 GHz - 76 GHz is generated by Double Side-Band Suppressed-Carrier (DSB-SC) optical modulation [41]. This is achieved by modulating the single wavelength from a 1550 nm external cavity laser with a single-drive Mach-Zehnder Modulator (MZM) biased at V_π , i.e. the MZM is operated at the Minimum Transmission Point (MTP) [41]. Hence, the frequency of the driving LO is doubled and consequently, a LO frequency of $f_{LO}/2 = 36.4$ GHz is used for generating a wireless carrier frequency of 72.8 GHz.

The generated optical mm-wave signal is then coupled to a second MZM which is biased at quadrature and modulated by a 1 Gbit/s Non-Return-to-Zero On-Off-Keying (NRZ-OOK) data signal. For our experiments, we used a pseudo-random binary sequence with a word length of $2^{31} - 1$. An Optical Band-Pass Filter (OBPF) is used to remove Amplified Spontaneous Emission (ASE) noise from the utilized Erbium Doped Fibre Amplifier (EDFA) and an optical attenuator is used for controlling the optical power (not shown in Figure 4.38). After fibre-optic transmission to the wireless RoF transmitter via standard Single Mode Fibre (SMF), the 1 Gbit/s signal is o/e-converted using the high-power 1.55 µm HS-PD described previously. As shown in Figure 4.37, a coplanar ground-signal-ground RF probe is used for electrical coupling. Additionally, an external bias-tee is employed to separate the RF signal from the bias voltage applied to the HS-PD. Thereafter, a coax-to-WR15-transition connects the bias-tee to a standard WR15 horn antenna with about 20 dB gain, where the RF signal is transmitted.

In the wireless receiver unit, the 72.8 GHz wireless signal is converted back into a baseband data signal using the Silicon lens integrated SBD module. This 1 Gbit/s baseband signal is further amplified by a Low Noise Amplifier (LNA) with 40 dB gain. For performing the Bit Error Rate (BER) measurements, the power into the HS-PD is varied. Figure 4.39 shows the measured BER versus the optical power launched into the high-power HS-PD. This figure also shows the eye diagram of the 1 Gbit/s transmitted signal, as applied to the data modulation MZM, as well as the received signal, amplified by the baseband amplifier after direct RF to baseband conversion in the Schottky diode, at the output SMA connector. The DC and RF (at 72.8 GHz delivered to 50 Ω) responsivities of the non-anti-reflection-coated HS-PD chip used in the

experiment were 0.31 A/W and 0.1 A/W, respectively. The responsivity of the antenna-integrated SBD module with the Silicon lens is 1326 V/W. The wireless carrier frequency and data rate were 72.8 GHz and 1 Gbit/s respectively.

As it can be seen in Figure 4.39, the eye of the received signal for the wireless transmission distance of 6 cm is clearly open. This is also reflected by the BER measurements, indicating "error-free" transmission with a BER $< 2 \cdot 10^{-10}$. No error floor is observed from Figure 4.39, i.e. the wireless distance can be extended. This is an indication that the system performance is noise limited by distance, and that additional RF amplifiers would be required to achieve distances in the meter or even kilometre range. Additionally, the transmitter power can also be improved incorporating thermal control to the photodiode.

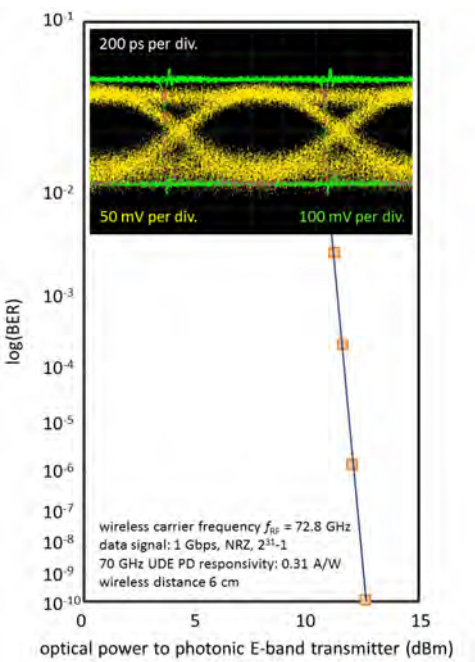

Figure 4.39: BER vs. optical power into the HS-PD and eye diagram of the transmitted (green, 100 mV/div) and received (yellow, 50 mV/div) 1 Gbit/s NRZ-OOK signal. Optical input power to the photonic transmitter was measured at the tapered single-mode fibre output.

4.3 Plasma-Wave Field-Effect-Transistor Detector Using Broadband and Active Planar Antennas

In this section, first steps towards the implementation of plasma-wave FET rectifiers detectors in CMOS technology working at 100 GHz and 100 GHz are presented. Two types of FET detectors are designed: single N channel MOSFET (N-MOSFET) detector with a bow-tie antenna with the possibility of including a silicon lens for increase directivity and differential N-MOSFET detector with differential patch antenna. Both designs are analysed and pros and contras of each of them are commented. Finally, different prototypes of both of them working at 100 GHz and 300 GHz with different transistor channel lengths are manufactured and first results are obtained.

This section is organized as follows. First, a brief introduction to plasma-wave FET rectifiers detectors is carried out. Some historical background, as well as state-of the art results are commented. In addition, a theoretical analysis is done and the main parameters are explained. Then, both topologies are analysed and optimised antennas are designed. Finally, different prototypes are manufactured with two foundries and preliminary results are obtained and commented.

4.3.1 Introduction to CMOS Plasma-Wave FET Detectors

Detectors based on III-V semiconductors, particularly the GaAs and InGaAs alloys, dominate the fields of heterodyne and direct detection at millimetre and THz waves. Improving the performance of these room temperature detectors is a challenge, but improvements continue to be made. Only in the last few years has the potential of a disruptive competing technology, based on silicon FETs, been recognised. Continuous improvements in CMOS technology have enabled the necessary few hundred nanometre scale, and smaller, structures to be realised. A number of groups have begun their research in this field and the test results from this relatively immature detector field are impressive in terms of response, noise and frequency coverage. Prototypes of a range of THz devices such as frequency multipliers, Schottky diodes and novel FET detectors have all been realised [42].

To understand the disruptive impact of silicon technology, one needs to note that the basic wafer material for III-V devices is expensive, and the device area are minimised to maximise yield. Completed detectors are soldered or epoxied to an antenna structure, and a separate pre-amplifier is then connected. Large area arrays are thus composed of devices interfacing with individually antennas, the latter being in planar or feed horn form. In comparison, the use of commercial CMOS technology allows integrating in only one silicon wafer all needed for a staring imaging array. This includes the planar antennas, detector devices, pre-amplifier components and connections to signal processing circuitry. Once the non-recurring foundry investment has been made, the processing costs and raw materials are comparatively inexpensive, offering a revolutionary alternative approach to detectors, detectors arrays and THz cameras.

The mechanism on which FETs operate is plasmonic mixing in the transistors' channels which was first considered and suggested as a rectifying detection principle by Dyakonov and Shur [9]. Recently, FET square-law power detectors at THz frequencies have been demonstrated [43] and the first monolithically integrated CMOS THz focal-plane array has been designed and validated [44]. In 2006, the first tentative experimental quantification of the responsivity and NEP at 700 GHz in commercial silicon MOSFET was done [45]. This represented a major milestone for the recognition of the practical potential of this detector concept. In plasma-wave THz/sub-THz detectors, the working frequency is much higher than the transit-time-limited cut-off frequency of the transistors. The performance of the MOSFETs as detectors profits from the low noise resulting from the zero source-drain-bias operation [46].

At THz/sub-THz radiation, standing plasma waves are developed in the transistor channel, which is associated to a very high, resonantly enhanced responsivity of the devices at these frequencies. HEMTs display this resonant behaviour pronouncedly at low temperature [47]. Silicon CMOS transistors at room temperature, on the other hand, usually do not because the plasma waves decay on a length scale of a few ten nanometer, shorter than or comparable to FET's gate length [44, 47]. Standing waves cannot build up or are weakly developed in this non-resonant case. Still, mixing is found to be effective enough even in these CMOS transistors resulting in a suitable comparison with the established

THz power detectors (Section 4.1.2). The response signal can be given as:

$$\Delta u = \frac{e \cdot u_a^2}{4 \cdot m_e \cdot s^2} \left[1 - \frac{1}{\sinh^2 Q + \cos^2 Q} \right] \tag{4.16}$$

where e is the electron charge, u_a is the THz voltage on the gate relative to the source, m_e is the effective mass of the electron, s is the plasma wave velocity and Q is the ratio of the gate length to the characteristic length of the voltage decay from source to drain. After some algebraic operations, in [48], the maximum value of the response signal is given as:

$$\Delta u = \frac{e \cdot u_a^2}{4 \eta k T} \tag{4.17}$$

where η is a parameter depending on the sub-threshold slope of the channel conductivity and k is the Boltzmann constant. From the previous expression, the responsivity that relates the detected signal to the THz power can be obtained. It can be seen that, ideally, the responsivity may become exponentially large below threshold. For actual conditions this is not realistic since it depends on the antenna coupling and on the loading effects. Thus, as the input impedance of the read-out circuit becomes smaller, due to a simple dividing effect, the detected signal will decrease. A similar effect can be extracted from the imaginary part of the input impedance since a small capacitance can lead to large RC constants. In this way an increase in the modulation frequency can also lead to a decrease in the detected signal.

Plasma-wave-based rectification in the non-resonant limit can also be understood to be an extension of the self-mixing resistive square-law MOSFET power detector circuit [44], as shown in Figure 4.40. It is similar to a FET resistive mixer [15] where a capacitor C_{gd} is included in order to facilitate self-mixing ($v(t)_{RF} = v(t)_{LO}$). A planar antenna is used to concentrate the THz/sub-THz radiation into the transistor, increasing the effective cross-section. Thus, the voltages at each port can be written as:

$$v_{gs}(t) = v_{RF}(t) + V_g \tag{4.18}$$

$$v_{ds}(t) = v_{RF}(t) + V_{RF} \sin \omega t \tag{4.19}$$

As the device is operated in the linear region, the drain current is obtained through the multiplication between the voltage and the transconductance as:

$$i_{ds}(t) = v_{RF}(t) \cdot g_{ds}(t) \tag{4.20}$$

The transconductance can be written as:

$$g_{ds}(t) = t\frac{W}{L} \cdot \mu \cdot C_{ox} \cdot \left[\frac{v_{RF}(t)^2}{2} + v_{RF}(t) \cdot (V_g - V_{th}) \right] \tag{4.21}$$

where W and L are the width and length of the device channel, C_{ox} is the gate oxide capacitance, μ is the electron mobility and V_{RF} is the amplitude of the RF signal.

By taking the DC term in the previous expression it can be seen that the read-out current is given:

$$I_{ds} = \frac{W}{L}\mu C_{ox}\frac{V_{RF}^2}{4} \tag{4.22}$$

The read-out voltage of the detector can be obtained by multiplying the dc current by the channel resistance. This can be written, whenever the drain-to-source voltage is in the linear region, as:

$$V_{ds} = \frac{I_{ds}}{G_{ds}} = \frac{V_{RF}^2}{4(V_g - V_{th})} \tag{4.23}$$

From this expression the voltage responsivity can be obtained as:

$$R_v = \frac{V_{ds}}{P_{in}} = \frac{\frac{V_{RF}^2}{4(V_g - V_{th})}}{\frac{V_{RF}^2}{R_{in}}} = \frac{R_{in}}{4\,(V_g - V_{th})} \tag{4.24}$$

The maximum responsivity is obtained in the sub-threshold region since the detection current is generated across a larger internal DC resistance. In Si CMOS technology, on-chip amplification close to the detector prevents external capacitive loading avoiding both the reduction of the responsivity and the reduction of the bandwidth.

Finally, the NEP defined as the power at which the signal to noise ratio is unity for a detector time constant of 1 s. It is given as the ratio between the spectral power density at the drain output and voltage responsivity.

$$NEP = \frac{\sqrt{N_0}}{R_v} \tag{4.25}$$

When maximum responsivity is obtained in the sub-threshold region, minimum NEP is not usually achieved since it requires a higher V_g bias point for lower channel resistance leading to the minimum noise power density.

In a resistive mixer, the transistor has to be biased to operate in the Ohmic region. The channel of a FET, at low drain-to-source voltages, is a good approximation of a linear resistor. The resistance can be modulated by applying a LO voltage to the gate. This voltage changes the depth of the depletion region under the gate and therefore the resistance of the channel. FET resistive mixers can achieve low conversion loss with low LO power [15]. Another advantage of resistive mixers is that RF input and IF output impedances are fortuitously usually around 50 Ω [15], so antennas can be designed to be matched to typical 50 Ω values and small losses are expected due to mismatch between the antenna and the active device. For accurate antenna design, the RF input impedance and the IF output impedance must be measured to minimize losses, as will be explained in the next section.

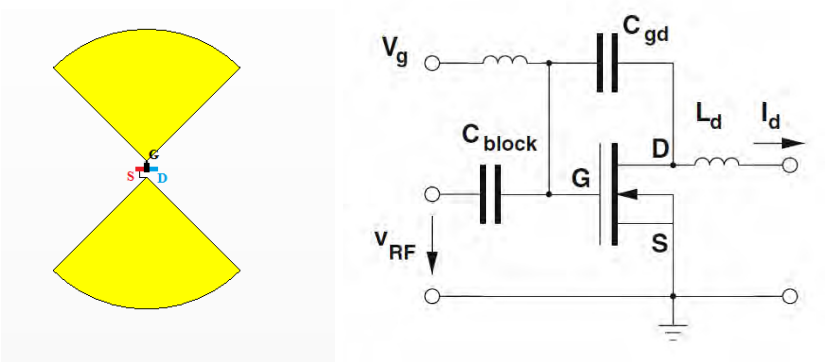

(a) **(b)**

Figure 4.40: Single MOSFET detector: (a) planar bow-tie antenna with integrated FET and (b) circuit implementation of a self-mixing square-law MOSFET RF power detector circuit.

At THz/sub-THz frequencies, the received field by an integrated antenna is guided to the source/gate contacts of the FET generating a strongly damped plasma wave which propagates from the source contact into the channel. The plasma wave is associated with an oscillating forward electric field which drives carriers along the channel, while, at the same time, the carrier density and, with it, the conductance are modulated by the gate voltage. The current hence depends (to the lowest order) quadratically on the oscillating electric field which implies a time-independent current contribution (rectification). As the mixing process occurs locally within the channel at any point reached by the plasma wave, the rectification process is not frequency-limited by the carrier transit time, which explains why one can detect signals at frequencies up to one hundred times higher than the cut-off frequency of the FETs, which nowadays is lower than 100 GHz [46]. Equivalent circuit at these frequencies is not the same as quasi-static one shown in Figure 4.40 and a distributed model must be take into account [44]. Advanced equivalent circuit of these detectors and responsivity and NEP estimations can be found in [3, 49].

Plasma-Wave FET Detectors State-of-the-Art

Several groups are developing THz/sub-THz detectors based on this relatively new technology. For instance, the group from Dr. H. G. Roskos at the Johann Wolfgang Goethe-Universität in Frankfurt am Main, Germany, have developed detectors based on patch antennas working at room temperature achieving 350 V/W responsivity at 595 GHz, 30 V/W at 2900 GHz and 5 V/W at 4100 GHz with a NEP of 42 pW/$\sqrt{\text{Hz}}$ at 595 GHz and 487 pW/$\sqrt{\text{Hz}}$ at 2900 GHz without amplification [50].

The group of Prof. Wojciech Knap in France has designed a broadband THz detector focal plane array with a responsivity value of 5.3 kV/W and NEP of 8 pW/$\sqrt{\text{Hz}}$ at 295 GHz and 55 V/W and 900 pW/$\sqrt{\text{Hz}}$ at 1.05 THz [51].

Wuppertal University group in Germany presented a focal plane array working at 650 GHz with a responsivity equal to 80 kV/W and NEP of 300 pW/$\sqrt{\text{Hz}}$ [44] and it is improved by the use o a silicon lens in [52], showing an improvement of a factor 2 in both responsivity and NEP. Authors also developed a 1 k-Pixel video camera for imaging in 65 nm CMOS [53]. The obtained responsivity is 140 kV/W (with amplification) and 100 pW/$\sqrt{\text{Hz}}$ at 856 GHz. The working frequency range is 790 GHz - 960 GHz.

It can be seen that results are really promising, even taking into account that this detector technology is relatively immature.

4.3.2 Sub-THz CMOS Plasma-Wave FET Detector Design and Characterization

From the antenna point of view only two parameters can be optimized in order to maximize the responsivity of the detector: the radiation efficiency, ϵ_{rad}, and the matching efficiency, M. The total efficiency can then be defined as the product of these two efficiencies and the polarization efficiency, ϵ_{pol}:

$$\epsilon_{tot} = \epsilon_{rad} \cdot M \cdot \epsilon_{pol} \tag{4.26}$$

This efficiency expresses how far the system deviates from the ideal detector performance. Maximizing ϵ_{tot} will enhance the performance of the detector and it is the key factor that we have used in the design of optimised planar antennas.

Two different topologies of detectors have been designed. The first, broadband, device consists of a bow tie antenna and a single resistive self-mixing N-MOSFET, as shown in Figure 4.40. The second, resonant, 300 GHz detector consists of differential patch antenna and a N-MOSFET pair in a differential circuit configuration: Figure 4.41.

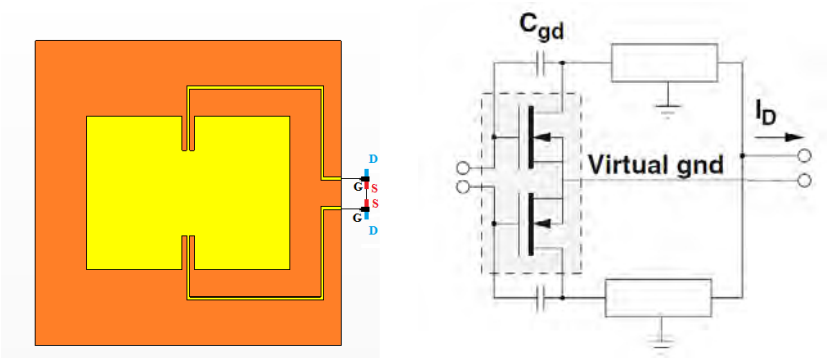

(a) **(b)**

Figure 4.41: Differential MOSFET-pair detector: (a) differential patch antenna and two FETs and (b) circuit implementation of a self-mixing square-law differential MOSFET RF power detector circuit.

Single NMOS Detector

With this configuration, low frequency dependence is expected because the bow-tie antenna has been designed to provide around 50 Ω source impedance when placed over a silicon substrate. However, since no ground plane is included, it is expected that its radiation pattern will be adversely affected by substrate waves in the silicon wafer. The inclusion of a hyperhemispherical silicon lens is currently under study in order to avoid such undesired waves and to increase the directivity of the antenna. Different detecting N-MOSFETs have been designed with channel lengths in the range 130 nm to 250 nm in order to study the effect on the frequency dependence and responsivity.

The bow tie antenna is a particular case of frequency independent antennas. Its input impedance is approximately given by [32]:

$$Z_{in} = \frac{60\pi}{\sqrt{\epsilon_r}} \approx 55\Omega \text{ (for silicon)} \tag{4.27}$$

Since this antenna has no ground plane, it is expected that radiation predominantly propagates into the high dielectric constant silicon substrate [33]. In order to reduce the effect of surface waves, as well as to increase the directivity of the antenna [33], a silicon hyperhemispherical lens will be included on the reverse of the silicon wafer. A typical lens of 10 mm diameter and 6.65 mm thickness is used for simulation purposes: Figure 4.42. The corresponding numerical predictions can be seen in Figure 4.43. A directivity value of 24 dB is obtained maintaining a reasonable value of radiation efficiency (77 %).

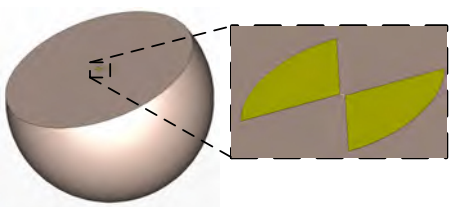

Figure 4.42: Schematic of the bow tie antenna with an underlying 10 mm diameter and 6.65 mm thickness hyperhemispherical silicon lens.

Differential NMOS Detector

In this second configuration, a differential patch antenna and two N-MOSFETs in a differential circuit topology have been designed. Patch antennas have many unique and attractive properties: low in profile, light in weight, compact and conformable in structure, and easy to fabricate and to be integrated with solid-state devices [32]. Differential patch antennas [54] have received great attention during the last years for their use in radio systems.

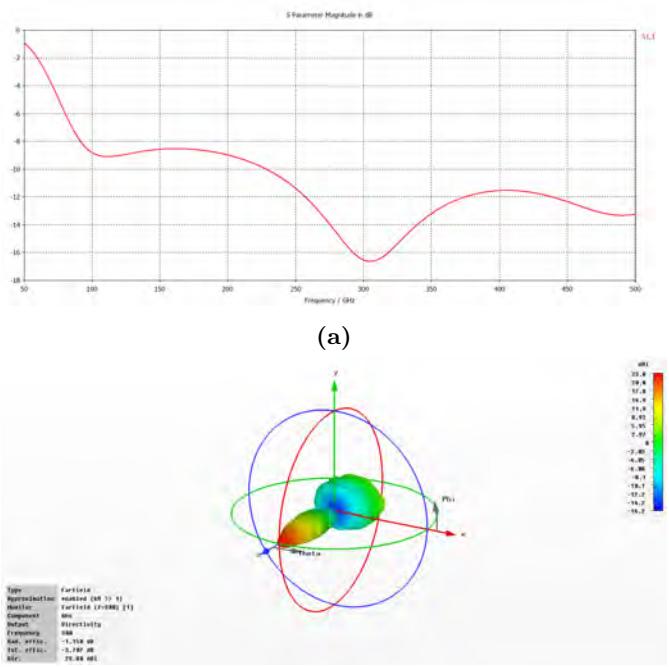

(a)

(b)

Figure 4.43: (a) Return losses of the bow tie antenna referred to 50 Ω and (b) radiation efficiency and 3D radiation pattern at 300 GHz.

This approach is expected to improve the overall behaviour because it can take advantage of both positive and negative signal cycles. In addition, differential patch antennas have a virtual ground on the symmetry axis. This removes the need for connecting the ground of the transistors with the antenna ground plane. As consequence, the parasitic effect caused by an interconnect is eliminated. The differentially-driven microstrip antenna can be treated as a two-port network. Its input impedance is given by [54]:

$$Z_d = 2(z_{11} - z_{21}) = 2(z_{22} - z_{12}) \tag{4.28}$$

And the reflection coefficient:

$$\Gamma_{in} = s_{11} - s_{21} = s_{22} - s_{12} \tag{4.29}$$

when $s_{11} = s_{22}$ and $s_{21} = s_{12}$. Full theoretical analysis of this kind of antenna can be found in [54].

Results of a differential patch working at 300 GHz can be seen on Figure 4.44.

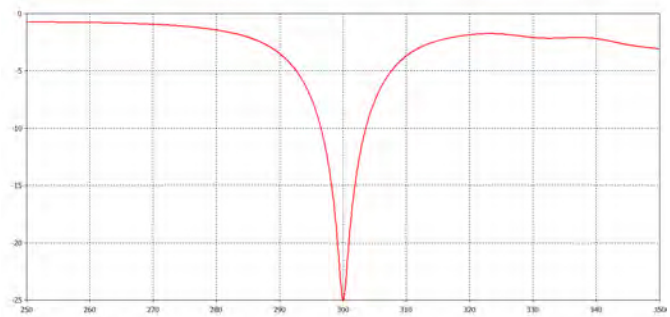

(a)

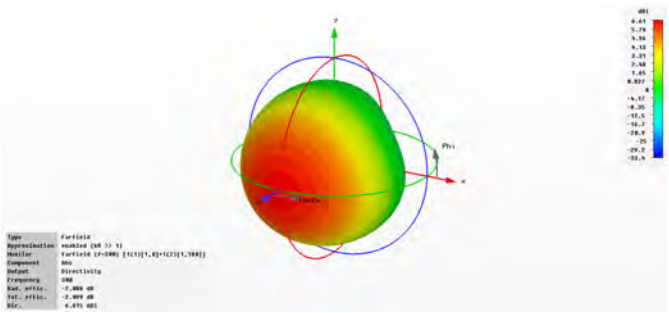

(b)

Figure 4.44: (a) Return losses of the differential patch antenna referred to 50 Ω. (b) Radiation efficiency and 3D radiation pattern at 300 GHz.

Detector Manufacturing

Two different foundries have been considered for the manufacturing of the prototypes. The main differences between them lies in the thickness of the metal and dielectric layers and the number of them, as well as material characteristics. An example of a typical CMOS manufacturing process can be seen on Figure 4.45.

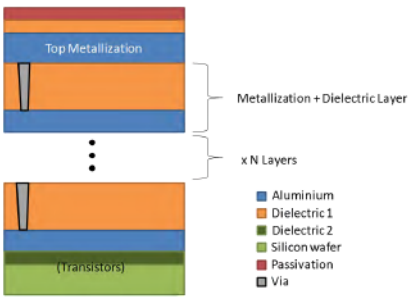

Figure 4.45: Example of a typical CMOS manufacturing process. The number of layers, dielectric constant, and thickness are foundry dependent.

For bow-tie designs, the lowest number of metallization + dielectric layers is used in order to reduce losses. On the other hand, in the design of the patch antennas, the ground plane is included in the metallization layer just above the dielectric 2 layer of Figure 4.45. In order to increase the radiation efficiency of the patch antenna, the maximum number of dielectric layers is included and aluminium layers in the substrate are removed. The metal patch is printed on the top metallization layer. It is well known that the thicker the dielectric layers are, the higher the radiation efficiency is. CMOS technology processing does not readily deliver a layer thickness, h, greater than 20 µm. In our particular case, h is restricted to be below 15 µm so patch antenna radiation efficiencies lower than 60 % are expected. Since this antenna has a ground plane, no dielectric lens is necessary and a reasonably value of directivity is expected. Figure 4.44 shows the predicted results from a design optimised for one of the two foundries: this exhibits good performance in terms of both the return loss and the radiation efficiency (60 %).

The mask top view of the manufactured detectors is shown in Figure 4.46. The smaller detectors are different patch antennas and bow-ties designed for 300 GHz detection. Three detectors for 100 GHz are also included (bigger patch, bow-tie and arc-ended bow-tie). These have also been optimised via the methods described above. In addition, a photograph of the detail of each type of antenna with the bonding wires to bias the transistors and get the output signal can be seen on Figure 4.47.

Preliminary measurements were undertaken in Rutherford Appleton Laboratories in the UK. To do so, either a multiplier chain or a photomixer based source were used. The detector was illuminated with such sub-millimetre wave source and best results show a voltage responsivity of 1.53 V/W for the 100 GHz bow-tie at a frequency of 90 GHz and 0.91 V/W for the 100 GHz patch at the same frequency. These results are still far away from the ones presented in the Section 4.3.1 and further investigation must be done.

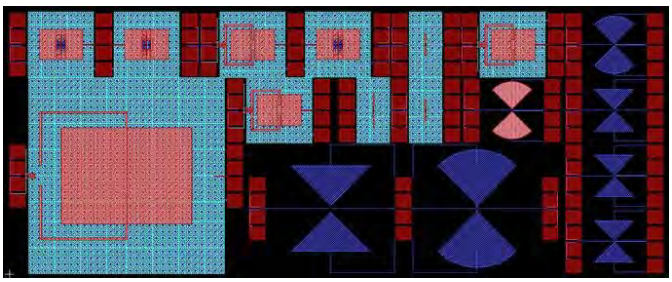

Figure 4.46: Mask top view of the manufactured detectors. Different colours represent the different metallization layers.

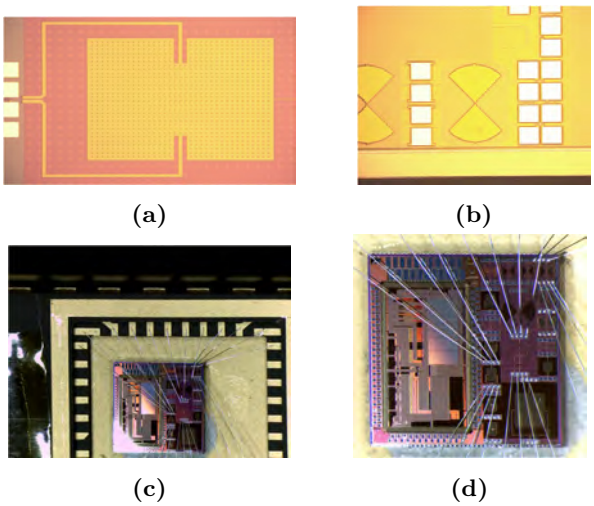

Figure 4.47: Photographs of the manufactured CMOS FET detectors. (a) Patch detail, (b) Bow Tie detail, (c) Bonding wires and (d) Bonding wires detail.

4.4 Conclusions

In this chapter, two of the most important THz/sub-THz detectors were analysed: QO SBD and FET detectors. This devices are ideal candidates for integration with other devices and on an array configuration due to their compactness, room-temperature operation and good performance.

In the first section of current chapter, THz/sub-THz detectors were introduced, showing the importance they have in current wireless systems. In addition, main detector parameters were presented, paying special attention to responsivity and NEP, which are the critical parameters that define the detector performance. Then, a classification on THz/sub-THz detectors was done. First classification differentiates between direct detection and heterodyne detection schemes. In this work, we focused on direct detectors which don't need a local oscillator source and then are easier to implement. Three main groups are differentiated between direct detectors: thermal detectors, photoconductive detectors and electronic rectifiers. Each of them has advantages and disadvantages, and depending on the application one type would be more suitable than the other.

After the introduction on THz/sub-THz detectors, two sections regarding the work carried out by the author are presented. Section 4.2 is devoted to the design, manufacture and characterization of a QO SBD detector. A zero bias Schottky diode was fully characterised and with those parameters three planar antennas were designed to provide different capabilities. The whole receiver was manufactured and packaged and it was fully characterised. Performance of three receivers was compared and results in the state of the art of this devices at these frequencies were obtained. Finally, one of the detectors was used as the receiver of a 1 Gbit/s data transmission wireless system showing good performance.

Section 4.3 was devoted to plasma-wave FET detectors based on CMOS technology. A brief introduction on working principle was carried out and state-of-the-art results were presented. This technology is a very promising candidate to fulfil the THz/sub-THz detector market since theoretically they can provide very good performance at room-temperature and everything can be integrated in a single package and

manufactured in the same wafer. Broadband (bow-tie) and resonant (differential patch) antennas were designed to be part of 100 GHz and 300 GHz plasma-wave FET detectors with FETs having different channel lengths. Various prototypes were manufactured and measurements were done. Unfortunately, the obtained results are far away from those reported by other authors and improvements must be undertaken.

The main contributions related with the fourth chapter have been published or presented in 2 journal papers and 6 conferences (see Publications section at the end of this document).

4.5 References

[1] R. A. Lewis, *Terahertz Physics*. Cambridge University Press, 2013.

[2] E. Bründermann, H.-W. Hübers, and M. Kimmitt, "Detectors," in *Terahertz Techniques*, ser. Springer Series in Optical Sciences. Springer Berlin Heidelberg, 2012, vol. 151, pp. 169–245.

[3] M. Sakhno, F. Sizov, and A. Golenkov, "Uncooled THz/sub-THz Rectifying Detectors: FET vs. SBD," *Journal of Infrared, Millimeter, and Terahertz Waves*, vol. 34, no. 12, pp. 798–814, 2013.

[4] F. Sizov, V. Reva, A. Golenkov, and V. Zabudsky, "Uncooled Detectors Challenges for THz/sub-THz Arrays Imaging," *Journal of Infrared, Millimeter, and Terahertz Waves*, vol. 32, no. 10, pp. 1192–1206, 2011.

[5] E. R. Brown, "Fundamentals of Terrestrial Millimeter-Wave and THz Remote Sensing," *International Journal of High Speed Electronics and Systems*, vol. 13, no. 04, pp. 995–1097, 2003.

[6] F. Sizov and A. Rogalski, "THz Detectors," *Progress in Quantum Electronics*, vol. 34, no. 5, pp. 278 – 347, 2010.

[7] Y.-S. Lee, "Continuous-Wave Terahertz Sources and Detectors," in *Principles of Terahertz Science and Technology*. Springer US, 2009, pp. 1–41.

[8] Virginia Diodes Inc. (2014, April) VDI. [Online]. Available: http://vadiodes.com/

[9] M. Dyakonov and M. Shur, "Plasma Wave Electronics: Novel Terahertz Devices Using Two Dimensional Electron Fluid," *IEEE Transactions on Electron Devices*, vol. 43, no. 10, pp. 1640–1645, Oct 1996.

[10] ESA Science and Technology. (2014, April) Herschel. [Online]. Available: http://sci.esa.int/herschel/

[11] V. Bozhkov, "Semiconductor Detectors, Mixers, and Frequency Multipliers for the Terahertz Band," *Radiophysics and Quantum Electronics*, vol. 46, no. 8-9, pp. 631–656, 2003.

[12] M. T. Faber, J. Chramiec, and M. E. Adamski, *Microwave and Millimeter-wave Diode Frequency Multipliers*, ser. Artech House Microwave Library. Boston: Artech House, 1995.

[13] J. Lee, J. Brini, and C. Dimitriadis, "Simple Parameter Extraction mMthod for Non-Ideal Schottky Barrier Diodes," *Electronics Letters*, vol. 34, no. 12, pp. 1268–1269, 1998.

[14] A. Cowley and H. O. Sorensen, "Quantitative Comparison of Solid-State Microwave Detectors," *IEEE Transactions on Microwave Theory and Techniques*, vol. 14, no. 12, pp. 588–602, Dec 1966.

[15] S. A. Maas, *Nonlinear Microwave and RF Circuits.* Artech House on Demand, 2003.

[16] G. D. Vendelin, A. M. Pavio, and U. L. Rohde, *Microwave Circuit Design using Linear and Nonlinear Techniques.* John Wiley & Sons, 2005.

[17] M. Hoefle, K. Haehnsen, I. Oprea, O. Cojocari, A. Penirschke, and R. Jakoby, "Highly Responsive Planar Millimeter Wave Zero-Bias Schottky Detector with Impedance Matched Folded Dipole Antenna," in *IEEE MTT-S International Microwave Symposium Digest (IMS), 2013*, June 2013, pp. 1–4.

[18] Advanced Compound Semiconductor GmbH. (2014, March) ACST. [Online]. Available: http://www.acst.de/

[19] M. Hoefle, K. Schneider, A. Penirschke, O. Cojocari, and R. Jakoby, "Characterization and Impedance Matching of New High Sensitive Planar Schottky Detector Diodes," in *Microwave Conference (GeMIC), 2011 German.* IEEE, 2011, pp. 1–4.

[20] Advanced Design System. Agilent. (2013, December) ADS. [Online]. Available: http://www.home.agilent.com/en/pc-1297113/advanced-design-system-ads?&cc=ES&lc=eng

[21] A. Technologies. (2014, April) TRL Calibration. [Online]. Available: http://na.tm.agilent.com/pna/help/latest/S3_Cals/TRL_Calibration.htm

[22] Microwave Office. (2014, April) AWR. [Online]. Available: http://www.awrcorp.com/es/products/microwave-office

[23] L. Liu, J. Hesler, H. Xu, A. Lichtenberger, and R. Weikle, "A Broadband Quasi-Optical Terahertz Detector Utilizing a Zero Bias Schottky Diode," *IEEE Microwave and Wireless Components Letters*, vol. 20, no. 9, pp. 504–506, 2010.

[24] D. Schoenherr, C. Bleasdale, T. Goebel, C. Sydlo, H. L. Hartnagel, R. Lewis, and P. Meissner, "Extremely Broadband Characterization of a Schottky Diode Based THz Detector," in *35th International Conference on Infrared Millimeter and Terahertz Waves (IRMMW-THz), 2010*, 2010, pp. 1–2.

[25] T. Nguyen, H. Han, and I. Park, "Full-Wavelength Dipole Antenna on a Hybrid GaAs Membrane and Si Lens for a Terahertz Photomixer," *Journal of Infrared, Millimeter, and Terahertz Waves*, vol. 33, no. 3, pp. 333–347, 2012.

[26] H. Ryu, S. Kim, M. Kwak, K. Kang, and S.-O. , "A Folded Dipole Antenna Having Extremely High Input Impedance for Continuous-Wave Terahertz Power Enhancement," in *33rd International Conference on Infrared, Millimeter and Terahertz Waves, 2008. IRMMW-THz 2008*, 2008, pp. 1–2.

[27] L. Liu, H. Xu, Y. Duan, A. Lichtenberger, J. Hesler, and R. Weikle, "A 200 GHz Schottky Diode Quasi-Optical Detector Based on Folded Dipole Antenna," in *Twentieth International Symposium on Space Terahertz Technology*, vol. 1, 2009, p. 145.

[28] S. M. Duffy, S. Verghese, A. McIntosh, A. Jackson, A. Gossard, and S. Matsuura, "Accurate Modeling of Dual Dipole and Slot Elements used with Photomixers for Coherent Terahertz Output Power," *IEEE Transactions on Microwave Theory and Techniques*, vol. 49, no. 6, pp. 1032–1038, 2001.

[29] D. Segovia-Vargas, D. Castro-Galan, L. E. García-Muñoz, and V. Gonzalez-Posadas, "Broadband Active Receiving Patch with Resistive Equalization," *IEEE Transactions on Microwave Theory and Techniques*, vol. 56, no. 1, pp. 56–64, 2008.

[30] R. E. Collin, *Foundations for Microwave Engineering*. Wiley. com, 2007.

[31] T. Endo, Y. Sunahara, S. Satoh, and T. Katagi, "Resonant Frequency and Radiation Efficiency of Meander Line Antennas," *Electronics and Communications in Japan (Part II: Electronics)*, vol. 83, no. 1, pp. 52–58, 2000.

[32] C. A. Balanis, *Antenna Theory: Analysis and Design*. John Wiley & Sons, 2012.

[33] D. B. Rutledge, D. P. Neikirk, and D. P. Kasilingam, "Integrated Circuit Antennas," *Infrared and millimeter waves*, vol. 10, no. part 2, pp. 1–90, 1983.

[34] D. F. Filipovic, S. S. Gearhart, and G. M. Rebeiz, "Double-Slot Antennas on Extended Hemispherical and Elliptical Silicon Dielectric Lenses," *IEEE Transactions on Microwave Theory and Techniques*, vol. 41, no. 10, pp. 1738–1749, 1993.

[35] Computer Simulation Technology. (2014, April) CST. [Online]. Available: https://www.cst.com/

[36] H. Ito, F. Nakajima, T. Ohno, T. Furuta, T. Nagatsuma, and T. Ishibashi, "InP-Based Planar-Antenna-Integrated Schottky-Barrier Diode for Millimeter-and Sub-Millimeter-Wave Detection," *Japanese Journal of Applied Physics*, vol. 47, p. 6256, 2008.

[37] V. Rymanov, M. Palandoken, S. Lutzmann, B. Bouhlal, T. Tekin, and A. Stohr, "Integrated Photonic 71 - 76 GHz Transmitter Module Employing High Linearity Double Mushroom-Type 1.55 μ m Waveguide Photodiodes," in *International Topical Meeting on Microwave Photonics (MWP), 2012*, 2012, pp. 253–256.

[38] V. Rymanov, S. Babiel, A. Stohr, S. Lutzmann, M. Palandoken, B. Bouhlal, and T. Tekin, "Integrated E-band Photoreceiver Module for Wideband (71 - 76GHz) Wireless Transmission," in *42nd European Microwave Conference (EuMC), 2012*, 2012, pp. 983–986.

[39] Y. M. El-Batawy and M. J. Deen, "Modeling of Mushroom Waveguide Photodetector," *Journal of Vacuum Science & Technology A: Vacuum, Surfaces, and Films*, vol. 22, no. 3, pp. 811–815, 2004.

[40] V. Rymanov, T. Tekin, and A. Stöhr, "Double Mushroom 1.55 μm Waveguide Photodetectors for Integrated E-band (60-90 GHz)

Wireless Transmitter Modules," in *SPIE OPTO*. International Society for Optics and Photonics, 2012, pp. 82 590E–82 590E.

[41] M. Weiss, M. Huchard, A. Stohr, B. Charbonnier, S. Fedderwitz, and D. Jager, "60-GHz Photonic Millimeter-Wave Link for Short- to Medium-Range Wireless Transmission Up to 12.5 Gb/s," *Journal of Lightwave Technology*, vol. 26, no. 15, pp. 2424–2429, 2008.

[42] E. Seok, D. Shim, C. Mao, R. Han, S. Sankaran, C. Cao, W. Knap, and K. Kenneth, "Progress and Challenges Towards Terahertz CMOS Integrated Circuits," *IEEE Journal of Solid-State Circuits*, vol. 45, no. 8, pp. 1554–1564, 2010.

[43] W. Knap, F. Teppe, Y. Meziani, N. , J. Lusakowski, F. Boeuf, T. Skotnicki, D. Maude, S. Rumyantsev, and M. Shur, "Plasma Wave Detection of Sub-Terahertz and Terahertz Radiation by Silicon Field-Effect Transistors," *Applied Physics Letters*, vol. 85, no. 4, pp. 675–677, 2004.

[44] E. Öjefors, A. Lisauskas, D. Glaab, H. G. Roskos, and U. R. Pfeiffer, "Terahertz Imaging Detectors in CMOS Technology," *Journal of Infrared, Millimeter, and Terahertz Waves*, vol. 30, no. 12, pp. 1269–1280, 2009.

[45] R. Tauk, F. Teppe, S. Boubanga, D. Coquillat, W. Knap, Y. M. Meziani, C. Gallon, F. Boeuf, T. Skotnicki, C. Fenouillet-Beranger, D. K. Maude, S. Rumyantsev, and M. Shur, "Plasma Wave Detection of Terahertz Radiation by Silicon Field Effects Transistors: Responsivity and Noise Equivalent Power," *Applied Physics Letters*, vol. 89, no. 25, pp. 253 511–3, Dec 2006.

[46] A. Lisauskas, S. Boppel, V. Krozer, and H. Roskos, "Silicon CMOS-based THz Detection," in *IEEE Sensors, 2011*, Oct 2011, pp. 55–58.

[47] W. Knap, M. Dyakonov, D. Coquillat, F. Teppe, N. Dyakonova, J. Lusakowski, K. Karpierz, M. Sakowicz, G. Valusis, D. Seliuta, I. Kasalynas, A. Fatimy, Y. Meziani, and T. Otsuji, "Field Effect Transistors for Terahertz Detection: Physics and First Imaging Applications," *Journal of Infrared, Millimeter, and Terahertz Waves*, vol. 30, no. 12, pp. 1319–1337, 2009.

[48] W. Knap, S. Rumyantsev, M. S. Vitiello, D. Coquillat, S. Blin, N. Dyakonova, M. Shur, F. Teppe, A. Tredicucci, and T. Nagatsuma, "Nanometer Size Field Effect Transistors for Terahertz Detectors," *Nanotechnology*, vol. 24, no. 21, p. 214002, 2013.

[49] S. Preu, S. Kim, R. Verma, P. G. Burke, M. S. Sherwin, and A. C. Gossard, "An Improved Model for Non-Resonant Terahertz Detection in Field-Effect Transistors," *Journal of Applied Physics*, vol. 111, no. 2, 2012.

[50] S. Boppel, A. Lisauskas, M. Mundt, D. Seliuta, L. Minkevicius, I. Kasalynas, G. Valusis, M. Mittendorff, S. Winnerl, V. Krozer, and H. Roskos, "CMOS Integrated Antenna-Coupled Field-Effect Transistors for the Detection of Radiation From 0.2 to 4.3 THz," *IEEE Transactions on Microwave Theory and Techniques*, vol. 60, no. 12, pp. 3834–3843, Dec 2012.

[51] F. Schuster, D. Coquillat, H. Videlier, M. Sakowicz, F. Teppe, L. Dussopt, B. Giffard, T. Skotnicki, and W. Knap, "Broadband Terahertz Imaging with Highly Sensitive Silicon CMOS Detectors," *Opt. Express*, vol. 19, no. 8, pp. 7827–7832, Apr 2011.

[52] H. Sherry, R. Al Hadi, J. Grzyb, E. Ojefors, A. Cathelin, A. Kaiser, and U. Pfeiffer, "Lens-Integrated THz Imaging Arrays in 65nm CMOS Technologies," in *IEEE Radio Frequency Integrated Circuits Symposium (RFIC), 2011*, June 2011, pp. 1–4.

[53] R. Al Hadi, H. Sherry, J. Grzyb, Y. Zhao, W. Forster, H. Keller, A. Cathelin, A. Kaiser, and U. R. Pfeiffer, "A 1 k-Pixel Video Camera for 0.7 - 1.1 Terahertz Imaging Applications in 65-nm CMOS," *IEEE Journal of Solid-State Circuits*, vol. 47, no. 12, pp. 2999–3012, Dec 2012.

[54] Y. P. Zhang and J. J. Wang, "Theory and Analysis of Differentially-Driven Microstrip Antennas," *IEEE Transactions on Antennas and Propagation*, vol. 54, no. 4, pp. 1092–1099, 2006.

CHAPTER 5

ALTERNATIVE SOLUTION TO IMAGING AT SUB-TERAHERTZ FREQUENCIES

This chapter is devoted to the design of a focusing system for a 300 GHz radar for security purposes. While previous chapters are focused on planar antennas and THz/sub-THz subsystems, in this case we will focus on the design of a complete system. The emitters and receivers designed in the previous chapters can be used in this focusing system design. In this case a horn antenna and elliptical mirrors are used, thus leading to a more complex structure. On the other hand it can handle more power and provide better focusing capabilities.

The main contribution of the chapter consists of designing the focusing system in such a way that it can provide scanning capabilities but, at the same time, the beam is not distorted because it always works "in-focus". The focusing system consists of a horn antenna as feeding element, two elliptical mirrors and a plane one to provide beam-steering by rotation. Since the only mirror that is rotated to provide scanning capabilities is the plane one, the target distance is always at the output focus of the second elliptical mirror, so the beam is not distorted even for big displacements.

In addition to the proposed system, the design methodology followed through the chapter is also relevant because it reduces computational

time and effort, and obtained results are accurate enough. This methodology consists on designing the overall system using QO Gaussian Beam Propagation approximation [1] and use thin lenses instead of mirrors. Once the main parameters are obtained, then they are translated into real elliptical mirrors and the overall system is simulated with a full-wave electromagnetic simulator [2].

5.1 Introduction

One of the main applications of THz and sub-THz technology is target detection for security purposes. This comes from the fact that most clothes and envelopes are reasonably transparent at these frequencies while, at the same time, high image resolution can be achieved. Nowadays, a great effort is being made in designing THz imaging systems for different purposes [3–5].

In order to identify objects hidden behind envelopes or clothes, a very high resolution (on the order of mm or cm) is needed and, for most cases, the target is placed at distances larger than a meter away from the radar. With these assumptions, a focusing system with very high directivity (and very high resolution as a consequence) is desirable. Such high directivity can only be obtained by using an array of antennas or a parabolic or elliptical mirror. In both cases, the structure is very big in terms of the wavelength, so a large number of computational resources and relatively long periods of time to carry out appropriate calculations are required. A tool capable of providing fast and accurate approximation of the performance of an electromagnetic system in the range of QOs is desirable and welcomed. The goal is not to completely solve the electromagnetic problem, but to develop a technique that greatly reduces the computation time, based on the theory of propagation of Gaussian beams [1]. Once the main variables are obtained, the whole electromagnetic problem can be solved by using commercial full-wave electromagnetic antenna software [2].

In this chapter a focusing system for a 300 GHz radar with 5 m target distance and 10 mm diameter spot size resolution, defined as the 3 dB beamwidth, is proposed. The objective afterwards is to include this focusing system in a THz radar, so the signal generation, as long as the

digital signal processing units, must be included thereafter. In addition, a fast and accurate design method which finds the optimal parameters and reduces the overall computation time is presented.

The resulting focusing system is formed by two elliptical mirrors to reduce the distortion and cross-polar level [6–8] and a planar one to provide scanning capabilities. It has to be mentioned that the only rotating mirror to provide scanning capabilities is the plane one, so this simple scheme reduces the complexity of previous solutions. Its main advantage is that it always works "in-focus", what means that the beam is almost not distorted when scanning the target. The overall system is designed in such a way that the output focus of the second elliptical mirror is 5 m away from it (target detection distance) so when the plane mirror is rotated the output focus is displaced but it is always 5 m away from the second elliptical mirror.

This chapter is organized as follows: first, the whole system is proposed and the feeding element is presented. In addition, the focusing system is analysed using Gaussian Beam QO propagation and the main parameters are obtained. Then those QO parameters are applied to the design of real sized parameters elliptical mirrors to obtain the actual focusing system. This system is validated using full-wave electromagnetic antenna software [2] and the obtained results are presented. Finally, some conclusions and future lines are introduced.

5.2 300 GHz "Always-in-Focus" Focusing System for Target Detection

In this section the design of a focusing system at 300 GHz is presented. First, basic QO Gaussian beam propagation theory is introduced and the main parameters are highlighted. Then, the focusing system is designed and simulated and its performance is analysed.

5.2.1 Quasi-Optical Gaussian Beam Propagation

Quasioptics deals with the propagation of a beam of radiation that is reasonably well collimated but has relatively small dimensions when measured in wavelengths, transverse to the axis of propagation. It spans the large middle ground between the optics ($\lambda \to 0$) and systems whose size is approximately equal to its wavelength. It is not the objective of this section to fully develop the QO Gaussian Beam propagation theory. For a detailed description of such theory the reader is suggested to use [1]. In this section main parameters are briefly presented and some interesting points are also discussed.

In systems with $\lambda \to 0$ geometrical optics and ray-tracing techniques can be used. These optical systems main characteristic is that the dimensions of all components (e.g., lenses, mirrors, apertures) are large enough to neglect the effects of the finite wavelength. On the other hand, on systems whose dimensions $\cong \lambda$, diffraction effects dominate the propagation of radiation. Diffraction is the tendency for radiation from a source, which is relatively small when measured in wavelengths, to change its distribution as the distance from the source varies. In this situations, which include the near field of an aperture or antenna, a complex formalism to analyse the behaviour of a beam is required, and performing accurate calculations for real systems is relatively time-consuming [1].

QO includes the realistic and important situation of a beam of radiation whose diameter is only moderately large when measured in wavelengths. This allows the theory of Gaussian beam modes and Gaussian beam propagation to be employed. This formalism includes the effects of diffraction within reasonable and generally not highly restrictive lim-

its [1]. The efficacy of Gaussian beam analysis is increased by the considerable variety of microwave and millimetre wave feed horn that radiate beams that are very nearly Gaussian in form. Thus, the radiation from such a device can be represented as coming from the Gaussian beam waist, as shown schematically in the Figure 5.1a. The action of focusing devices, such as the lens shown in the Figure 5.1b, is also relatively straightforward to calculate using Gaussian beam formation [1].

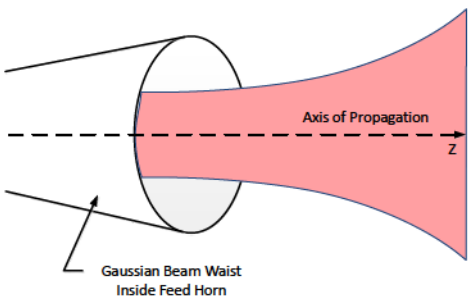

(a)

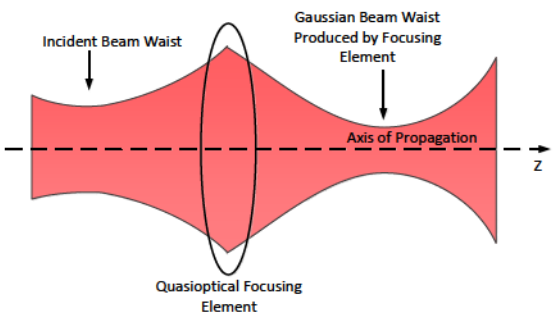

(b)

Figure 5.1: (a) Gaussian Beam produced by feed horn. (b) Gaussian Beam transformation by a QO focusing system. Based on [1].

The Paraxial Wave Equation

If we consider a wave propagating along the positive z-direction, the distribution of the electric field for any component can be written as (suppressing the time dependence):

$$E(x, y, z) = u(x, y, z)\, e^{-\jmath kz} \tag{5.1}$$

where u is a complex scalar function that defines the non-plane wave part of the beam. Helmholtz equation is:

$$\left(\nabla^2 + k^2\right) \Psi = 0 \tag{5.2}$$

where Ψ represents any component of $\mathbf{E}$ or $\mathbf{H}$. This equation in rectangular coordinates reduces to:

$$\frac{\partial^2 E}{\partial x^2} + \frac{\partial^2 E}{\partial y^2} + \frac{\partial^2 E}{\partial z^2} + k^2 E = 0 \tag{5.3}$$

and if the quasi-plane wave solution shown in Equation 5.1 is included it is obtained:

$$\frac{\partial^2 u}{\partial x^2} + \frac{\partial^2 u}{\partial y^2} + \frac{\partial^2 u}{\partial z^2} - 2\jmath k \frac{\partial u}{\partial z} = 0 \tag{5.4}$$

which is sometimes called the *reduced wave equation* [1].

The paraxial approximation consists of assuming that the variation along the direction of propagation of the amplitude u (due to diffraction) will be small over a distance comparable to the wavelength, and that the axial variation will be small compared to the variation perpendicular to this direction. With such assumptions, Equation 5.4 reduces to:

$$\frac{\partial^2 u}{\partial x^2} + \frac{\partial^2 u}{\partial y^2} - 2\jmath k \frac{\partial u}{\partial z} = 0 \tag{5.5}$$

which is called the *Paraxial wave equation*. Solutions to the paraxial wave equation are the Gaussian beam modes that form the basis of QO system design [1].

Gaussian Beam Parameters

The simplest solution of the axially symmetric paraxial wave equation can be written in the form (cylindrical coordinates):

$$u(r,z) = A(z)\, exp\left[\frac{-\jmath k r^2}{2q(z)}\right] \tag{5.6}$$

with A and q being two complex functions (of z only).

Beam Parameter Is a complex parameter which can be also referred as complex beam parameter or Gaussian beam parameter. Normally it is represented as:

$$\frac{1}{q} = \left(\frac{1}{q}\right)_r - \jmath\left(\frac{1}{q}\right)_i \tag{5.7}$$

where the subscripted terms are the real and imaginary parts of the quantity $1/q$, respectively.

Radius of Curvature Determines the radius of the spherical wave front at an equiphase point (R in the Figure 5.2b). When $r \ll R$:

$$\left(\frac{1}{q}\right)_r = \frac{1}{R} \tag{5.8}$$

Since q is a function of z, it is evident that the radius of curvature of the beam will depend on the position along the axis of propagation (Figure 5.2b).

Beam Radius The beam radius (w in the Figure 5.2b) is the value of the radius at which the field falls to $1/e$ relative to its on-axis value. It is given by the following equation [1]:

$$\left(\frac{1}{q}\right)_i = \frac{\lambda}{\pi w^2} \tag{5.9}$$

Since q is a function of z, the beam radius will depend on the position along the axis of propagation.

Beam Waist Radius At $z = 0$ we have from Equation 5.6, $u(r, 0) = A(0)\exp[-jkr^2/2q(0)]$, and if we choose w_0 such that $w_0 = [\lambda q(0)/j\pi]^{0.5}$, we find the relative field distribution at $z = 0$ to be:

$$u\left(r, 0\right) = u\left(0, 0\right) exp\left(\frac{-r^2}{w_o^2}\right) \tag{5.10}$$

where w_0 denotes the beam radius at $z = 0$, which is called the beam waist radius.

In the Figure 5.2, an schematic diagram of Gaussian beam propagation with main parameters is depicted.

5.2.2 System Design

In this section the proposed system is presented and an analysis based on Gaussian beam QO propagation [1] is performed. The design is based on a Gaussian beam telescope, where the separation between the two focusing elements is the sum of their focal lengths. Figure 5.3 shows a schematic of the proposed focusing system. In this section they will be represented as thin lenses in order to simplify QO calculations while in Section 5.2.3 they will be replaced with elliptical mirrors. Elliptical mirrors have been chosen because, if properly designed, they can reduce the distortion effects and the cross polar level [6–8]. Moreover, a paraboloid system (more than one paraboloid) have fewer degrees of freedom in the design and a relatively high blockage inevitably happens [1].

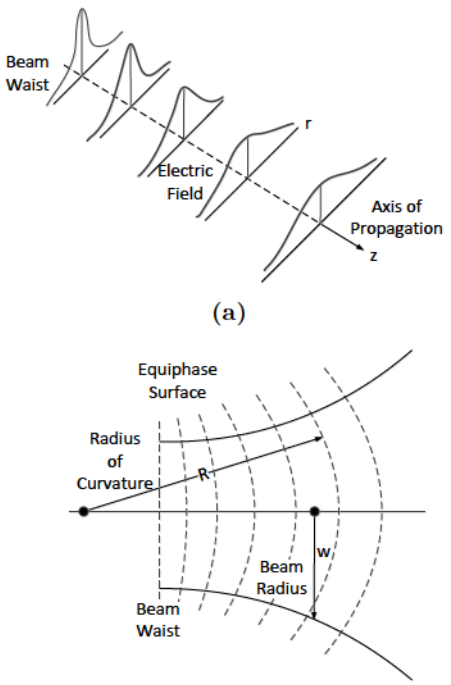

Figure 5.2: Schematic diagram of Gaussian beam propagation. (a) Propagating beam indicating increase in beam radius and diminution of peak amplitude as distance from waist increase. (b) Cut through beam showing equiphase surfaces (dashed lines), beam radius w, and radius of curvature R. Based on [1].

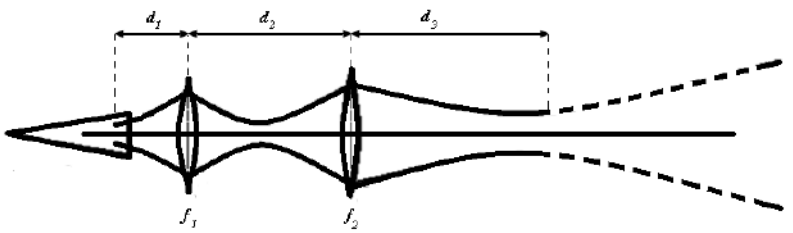

Figure 5.3: QO path schematic of the Gaussian beam telescope [9].

Feeding Element

A corrugated conical horn antenna has been chosen as the feeding source for the system, since it provides a very good Gaussian beam over, at least, 1.5:1 frequency range [1]. Moreover, it can handle more power than any of the current antennas working at these frequencies. Its dimensions are $L_h = 20\,\text{mm}$ and $a = 3.3\,\text{mm}$ (see Figure 5.4), which are typical ones for 300 GHz operation ($\lambda = 1\,\text{mm}$). With these values the beam waist (w_0) and the location of that beam waist (z_0) can be obtained as [1, 10]:

$$w_0^2 = \frac{(0.644a)^2}{1 + 0.644^4 \left(\frac{\pi a^2}{\lambda L_h}\right)^2} \tag{5.11}$$

$$z_0 = L_h - \frac{(0.644a)^2 \pi^2 w_0^2}{L_h \lambda^2} \tag{5.12}$$

For our particular case, $w_0 = 1.7\,\text{mm}$ and $z_0 = 13.3\,\text{mm}$, so distance from the beam waist of the horn to its aperture is 6.7 mm ($L_h - z_0 =$ 20 mm - 13.3 mm = 6.7 mm). Other QO parameters shown in Figure 5.4 are the distance from the beam waist (z), the beam radius at that position (w) and the radius of curvature at z (R_z). The predicted 3 dB beamwidth of the horn is 6.1° while its directivity is 24.1 dB in the far-field.

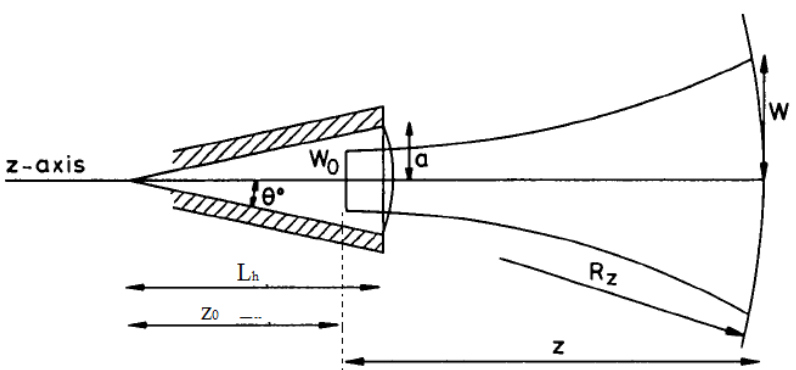

Figure 5.4: Corrugated conical horn antenna [10].

Quasi-Optical Design

Taking advantage of the developed tool it is possible now to quickly calculate the main parameters of our system. The parameters associated to the feed have already been calculated, so it is necessary to calculate the other ones in order to obtain a resolution of 10 mm diameter spot size at 5 m.

Based on the QO Gaussian beam propagation theory the following ABCD matrix for the system shown in Figure 5.3 is obtained [1]:

$$\begin{bmatrix} A & B \\ C & D \end{bmatrix} = \begin{bmatrix} 1 & d_3 \\ 0 & 1 \end{bmatrix} \cdot \begin{bmatrix} 1 & 0 \\ \frac{-1}{f_2} & 1 \end{bmatrix} \cdot \begin{bmatrix} 1 & d_2 \\ 0 & 1 \end{bmatrix} \cdot \begin{bmatrix} 1 & 0 \\ \frac{-1}{f_1} & 1 \end{bmatrix} \cdot \begin{bmatrix} 1 & d_1 \\ 0 & 1 \end{bmatrix} \tag{5.13}$$

Distance d_1 has been considered as the distance from the beam waist of the horn antenna to the first thin lens; d_2 is the distance between the two thin lenses; and d_3 the target distance (not the distance from the second thin lens to the output beam waist).

From the ABCD matrix the output beam parameter of the system (q_{out}) can be obtained as [1]:

$$q_{out} = \frac{A \cdot q_{in} + B}{C \cdot q_{in} + D} \tag{5.14}$$

where q_{in} is the input beam parameter of the system which depends on the feeding element in the following way:

$$q_{in} = \frac{\jmath \pi w_0^2}{\lambda} \tag{5.15}$$

with w_0 the beam waist of the horn antenna. The beam radius and radius of curvature at the output of the system (w_{out} and R_{out}) are given as:

$$w^{out} = \left[\frac{\lambda}{\pi \Im\left(-\frac{1}{q_{out}} \right)} \right] \tag{5.16}$$

$$R^{out} = \left[\Re\left(\frac{1}{q_{out}}\right)\right]^{-1} \tag{5.17}$$

while the beam waist of the output beam (w_0^{out}) and the distance from the beam waist where equations 5.16 and 5.17 are obtained (z_{out}) can be calculated as:

$$w_0^{out} = \frac{w^{out}}{\left[1 + \left(\frac{\pi(w^{out})^2}{\lambda R^{out}}\right)^2\right]^{0.5}} \tag{5.18}$$

$$z^{out} = \frac{R^{out}}{1 + \left(\frac{\lambda R^{out}}{\pi(w^{out})^2}\right)^2} \tag{5.19}$$

Then, the transverse field distribution of the fundamental mode at z_{out} is obtained [1]:

$$E(r, z^{out}) = \left[\frac{2}{\pi(w^{out})^2}\right]^{0.5} \times \exp\left[-\frac{r^2}{(w^{out})^2} - j\frac{2\pi}{\lambda}z^{out} - j\frac{\pi r^2}{\lambda R^{out}} + j\phi_0(z^{out})\right] \tag{5.20}$$

$$\phi_0(z^{out}) = \tan^{-1}\left(\frac{\lambda z^{out}}{\pi w_0^2}\right) \tag{5.21}$$

where r represents the perpendicular distance from the axis of propagation and $\phi_0(z^{out})$ is the phase shift from the beam waist. Now it is easy to obtain the 3 dB beamwidth of equation 5.20 and, as a consequence, the spot size.

In Figure 5.5a, the size of the semi-spot (half the beam) at a distance of 5 m as a function of f_1 and f_2 when $d_1 = 306.7$ mm (300 mm distance between horn aperture and first thin lens + 6.7 mm distance from beam waist to horn aperture) and $d_2 = 500$ mm is depicted. Semi-spots larger than 15 mm have been fixed to 15 mm in order to have a friendlier picture. From Figure 5.5a it can be seen that for the shown values for f_1 and f_2, only a very small margin of values (associated to the central strip) satisfy the resolution goal. A pair of f_1 and f_2 having 5 mm semi-spot is highlighted. A similar plot can be obtained for different distances d_1 and d_2, as well as for different target distances (d_3). The overall simulation time on an Intel®Core^{TM}i5 CPU at 2.67 GHz has been 2 minutes.

The idea after the QO design is to convert QO parameters into physical ones. Each thin lens is converted into an elliptical mirror and it has been observed that the mirror that imposes the dimension of the overall system is the second one (second thin lens, f_2) since it is the biggest. For that reason, a study on the second mirror diameter depending on the other parameters has been undertaken. QO Gaussian beam propagation theory states that a diameter of four times the beam radius ($4w$) truncates the beam at a level 34.7 dB below that on the axis of propagation and includes 99.97 % of the power in the fundamental mode Gaussian beam. This is generally sufficient to make the effects of diffraction by the truncation quite small. So the minimum diameter of that mirror has been obtained by taking into account that it must be at least four times the beam radius [1].

It has been observed that the smallest diameter of the second mirror that can be obtained does not depend on the distances d_1 and d_2 nor on f_1 and f_2, and it is imposed by the target distance d_3 and by the spot size. Figure 5.5b shows the minimum diameter of the second mirror as a function of the desired spot size for two different target distances (5 m and 10 m).

d_1 [mm]	d_2 [mm]	d_3 [mm]	f_1 [mm]	f_2 [mm]
306.7	500	5000	83.86	357.15

Table 5.1: QO Parameters

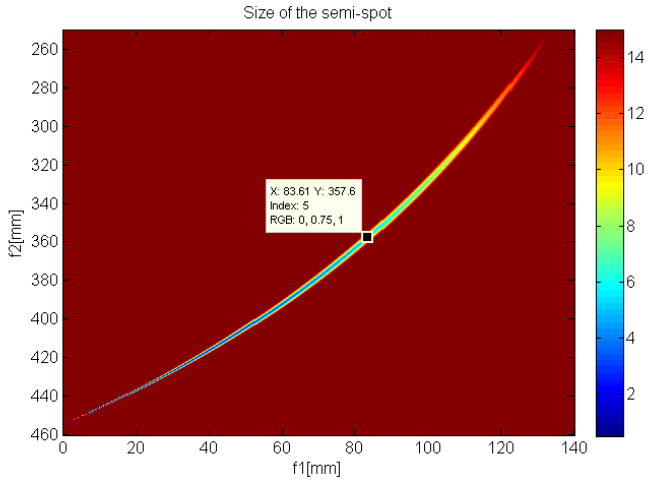

(a)

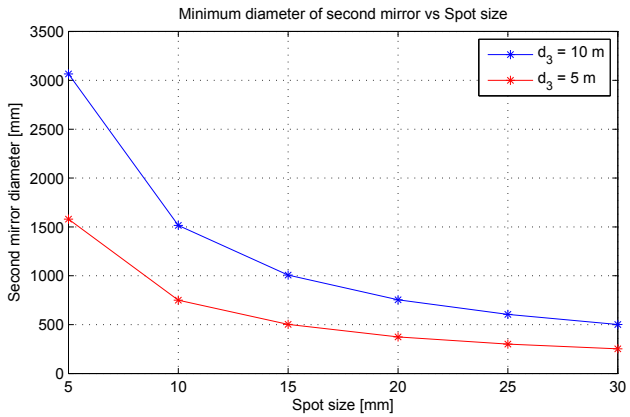

(b)

Figure 5.5: (a) Size of the semi-spot as a function of the focus of the two thin lenses with $d_1 = 306.7\,\text{mm}$ and $d_2 = 500\,\text{mm}$. (b) Second elliptical mirror diameter as a function of the desired spot size and target distance [9].

Once the minimum diameter has been obtained, the pair f_1 and f_2 which obtains that value for the pair $d_1 = 306.7\,\text{mm}$ and $d_2 = 500\,\text{mm}$ is selected and the focusing system based on thin lenses is designed. The main parameters of the system are presented in Table 5.1. With those parameters, $w^{out} = 8.31\,\text{mm}$, $R^{out} = 3973\,\text{mm}$, $w_0^{out} = 8.3\,\text{mm}$ and $z_{out} = 11.81\,\text{mm}$ are obtained, with a diameter spot size of 10 mm at 5 m target distance. It can be noted that the beam waist is not exactly at 5000 mm (target distance) but very close ($d_3 + z_{out} = 5011.81\,\text{mm}$).

5.2.3 System Validation

The previously designed focusing system using QO theory has been validated by using the commercial electromagnetic simulation software, GRASP [2], in order to validate the design process. The methods used by GRASP are the highly efficient PO algorithms and the General Theory of Diffraction (GTD). The first step consists on translating the QO parameters obtained in the previous section when we use thin lenses into physical parameters to build the elliptical mirrors. This relationship is given by:

$$f = \frac{R_1 R_2}{R_1 + R_2} \tag{5.22}$$

where R_1 is the distance from the elliptical mirror to its input focus and R_2 is the distance from the elliptical mirror to its output focus. Following the labels in Figure 5.6a, R_1 will be equal to the distance from the waist of the horn antenna to the first elliptical mirror; R_2 will be the distance from the first elliptical mirror to the common focus; R_3 will be the distance from that common focus to the second elliptical mirror; and R_4 will be the distance from the second mirror to the output focus. For the particular case represented in Table 5.1:

$$\left.\begin{aligned} R_1 = d_1 = 306.7mm \\ f_1 = 83.86mm \end{aligned}\right\} \rightarrow R_2 = \frac{R_1 f_1}{R_1 - f_1} = 115.42mm \tag{5.23}$$

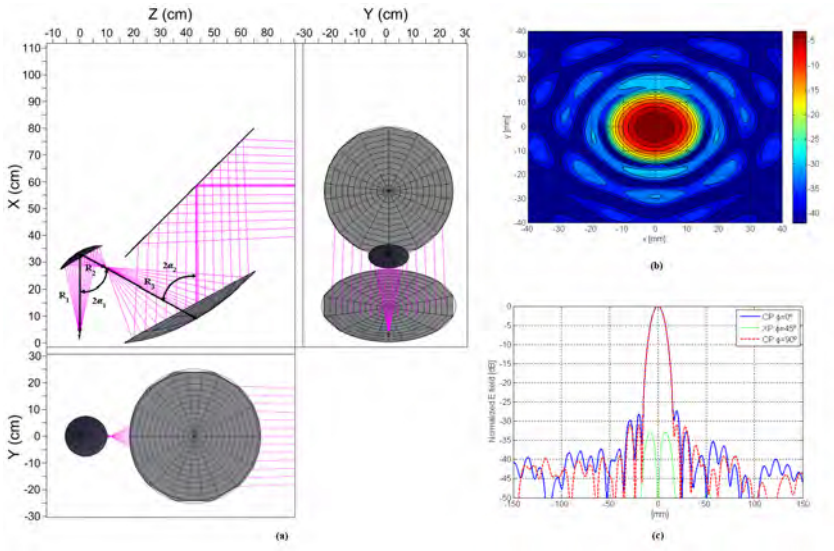

Figure 5.6: (a) Designed focusing system to detect targets at 5 m with a resolution of 10 mm. Origin of coordinates is at the feed of the horn antenna. (b) 2D normalized E-field module at 5 m and (c) Co-polar and cross-polar component of the focusing system in three planes when no scanning is performed. Represented normalized E-field is calculated at detection distance (5 m) [9].

$$\left.\begin{aligned} R_3 = d_2 - R_2 = 384.58mm \\ f_2 = 357.15mm \end{aligned}\right\} \rightarrow R_4 = \frac{R_3 f_2}{R_3 - f_2} = 5007.1mm \quad (5.24)$$

The obtained parameters for the system are summarized in Table 5.2. The angles have been chosen to reduce the overall size of it.

R_1 [mm]	R_2 [mm]	R_3 [mm]	R_4 [mm]	$2\alpha_1[^\circ]$	$2\alpha_2[^\circ]$
306.7	115.4	384.6	5007.1	60	60

Table 5.2: Physical parameters of elliptical mirrors

The system with its physical dimensions can be seen in Figure 5.6a. A plane mirror with a slightly larger diameter than the second elliptical mirror has been included in order to have a focusing system with scanning capabilities. This plane mirror is the only part of the system that is rotated to provide scanning capabilities. Diameters of the mirrors are 17 cm and 55 cm for elliptical ones and 68 cm for the plane one. The f/D ratios of the elliptical mirrors are 0.52 and 0.65 respectively. These values are in the range of $f/D \geq 0.5$ for $\alpha_i \leq 30^\circ$ which guarantee that the beam is almost not distorted [1, 6, 8].

The obtained spot with the focusing system at 5 m is plotted in Figure 5.6b and the radiation pattern at that distance in three different planes can be seen in Figure 5.6c. It can be noted that the 3 dB beamwidth is 10 mm, the side lobes are 30 dB lower than the main lobe in both $\phi = 0^\circ$ (XZ plane) and $\phi = 90^\circ$ (YZ plane) planes (with ϕ the angle defined over XY plane starting from x-axis) and the cross polar component is more than 30 dB lower in the $\phi = 45^\circ$ plane. With this system 70.1 dB gain is obtained at 5 m and the overall simulation time on the same computer as in Section 5.2.2 was 1 hour and 51 minutes. From this simulation time it is clear that the optimization of the system takes a lot of time.

The scanning capabilities of the system have also been explored. As previously mentioned, a plane mirror at the output of the second elliptical mirror has been included to add scanning capabilities to the focusing system. Figure 5.7a shows the $\phi = 90^\circ$ cut at 5 m when the system is scanning in the $\phi = 0^\circ$ plane. The same performance is obtained when the scanning is performed on the $\phi = 90^\circ$ plane. The scale of the figure has been changed in order to appreciate the distortion of the beam in a better way. The radiation pattern is almost not distorted even when the displacement is relatively high (500 mm). A scanning displacement of 500 mm is equal to a rotation in the azimuth and elevation plane of the plane mirror of 2.85° respectively. The scanning can be realized by rotating the mirror about two perpendicular axes. It can be placed on an axis spinning with a typical rotation mirror of 600 Revolutions Per Minute (RPM) which causes a circular path at the target distance. A slower rotary stage turns the spinning axis in a direction perpendicular to it with a speed of about 1°/s. This leads to linear movement of the circular path. With such set-up, the scanning of a 500 mm × 500 mm target placed at 5 m can be done in less than 10 s.

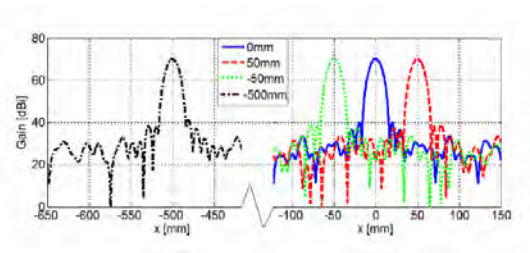

(a)

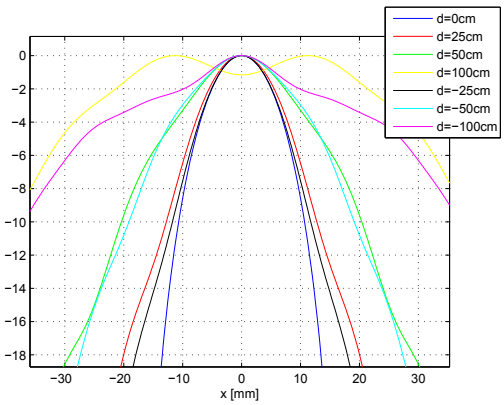

(b)

Figure 5.7: (a) Scanning capability in the $\phi = 0^\circ$ plane of the focusing system. (b) Normalized E-field vs the position for several displacement of the target distance. Represented normalized E-field is calculated at detection distance (5 m) [9].

In addition, the distortion of the beam when the target is closer to or away from has also been analysed. The results can be seen in Figure 5.7b. Positive displacements mean that the target is further away from the source while negative ones mean that the target is closer to the source. As we move away from the target distance the beam is distorted due to the fact that the beam is not in the output focus of the second elliptical mirror. Diffraction effects appear and, in some cases, even the beam losses its gaussicity. It can be noticed that the system is robust for displacements of a target distance up to half a meter closer to or away from.

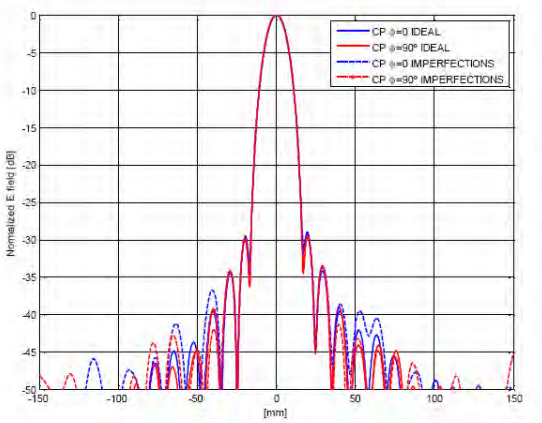

Figure 5.8: Simulation of manufacture process imperfections. Continuous lines ($\phi = 0^\circ$ in blue and $\phi = 90^\circ$ in red cuts) represent the radiation pattern when perfect mirrors are used while dashed lines ($\phi = 0^\circ$ in blue and $\phi = 90^\circ$ in red cuts) represent the radiation pattern when a random distortion is inserted in the mirrors' surface. Represented normalized E-field is calculated at detection distance (5 m) [9].

A very important issue that has to be taken into account when manufacturing the proposed system is the possible flaws associated to it. The most critical problems that may appear are changes in the roughness of the mirrors, as well as non-idealities on their borders. Since the mirrors have been designed in such a way that the beam is truncated at a power level of 34.7 dB below that on the axis of propagation, the effects of these last non-idealities can be neglected. As a consequence, the most important issue to be taken into account is the roughness of the surface of the mirrors. To do so, a parametric study has been carried out to check the system robustness against potential flaws in the manufacturing process. The surface roughness has been modelled as a zero mean uniform distribution with a variance of 20 µm that is 2 % of the wavelength. This is a typical value for manufacturing tolerances of such mirrors. The obtained results (Figure 5.8) are pretty similar to the ideal ones, and the only difference is that the secondary lobes level is higher than that of ideal mirrors. In any case, that level is 35 dB lower than the main lobe for places 50 mm far away from it. Then, the system is expected to be robust in terms of manufacturing flaws.

Once the spot, the scanning capabilities and the target distance displacements of the system have been analysed, as well as manufacturing flaws, a simple software simulation of the behaviour of the focusing system on a real environment has been undertaken. A target placed at 5 m (Figure 5.9a) has been scanned with the proposed system. The size of two of the spots is plotted in the same scale as the scanning target in order to compare the size of them with the overall target (Figure 5.9b). Four different hidden objects (a gun, a circle, a key and a cross) have been drawn inside the body of the target (Figure 5.9c) and the results obtained after scanning the target with the designed focusing system are plotted (Figure 5.9d). The simulation consists on taking a picture of the target and turns it into a grey scale. After that, the metallic parts have been painted in white while the non-metallic parts have been painted in black. Then, the normalized spot at 5 m plotted in Figure 5.6b is multiplied by that figure with displacements of 5 mm from left to right and up and down until the whole figure is scanned. It has to be mentioned that the simulation does not take into account any of scattering properties, the return path loss and clothing effects, but it gives a general idea of how this focusing system will behave on an ideal environment.

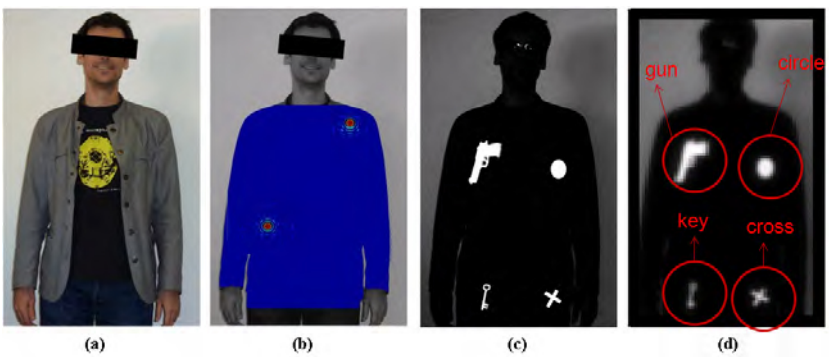

Figure 5.9: Software simulation of the behaviour of the first focusing system. (a) Photograph of the target we want to scan. (b) 2D normalized E-field module at 5 m together with the target to compare target and spot sizes. (c) Body of the target has been painted completely in black, while hidden items (key, gun, circle and cross) were painted in white. (d) Result of the simulation of scanning the picture in Figure 5.9c with the designed focusing system [9].

5.3 Conclusions

A focusing system with a target distance of 5 m and a spot of 10 mm diameter spot size working at 300 GHz has been presented. The focusing system always work in the output focus of the second elliptical mirror, which means that the beam is almost not distorted when scanning. In addition, only the plane mirror rotates to provide scanning capabilities thus reducing the complexity of previous solutions. This focusing system needs to be included with all the necessary electrical components to generate the 300 GHz signal and with the signal processing capabilities to detect weapons or other objects hidden in the scanning targets to construct a THz radar.

The focusing system is based on a Gaussian telescope scheme and an analysis tool has been implemented in Matlab based on QO Gaussian beam propagation theory. With this tool, the basic parameters of them can be easily calculated to have the desired spot size and target distance.

Once the system based on thin lenses was designed, it has been transferred into elliptical mirrors with real dimensions and validated using a full-wave electromagnetic simulator. The obtained results agree with those previously reported by QO theory. With the proposed designing method, a robust focusing system with the desired resolution and target distance can be easily designed. The main advantages are that it reduces the computational resources needed and, as a consequence, the overall time for designing such kind of systems.

Moreover, scanning capabilities of the focusing system have also been analysed, showing great results because the beam is almost not distorted for large displacements of it along horizontal or vertical axis. Besides, the target can be half a meter closer to or away from the designed target distance (5 m) and the beam is almost not distorted. The flaws that may appear in the manufacturing process have been studied and the roughness of the surface of the mirrors has been simulated, concluding that the system is also robust against small changes in the surface of the mirrors. The absence of distortion on the beam, as well as its simplicity, makes the proposed focusing system suitable for target detection applications at THz and sub-THz frequencies.

This chapter of the thesis has led to the publication of a journal paper and 2 conference contributions (see Publications section at the end of this document).

5.4 References

[1] P. F. Goldsmith, *Quasioptical System: Gaussian Beam Quasioptical Propagation and Applications*. IEEE Press Piscataway, 1998.

[2] General Reflector and Antenna Arm Analysis Software. (2014, January) GRASP. [Online]. Available: http://www.ticra.com/products/software/grasp

[3] C. Jansen, S. Wietzke, O. Peters, M. Scheller, N. Vieweg, M. Salhi, N. Krumbholz, C. Jördens, T. Hochrein, and M. Koch, "Terahertz Imaging: Applications and Perspectives," *Applied optics*, vol. 49, no. 19, pp. E48–E57, 2010.

[4] K. B. Cooper, R. J. Dengler, N. Llombart, T. Bryllert, G. Chattopadhyay, E. Schlecht, J. Gill, C. Lee, A. Skalare, I. Mehdi *et al.*, "Penetrating 3-D Imaging at 4-and 25-m Range Using a Submillimeter-Wave Radar," *IEEE Transactions on Microwave Theory and Techniques*, vol. 56, no. 12, pp. 2771–2778, 2008.

[5] I. Ederra, R. Gonzalo, B. Alderman, P. G. Huggard, B. P. de Hon, M. C. van Beurden, A. Murk, L. Marchand, and P. de Maagt, "Sub-Millimeter-Wave Imaging Array at 500 GHz Based on 3-D Electromagnetic-Bandgap Material," *IEEE Transactions on Microwave Theory and Techniques*, vol. 56, no. 11, pp. 2556–2565, 2008.

[6] J. A. Murphy, "Distortion of a Simple Gaussian Beam on Reflection from Off-Axis Ellipsoidal Mirrors," *International Journal of Infrared and Millimeter Waves*, vol. 8, no. 9, pp. 1165–1187, 1987.

[7] A. Baryshev and W. Wild, "ALMA Band 9 Optical Layout," *ALMA Memo Series*, vol. 394, 2001.

[8] J. A. Murphy and S. Withington, "Perturbation Analysis of Gaussian-Beam-Mode Scattering at Off-Axis Elipsoidal Mirrors," *Infrared Physics & Technology*, vol. 37, no. 2, pp. 205–219, 1996.

[9] J. Montero-de Paz, L. E. García-Muñoz, and D. Segovia-Vargas, "A 300 GHz "Always-In-Focus" Focusing System for Target Detection," *Radioengineering*, vol. 22, no. 2, p. 611, 2013.

[10] R. J. Wylde, "Millimeter-Wave Gaussian Beam-Mode Optics and Corrugated Feed Horns," *IEE Proceedings*, vol. 131, no. 4, pp. 258–262, 1984.

CHAPTER 6

FINAL CONCLUSIONS AND FUTURE LINES

6.1 Final Conclusions

THz and sub-THz technology is a field of big expansion nowadays due to the improvements made in both emitters and detectors and the big amount of applications where this technology can be used. This Ph.D. dissertation presents the results of more than 4 years of research in the THz and sub-THz field trying to improve devices performance from the antenna point-of-view. It has been demonstrated that making use of a joint design of the antenna and the active device the performance of the overall system is improved. During the Ph.D. dissertation both THz emitters and sub-THz detectors have been improved by an optimized design of the antenna, whereas in the final chapter a full system has also been optimized to provide outstanding scanning capabilities.

After an introduction where the importance of the THz waves was highlighted and the current main applications of THz waves were commented, the most important parameters of antennas were described and the most commonly used THz antenna topologies were presented. This chapter serves as an starting point to understand the work that has been done during this Ph.D. dissertation.

In the second chapter, the radiation pattern of planar antennas lying on dielectric substrate was analysed. First of all, an introduction explaining how the substrate affects the radiation pattern at THz and sub-THz frequencies and the importance of correctly analysing it was presented. Then, a MoM based software to analyse antennas lying on both semi-infinite and multilayered substrates was developed and radiation patterns were analysed. Once the radiation patterns were presented, the two main contributions of the chapter were discussed. The first one consists on explaining the anomalies that appear in the radiation pattern of both vertical and horizontal dipoles when laying on the interface between vacuum and a semi-infinite substrate while the second one consists on designing a software capable of analysing the radiation patterns of any antenna having an extended hemispherical dielectric lens as substrate. The developed tools for obtaining the radiation pattern of antennas both over multilayered substrate or dielectric lens were used in Chapters 3 and 4 in order to calculate the radiation pattern of the so called LAEs and the radiation pattern of the developed detectors (Schottky and MOSFET).

Regarding THz emitters, Chapter 3 was focused on CW Photomixer based THz emitters. Two approaches have been followed to improve the radiated THz power. The first one consists on an AE where the antenna has been designed in such a way that the emitted power is maximized and the overall emitter has been simplified because the typical RF choke has been eliminated. The second approach is an antenna-free scheme of photomixing where the THz radiation is directly originated from the acceleration of photo-induced charge carriers generated within a large semiconductor area. This is called LAE and the work developed in this Ph.D. dissertation consists on designing an electromagnetic equivalent circuit based on infinitesimal dipoles to estimate the radiation pattern of it. This LAE approach theoretically eliminates the optical power constraints that antenna emitters have and the THz emitted power can be increased, theoretically, up to infinite. Some future lines related with this topic will be proposed below.

Chapter 4 was devoted to sub-THz detectors and the work developed consists on designing two direct detectors: a QO SBD detector working within the E-Band (60 GHz - 90 GHz) and a plasma-wave FET CMOS detector working at 300 GHz. A complete QO SBD receiver design and characterization was carried out in this chapter. The receiver

was meant to take part of a very-high speed data wireless transmission system (> 1 Gb/s). Regarding the FET direct detector, the very first steps for a 300 GHz receiver were presented. Its main application is an array for imaging applications (security). Both designs were formed from a planar antenna and a detector (either SBD or FET), with the possibility of including an optical device (lens). Their performance was improved by designing the antenna of each receiver in such a way that the total efficiency was maximized.

Regarding THz systems, a focusing system was designed for a 300 GHz radar for security purposes. While previous chapters were focused on planar antennas, in this case a horn antenna and elliptical mirrors were used, thus leading to a more complex structure. On the other hand it can handle more power and provide better focusing capabilities. The main contribution of the chapter was designing the focusing system in such a way that it can provide scanning capabilities but, at the same time, the beam is not distorted because it always works "in-focus". The focusing system consists of a horn antenna as feeding element, two elliptical mirrors and a plane one to provide beam-steering by rotation. Since the only mirror that is rotated to provide scanning capabilities is the plane one, the target distance is always at the output focus of the second elliptical mirror, so the beam is not distorted even for big displacements. In addition to the proposed system, the design methodology followed through the chapter is also relevant because it reduces computational time and effort, and obtained results are accurate enough. Some future research lines will be outlined below.

Finally, it is remarked that the work presented in this Ph.D. dissertation has led to 6 journal papers and a book chapter, as well as it has been presented in 14 conferences. The list of contributions is detailed in the *Publications* section at the end of this book.

6.2 Future Lines

In this section, the proposed future lines for the work developed during this Ph.D. dissertation are described. Three main sections are differentiated: THz emitters, sub-THz detectors and the focusing system.

6.2.1 THz Emitters

Regarding the THz emitters presented in this Ph.D. dissertation two main future lines can be followed. The 1.05 THz meander dipole antenna emitter is intended to be the local oscillator source of one of the heterodyne detectors in the SOFIA [1], so integration in the receiver and test the overall behaviour will be the next development step.

Figure 6.1: NASA's SOFIA.

The other THz emitter presented in this Ph.D. dissertation, the LAE, are in the manufacture and measure stage. First prototypes have been manufactured and they are expected to be measured during the next months. It has to be mentioned that that the full measurement and characterization of them is a tricky task and is out of the scope of the present work. Precisely preparing the measurements set-up will take some time and measuring the radiation patterns, as well as the THz output power for different optical spot size illuminations requires a big effort. With such measurements it is expected to validate the radiation equivalent circuit presented in the Chapter 3 of this book.

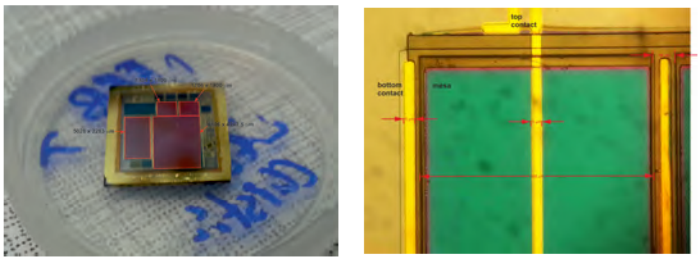

(a) (b)

Figure 6.2: (a) Manufactured LAE devices and (b) Detail of one of the mesas.

6.2.2 Sub-THz Detectors

In the sub-THz detectors chapter, two main technologies were discussed. The first one is a QO SBD detector working within the E-Band. This detector is nowadays a product developed by ACST GmbH [2] and can be acquired in that company. This work was also translated to higher frequencies and different detectors can be bought. One future work that can be done is to include a video amplifier at the output of the 50 Ω transition in order to increase the detector responsivity.

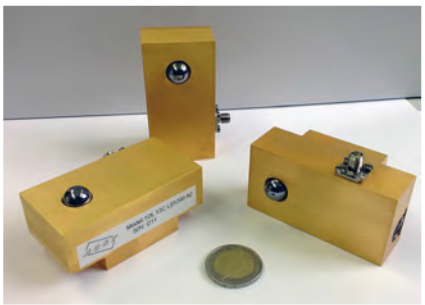

Figure 6.3: ACST's QO detector modules [2].

Regarding the CMOS technology detectors developed in the Chapter 4 a higher effort shall be done to increase the responsivity values and reach the state-of-the-art results. It has to be mentioned that measurements were taken without a video amplifier, so responsivity values are expected to be worse, but they are not as good as expected. Three main

research lines can be followed to improve those devices. First one may consist on including a video amplifier so the output signal will be amplified thus the responsivity. The second one is a more tricky one and will consist on measuring or estimating the input impedance of the transistors at these frequencies (300 GHz) and design the antenna in such a way that maximum power is transferred from the antenna to the active device. With such information the optimal antenna can be designed and the responsivity will be increased. Finally, an array topology can be considered either to increase the responsivity either to have an imaging array.

6.2.3 Focusing System

The main drawback of the proposed focusing system is that only simulation results are provided, although the software used to validate the design process, GRASP [3], has proved its accuracy over decades. This is due to the fact that the expenses of manufacturing the overall system are very high and our research group can not afford such quantity. So the straightforward future line for the proposed system is to manufacture, measure and validate the obtained results.

Once the focusing system is tested and characterized, it needs to be included with all the necessary electrical components to generate the 300 GHz signal and with the signal processing capabilities to detect weapons or other objects hidden in the scanning targets to construct a terahertz radar.

6.3 References

[1] Stratospheric Observatory for Infrared Astronomy. (2014, June) SOFIA. [Online]. Available: http://www.sofia.usra.edu/index.html

[2] Advanced Compound Semiconductor GmbH. (2014, March) ACST. [Online]. Available: http://www.acst.de/

[3] General Reflector and Antenna Arm Analysis Software. (2014, January) GRASP. [Online]. Available: http://www.ticra.com/products/software/grasp

PUBLICATIONS

The work developed in this Ph.D. dissertation has led to several journal, book and conference contributions. The complete list is detailed below.

Journal papers (6):

Related with Chapter 2:

- L. E. García-Muñoz, E. Ugarte-Muñoz, J. Montero-de-Paz, A. Rivera-Lavado, D. Segovia-Vargas, "Anomalous Behavior in the Radiation Patterns," *IEEE Transactions on Antennas and Propagation*, vol. 61, no. 2, pp. 973-976, Feb. 2013.

Related with Chapter 3:

- J. Montero-de-Paz, E. Ugarte-Muñoz, L. E. García-Muñoz, I. Cámara-Mayorga, D. Segovia-Vargas, "Meander Dipole Antenna to Increase CW THz Photomixing Emitted Power," *IEEE Transactions on Antennas and Propagation*, accepted for publication.

- G. H. Döhler, L. E. García-Muñoz, S. Preu, S. Malzer, S. Bauerschmidt, J. Montero-de-Paz, E. Ugarte-Muñoz, A. Rivera-Lavado, V. Gonzalez-Posadas, D. Segovia-Vargas, "From Arrays of THz Antennas to Large-Area Emitters," *IEEE Transactions on Terahertz Science and Technology*, vol. 3, no. 5, pp. 532-544, Sep. 2013.

Related with Chapter 4:

- J. Montero-de-Paz, I. Oprea, V. Rymanov, S. Babiel, L. E. García-Muñoz, A. Lisauskas, M. Hoefle, A. Jiménez, O. Cojocari, D. Segovia-Vargas, M. Palandöken, T. Tekin, A. Stöhr, G. Carpintero, "Compact Modules for Wireless Communication Systems in the E-Band (71 - 76 GHz)," *Journal of Infrared, Millimeter, and Terahertz Waves*, vol. 34, no. 3-4, pp. 251-266, Apr. 2013.
- J. Montero-de-Paz, I. Oprea, V. Rymanov, S. Babiel, L.E. García-Muñoz, A. Lisauskas, M. Hoefle, A. Jiménez, O. Cojocari, D. Segovia-Vargas, A. Stöhr, G. Carpintero,"E-band (71–76 GHz) wireless link using compact modules," *IET Electronics Letters*, vol 49, no. 7, pp. 476-477, Mar. 2013.

Related with Chapter 5:

- J. Montero-de-Paz, L. E. García-Muñoz, D. Segovia-Vargas, "A 300 GHz Always-In-Focus Focusing System for Target Detection," *Radioengineering*, vol. 22, no. 2, pp. 610-617, Jun. 2013.

Book chapters (1):

Related with Chapters 2 and 3:

- Semiconductor THz Technology: From Components to Systems. Chapter 3: Principles of emission of THz waves. Wiley. To be published.

Conferences (13):

Related with Chapter 2:

- J. Montero-de-Paz, J. Ancizu-Vergara, B. Andrés-García, L. E. García-Muñoz, D. Segovia-Vargas, "Diseño de Lentes Hemisféricas Extendidas para Antenas Planas en el Régimen de Milimétricas y Sub-Milimétricas," *XXV Simposium Nacional de la Unión Científica Internacional de Radio*, Bilbao, Sep. 2010.

Related with Chapter 3:

- L. E. García-Muñoz and J. Montero-de-Paz, "THz beam steering and power enhancement based on photomixer technology," *Nano and Giga Challenges in Electronics, Photonics and Renewable Energy*, Phoenix, Arizona, US, March 2014.
- L. E. García-Muñoz, J. Montero-de-Paz, A. Rivera-Lavado, I. Cámara-Mayorga, R. Güsten, A. Generalov, D. Lioubtchenko, P. Acedo-Gallardo, C. de-Dios, R. Criado, E. Ugarte-Muñoz, A.V. Räisänen, D. Segovia, "THz Antenna Array Based on Photomixers for Radioastronomy Applications," *7th European Conference on Antennas and Propagation*, Gothenburg, Apr. 2013.
- L. E. García-Muñoz, G. Döhler, J. Montero-de-Paz, E. Ugarte-Muñoz, A. Rivera-Lavado, S. Preu, S. Malzer, S. Bauerschmidt, V. González-Posadas, D. Segovia-Vargas, "New Device for Continuous-Wave THz Emission: Large Area Emitter," *7th European Conference on Antennas and Propagation*, Gothenburg, Apr. 2013.
- A. Rivera-Lavado, L. E. García-Muñoz, G. Döhler, S. Malzer, V. Izquierdo-Vermúdez, S. Preu, J. Montero-de-Paz, E. Ugarte-Muñoz, S. Bauerschmidt, D. Segovia, "Nuevo dispositivo para la generación de THz (Large Area Emitter)," *XXVII Simposium Nacional de la Unión Científica Internacional de Radio*, Elche, Sep. 2012.

Related with Chapter 4:

- D. Segovia-Vargas, J. Montero-de-Paz, A. Portillo-López-Mingo, J. Crooks, P. G. Huggard, L. E. García-Muñoz, V. González-Posadas, B. Alderman, R. Turchetta, "Receptores Homodinos a 300 GHz basados en tecnología CMOS," *XXVIII Simposium Nacional de la Unión Científica Internacional de Radio*, Santiago de Compostela, Sep. 2013.

- D. Segovia-Vargas, J. Montero-de-Paz, J. Crooks, P. G. Huggard, L. E. García, V. González-Posadas, "300 GHz CMOS Video Detection using Broadband and Active Planar Antennas," *7th European Conference on Antennas and Propagation*, Gothenburg, Apr. 2013.

- S. Babiel, I. Flammia, A. Stöhr, J. Montero, L. E. García, D. Segovia, G. Carpintero, O. Cojocari, Alvydas Lisauskas, "Compact transmitter and receiver modules for E-band wireless links," *Optical Fiber Communication Conference and Exposition (OFC) and The National Fiber Optic Engineers Conference (NFOEC)*, Anaheim, Mar. 2013.

- J. Montero-de-Paz, M. Hoefle, I. Oprea, O. Cojocari, L. E. García-Muñoz, D. Segovia-Vargas, R. Jakoby, G. Carpintero, "Compact Schottky Barrier Diode Receiver for E-Band (60–90 GHz) Wireless Communications," *2012 International Topic Meeting on Microwave Photonics*, Noordwijk, Sep. 2012.

- J. Montero-De-Paz, E. Ugarte-Muñoz, L. E. García-Muñoz, D. Segovia-Vargas, "Receptor a 75 GHz basado en antena folded dipole y diodo Schottky para máxima transferencia de potencia," *XXVII Simposium Nacional de la Unión Científica Internacional de Radio*, Elche, Sep. 2012.

- J. Montero-de-Paz, E. Ugarte-Muñoz, L. E. García-Muñoz, D. Segovia-Vargas, D. Schoenherr, I. Oprea, A. Amrhein, O. Cojocari, H. L. Hartnagel, "Millimeter-Wave Receiver Based on a Folded Dipole Antenna and Schottky Diode for Maximum Power Transfer," *6th European Conference on Antennas and Propagation*, Prague, Mar. 2012.

Related with Chapter 5:

- J. Montero-de-Paz, O. García-Pérez, A. Rivera-Lavado, E. Ugarte-Muñoz, B. Andrés-García, M. Molina-Romero, T. Finn, J. A. López-Fernández, V. González-Posadas, L. E. García-Muñoz, D. Segovia-Vargas, "Sistema de Enfoque Basado en Dos Espejos Elípticos y Un Espejo Plano Rotatorio para un Radar a 300GHz," *XXVI Simposium Nacional de la Unión Científica Internacional de Radio*, Leganés, Sep. 2011.
- J. Montero-de-Paz, O. García-Perez, A. Rivera-Lavado, E. Ugarte-Muñoz, B. Andrés-García, M. Molina-Romero, T. Finn, J. A. López-Fernández, V. González-Posadas, L. E. García-Muñoz, D. Segovia-Vargas, "Focusing System for a 300 GHz Radar with Two Target Distances," *5th European Conference on Antennas and Propagation*, Rome, Apr. 2011.

OTHER PUBLICATIONS

In addition to the previous publication list, the author has done the following work not directly related to the main topic of this Ph.D. dissertation.

Journal papers (5):

- A. Rivera-Lavado, L. E. García-Muñoz, G. Döhler, S. Malzer, S. Preu, S. Bauerschmidt, J. Montero-de-Paz, E. Ugarte-Muñoz, B. Andrés-García, V. Izquierdo-Bermúdez, D. Segovia- Vargas, "Arrays and New Antenna Topologies for Increasing THz Power Generation Using Photomixers," *Journal of Infrared, Millimeter, and Terahertz Waves*, vol. 34, no. 2, pp. 97-108, Feb. 2013.

- A. R. Criado, J. Montero-de-Paz, C. De-Dios, L.E. García-Muñoz, D. Segovia-Vargas, P. Acedo, "Photonic Heterodyne Pixel for Imaging Arrays at Microwave and MM-Wave Frequencies," *Advances in Optical Technologies*, vol. 2012, article ID 792571, 7 pages, 2012.

- J. Montero-de-Paz, , E. Ugarte-Muñoz, F.J. Herraiz-Martínez, V. González-Posadas, L.E. García-Muñoz and D. Segovia-Vargas, "Multifrequency self-diplexed single patch antennas loaded with split ring resonators," *Progress in Electromagnetics Research*, 113, pp. 47-66, 2011.

- E. Ugarte-Muñoz, F.J. Herraiz-Martínez, J. Montero-de-Paz, L.E. García-Muñoz and D. Segovia-Vargas, "Planar superstrate for dual-frequency RHCP-LHCP array," *Applied Physics A: Materials Science and Processing*, 103 (3), pp. 843-848, 2011.
- D. Segovia-Vargas, F.J. Herraiz-Martínez, E. Ugarte-Muñoz, J. Montero-de-Paz, V. González-Posadas and L.E. García-Muñoz, "Multifrequency printed antennas loaded with metamaterial particles," *Radioengineering*, 18 (2), pp. 129-143, 2009.

Conferences (13):

- A. Rivera-Lavado et al., "Ultra-Wideband Dielectric Rod Waveguide Antenna as Photomixer-Based THz Emitter," *Proceedings of the 8th European Conference on Antennas and Propagation (EUCAP)*, The Hague, The Netherlands, 2014.
- I. Fernández Rodríguez et al., "Diseño y Fabricación de una Transición Guía Onda a Microstrip en Banda F," *XXVIII Simposium Nacional de la Unión Científica Internacional de Radio*, Santiago de Compostela, Spain, September 2013.
- A. R. Criado et al., "Optoelectronic Imaging Array for Microwave and mm-wave Frequency Range", *XXVII Simposium Nacional de la Unión Científica Internacional de Radio URSI*, Elche, Spain, 2012.
- A. R. Criado et al., "Implementación de un Pixel para Detección Heterodina en el Rango de Ondas Milimétricas usando Oscilador Local y Mezclado Fotónico", *XXVI Simposium Nacional de la Unión Científica Internacional de Radio URSI*, Leganés, Spain, 2011.
- J. Montero-de-Paz et al., "Dual-Frequency Self-Diplexed Single Patch Antenna Loaded With Split-Ring Resonators," *Young Scientist Meeting On Metamaterials 2011 (YSMM 2011)*, Valencia, Spain, February 2011.

- E. Ugarte Muñoz et al., "Superestratos Planos para Antenas Multi-Frecuencia con Polarización Dual o Circular," *XXV Simposium Nacional de la Unión Científica Internacional de Radio URSI*, Bilbao, Spain, 2010.
- E. Ugarte-Muñoz, et al., "Planar superstrate made with metamaterial particles for dual-polarized dual-frequency antennas and circularly polarized antennas," *IEEE International Symposium on Antennas and Propagation, AP-S/URSI*, Toronto, Canada, art. no. 5561162, 2010.
- J. Montero-De-Paz, et al., "Multifrequency single patch antennas loaded with Split Ring Resonators," *The 4th European Conference on Antennas and Propagation*, Barcelona, Spain, art. no. 5505645, 2010.
- E. Ugarte Muñoz et al., "Planar Superestrates For Dual Frequency RHCP-LHCP Arrays," *META'10*, El Cairo, Egypt, February 2010.
- J. Montero-de-Paz et al., "Antenas Multifrecuencia con Split-Ring-Resonators Parásitos en Banda X," *XXIV Simposium Nacional de la Unión Científica Internacional de Radio URSI*, Santander, Spain, 2009.
- J. Montero-de-Paz et al., "Multifrequency Patch Antennas With Parasitic SRRs in X-Band," *Young Scientist Meeting on Metamaterials (YSMM 2009)*, Madrid, Spain, July 2009.
- E. Ugarte-Muñoz et al., "Planar Meta-Surfaces For Dual-Polarized Dual-Frequency Antennas," *Young Scientist Meeting on Metamaterials (YSMM 2009)*, Madrid, Spain, July 2009.
- F. J. Herráiz-Martínez et al., "Applications of Metamaterials Loaded Antennas," *Young Scientist Meeting on Metamaterials (YSMM 2009)*, Madrid, Spain, July 2009.

About the Author

Javier Montero de Paz was born in Madrid, Spain, on May 29, 1984. He received the Master degree in Telecommunications Engineering from Carlos III University, Madrid, Spain, in 2009, and the Master degree in Multimedia and Communications from Carlos III University, Madrid, Spain, in 2011. Since 2009 he is working with the Group of Radiofrequency, Electromagnetism, Microwaves and Antennas at Carlos III University. He as authored or co-authored 11 JCR journal papers, 30 conferences contributions and a national patent. He has participated in 9 research and development projects and he has been teacher of different Grade and Master level subjects at the university. He has also supervised 5 Master Theses and his research lines are terahertz antennas, active integrated antennas, Schottky diodes, dielectric lenses, CMOS THz detectors and metamaterials.